Title
Asperity-scale surface mechanics - Implications to adhesive contacts and microscale deformation behavior of rough surfaces

Author
Xu, Huaming

Publication Date
2012

Peer reviewed|Thesis/dissertation

Asperity-scale surface mechanics - Implications to adhesive contacts and microscale deformation behavior of rough surfaces

by

Huaming Xu

A dissertation submitted in partial satisfaction of the

requirements for the degree of

Doctor of Philosophy

in

Engineering – Mechanical Engineering

in the

Graduate Division

of the

University of California at Berkeley

Committee in charge:
Professor Kyriakos Komvopoulos, Chair
Professor David A Dornfeld
Professor Ronald S Fearing

Fall 2012

Abstract

Asperity-scale surface mechanics - Implications to adhesive contacts
and microscale deformation behavior of rough surfaces

by

Huaming Xu

Doctor of Philosophy in Engineering-Mechanical Engineering

University of California, Berkeley

Professor Kyriakos Komvopoulos, Chair

The principal objective of this dissertation was to develop numerical and analytical mechanics models accounting for nano-/micro-scale solid surface interaction. This was accomplished by developing finite element models of an asperity in adhesive sliding contact with a homogenous half-space and asperity micro-fracture due to normal and sliding contact of homogenous or layered half-spaces, and analytical models of nanoscale surface polishing and nanoparticle embedment on rough surfaces using a probabilistic approach.

Adhesive interaction of a rigid asperity moving over a homogeneous elastic-plastic half-space was modeled by nonlinear springs obeying a constitutive law derived from the Lennard-Jones potential. The evolution of the normal and friction forces, subsurface stresses, and plastic deformation at steady-state sliding was examined in terms of the work of adhesion, interaction distance (interfacial gap), Maugis parameter, and plasticity parameter, using the finite element method (FEM). The deformation behavior of homogeneous elastic-perfectly plastic (EPP) and elastic-linear kinematic hardening plastic (ELKP) half-spaces subjected to repeated adhesive sliding contacts was also the objective of this analysis. Numerical results provided insight into the effects of the aforementioned parameters on the friction and normal forces, stress-strain response, and evolution of subsurface plasticity with the accumulation of sliding cycles. The steady-state mode of deformation due to repeated adhesive sliding contacts was examined for both EPP and ELKP material behavior.

Subsurface cracking in a layered medium consisting of an elastic hard layer and an elastic-plastic substrate due to adhesive sliding against a rigid asperity was analyzed using linear elastic fracture mechanics (LEFM) and FEM model. The dominance of shear and tensile mode of crack propagation was examined in terms of the interaction depth, layer thickness, crack location, crack length, work of adhesion, and mechanical properties of the thin layer and substrate materials. The effect of adhesion on asperity failure due to normal contact was also studied. The crack growth direction, dominant fracture mode, and crack growth rate were predicted as functions of the initial crack position, asperity interaction distance, interfacial properties, and

mechanical properties. FEM results showed the occurrence of different crack mechanisms, such as of crack-face opening, slip, and stick.

The evolution of the surface topography during nanoscale surface polishing was studied with a three-dimensional stochastic model that accounts for a multi-scale (fractal) surface roughness and elastic, elastic-plastic, and fully-plastic deformation of the asperities on the polished surface caused by hard abrasive nanoparticles embedded in the soft surface layer of a rigid polishing countersurface. Numerical results of the steady-state roughness of the polished surface, material removal rate, and wear coefficient were determined in terms of the apparent contact pressure, polishing speed, original topography and mechanical properties of the polished surface, average size and density of the nanoparticles, and surface roughness of the polishing plate. The density of hard abrasive nanoparticles embedded in the soft countersurface was predicted by a probabilistic-hydrodynamic model in terms of the surface topographies, particle size distribution, applied forces, macroscopic geometry of the moving surfaces, surface kinematics, and fluid properties.

The findings of this dissertation yield new insight into the deformation behavior of adhesive contacts involving homogeneous and layered half-spaces, from the single asperity level to surfaces with multi-asperity topographies. The significance of the interfacial properties and material properties on adhesive asperity sliding contact, the effects of interfacial adhesion and crack properties on asperity cracking and subsurface cracking, and the dependence of the surface topography evolution during nanoscale polishing on the surface topographies, material properties, and abrasive nanoparticle size were examined in the context of numerical and analytical results. The results of this thesis elucidate the mechanical aspects of surface contact interaction in nano/microscale engineering components and surfacing processes, such as hard-disk drives, micro-electro-mechanical systems, and nanoscale surface polishing, and provide insight into the underlying reasons leading to mechanical failure of homogeneous and layered half-spaces subjected to surface tractions. Solutions and FEM results for single-asperity contacts obtained in this work can be integrated into probabilistic analyses of contacting rough surfaces to advance the current state of contact mechanics of surfaces exhibiting multi-asperity topographies.

Table of Contents

List of Figures

Acknowledgements

I would like to express my most sincere gratitude to my research advisor, Professor Kyriakos Komvopoulos, for his encouragement, guidance, enthusiasm, moral and intellectual support, and endless patience, without which this dissertation is never possible.

I greatly appreciate Professor David A. Dornfeld and Professor Ronald S. Fearing for serving on my dissertation committee; Professor Hari Dharan, Professor David B. Bogy, Professor Tarek Zohdi and Professor John W. Morris on my qualifying exam committee. Their advice and invaluable help make me finish my study at Berkeley much smoother.

I would like to thank all the members in Surface Sciences and Engineering Laboratory (SSEL) and Computational Surface Mechanics Laboratory (CSML), who have provided discussion and support on my research or course work.

I also would like to thank my friends, Chunhui Gu, Xingwei Wu, Song Deng, Yingqi Jiang, Jian Ding, Huanhuan Qi, etc., for their friendship and support.

Finally, I owe my deepest gratitude to my parents and my sister for their invaluable support and patience through years of my study. I really appreciate my girlfriend Xiaolu Zhou for her love, encouragement and support to make me finish my dissertation.

Chapter 1
Introduction

Friction and wear are common phenomena in today's industrial world, mostly encountered at components with contacting surfaces in relative motion, such as human joints, gears, bearings, head and disk of hard-disk drives, microswitches, microrelays, and other microelectromechanical systems. Understanding the interaction between surfaces in relative motion is critical for reducing friction and wear of mechanical devices, conserving energy, and improving the efficiency and lifetime of mechanical systems.

Contact mechanics, the field concerned with the stresses and deformation of solid bodies in contact is of great importance in the study of interface contact interactions. The origin of contact mechanics probably dates back to the pioneering study of Hertz (1882), who derived closed-form solutions for the contact pressure distribution and contact area established between two solids of revolution in frictionless contact. Hertz's theory formed the basis for subsequent studies of rolling and sliding elastic contacts, such as those in railways and marine gears. With the development of plasticity theory, contact deformation of elastic-plastic solids was analyzed under various loading conditions, thereby enabling the design of more durable bearing components. Because analytical approaches were inhibited by complex structural and elastic-plastic material behaviors, numerical methods, such as the finite element method, introduced in the 1970s were widely used to solve various elastic-plastic contact problems, especially with the rapid advances in computing capabilities.

Owing to the high wear resistance and low friction characteristics, various coating or thin film materials have been often used in mechanical, electronic, magnetic, and optical devices to improve the performance and prolong the longevity by suppressing plastic deformation and contact fatigue. Because it is difficult to obtain closed-form solutions for elastic-plastic contact of layered-media using analytical methods, numerical techniques were widely used in contemporary contact mechanics. The efficacy of a hard surface layer to reduce plastic deformation in the substrate material by confining the high stresses within its bulk has been observed in numerous finite element analyses. The increase of contact stress due to excessive loads leads to plastic flow of the near-surface material, often followed by crack initiation and propagation, resulting in rapid surface degradation and eventual cessation of the device operation. Understanding of elastic-plastic deformation and fracture in homogeneous and layered media subjected to surface traction enabled studies of wear particle formation to be carried out. In particular, the criteria of the maximum tensile stress and strain energy density were commonly used for static loading, whereas criteria based on the concept of the maximum stress intensity factor range were developed for cyclic contact loading.

Despite significant insight into contact deformation phenomena derived from numerical and analytical contact mechanics studies, the majority of the obtained results are only applicable to macroscopically smooth surfaces. However, real surface topographies consist of smaller-on-larger asperity hierarchies spanning a wide range of length scales, which are of great importance to the contact behavior. Traditionally, surface topographies have been characterized by statistical

roughness parameters that depend on the sample length. One of the most widely quoted contact models accounting for roughness effects is that of Greenwood and Williamson (1966), known as the GW model in which the asperity heights are assumed to follow a normal distribution, while the asperity radius is fixed. However, microscopy observations indicate that most engineering surfaces exhibit multi-scale roughness that exhibits fractal behavior, which is characterized by the properties of continuity, non-differentiability, scale invariance (i.e., independent of the sample length), and self-affinity (i.e., similar surface features are observed at different magnifications). Because fractal geometry can describe the multi-scale nature of the surface roughness, it provided an effective means estimating the contact area, contact load, interfacial temperature rise due to friction heating, and deformation at the asperity scale on rough surfaces of homogenous half-spaces and layered media.

In view of the multi-scale roughness of real surfaces, the accuracy of contact analyses of rough surfaces greatly depends on the constitutive relations applicable at the asperity level. The contact analysis is further perplexed by adhesion effects that play particularly important role in asperity-asperity interactions under light contact loads. Since the first elastic adhesive contact model of Bradley (1932), significant progress has been made in the study of elastic adhesive contacts. According to the Bradley model, the pull-off force F_{po} at the instant of separation of two rigid spheres is given by $F_{\mathrm{po}} = 2\pi R\Delta\gamma$, where R is the equivalent radius of curvature ($R = [1/R_1 + 1/R_2]^{-1}$, where R_1 and R_2 are the radii of curvature of the two spheres) and $\Delta\gamma$ is the work of adhesion ($\Delta\gamma = \gamma_1 + \gamma_2 - \gamma_{12}$, where γ_1 and γ_2 are the surface energies of the two spheres and γ_{12} is the surface energy of the contact interface). A similar equation of the pull-off force is given by the DMT model developed by Derjaguin et al. (1975), while the JKR model proposed by Johnson et al. (1971) yields $F_{\mathrm{po}} = (3/2)\pi R\Delta\gamma$. This discrepancy in the pull-off force is attributed to differences in the interfacial conditions and stiffness of the contacting solid surfaces. Tabor (1977) has argued that the DMT (rigid contact) and the JKR (elastic contact) models represented upper and lower limits, respectively, of the pull-off force. Maugis (1992) used the Dugdale approximation to describe interfacial adhesion and obtained an analytical solution of the pull-off force for the transition range bounded by the DMT and JKR solutions, which was found to be in good agreement with the numerical solutions using the Lennard-Jones (L-J) potential to model adhesion.

In addition to the study of contacting spherical bodies, significant effort was also devoted to the study of cylindrical contacts. In contrast to spherical contacts, the pull-off force of cylindrical contacts depends on the effective elastic modulus. For instance, the pull-off force (per unit length) of elastic cylindrical contacts obtained by Chaudhury et al. (1996) using a two-dimensional (2D) JKR model is given by $F_{\mathrm{po}} = (3/4)(4\pi E^* R\Delta\gamma^2)^{1/3}$, whereas the pull-off forces of rigid cylindrical contacts derived from the 2D Bradley model and the 2D DMT model is equal to $(5.9248\lambda)^{1/2}(E^* R\Delta\gamma^2)^{1/3}$ and $(8\lambda)^{1/2}(E^* R\Delta\gamma^2)^{1/3}$, respectively. Using the Lennard-Jones (L-J) potential to model adhesion, Wu (2009) obtained a numerical solution of the pull-off force in the transition range bounded by the 2D JKR and 2D Bradley solutions, which was different with that obtained by Johnson and Greenwood (2008) with a 2D Maugis model with the pull-off force in the transition range bounded by the 2D JKR and 2D DMT solutions. These studies of adhesive elastic contacts spurred interest on the analyses of elastic-plastic adhesive contact problems, such as load/unload behavior of adhesive elastic-plastic contacts, adhesion-induced contact

instabilities (jump-in and jump-out), and force-distance response due to cyclic contact loading, and the role of interfacial adhesion on the evolution of plasticity and cracking under various loading conditions.

Despite invaluable insight into the role of adhesive surface interactions in surface mechanics provided by previously discussed studies, it is questionable whether the results of these studies can be directly applied to adhesive sliding contacts, for which continuum mechanics studies are sparse. Even though molecular dynamics (MD) simulations have shed some light into adhesion (friction) contact phenomena at scales approaching those of atomic force and surface force microscopy, the incorporation of the computationally intensive MD codes into continuum mechanics analysis is a challenging task. The objectives of this dissertation were to perform comprehensive analyses of adhesive sliding contacts based on continuum mechanics with emphasis on the analysis of (a) asperity-scale adhesive sliding contact behavior under static and cyclic contact loads, (b) subsurface cracking in layered media subjected to adhesive sliding traction, (c) asperity cracking due to adhesive contact, and (d) surface topography evolution of polishing process studied by a probabilistic method including the integration of asperity-scale stress-strain governing equations into the rough-surface model. A brief description of the main contents of Chapters 2 through 9 is given below.

Chapter 2 presents finite element study of the effect of adhesion on elastic-plastic deformation of sliding contacts. Adhesive interaction of a rigid asperity moving over a homogeneous elastic-plastic half-space is modeled by nonlinear springs obeying a constitutive law derived from the L-J potential. The effects of the work of adhesion, interaction distance (interfacial gap), Maugis parameter, and plasticity parameter (defined as the work of adhesion divided by the half-space yield strength and the intermolecular equilibrium distance) on the evolution of normal and friction forces, subsurface stresses, and plastic deformation at steady-state sliding are interpreted in light of finite element results of displacement-control simulations of sliding contact. Both normal and friction forces and the rate of energy dissipation due to plastic deformation at steady-state sliding are shown to sharply increase with the interaction distance. Although a higher work of adhesion yields a lower normal force, it intensifies the friction force, enhances the pile-up of material ahead of the sliding asperity, and exacerbates the asymmetry of the deformed surface profile and normal stress field. The variation of the normal force with the plasticity parameter is explained by the dominant effect of subsurface plastic deformation above a critical plasticity parameter. In addition, simulation results are shown to be in good agreement with those of previous experimental and numerical studies.

Chapter 3 examines the deformation of homogeneous elastic-perfectly plastic (EPP) and elastic-linear kinematic hardening plastic (ELKP) half-spaces due to repeated adhesive sliding contact, using a finite element model similar to that used in Chapter 2. Deformation behavior is interpreted in terms of dimensionless parameters, such as the Maugis parameter, interaction distance (interfacial gap), and plasticity parameter. Numerical results provide insight into the stress-strain response and evolution of subsurface plasticity. The effects of interaction distance, plasticity parameter, interfacial adhesion, and Maugis parameter on the friction and normal forces and the accumulation of plasticity are analyzed in terms of the sliding cycles. Deformation maps providing information about the steady-state mode of deformation are presented for both EPP and ELKP material behaviors. The results presented in this chapter illustrate the importance

of elastic-plastic material behavior and interfacial adhesion in contact deformation due to repeated surface sliding.

Chapter 4 includes an analysis of subsurface cracking in layered media subjected to adhesive sliding contact by a rigid asperity. The analysis is based on linear-elastic fracture mechanics, the finite element method (FEM), and the L-J potential. The layer medium consists of an elastic hard layer and an elastic-perfectly plastic substrate. Tensile and shear mode fracture directions are determined by the directions of the maximum tensile and shear stress intensity factors, respectively, whereas tensile and shear mode fatigue-crack growth directions are determined by the directions of the maximum ranges of tensile and shear mode stress intensity factors, respectively. The propensity for fracture or fatigue and associated tensile and shear mode crack growth directions are interpreted in terms of the interaction depth, layer thickness, initial crack position, crack length, surface adhesion, and material properties of the layer and the substrate. It is shown that the tendency for fracture and the fatigue-crack growth rate are enhanced by the increase of the interaction depth, the Maugis parameter, and the interfacial adhesion, or with the decrease of the layer thickness. Out-of-plane tensile mode crack propagation is more favored under fracture conditions, whereas in-plane shear mode crack propagation is more likely to occur under fatigue conditions.

Chapter 5 provides an analysis of asperity cracking due to repetitive adhesive contact against a rigid plane based on linear elastic fracture mechanics (LEFM) and the FEM. Using the Derjaguin approximation, adhesion between the rigid plane and the elastic asperity is modeled by nonlinear spring elements attached to the rigid plane and asperity surface nodes. The spring elements follow a non-linear force-distance relation that obeys the L-J potential. The direction, rate, and dominant mode of crack propagation are determined by the maximum range of the tensile and shear stress intensity factors (SIFs) in terms of the initial crack position, crack-face friction, maximum indentation displacement, and the Maugis parameter. It is shown that the Maugis parameter and the maximum indentation displacement exhibit the most pronounced effects on the crack growth direction and the growth rate. A shear-to-tensile dominant mode of crack growth transition is observed with the increase of the Maugis parameter and/or the decrease of the maximum indentation displacement. Crack-face opening, slip, and static mechanisms are discussed in the light of crack mechanism maps obtained for different values of the indentation displacement and/or the Maugis parameter.

Cracking of a deformable asperity due to repetitive sliding against a rigid asperity is analyzed in Chapter 6 using LEFM and the FEM. The effects of asperity interaction depth, sliding friction, initial crack position, crack-face friction, and material properties on the direction, rate, and dominant mode of crack growth are determined based on the maximum range of the tensile and shear SIFs. The asperity interaction depth and sliding friction demonstrate the most pronounced effect on the crack growth direction and the growth rate. A shear-to-tensile dominant mode of crack growth transition is again observed with the increase of the asperity interaction depth and/or sliding friction coefficient. Crack mechanism maps of different crack-face friction coefficients, asperity interaction depths, and sliding friction coefficients elucidate the evolution of opening, slip, and stick mechanisms between the crack faces.

A quasi-static analysis of nanoscale surface polishing that provides insight into the surface topography evolution and the removal of material at the asperity level is presented in Chapter 7. The analysis is based on a three-dimensional stochastic model that accounts for multi-scale (fractal) surface roughness and elastic, elastic-plastic, and fully-plastic deformation of asperities on the polished surface caused by hard abrasive nanoparticles embedded into the soft surface layer of a rigid polishing plate. Numerical results of the steady-state roughness of the polished surface, material removal rate, and wear coefficient are discussed in terms of the apparent contact pressure, polishing speed, original topography and mechanical properties of the polished surface, average size and density of the nanoparticles, and surface roughness of the polishing plate. Simulation trends are associated with elastic-plastic and fully-plastic asperity contacts, responsible for irreversible topography changes (roughening effect) and the removal of material (smoothening effect), respectively. Analytical trends and predictions of the final roughness of the polished surface and the steady-state material removal rate are shown to be in good agreement with experimental results of the present and other studies of nanoscale surface polishing (lapping) of magnetic recording ceramic heads.

Chapter 8 introduces a probabilistic model of third-body particle embedment for surfaces separated by a hydrodynamic slurry film. The analysis yields estimates of the embedded particle density in terms of surface topography parameters, particle size distribution, and mean surface separation distance, which is determined by a hydrodynamic model in terms of the applied normal load, the macroscopic geometry of the moving surfaces, the friction coefficients between the top plate and the rollers, the problem kinematics, and the fluid properties. The model has direct application to chemical-mechanical polishing and the fabrication of lapping plates for polishing magnetic recording heads. Numerical results show that the density of the embedded particles can be increased by reducing the mean surface separation distance. This can be accomplished by either increasing the applied load or by decreasing the slurry viscosity, the bottom-plate rotational speed, or the ratio of the friction coefficients between the rollers and the top plate. It is also shown that the density of the embedded particles is a strong function of the mean particle size.

Finally, Chapter 9 summarizes the main findings of this thesis.

Chapter 2
Elastic-plastic analysis of adhesive sliding contacts

2.1 Introduction

Adhesion is an important phenomenon affecting the performance and reliability of various mechanical components with contact interfaces, especially at submicrometer scales where surface forces dominate bulk forces. Adhesion intensifies surface interaction, leading to energy loss to friction, surface damage, wear, and, ultimately, cessation of the device operation. For example, adhesion forces at interfacial gaps of microelectromechanical systems (Komvopoulos, 1996; Kim et al., 2007) and the head-disk interface of hard-disk drives (Komvopoulos, 2000) are the prime cause of premature failure. In addition to the durability of load-bearing mechanical components, adhesion affects the efficiency of several micro/nanoscale manufacturing processes, such as chemical mechanical polishing of wafers and fine-scale polishing (lapping) of magnetic recording heads. Therefore, insight into the role of adhesion in surface sliding is of paramount importance to the design of reliable mechanical systems and the efficiency of mechanical surfacing processes requiring precise control of material removal at submicrometer scales.

Since the first adhesive contact model of Bradley (1932), significant effort has been devoted to the study of adhesive contacts. According to the former model, the pull-off force $F_{\rm po}$ at the instant of separation of two rigid spheres is given by $F_{\rm po} = 2\pi R\Delta\gamma$, where R is the equivalent radius of curvature ($R = [1/R_1 + 1/R_2]^{-1}$, where R_1 and R_2 are the radii of curvature of the two spheres) and $\Delta\gamma$ is the work of adhesion ($\Delta\gamma = \gamma_1 + \gamma_2 - \gamma_{12}$, where γ_1 and γ_2 are the surface energies of the two spheres and γ_{12} is the surface energy of the contact interface). A similar equation of the pull-off force is given by the DMT model (Derjaguin et al., 1975). The JKR model (Johnson et al., 1971) yields a pull-off force $F_{\rm po} = (3/2)\pi R\Delta\gamma$, which is less than that predicted by the Bradley and DMT models. Tabor (1977) argued that the pull-off forces given by the DMT (rigid contact) and JKR (elastic contact) models represent upper and lower limits, respectively, and examined the transition of the pull-off force between the values given by the DMT model ($\mu < 0.1$) and the JKR model ($\mu > 3$) in terms of a dimensionless parameter μ (referred to as the Tabor parameter) defined as

$$\mu = \left(\frac{R\Delta\gamma^2}{E^{*2}\varepsilon^3}\right)^{1/3}, \tag{2.1}$$

where E^* is the equivalent elastic modulus ($E^* = [(1-\nu_1^2)/E_1 + (1-\nu_2^2)/E_2]^{-1}$, where E_1 and E_2 are the elastic moduli and ν_1 and ν_2 are the Poisson's ratios of the two adhering spheres, respectively) and ε is the intermolecular equilibrium distance. Maugis (1992) used the Dugdale approximation to model adhesive surface interaction and obtained an analytical solution of the pull-off force that provides a smooth transition between the DMT and JKR solutions. Numerical results of the pull-off force for the same transition range have also been reported by Muller et al. (1980), Attard and Parker (1992), and Greenwood (1997), who modeled surface adhesion by the Lennard-Jones (L-J) potential (Israelachvili, 1992). Kadin et al. (2008a and 2008b) used the finite element method and the L-J potential to analyze adhesive contact of a

rigid flat surface with an elastic-plastic sphere exhibiting isotropic or kinematic strain hardening and reported a dependence of the load-unload behavior on Tabor parameter, maximum surface approach, and evolution of plasticity. Song and Komvopoulos (2011) examined adhesion-induced contact instabilities, such as instantaneous surface contact (jump-in) and separation (jump-out) during loading and unloading of a rigid sphere on an elastic-plastic half-space, and interpreted the force-distance response produced from several approach-retraction cycles in the context of elastic and plastic shakedown.

In contrast to the pull-off force of spherical bodies (point contacts), the pull-off force of cylindrical surfaces (line contacts) depends on the equivalent elastic modulus. Using a two-dimensional (2D) JKR model, Chaudhury et al. (1996) showed that the pull-off force (per unit length) of line contacts is given by $F_{\mathrm{po}} = (3/4)(4\pi E^* R\Delta\gamma^2)^{1/3}$. Leng et al. (2000) and Johnson and Greenwood (2008) used a 2D Maugis model to obtain a solution of the pull-off force in the transition range between the 2D JKR model and the 2D DMT model, which gives different estimate of the pull-off force than the 2D Bradley model. Wu (2009) modeled adhesive contact between a cylinder and a half-space with the L-J potential and obtained a numerical solution of the pull-off force, which is in close agreement with that reported by Johnson and Greenwood (Johnson and Greenwood, 2008) for the transition range between 2D JKR and Bradley models.

Despite valuable insight into the role of adhesion in surface mechanics derived from above analytical and numerical studies, results were reported only for normal contact conditions. However, it is questionable if these results can be directly applied to adhesive sliding contacts, for which continuum mechanics studies are sparse. Although molecular dynamics (MD) simulations (Komvopoulos and Yan, 1997b; Yan and Komvopoulos, 1998b; Ringlein and Robbins, 2004; Yang and Komvopoulos, 2005b; Gao et al., 2007; Chandross, et al, 2008; Mo et al., 2009) have elucidated adhesion (friction) contact phenomena at scales approaching those of atomic force and surface force microscopy (Hu et al., 1995; Carpick et al., 1996; Wei and Komvopoulos, 1996; Mailhot et al., 2001; Riedo et al., 2001), integration of computationally intensive MD methods with continuum mechanics analysis presents a formidable challenge.

The objective of this chapter was to develop a comprehensive analysis of adhesive sliding contact at the asperity level. This was accomplished by incorporating atomic-scale adhesion interaction (modeled by nonlinear springs obeying a constitutive relation derived from the L-J potential) into a continuum mechanics analysis based on the finite element method. Numerical results of normal and friction force, subsurface stresses, and evolution of plasticity in an elastic-plastic half-space are interpreted in terms of interaction distance (interfacial gap), mechanical properties of the half-space, and work of adhesion of the interacting surfaces to elucidate the role of adhesion in sliding contacts.

2.2 Analysis

2.2.1 Contact problem

Contact between surfaces exhibiting multi-scale roughness occurs at surface summits, known as asperities. Therefore, understanding the role of adhesion in sliding contacts requires knowledge of surface interaction at the asperity level. This can be accomplished by considering the quasi-static 2D model of a rigid cylindrical asperity sliding over a homogenous elastic-perfectly plastic half-space, shown schematically in Fig. 2.1(a). The *x*-*y* coordinate system

represents the local coordinates of the sliding asperity. The interaction distance δ is defined as the distance between the bottom point of the asperity surface and the undeformed surface of the half-space; thus, $\delta < 0$ implies that the asperity is above the undeformed surface. The horizontal displacement of the asperity x_s (measured from the initial position of the asperity center) defines the total sliding distance. Sliding simulations were performed by positioning the asperity over the half-space (x_s = 0) at a distance resulting in negligible adhesion force, displacing the asperity in the *y*-direction by a given interaction distance δ, and, finally, displacing the asperity in the *x*-direction by a total distance x_s, while keeping the interaction distance δ fixed through the entire sliding phase of the simulation.

2.2.2 Finite element model

Figure 2.1(b) shows the finite element mesh of the elastic-plastic half-space. The mesh consists of 70984 isoparametric, four-node, bilinear, reduced-integration, plane-strain elements with a total of 71572 nodes. To improve the accuracy and convergence, the mesh at the half-space surface is refined with square elements of sides equal to $0.004R$, where R is the asperity radius. The vertical and horizontal mesh dimensions are equal to $20.5R$ and $43R$, respectively. Nodes at the bottom boundary of the mesh are constrained against displacement in the *x*- and *y*-direction. In all simulations, the total sliding distance and maximum sliding increment are equal to $2R$ and $0.02R$, respectively.

Surface adhesion between the moving asperity and the stationary half-space is modeled by nonlinear springs, attached to the asperity center and surface nodes of the half-space (Fig. 2.2). The springs obey a constitutive relation derived from the L-J potential (see section 2.3). The model uses a total of 911 nonlinear springs attached to surface nodes of the finite element mesh from $x_s = -0.8R$ to $x_s = 2.8R$. The springs remain attached to the moving asperity and surface nodes of the mesh during the entire sliding phase of a simulation. All simulations were performed with the multi-purpose finite element code ABAQUS/Standard (version 6.9-EF2).

2.2.3 Interfacial adhesion model

According to the L-J potential, the force per unit area (also referred to as the adhesive pressure) p between two parallel flat surfaces is given by (Muller et al., 1980)

$$p = \frac{8\Delta\gamma}{3\varepsilon}\left[\left(\frac{\varepsilon}{h}\right)^3 - \left(\frac{\varepsilon}{h}\right)^9\right], \tag{2.2}$$

where h is the gap between the surfaces. The first and second terms of Eq. (2.2) represent long-range attraction and short-range repulsion, respectively. In previous studies (Muller et al., 1980; Attard and Parker, 1992; Greenwood, 1997; Kadin et al., 2008a and 2008b; Wu, 2009), the contact region of two solids was discretized into numerous small segments, and the total adhesion force was calculated as the sum of the forces generated by all segments obtained from Eq. (2.2). However, because the adhesion force between a cylindrical asperity and a small surface segment arises in the radial direction (Fig. 2.2), it consists of vertical and horizontal components. Hence, the previous method based on Eq. (2.2) cannot be used to model adhesive sliding contact between non-planar surfaces. Thus, a different equation of the adhesive pressure must be used in the present analysis.

The net interaction energy due to a single atom at a distance r' from a line of atoms (Fig. 2.3(a)) can be obtained as the sum of the interaction energies between the single atom and each line atom. The distance between the single atom and an infinitesimally small segment dx at a horizontal distance x from the single atom is expressed as $[(r')^2 + x^2]^{1/2}$. The number of atoms in the small segment is equal to $\rho_l dx$, where ρ_l is the number density of line atoms. For two-atom interaction described by a potential function $w(r) = -C/r^{2n}$, where r is the atom-to-atom distance, the net interaction energy is obtained as

$$w_l(r') = -\int_{-\infty}^{+\infty} \frac{C\rho_l}{[(r')^2+x^2]^n} dx = -C\pi\rho_l \frac{(2n-3)!}{2^{2n-3}(n-1)!(n-2)!} \left(\frac{1}{r'}\right)^{2n-1}. \quad (2.3)$$

For a L-J potential of the general form $w(r) = -C_1/r^6 - C_2/r^{12}$, the net interaction energy due to an atom at a distance r' from a line of atoms can be obtained from Eq. (2.3) as the superposition of two interaction energies $w(r')$ with n = 3 and 6, i.e.,

$$w_l(r') = -\pi\rho_l \left[\frac{3C_1}{8}\left(\frac{1}{r'}\right)^5 + \frac{63C_2}{256}\left(\frac{1}{r'}\right)^{11}\right]. \quad (2.4)$$

For atoms in a circular zone of radius r' and area equal to $2\theta r' dr'$ of a cylindrical asperity (Fig. 2.3(b)), $r' = [D^2 + 2z(R + D)]^{1/2}$ and $\theta = \sin^{-1}[z(2R - z)/(r')^2]^{1/2}$, where $0 \le z \le 2R$ and D is the minimum distance of the single atom from the asperity. Thus, the net interaction energy can be obtained as

$$w(D) = \int_D^{D+2R} 2\rho_a w_l(r')\theta(r')r' dr', \quad (2.5)$$

where ρ_a is the area density of asperity atoms.

Substitution of Eq. (2.4) into Eq. (2.5) gives

$$w(D) = -2\pi\rho_c \int_D^{D+2R} \left[\frac{3C_1}{8}\left(\frac{1}{r'}\right)^4 + \frac{63C_2}{256}\left(\frac{1}{r'}\right)^{10}\right] \theta(r')dr' , \quad (2.6)$$

where ρ_c (=$\rho_l\rho_a$) is the volume density of asperity atoms.

The interaction energy between all asperity atoms and a column of half-space atoms of unit cross-sectional area and infinite length (Fig. 2.3(c)) can be written as

$$W(D) = \int_D^{+\infty} \rho_{hs}\, w(D)dD, \quad (2.7)$$

where ρ_{hs} is the volume density of half-space atoms.

From Eqs. (2.6) and (2.7), the interaction pressure between a unit surface area of the half-space and the asperity $p(D)$ can be obtained as

$$p(D) = \frac{\partial W(D)}{\partial D} = -\rho_{hs}\, w(D) = 2\pi\rho_{hs}\rho_c \int_D^{D+2R} \left[\frac{3C_1}{8}\left(\frac{1}{r'}\right)^4 + \frac{63C_2}{256}\left(\frac{1}{r'}\right)^{10}\right] \theta(r')dr' . \quad (2.8)$$

The L-J potential can be expressed as (Israelachvili, 1992)

$$w(r) = 4K\left[\left(\frac{\sigma}{r}\right)^{12} - \left(\frac{\sigma}{r}\right)^{6}\right], \tag{2.9}$$

where K is the minimum potential and σ is the zero-potential distance. From the general form of the L-J potential $w(r) = -C_1/r^6 - C_2/r^{12}$ and Eq. (2.9), it follows that $C_1 = 4K\sigma^6$ and $C_2 = -4K\sigma^{12}$. Hence, Eq. (2.8) becomes

$$p(D) = 3\pi\rho_{hs}\rho_c K\sigma^6 \int_D^{D+2R}\left[\left(\frac{1}{r'}\right)^4 - \frac{21\sigma^6}{32}\left(\frac{1}{r'}\right)^{10}\right]\theta(r')dr' \quad . \tag{2.10}$$

After introducing the relations $\Delta\gamma = (15\pi/8)K\varepsilon^4\rho_{hs}\rho_c$ and $\sigma = (15/2)^{1/6}\varepsilon$ derived by Song and Komvopoulos (Song and Komvopoulos, 2011) into Eq. (2.10), the interaction pressure is given by

$$p(D) = 12\Delta\gamma\varepsilon^2 \int_D^{D+2R}\left[\left(\frac{1}{r'}\right)^4 - \frac{315}{64}\varepsilon^6\left(\frac{1}{r'}\right)^{10}\right]\theta(r')dr' \, . \tag{2.11}$$

Because Eq. (2.11) does not have a closed-form solution, it is necessary to obtain an approximate relation of the constitutive law of the nonlinear springs used in the present finite element model. This can be accomplished by considering that only small z values contribute to the integral of Eq. (2.11), i.e., $z \ll R$. With this simplification, integration of Eq. (2.11) gives the following analytical solution of the adhesion force per unit area (adhesive pressure):

$$p(D) = \frac{2\Delta\gamma}{3\varepsilon}\frac{\left(\frac{\varepsilon}{D}\right)^3}{\left(1+\frac{D}{R}\right)^{1/2}}\left[4 - \frac{D}{R} - \left(4 - \frac{D}{4R}\right)\left(\frac{\varepsilon}{D}\right)^6\right] \, . \tag{2.12}$$

It is noted that for two flat surfaces (i.e., $R \to \infty$) Eq. (2.12) reduces to

$$p(D) = \frac{8\Delta\gamma}{3\varepsilon}\left[\left(\frac{\varepsilon}{D}\right)^3 - \left(\frac{\varepsilon}{D}\right)^9\right] \, , \tag{2.13}$$

which is identical to the relation derived from the L-J potential (Eq. (2.2)).

Because the validity of Eq. (2.12) depends on condition $z \ll R$, the analysis is limited to cases of sufficiently large R values. To determine a cut-off value of the dimensionless radius R/ε, results obtained from numerical integration of Eq. (2.11) were compared with those obtained from Eq. (2.12) for different values of R/ε. For R/ε = 50 and ~200, the maximum error between results obtained from Eqs. (2.11) and (2.12) was found to be equal to 2% and 0.05%, respectively. The small error validates the use of Eq. (2.12) as the constitutive relation of the nonlinear springs used to model interfacial adhesion. All simulations were performed for $R/\varepsilon \approx$ 200, which satisfies the requirement of an asperity radius at least an order of magnitude larger than the lattice dimensions in order for continuum description to hold.

2.2.4 Plasticity models

Yielding is determined based on the von Mises yield criterion, expressed as

$$\sigma_{\mathrm{M}} = \left[\frac{3}{2}S_{\mathrm{ij}}S_{\mathrm{ij}}\right]^{1/2} = Y, \tag{2.14}$$

where σ_{M} is the von Mises equivalent stress, S_{ij} are components of the deviatoric stress tensor, and Y is the yield strength in uniaxial tension.

The evolution of plasticity in the half-space during sliding is tracked by the equivalent plastic strain $\varepsilon_{\mathrm{eq}}^{\mathrm{p}}$, defined as

$$\varepsilon_{\mathrm{eq}}^{\mathrm{p}} = \int_{\Omega} \left[\frac{2}{3} d\varepsilon_{ij}^{\mathrm{p}} d\varepsilon_{ij}^{\mathrm{p}}\right]^{1/2} \tag{2.15}$$

where Ω is the strain path and $d\varepsilon_{ij}^{\mathrm{p}}$ is the plastic strain increment.

Plastic deformation is modeled with the usual associated flow rule, assuming negligible plastic volume change. Thus, the standard elastic constitutive equation is used for $\sigma_{\mathrm{M}} < Y$ and the plastic flow rule is applied for yielding material ($\sigma_{\mathrm{M}} = Y$).

2.3 Results and discussion

2.3.1 Adhesive contact

In 2D line contacts, the transition from elastic behavior (JKR model) to rigid behavior (Bradley or DMT models) can be described by the Maugis parameter λ, given by (Johnson and Greenwood, 2008; Wu, 2009)

$$\lambda = \frac{9\sqrt{3}}{16}\left(\frac{R\Delta\gamma^2}{E^{*2}\varepsilon^3}\right)^{1/3} . \tag{2.16}$$

From Eqs. (2.1) and (2.16), it follows that $\lambda = (9\sqrt{3}/16)\mu$. The pull-off force is usually encountered at the instant of abrupt surface separation (jump-out), implying abrupt change from finite contact area (JKR model) to zero contact area (Bradley model). As mentioned earlier, the pull-off force of line contacts depends on the effective elastic modus. Johnson and Greenwood (2008) used a 2D Maugis model to analyze adhesive line contacts and observed that, for $\lambda > 3$, the pull-off force is close to that predicted by the 2D JKR model, i.e., $F_{\mathrm{po}} = (3/4)(4\pi E^* R\Delta\gamma^2)^{1/3}$, while for $\lambda < 0.1$, the pull-off force is equal to that predicted by the 2D DMT model, i.e., $F_{\mathrm{po}} = (8\lambda)^{1/2}(E^* R\Delta\gamma^2)^{1/3}$. Wu (2009) used the L-J potential to model adhesion and the Maugis parameter to study the transition from elastic contact (JKR model) to rigid contact (Bradley model) behavior, and showed that the pull-off force given by the Bradley model can be expressed as $F_{\mathrm{po}} = (5.9248\lambda)^{1/2}(E^* R\Delta\gamma^2)^{1/3}$. Thus, unlike adhesive point contacts, such as those involving two spherical bodies, the pull-off force of adhesive line contacts derived from the Bradley model differs from that obtained from the DMT model.

Figure 2.4 shows analytical and numerical results of the dimensionless pull-off force of elastic line contacts $\bar{F}_{\mathrm{po}} = F_{\mathrm{po}}/(E^* R\Delta\gamma^2)^{1/3}$ versus the Maugis parameter λ (Eq. (2.16)). Solutions of the pull-off force obtained from the analysis of Johnson and Greenwood (2008) based on the Maugis model and the numerical analysis of Wu (2009) based on the L-J potential were obtained from the following Eqs. (2.17) and (2.18), respectively,

$$\bar{F}_{\mathrm{po}} = \left[\frac{1}{\left(\frac{1}{1.7437}\right)^4 + \left(\frac{1}{8\lambda}\right)^2}\right]^{1/4} , \tag{2.17}$$

and

$$\bar{F}_{\mathrm{po}} = \left[\frac{1}{\left(\frac{1}{1.7437}\right)^4 + \left(\frac{1}{5.9248\lambda}\right)^2}\right]^{1/4} . \tag{2.18}$$

For $\lambda < 3$, the pull-off force given by Eq. (2.17) (Maugis model) shows a smooth transition from the DMT solution to the JKR solution, but exceeds the pull-off force given by Eq. (2.18) (L-J potential). For $\lambda > 3$, both Eq. (2.17) and Eq. (2.18) give $\bar{F}_{\mathrm{po}} = 1.7437$, which is the value obtained with the JKR model. The pull-off force determined from the present analysis shows a gradual transition from the Bradley solution to the JKR solution and is in excellent agreement with Eq. (2.18), although it is slightly lower than that calculated from Eq. (2.17) in the range $\lambda < 3$.

2.3.2 Force analysis

The evolution of dimensionless normal and friction force, $L/R\Delta\gamma$ and $F/R\Delta\gamma$, respectively, is examined in terms of dimensionless interaction distance δ/ε, work of adhesion $\Delta\gamma$, and elastic-plastic material properties of the half-space. Analytical results are presented in terms of the Maugis parameter λ (Eq. (2.16)) and the plasticity parameter S, defined as

$$S = \frac{\Delta\gamma}{\varepsilon Y} . \tag{2.19}$$

In view of Eq. (2.19), low (high) S may be interpreted as a half-space of low (high) surface energy and/or high (low) yield strength. In the present analysis, S is varied in the range of 0.5–2.2.

According to the adhesion map of Johnson and Greenwood (1997), the effect of adhesion on contact deformation of two elastic spheres subjected to a high normal force is negligible. Therefore, to ensure significant adhesion effects in the present study, sliding contact was simulated for relatively small interaction distances, i.e., low normal forces. Figure 2.5 shows the normal and friction force, $L/R\Delta\gamma$ and $F/R\Delta\gamma$, respectively, versus sliding distance x_s/ε and interaction distance δ/ε for λ = 0.306 and S = 1.46. Both forces were affected by contact area variations during the initial stage of sliding, particularly the friction force. Steady-state force responses were obtained after sliding for a distance $x_s/\varepsilon > 80$. Increasing the interaction distance intensified both normal and friction forces, causing the normal force to change from attractive to repulsive due to the dominance of short-range repulsion at large interaction distances (small gaps), as evidenced from Eq. (2.12). This implies that the total normal force consists of attractive and repulsive force components. Because steady-state force responses were encountered after a very small sliding distance, further analysis of the effect of the work of adhesion on contact behavior will be based on steady-state force responses.

Figure 2.6 shows the friction force $F/R\Delta\gamma$ versus normal force $L/R\Delta\gamma$ at steady-state sliding for λ = 0.306 and S = 1.46. A similar trend was obtained with other combinations of λ and S. The nonzero friction force for zero normal force is characteristic of adhesive contacts. The friction force demonstrates a nonlinear dependence on normal force. The gradual increase of the force slope (coefficient of friction) with the normal force may be associated with an elastic-plastic change in the dominant mode of deformation, implying a transition from wearless to wearing sliding contact conditions with increasing normal force.

2.3.3 Effect of interaction distance

Figure 2.7(a) shows the variation of the steady-state normal force $L/R\Delta\gamma$ with interaction distance δ/ε and plasticity parameter S for λ = 0.306. Indentation results are also included for comparison. In both sliding and indentation simulations, the normal force increases sharply with interaction distance, apparently due to the increase of the contact area, demonstrating a transition from attraction to repulsion at $\delta/\varepsilon \approx -0.6$. For large interfacial gaps (small δ/ε), deformation is predominantly elastic and the normal force is controlled by the elastic modulus of the half-space. Thus, the plasticity parameter effect is encountered only for relatively small interfacial gaps (i.e., $\delta/\varepsilon > 0.5$) resulting in significant plastic deformation. The increasing discrepancy between sliding and indentation solutions with decreasing interfacial gap (increasing δ/ε) is attributed to the enhancement of plasticity due to the increase of shear (friction) traction. Figure 2.7(b) shows the effects of interaction distance δ/ε and plasticity parameter S on friction force $F/R\Delta\gamma$. The continuous increase of the friction force with both δ/ε and S may be attributed to the increase of plasticity with decreasing half-space yield strength and interfacial gap (resulting in higher normal force (Fig. 2.7(a))) and increasing work of adhesion.

Further insight into the effects of interaction distance and plasticity parameter on the evolution of plastic deformation at steady-state sliding can be obtained by considering the variation of the dimensionless rate of energy dissipation in the form of plastic deformation $\dot{E}_{\mathrm{p}}/R\Delta\gamma$ with the interaction distance δ/ε, shown in Fig. 2.7(c), where $\dot{E}_{\mathrm{p}} = dE_{\mathrm{p}}/dx_{\mathrm{s}}$ was determined numerically at steady state. Because all of the nonlinear springs were attached to the moving asperity and surface nodes of the half-space, energy was not dissipated by the springs during sliding. The increase in $\dot{E}_p/R\Delta\gamma$ with δ/ε and S closely resembles the trend of the steady-state friction force (Fig. 2.7(b)), implying a direct correlation between friction force and energy dissipation rate due to the accumulation of plasticity. In view of Fig. 2.7(a) and Eq. (2.19), it may be inferred that the rate of energy dissipation due to plastic deformation increases with the normal force and work of adhesion, but decreases with increasing yield strength of the half-space, in accord with practical experience.

Figure 2.8 shows contours of normal stress σ_{yy}/Y in the elastic-plastic half-space at steady-state sliding for different interaction distances δ/ε, λ = 0.306, and S = 1.46. It can be seen that adhesion distorted the symmetry of the stress field, especially with the increase of the interaction distance. The center interface is under compression (repulsive force), while regions near the interface edges are under tension (attractive force), in agreement with a previous study of adhesive contact by Luan and Robbins (2005). Increasing the interaction distance causes the subsurface region of compressive stress to expand in the *y*-direction and the maximum compressive stress to reach a value depending on the yield strength of the half-space. Conversely to the compressive stress, the effect of the interaction distance on the regions of tensile stress is secondary.

The distribution of the equivalent plastic strain $\varepsilon_{\mathrm{eq}}^{\mathrm{p}}$ in the half-space provides insight into the frictional work dissipated by plastic deformation. Figure 2.9 shows contours of $\varepsilon_{\mathrm{eq}}^{\mathrm{p}}$ corresponding to the stress contours shown in Fig. 2.8. Both the magnitude of $\varepsilon_{\mathrm{eq}}^{\mathrm{p}}$ and size of the plastic zone increase with the decrease of the interfacial gap. In addition, the maximum $\varepsilon_{\mathrm{eq}}^{\mathrm{p}}$ moves closer to the surface as a result of the increase of both normal and friction forces with δ/ε

(Figs. 2.5, 2.7(a), and 2.7(b)), in agreement with previous studies dealing with the effect of interfacial friction on elastic-plastic deformation of half-spaces sliding against a rigid surface (Tian and Saka, 1991; Kral and Komvopoulos, 1996a and 1997). As shown in Fig. 2.9, the maximum ε_{eq}^{p} arises below the surface and left of the asperity center ($x = 0$). This is attributed to variations in plastic strain accumulation as each material point of the half-space experiences the compressive and tensile stress fields produced by the sliding asperity. Thus, the maximum plastic strain arises in the subsurface behind the center of the contact interface.

Figure 2.10 shows deformed surface profiles at steady-state sliding for different interaction distances δ/ε, λ = 0.306, and S = 1.46. The increase of surface deformation with decreasing interfacial gap exacerbated the asymmetry of the deformed surface profile. The formation of a large pile-up ahead of the sliding asperity for large interaction distance (δ/ε = 0.466 and 0.933) is indicative of the enhancement of plasticity and dominance of plowing friction in the case of relatively high surface tractions, in agreement with a previous study of nanoscale plowing friction (Mishra and Szlufarska, 2012).

2.3.4 Effect of work of adhesion

Figure 2.11 shows the normal and friction force, $L/R\Delta\gamma$ and $F/R\Delta\gamma$, respectively, versus work of adhesion $\Delta\gamma/E^{*}R$ for δ/ε = 0 and E^{*}/Y = 110. Higher work of adhesion results in lower normal force (Fig. 2.11(a)). As mentioned earlier, the normal force consists of attractive and repulsive force components that depend on the work of adhesion and material properties of the half-space, respectively. Thus, the attractive force component increases with $\Delta\gamma/E^{*}R$, whereas the repulsive force component remains constant because E^{*} and Y are fixed, as in the simulation cases shown in Fig. 2.11. This explains the decrease of the normal force with increasing work of adhesion. This trend of the normal force may also be interpreted in terms of the proportional decrease of E^{*} and Y so that E^{*}/Y to remain equal to 110. Figure 2.11(b) shows that the friction force follows a trend opposite from that of the normal force. The friction force increases with the work of adhesion, in agreement with experimental evidence. The increase of the work of adhesion enhances the shear traction at the contact interface, resulting in more plastic deformation in the half-space (as indicated by the increase of the friction force) and larger discrepancy between sliding and indentation solutions.

The effect of the work of adhesion on contact deformation can be further interpreted in light of subsurface stress and strain results. Figure 2.12 shows contours of normal stress σ_{yy}/Y in the elastic-plastic half-space at steady-state sliding for different values of $\Delta\gamma/E^{*}R$, δ/ε = 0, and E^{*}/Y = 110. The increase of the work of adhesion (or proportional decrease of E^{*} and Y) causes the surface and subsurface regions of attractive (tensile) stress to intensify and enlarge; however, the effect on the region of compressive stress below the center of contact is secondary. This provides explanation for the decreasing trend of the normal force shown in Fig. 2.11(a). In addition, the increase of the asymmetry of the stress field with the work of adhesion indicates an enhancement of the friction force, in agreement with Fig. 2.11(b). Figure 2.13 shows contours of ε_{eq}^{p} corresponding to the stress contours shown in Fig. 2.12. Both the maximum ε_{eq}^{p} and the plastic zone size increase with the work of adhesion (or proportional decrease of $E^{*}$and Y). For example, a comparison of Figs. 2.13(a) and 2.13(d) shows that an increase in $\Delta\gamma/E^{*}R$ by a factor of ~3.6 leads to an increase of maximum ε_{eq}^{p} by a factor of ~150. The increase in work of adhesion not only enhances plasticity, but also causes the maximum ε_{eq}^{p} to shift closer to the

surface. The intensification of the tensile stress close to the surface (Fig. 2.12) and change of dominant deformation mode from elastic to plastic (Fig. 2.13) induced by the increase of the work of adhesion indicate a transition from low-adhesion contact conditions resulting in negligible surface damage to high-adhesion contact conditions that may be conducive to surface cracking and wear.

Figure 2.14 shows that the increase of the work of adhesion exacerbates the asymmetry of the deformed surface profile at steady-state sliding. Intensification of the attractive surface traction due to the increase of the work of adhesion by a factor of ~3.6 leads to the formation of large pile-ups (not observable under low-adhesion contact conditions) that contribute to the increased asymmetry of the stress field. This is further evidence of increased plastic deformation in sliding contacts due to the effect of adhesion. Thus, the extent of the asymmetry of the normal stress field and deformed surface profile is illustrative of the enhancement of plasticity by adhesion.

2.3.5 Effect of plasticity parameter

Figure 2.15 shows the steady-state normal and friction force, $L/R\Delta\gamma$ and $F/R\Delta\gamma$, respectively, versus plasticity parameter S and interaction distance δ/ε for $\lambda = 0.306$. Figure 2.15(a) shows that the normal force is a strong function of the interaction distance for both sliding and indentation contact conditions. The general trend is for the indentation normal force to decrease slightly with increasing plasticity parameter. The normal forces due to indentation and sliding coincide up to a critical S value, above which the normal force due to sliding decreases sharply. Similar results were obtained for other δ/ε values. Because low S implies less plastic deformation, the normal force depends mostly on the elastic modulus of the half-space. This explains the very small negative slope of the normal force in the low range of plasticity parameter. Alternatively, because high S implies excessive plastic deformation, the decrease of the normal force in the high range of plasticity parameter is attributed to the decrease of the half-space deformation resistance. For a given δ/ε and in the presence of shear (friction) surface traction, the normal force decreases sharply due to the increase of plasticity. This explains the deviation of the sliding solutions from the indentation solutions in the high range of plasticity parameter. A transition from repulsive to attractive normal force is observed for high S values and relatively small ($\delta/\varepsilon = -0.466$) and intermediate ($\delta/\varepsilon = 0$) interaction distances. This is attributed to the significant decrease of the repulsive force component, a consequence of excessive plasticity, and the constancy of the attractive force component due to its independence on S. Because the increase of S (or decrease of Y) implies an enhancement of plasticity during sliding, the increase of the friction force with S (Fig. 2.15(b)) is due to more work dissipation in the form of plastic deformation. Below a threshold value of S that decreases with increasing δ/ε, deformation is predominantly elastic, implying zero friction force and, in turn, negligible shear induced surface damage and sliding wear.

2.3.6 Effect of Maugis parameter

The effect of the Maugis parameter λ on the evolution of plasticity can be understood by considering the variation of the equivalent plastic strain $\varepsilon_{\mathrm{eq}}^{\mathrm{p}}$ with λ. Figure 2.16 shows contours of $\varepsilon_{\mathrm{eq}}^{\mathrm{p}}$ below the half-space surface obtained at steady-state sliding for different λ values and fixed interaction distance ($\delta/\varepsilon = 0$) and plasticity parameter ($S = 1.46$). Both maximum $\varepsilon_{\mathrm{eq}}^{\mathrm{p}}$ and

plastic zone size decrease with increasing λ. This is attributed to the decrease of the half-space stiffness with increasing λ (Eq. (2.16)), resulting in the distribution of the normal force over a larger area, which reduces the magnitude of the surface traction and, in turn, the extent of plasticity. A similar trend is observed in Fig. 2.17 for a lower plasticity parameter (S = 1.17) and same interaction distance ($\delta/\varepsilon = 0$). Contours of $\varepsilon_{\mathrm{eq}}^{\mathrm{p}}$ for S = 1.17 and λ = 0.485 are not shown in Fig. 2.17 because this simulation case resulted in purely elastic deformation.

The plasticity parameter effect on the evolution of plastic deformation at steady-state sliding can be understood by contrasting $\varepsilon_{\mathrm{eq}}^{\mathrm{p}}$ distributions with identical λ and δ/ε values but different S values. For fixed λ and δ/ε, the general trend is for the maximum $\varepsilon_{\mathrm{eq}}^{\mathrm{p}}$ and the plastic zone size to increase with S. As an example, for λ = 0.485, significant plastic deformation is shown for S = 1.46 (Fig. 2.16(d)), while for S = 1.17 deformation is purely elastic. The plasticity parameter effect on plastic deformation becomes less pronounced with the decrease of the Maugis parameter. Indeed, a comparison of Figs. 2.16(a), 2.16(c), 2.17(a), and 2.17(c) shows that the effect of plasticity parameter on the distribution and magnitude of $\varepsilon_{\mathrm{eq}}^{\mathrm{p}}$ is secondary at low values of the Maugis parameter (e.g., λ = 0.105). The results shown in Figs. 2.15–2.17 indicate that wearless sliding contacts may be characterized by low S and/or high λ values.

Figure 2.18 shows the steady-state normal and friction force, $L/R\Delta\gamma$ and $F/R\Delta\gamma$, respectively, versus Maugis parameter λ for $\delta/\varepsilon = 0$ and S = 1.17 and 1.46. Results from indentation simulations are also shown to reveal the effect of sliding friction on contact deformation. As shown by Eq. (2.16), a high value of the Maugis parameter may be interpreted as high work of adhesion and/or low elastic modulus. Usually, high λ results in predominantly elastic deformation. This is because the normal force for a given interfacial gap decreases with the half-space elastic stiffness, which is conducive to the decrease of plastic deformation as seen in Figs. 2.16 and 2.17. Figure 2.18(a) shows the effect of λ on the normal force due to indentation and sliding. Indentation simulations produced almost identical results, independent of plasticity parameter, evidently due to limited plasticity for $\delta/\varepsilon = 0$. The continuous decrease of the indentation normal force with increasing λ is attributed to the decrease of the half-space elastic stiffness. Friction traction increased plastic deformation in the sliding simulations. In the low range of λ, the attractive normal force component increases faster than the repulsive normal force component with decreasing λ, while the opposite trend is observed in the high range of λ. This explains the trend of the normal force in the sliding simulations shown in Fig. 2.18(a).

A general trend for the steady-state friction force to decrease with increasing λ is shown in Fig. 2.18(b). This can be attributed to the decrease of the half-space stiffness, which, for a given interfacial gap, contributes to the accumulation of less plasticity, as explained previously (Figs. 2.16 and 2.17). The friction force curves intersect at $\lambda \approx 0.15$. For $\lambda < 0.15$, plastic deformation for S = 1.17 and 1.46 is almost the same (Figs. 2.16(a) and 2.17(a)); therefore, the lower friction force for S = 1.46 is attributed to the lower shear resistance (yield strength) in this simulation case. The opposite trend observed in the range $\lambda > 0.15$ is attributed to the accumulation of significantly more plastic deformation for S = 1.46 (Fig. 2.16(c)) than S = 1.17 (Fig. 2.17(c)).

The above analysis is applicable to cases where one surface is considerably rougher (and harder) than the countersurface, such as in traditional surface grinding, chemomechanical polishing of wafers, lapping (polishing) of ceramic magnetics recording heads, nanoscale polishing (burnishing) of lenses and precious stones, and atomic force microscope imaging of

smooth surfaces. The main objective of this chapter was to examine the effects of interaction distance (interfacial gap), work of adhesion, Maugis parameter, and plasticity parameter on adhesive sliding contact deformation, using a continuum description and nonlinear spring elements for modeling adhesion. The present model can be used to perform a parametric study of the dimensionless parameters used in this chapter, e.g., $L/R\Delta\gamma$ and $F/R\Delta\gamma$ versus δ/ε, λ, and S, leading to the development of constitutive force relations force at the asperity level, which can be used to analyze sliding of elastic-plastic rough surfaces.

2.4 Conclusions

Adhesive sliding contact between a rigid asperity and an elastic-plastic half-space was examined in the context of analytical and finite element results. Adhesive surface interaction was modeled by nonlinear springs obeying a constitutive relation derived from the L-J potential. Displacement-control sliding simulations yielded solutions of the pull-off force, normal and friction force, and subsurface stresses and strains, which provide insight into the effects of work of adhesion, interaction distance (interfacial gap), and elastic-plastic material properties of the half-space on sliding contact behavior. Based on the presented results and discussion, the following main conclusions can be drawn from this chapter.

1. The solution of the pull-off force obtained from the present analysis shows a smooth transition from rigid contact (Bradley model) to elastic contact (JKR model) behavior with increasing Maugis parameter and is in good agreement with the solution of a previous numerical analysis of adhesive line contacts based on the L-J potential.
2. Both normal and friction forces increase with the interaction distance, demonstrating a nonlinear interdependence.
3. The normal and friction forces and the rate of energy dissipation due to plastic deformation increase sharply with the interaction distance due to the enhancement of plasticity. The increase of the interaction distance exacerbates the asymmetry of the normal stress field and promotes the formation of a pile-up at the front of the sliding asperity.
4. Higher work of adhesion produces lower normal force and higher friction force at steady-state sliding due to the increase of the attractive normal force component and plasticity, respectively. In addition, the size of the pile-up and the asymmetry of the deformed surface profile and the normal stress field increase with the work of adhesion.
5. The normal force at steady-state sliding decreases slightly with increasing plasticity parameter up to a critical value, depending on the interaction distance, above which it decreases sharply, while the friction force shows an opposite trend. These behaviors are attributed to the dominance of subsurface plasticity above a threshold value of the plasticity parameter.
6. The indentation normal force and steady-state friction force decrease continuously with increasing Maugis parameter, while the normal force at steady-state sliding increases slowly, approaching the indentation normal force in the high range of Maugis parameter, where it decreases gradually.

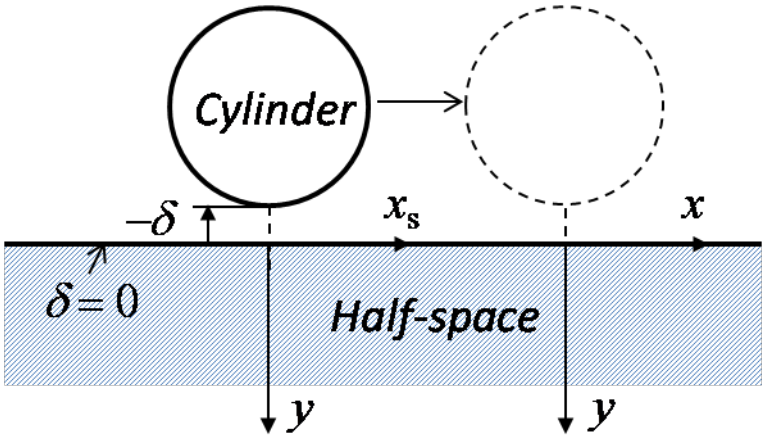

(a)

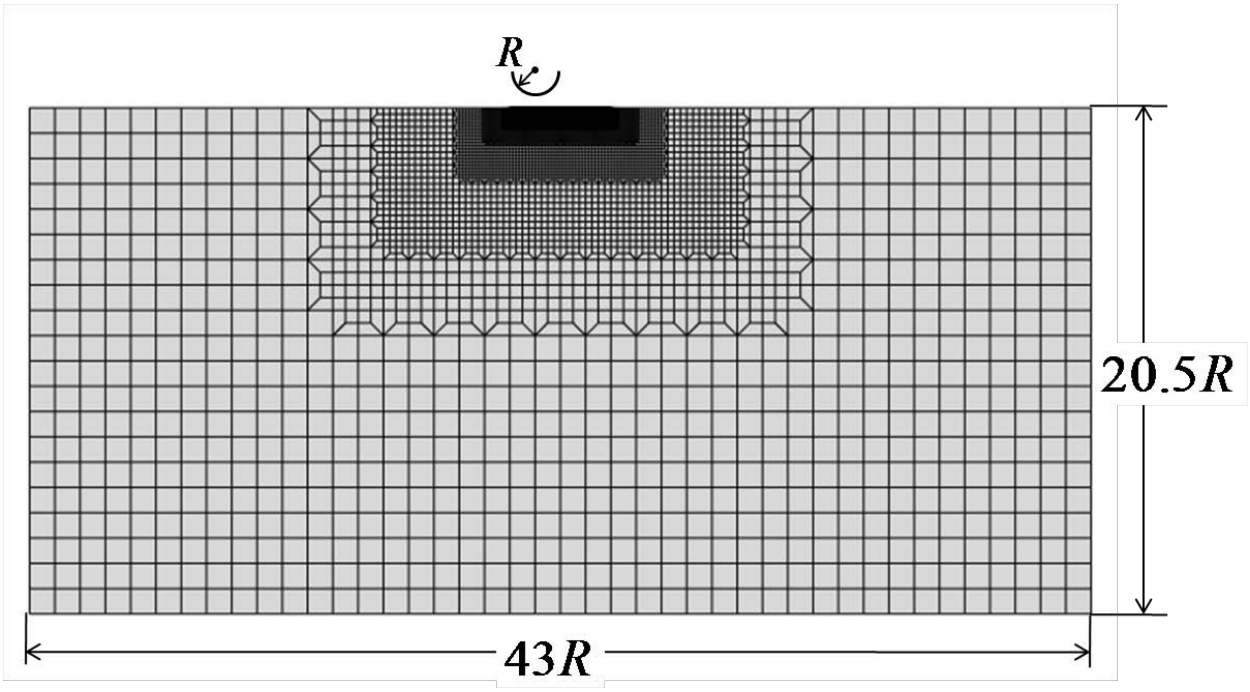

(b)

Figure 2.1 (a) Schematic of a cylinder (asperity) moving over a half-space and (b) finite element mesh of the half-space.

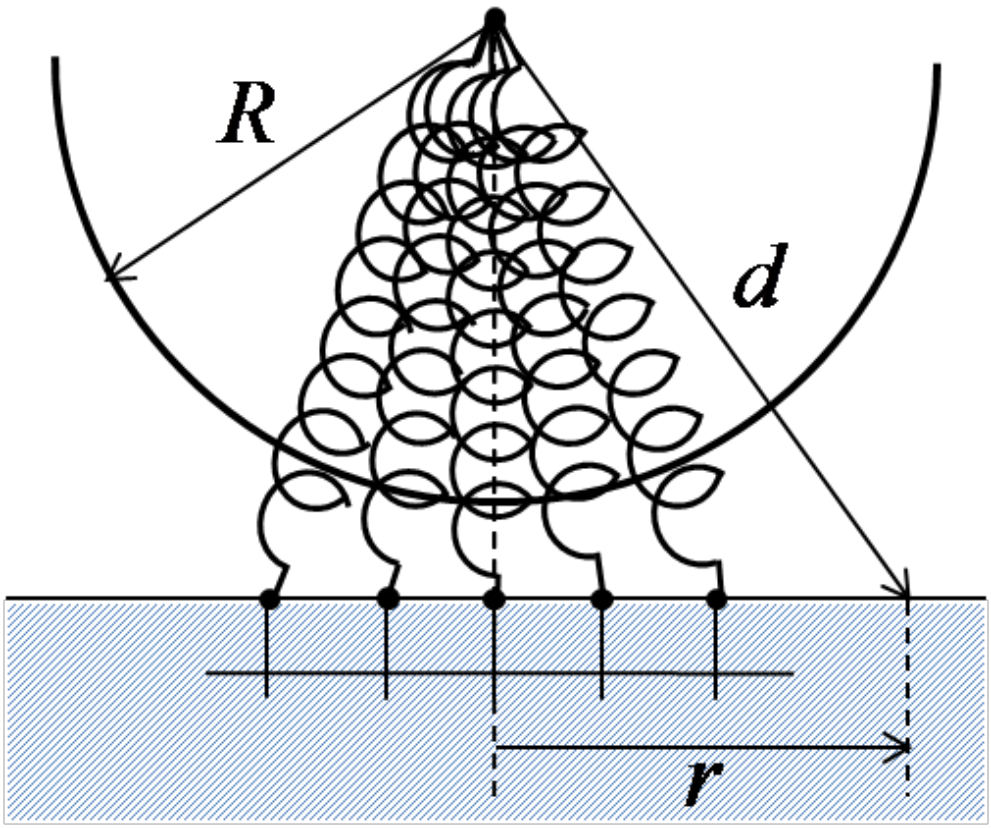

Figure 2.2 Cross-sectional schematic of a cylindrical asperity in close proximity with a half-space. Adhesion forces are modeled by nonlinear springs attached to the asperity center and surface nodes of the half-space.

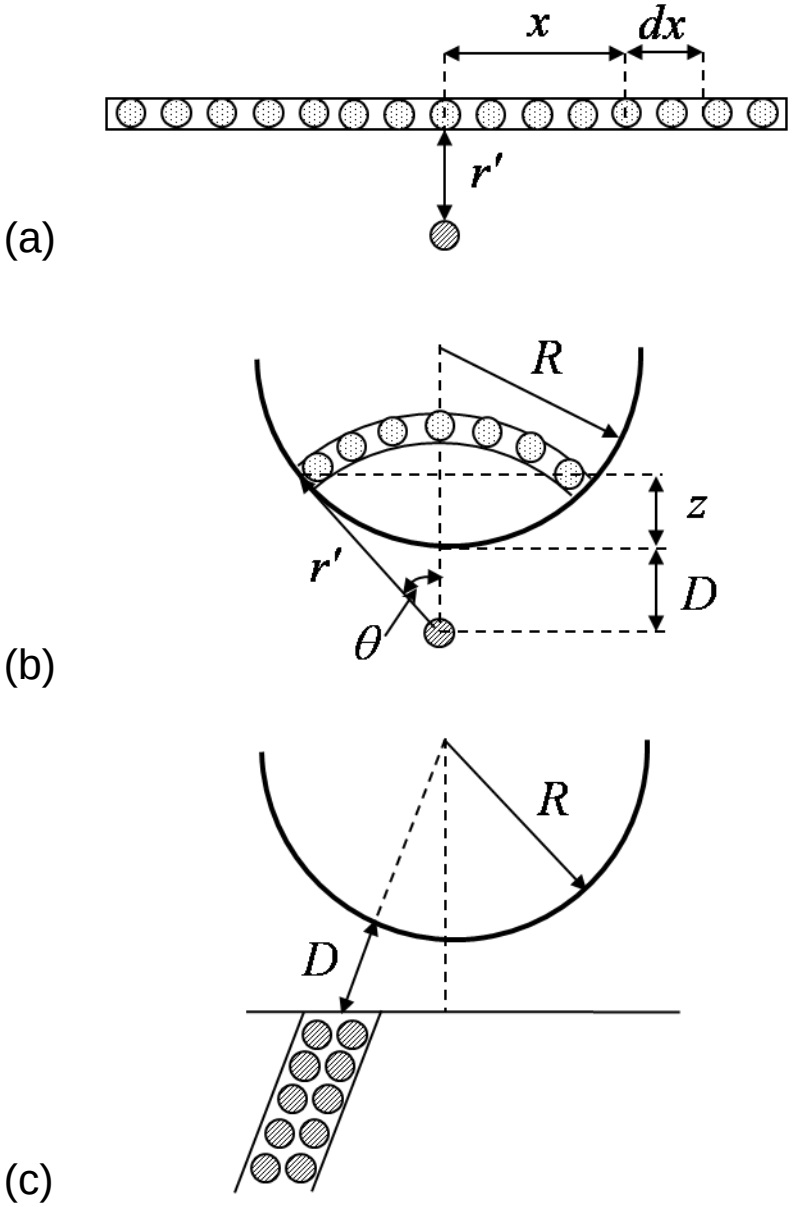

Figure 2.3 Illustration of the method used to obtain the interaction energy of macroscopic solid bodies from the interaction energy of atoms: (a) a single atom close to a line of atoms, (b) a single atom close to a cylindrical asperity, and (c) a column of atoms in a half-space close to a cylindrical asperity.

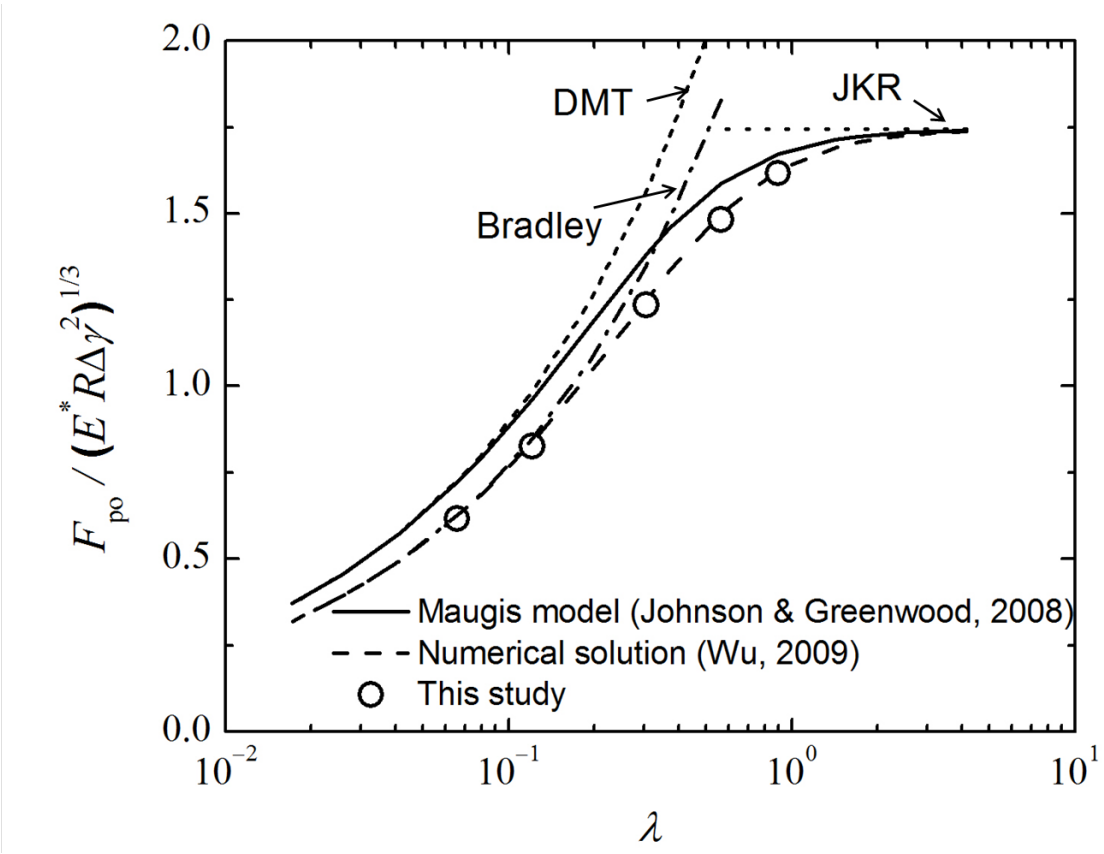

Figure 2.4 Solutions of the pull-off force $F_{po}/(E^*R\Delta\gamma^2)^{1/3}$ versus Maugis parameter λ obtained from different 2D adhesion models of elastic line contact: (–·–·–) Bradley model, (----) DMT model, (**….**) JKR model, (——) Maugis model (Johnson and Greenwood, 2008), (– – –) numerical solution (Wu, 2009), and (o) this study.

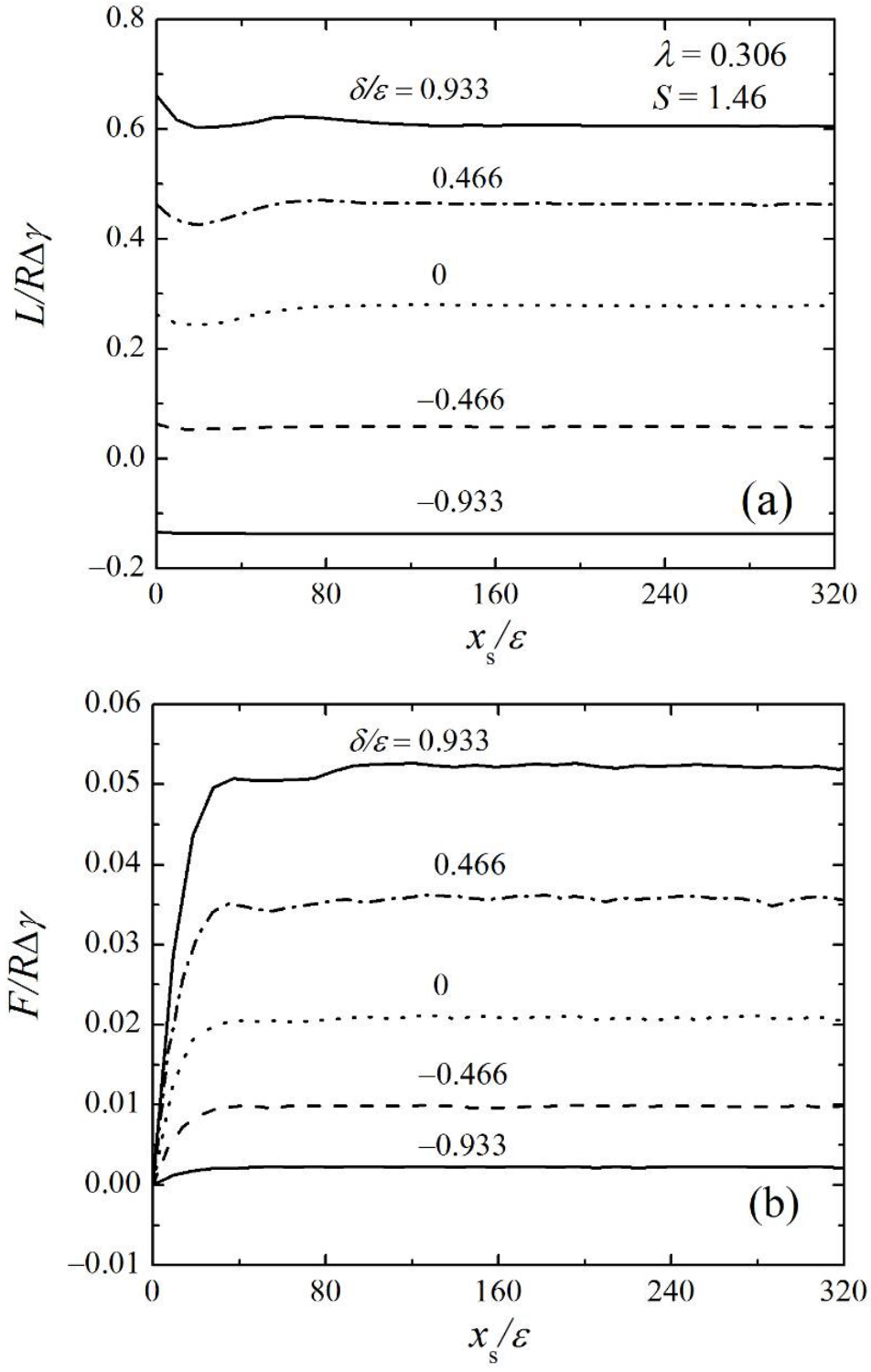

Figure 2.5 (a) Normal force $L/R\Delta\gamma$ and (b) friction force $F/R\Delta\gamma$ versus sliding distance x_s/ε for δ/ε = –0.933, –0.466, 0, 0.466, and 0.933, λ = 0.306, and S = 1.46.

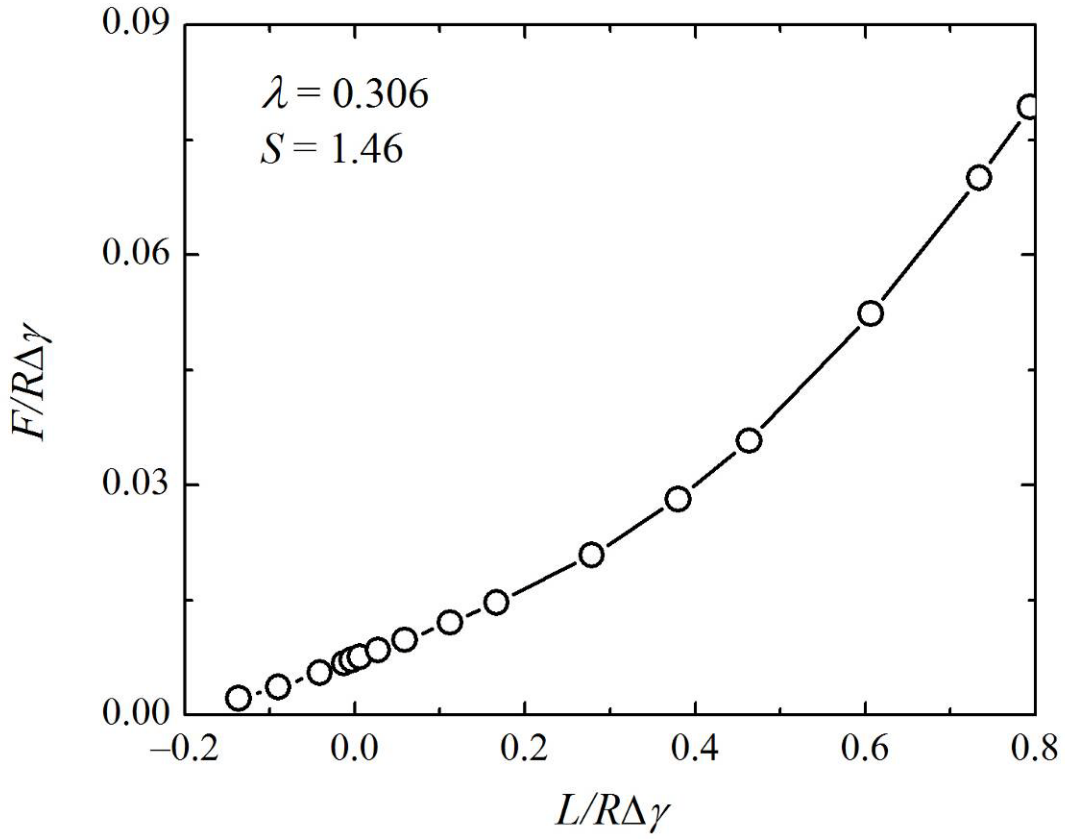

Figure 2.6 Friction force $F/R\Delta\gamma$ versus normal force $L/R\Delta\gamma$ at steady-state sliding for λ = 0.306 and S = 1.46.

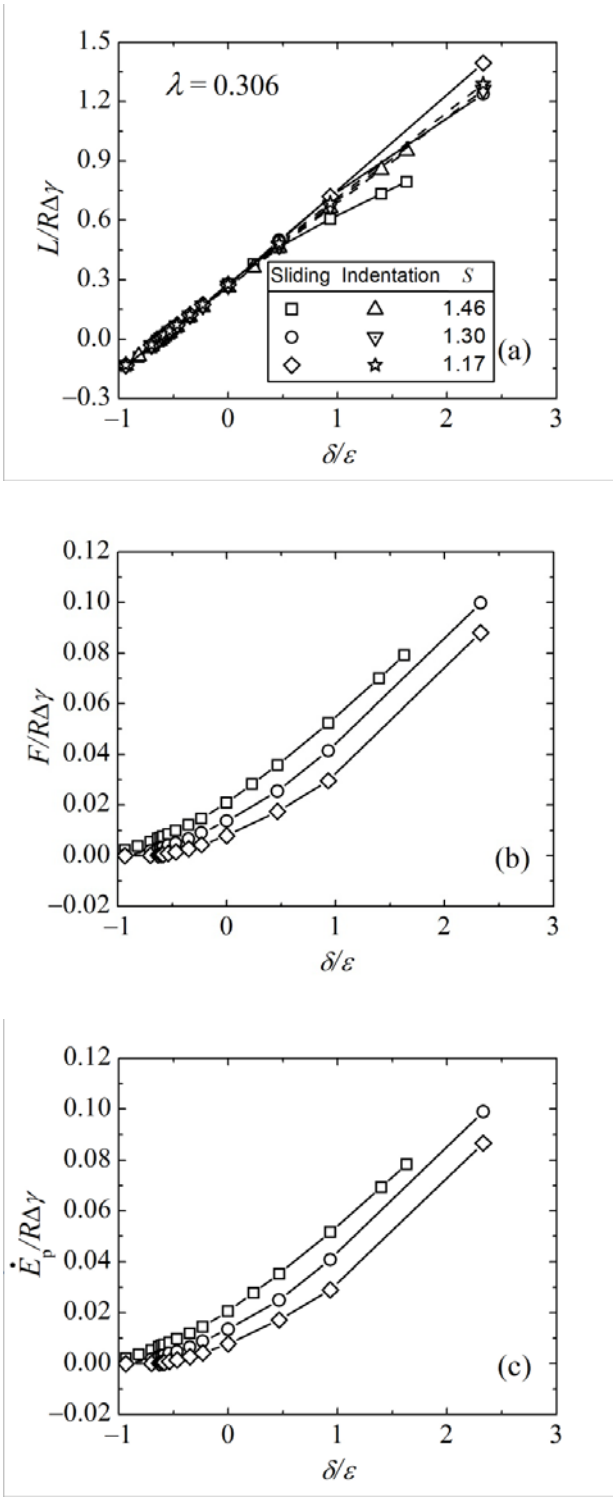

Figure 2.7 (a) Normal force $L/R\Delta\gamma$ due to sliding and indentation, (b) friction force $F/R\Delta\gamma$, and (c) rate of energy dissipation in the form of plastic deformation $\dot{E}_{\mathrm{p}}/R\Delta\gamma$ versus interaction distance δ/ε for λ = 0.306 and S = 1.17, 1.30, and 1.46. Sliding results are for steady-state sliding.

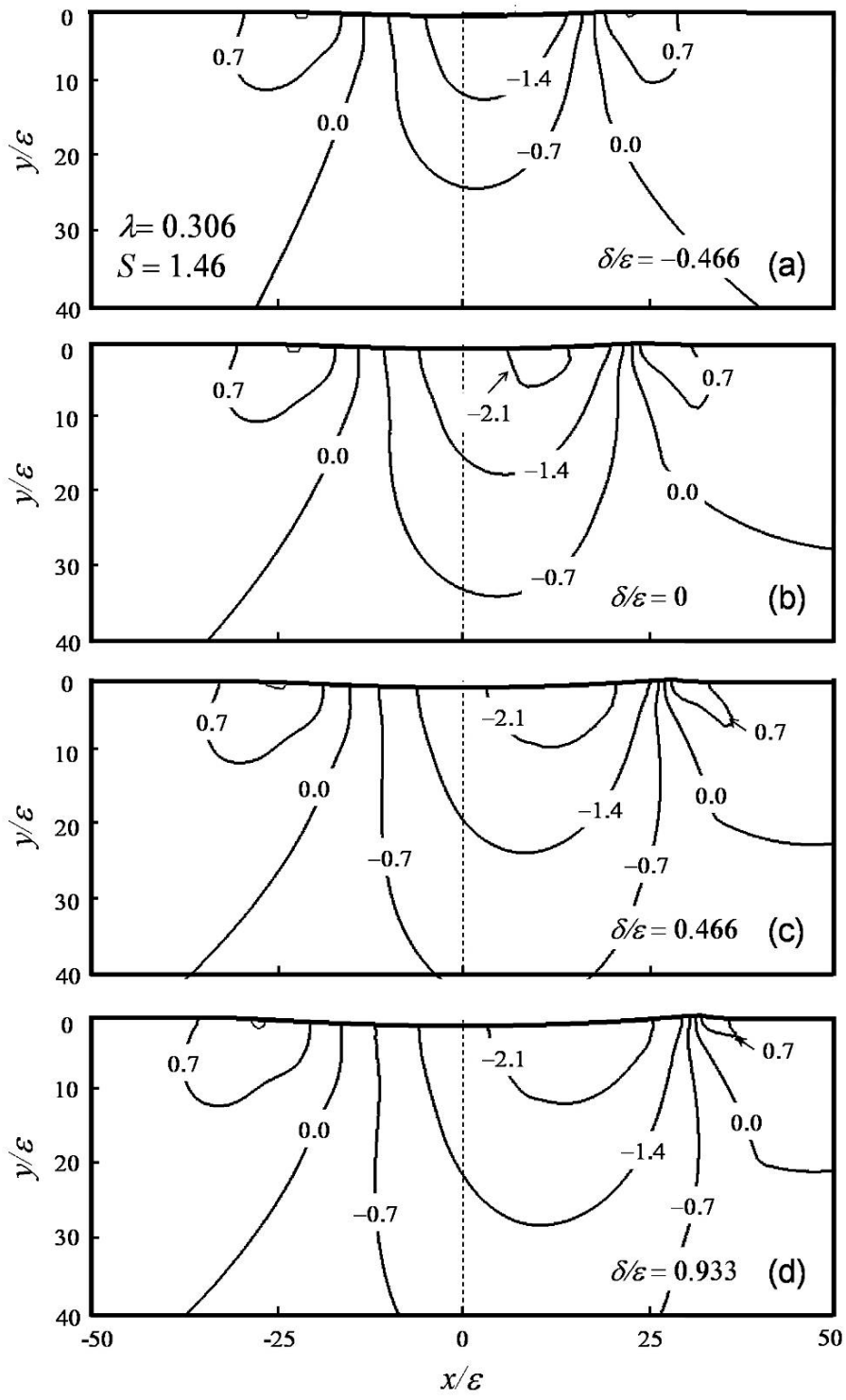

Figure 2.8 Distributions of normal stress σ_{yy}/Y at steady-state sliding for δ/ε equal to (a) −0.466, (b) 0, (c) 0.466, and (d) 0.933, λ = 0.306, and S = 1.46. (The center of the sliding asperity is at x/ε = 0.)

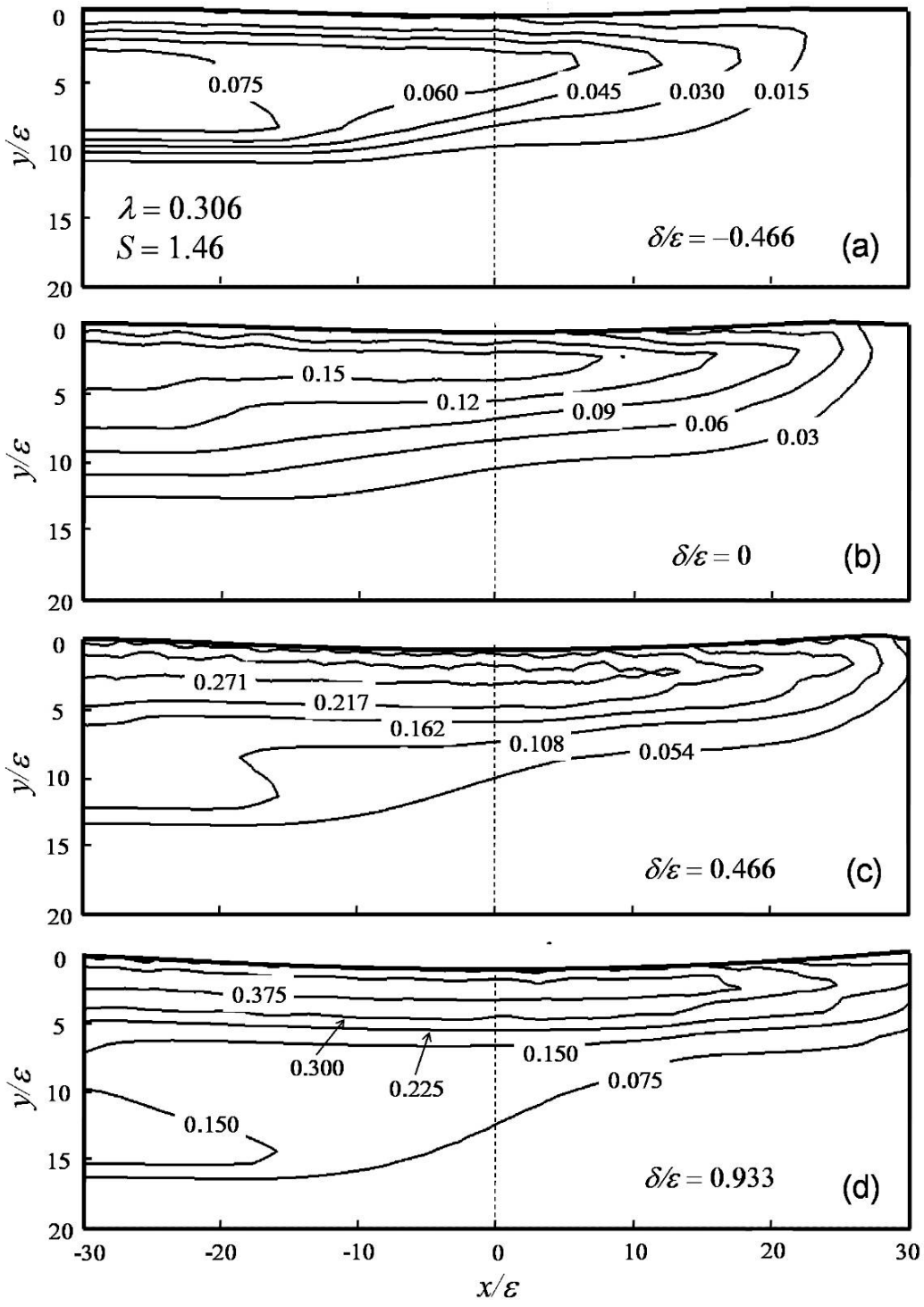

Figure 2.9 Distributions of equivalent plastic strain $\varepsilon_{\mathrm{eq}}^{\mathrm{p}}$ at steady-state sliding for δ/ε equal to (a) –0.466, (b) 0, (c) 0.466, and (d) 0.933, λ = 0.306, and S = 1.46. (The center of the sliding asperity is at x/ε = 0.)

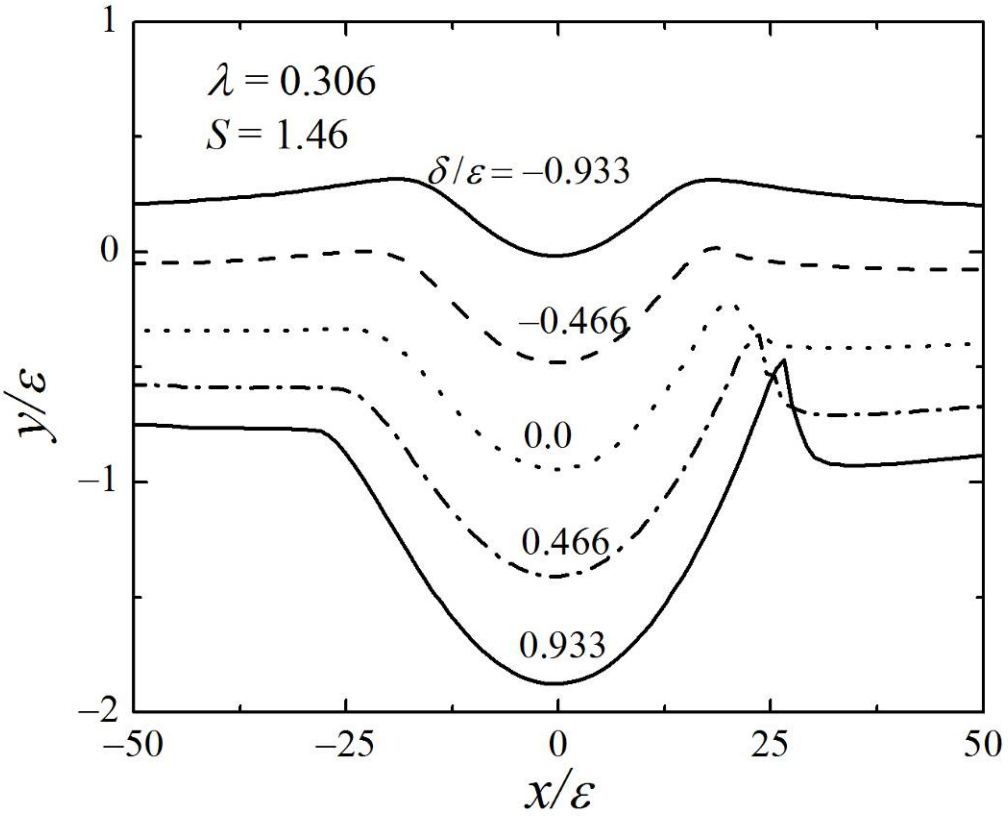

Figure 2.10 Deformed surface profiles at steady-state sliding for δ/ε = –0.933, –0.466, 0, 0.466, and 0.933, λ = 0.306, and S = 1.46. (Note the significantly different scales on the *x*- and *y*-axis. The center of the sliding asperity is at x/ε = 0.)

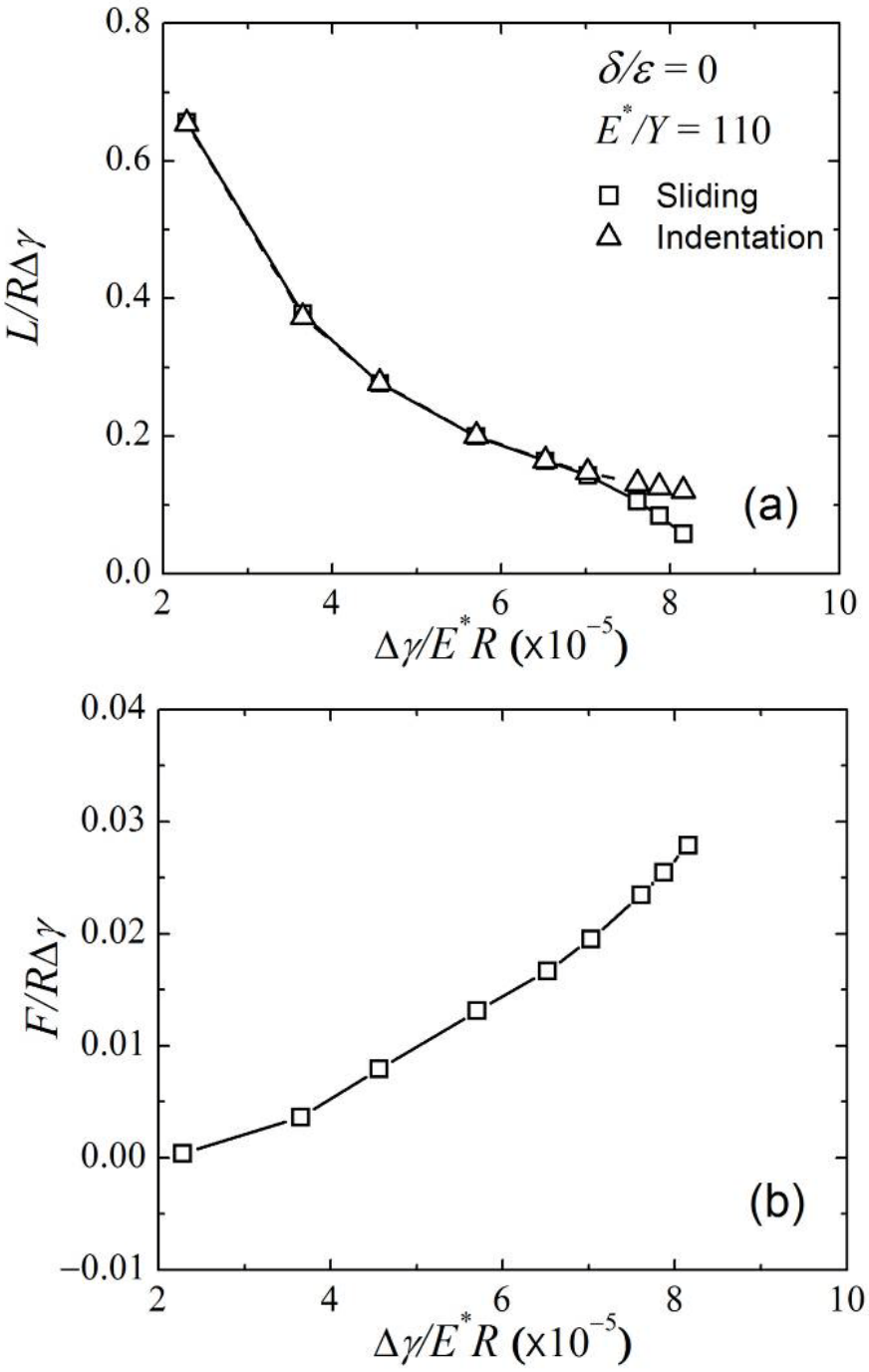

Figure 2.11 (a) Normal force $L/R\Delta\gamma$ due to sliding and indentation and (b) friction force $F/R\Delta\gamma$ versus work of adhesion $\Delta\gamma/E^*R$ for δ/ε =0 and E^*/Y = 110. Sliding results are for steady-state sliding.

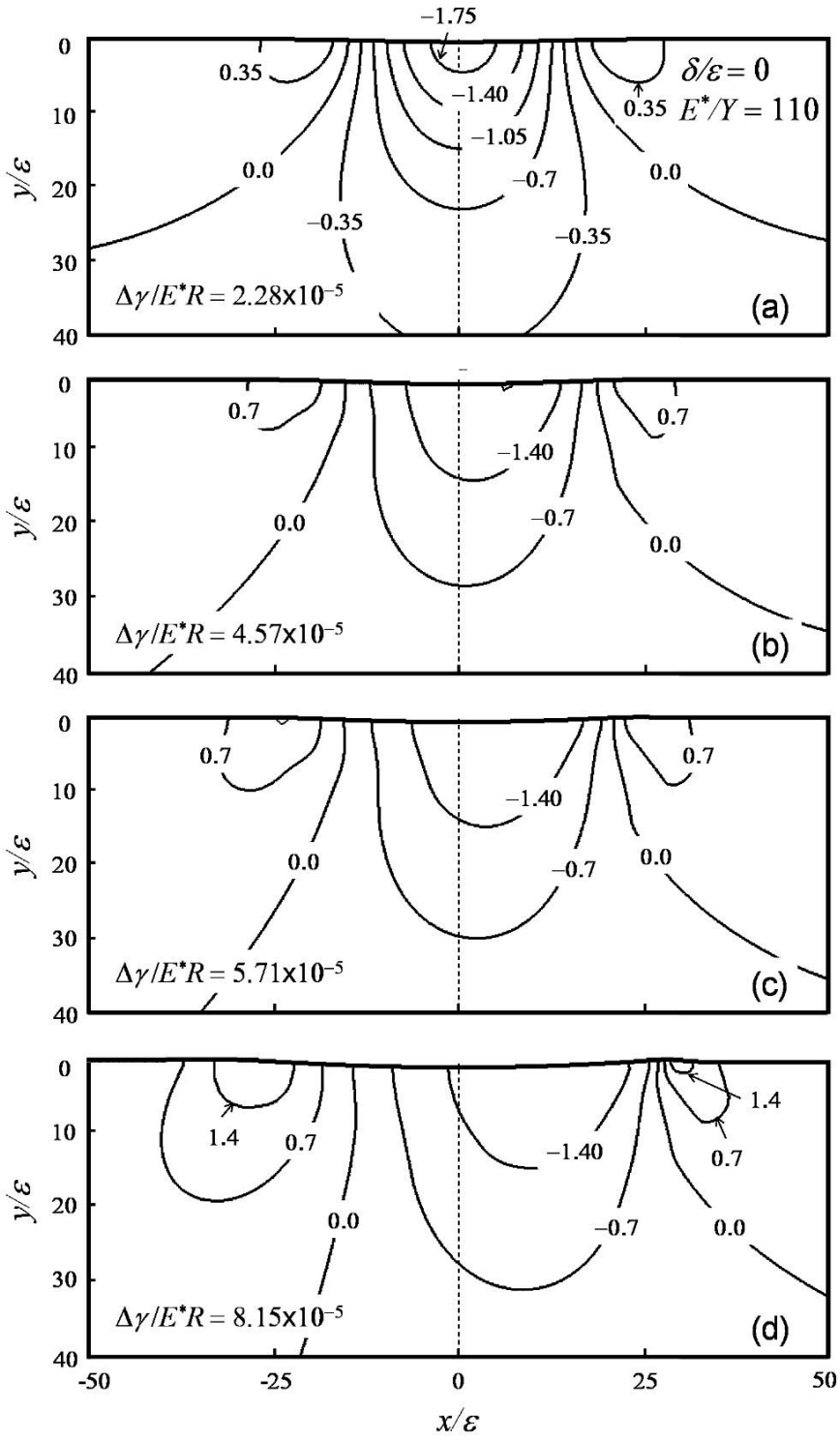

Figure 2.12 Distributions of normal stress σ_{yy}/Y at steady-state sliding for $\delta/\varepsilon = 0$ and $E^*/Y = 110$: (a) $\Delta\gamma/E^*R = 2.28 \times 10^{-5}$ ($\lambda = 0.193$, $S = 0.59$), (b) $\Delta\gamma/E^*R = 4.57 \times 10^{-5}$ ($\lambda = 0.306$, $S = 1.17$), (c) $\Delta\gamma/E^*R = 5.71 \times 10^{-5}$ ($\lambda = 0.355$, $S = 1.46$), and (d) $\Delta\gamma/E^*R = 8.15 \times 10^{-5}$ ($\lambda = 0.450$, $S = 2.09$). (The center of the sliding asperity is at $x/\varepsilon = 0$.)

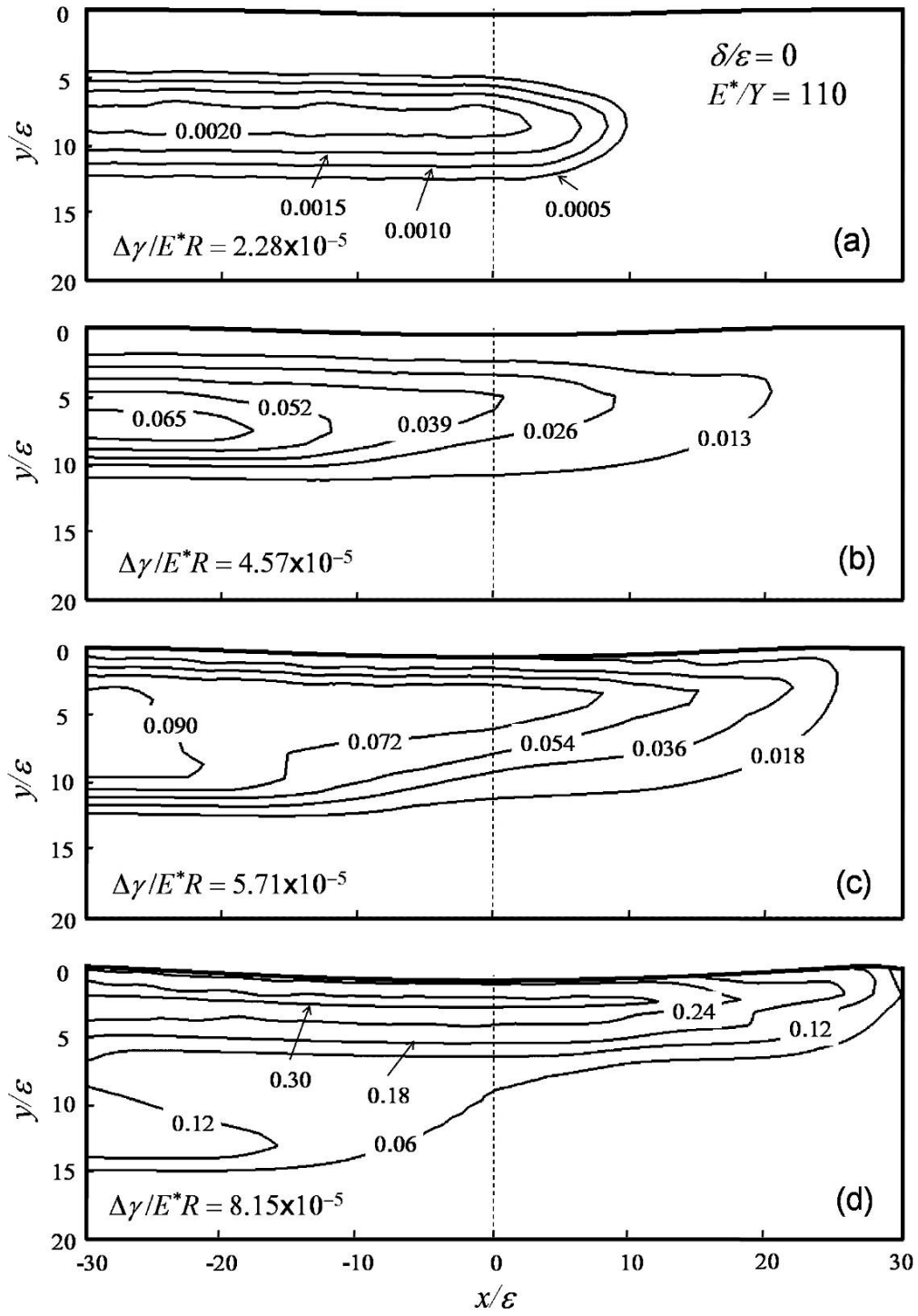

Figure 2.13 Distributions of equivalent plastic strain ε_{eq}^{p} at steady-state sliding for δ/ε =0 and E^*/Y = 110: (a) $\Delta\gamma/E^*R$ = 2.28 × 10^{-5} (λ = 0.193, S = 0.59), (b) $\Delta\gamma/E^*R$ = 4.57 × 10^{-5} (λ = 0.306, S = 1.17), (c) $\Delta\gamma/E^*R$ = 5.71 × 10^{-5} (λ = 0.355, S = 1.46), and (d) $\Delta\gamma/E^*R$ = 8.15 × 10^{-5} (λ = 0.450, S = 2.09). (The center of the sliding asperity is at x/ε = 0.)

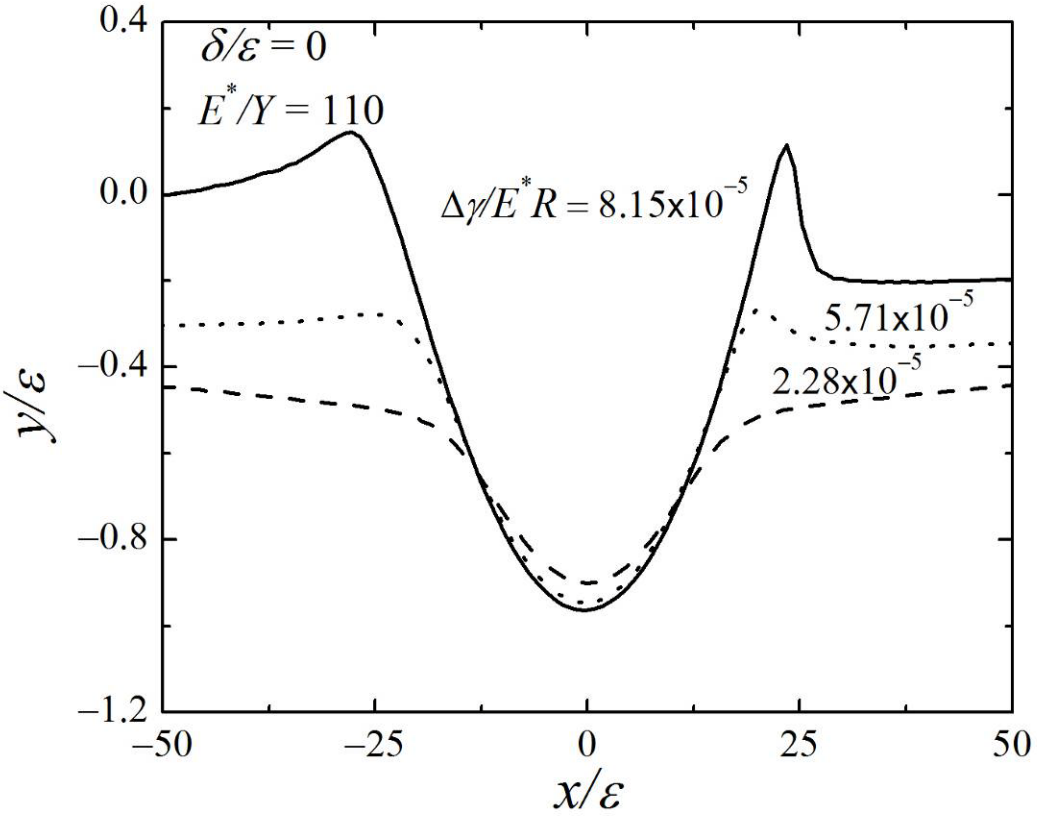

Figure 2.14 Deformed surface profiles at steady-state sliding for $\delta/\varepsilon = 0$, $E^*/Y = 110$, and $\Delta\gamma/E^*R = 2.28 \times 10^{-5}$ ($\lambda = 0.193$, $S = 0.59$), 5.71×10^{-5} ($\lambda = 0.355$, $S = 1.46$), and 8.15×10^{-5} ($\lambda = 0.450$, $S = 2.09$). (Note the significantly different scales on the *x*- and *y*-axis. The center of the sliding asperity is at $x/\varepsilon = 0$.)

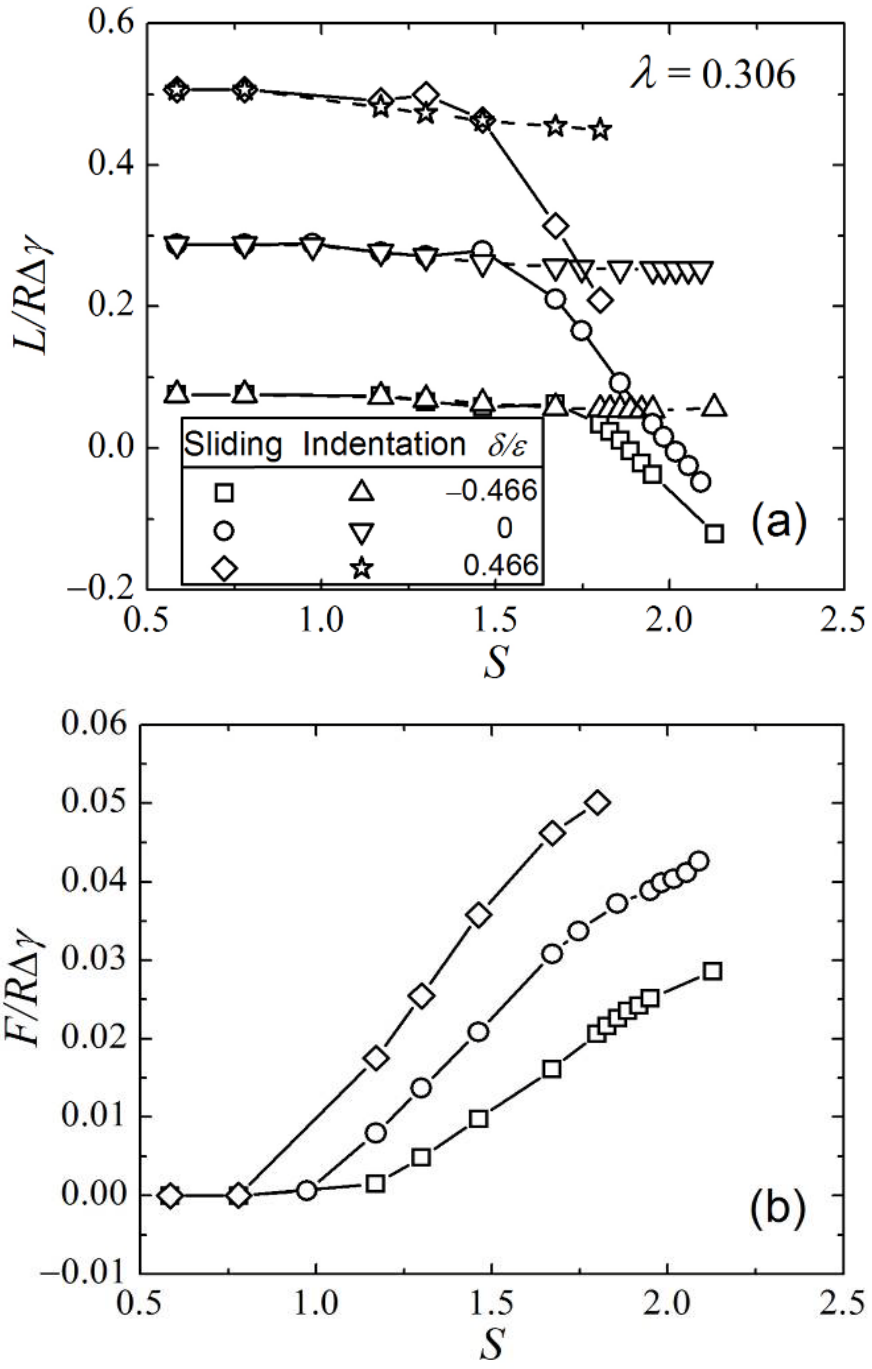

Figure 2.15 (a) Normal force $L/R\Delta\gamma$ due to sliding and indentation and (b) friction force $F/R\Delta\gamma$ versus plasticity parameter S for δ/ε = –0.466, 0, and 0.466 and λ = 0.306. Sliding results are for steady-state sliding.

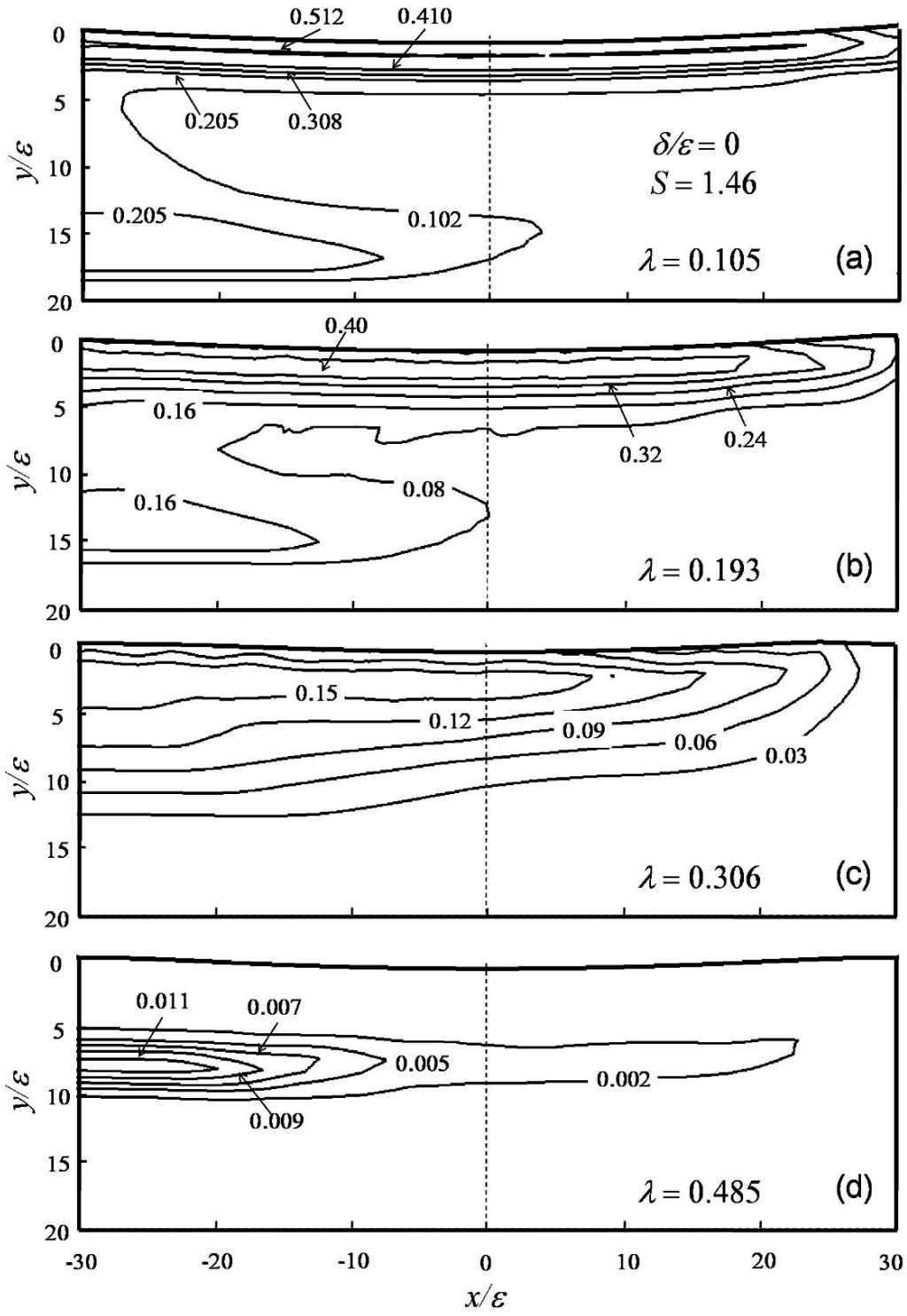

Figure 2.16 Distributions of equivalent plastic strain $\varepsilon_{\mathrm{eq}}^{\mathrm{p}}$ at steady-state sliding for $\delta/\varepsilon = 0$, $S = 1.46$, and λ equal to (a) 0.105, (b) 0.193, (c) 0.306, and (d) 0.485. (The center of the sliding asperity is at $x/\varepsilon = 0$.)

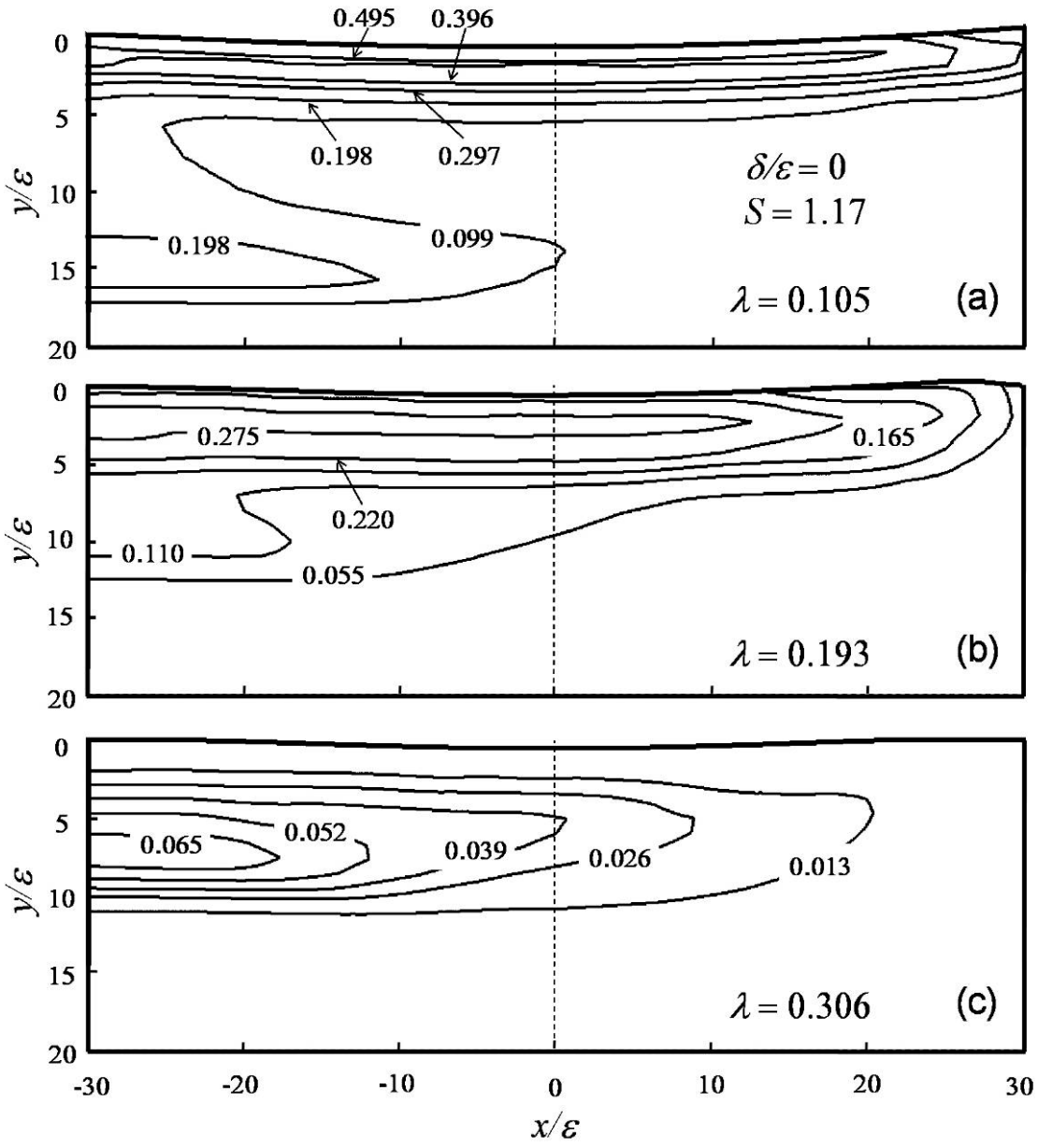

Figure 2.17 Distributions of equivalent plastic strain ε_{eq}^{p} at steady-state sliding for δ/ε =0, S = 1.17, and λ equal to (a) 0.105, (b) 0.193, and (c) 0.306. (The center of the sliding asperity is at x/ε = 0.)

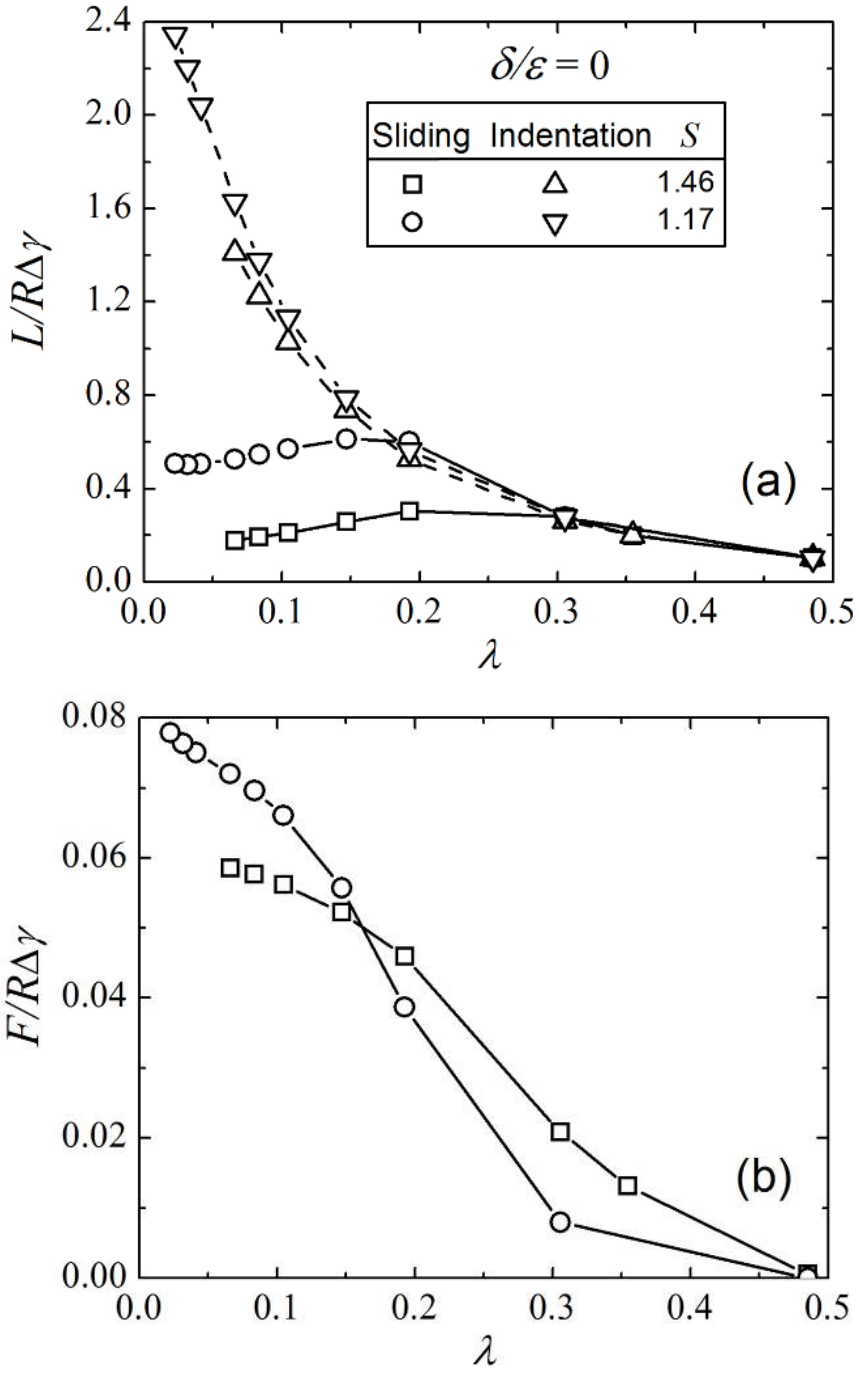

Figure 2.18 (a) Normal force $L/R\Delta\gamma$ due to sliding and indentation and (b) friction force $F/R\Delta\gamma$ versus Maugis parameter λ for δ/ε = 0 and S = 1.46 and 1.17. Sliding results are for steady-state sliding.

Chapter 3
Surface adhesion and hardening effects on elastic-plastic deformation, shakedown and ratcheting behavior of half-spaces subjected to repeated sliding contact

3.1 Introduction

Failure of contact-mode mechanical components undergoing repeated sliding is often a consequence of excessive plastic deformation. This is usually observed with microscopic devices where surface adhesion forces dominate bulk forces. For example, contact fatigue and wear due to high adhesion limit the longevity of miniaturized devices, such as microelectromechanical systems (Komvopoulos, 1996, 2003; Kim et al., 2007; Maboudian et al., 2002) and hard-disk drives (Komvopoulos, 2000). Moreover, adhesion controls the efficiency of high-precision material removal and surface finishing processes, such as chemical-mechanical polishing of semiconductor devices and lapping of magnetic recording heads. Therefore, insight into adhesion effects on contact deformation due to repeated surface sliding is of paramount importance to the durability of microdevices and process optimization of material removal at the micro/nano-scale.

The mechanical response of structural components to cyclic loading depends on the material characteristics (e.g., yield strength and post-yield behavior) and magnitude of applied load(s). Purely elastic deformation occurs when the effective stress is below the elastic limit of the material. Stresses moderately higher than the elastic limit, particularly cyclic stresses, induce mild plastic deformation only in the first loading cycle, because the resulting residual stresses prevent further plastic strain accumulation. Since this leads to a purely elastic response at steady state, this phenomenon is known as elastic shakedown. Above the elastic shakedown limit, the material demonstrates closed-cycle plasticity or incremental plasticity, referred to as plastic shakedown and ratcheting, respectively. Low and upper bounds of the elastic shakedown limit of elastic-perfectly plastic materials can be determined from statical (Melan, 1938) and kinematical (Koiter, 1956) theorems, respectively. Elastic shakedown limits of elastic-perfectly plastic solids subjected to repeated (cyclic) rolling or combined rolling and sliding contact have been obtained by Johnson (1962, 1985) and Johnson and Jefferis (1963), respectively. Kapoor and Williams (1994) analyzed the sliding behavior of a surface-hardened half-space and observed a dependence of the elastic shakedown limit on surface roughness and hardness. Ponter et al. (1985) used the kinematical theorem to analyze repeated rolling and sliding of point contacts and compared the resulting behavior with that of two-dimensional (2D) line contacts.

In addition to the elastic shakedown limit, knowledge of the plastic flow behavior is critical to understanding material failure due to cyclic loading. Bower and Johnson (1991) used a simple non-linear kinematic hardening constitutive relation to analyze elastic shakedown and plastic deformation in rails subjected to cyclic contact loading. In addition, Bower and Johnson (1989) examined the effect of strain hardening on cumulative surface and subsurface plasticity due to repeated rolling and sliding and reported a good agreement between analytical and experimental

results of rolled copper surfaces. Merwin and Johnson (1963) presented an approximate analysis of forward plastic flow in elastic-perfectly plastic materials subjected to cyclic rolling contact. Bhargava et al. (1985) analyzed deformation of an elastic-plastic half-space due to repeated rolling contact with the finite element method (FEM) and obtained results similar to those of Merwin and Johnson, except for residual shear strain increment. Yu et al. (1993) used an analytical technique and the FEM to determine the elastic shakedown limit and stress/stain fields in 2D elastic-plastic rolling contact, while Kulkarni et al. (1990, 1991) used a three-dimensional (3D) FEM model to examine the development of residual stresses and plastic deformation in elastic-perfectly plastic and elastic-linear-kinematic-hardening materials subjected to rolling contact loads at and above the elastic shakedown limit. Kral and Komvopoulos (1996b) performed a 3D FEM analysis of repeated sliding contact on layered elastic-plastic media and discussed plastic shakedown, layer decohesion, and crack initiation in the context of numerical results of subsurface stress and strain fields.

Despite important insight into plastic flow and shakedown/ratcheting behavior of elastic-plastic media subjected to repeated rolling and sliding contact obtained from the previously mentioned studies, knowledge of adhesion effects on elastic-plastic contact deformation due to repeated contact loading is limited to global parameters, such as contact force, interfacial force at the instant of surface separation (jump-out), and contact area. Since the study of adhesive contacts by Bradley (1932), significant effort has been devoted to the investigation of surface adhesion effects on contact deformation. Johnson et al. (1971) and Derjaquin et al. (1975) developed analytical models of adhesive contact between elastic spheres, known as the JKR and DMT models, respectively. These studies show that the interfacial force at the instant of surface separation (pull-off force) F_{po} is equal to $1.5\pi R\Delta\gamma$ (JKR) and $2\pi R\Delta\gamma$ (DMT), where $R = R_1R_2/(R_1+R_2)$ is the equivalent radius of curvature (R_1 and R_2 are the radii of curvature of the spheres) and $\Delta\gamma = \gamma_1 + \gamma_2 + \gamma_{12}$ is the work of adhesion (γ_1 and γ_2 are the surface energies of the spheres and γ_{12} is the interface energy). Tabor (1977) examined the variation of the pull-off force in terms of dimensionless parameter $\mu = [(R\Delta\gamma^2)/(E^{*2}\varepsilon^3)]^{1/3}$, where $E^* = [(1-\nu_1^2)/E_1 + (1-\nu_2^2)/E_2]^{-1}$ is the effective elastic modulus (E_1, E_2 and ν_1, ν_2 are the elastic moduli and Poisson's ratios of the two spheres, respectively) and ε is the equilibrium interatomic distance between two parallel half-spaces, and showed that the JKR and DMT solutions correspond to rather extreme contact systems in the ranges $\mu > 3$ and $\mu < 0.1$, respectively.

Analytical solutions of the pull-off force in the transition range $0.1 < \mu < 3$ have also been reported by Maugis (1992), who used the Dugdale approximation to model adhesive contact. Muller et al. (1980), Attard and Parker (1992), and Greenwood (1997) modeled adhesive surface interaction by the Lennard-Jones (LJ) potential (Israelachvili, 1992) and reported numerical results of the pull-off force in good agreement with the Maugis solution. Leng et al. (2000) and Johnson and Greenwood (2008) used a 2D Maugis analysis to determine the variation of pull-off force between the solutions of the 2D DMT model ($F_{po} = (8\lambda)^{1/2}(E^*R\Delta\gamma^2)^{1/3}$, $\lambda < 0.1$) and the 2D JKR model introduced by Chaudhury et al. (1996) ($F_{po} = (3/4)(4\pi E^*R\Delta\gamma^2)^{1/3}$, $\lambda > 3$), where $\lambda = (9\sqrt{3}/16)\mu$ is known as the Maugis parameter. Wu (2009) extended Bradley's model to 2D contacts and reported that the pull-off force obtained from modeling adhesion with the L-J potential ($F_{po} = (5.9248\lambda)^{1/2}(E^*R\Delta\gamma^2)^{1/3}$) is close to that in the transition range between the 2D JKR model of Chaudhury et al. and the 2D Bradley model, but differs from the pull-off force

solution obtained from the 2D DMT model. Kadin et al. (2008b) used the LJ potential to model adhesion between spherical microcontacts (asperities) and the FEM to analyze elastic-plastic deformation of asperity microcontacts demonstrating kinematic hardening and observed a dependence of plastic shakedown on plasticity parameter $S = \Delta\gamma/\varepsilon Y$, where Y is the yield strength.

Although the previous studies provide valuable information about elastic and elastic-plastic deformation in adhesive contacts due to repeatedly applied normal surface traction, they do not elucidate the effect of adhesion on deformation at the asperity level due to repeated sliding contact. Consequently, the objective of this chapter was to develop a comprehensive analysis of repeated sliding of a single asperity over a homogeneous half-space that accounts for both adhesion and material deformation effects. To accomplish this objective, a continuum elastic-plastic FEM analysis was performed in which surface interaction is modeled by nonlinear springs obeying a constitutive force-distance relation derived from the LJ potential. FEM results of the normal and friction force, stress/strain fields, and development of plasticity are discussed in terms of elastic-plastic and surface material properties, sliding cycles, and interaction distance to illustrate the effects of adhesion and plasticity on the initial and steady-state deformation behavior of sliding contacts.

3.2 Analysis

3.2.1 Description of contact problem

Surface contact is usually confined at the tallest protrusions (asperities) of real surfaces. Consequently, the analysis of repeated sliding contact requires modeling of surface interaction at the asperity scale. Fig. 3.1(a) shows schematically the 2D contact problem examined in this study, i.e., a rigid cylindrical asperity of radius R sliding over a stationary, homogenous, elastic-plastic half-space. The (x,y) coordinate system represents the global coordinates of the moving asperity. The distance between the bottom-point of the rigid asperity and the undeformed half-space surface is defined as the interaction distance δ; thus, $\delta < 0$ implies that the asperity bottom-point is above the undeformed surface. A sliding cycle is defined as the asperity movement from $x = -a$ to $x = a$. Normal displacement-control, quasi-static sliding simulations were performed by positioning the asperity over the half-space at $x = -a$ at a sufficiently large vertical distance for negligible adhesion force, and then displacing the asperity downward by a distance δ and, subsequently, horizontally up to $x = a$, while keeping the interaction distance fixed. Consequently, the asperity was retracted vertically by a distance resulting in negligible adhesion force, and the simulation process was repeated by returning the asperity to its original position. Thus, in each sliding cycle, the asperity is displaced incrementally along the x-direction by a total distance of $2a$, while the interaction distance δ is set equal to that of the first cycle. Each simulation comprises a total of six sliding cycles.

3.2.2 Finite element model

Fig. 3.1(b) shows the FEM mesh of the deformable half-space. The mesh consists of 70,984 isoparametric, four-node, bilinear, reduced-integration, plane-strain elements with a total of 71,572 nodes. To enhance the computational accuracy and numerical convergence, the mesh at the half-space surface is refined by square elements of sides equal to $0.004R$. The vertical and

horizontal dimensions of the mesh are equal to 20.5R and 43R, respectively. The nodes at the bottom boundary of the mesh are constrained against displacement in both x- and y-direction. All simulation results are for $a = R$ and maximum increment of asperity x-displacement fixed at 0.02R.

The half-space surface is discretized by small segments of size equal to 0.004R with a surface node in their middle-point distance. The total adhesive force between the sliding asperity and the stationary half-space is obtained as the sum of the adhesion forces between the small surface segments and the asperity. The adhesive force per unit area (pressure) between a half-space surface and a cylindrical asperity is given by (Chapter 2)

$$p(D) = \frac{2\Delta\gamma}{3\varepsilon}\frac{\left(\frac{\varepsilon}{D}\right)^3}{\left(1+\frac{D}{R}\right)^{1/2}}\left[\left(4-\frac{D}{R}\right)-\left(4-\frac{D}{4R}\right)\left(\frac{\varepsilon}{D}\right)^6\right] \tag{3.1}$$

where $D = d - R$, and d is the distance between the asperity center and the mid-point node of a surface segment (Fig. 3.2). Because the adhesion force given by Eq. (3.1) is acting in the radial direction, it consists of vertical and horizontal force components. The pull-off force obtained from Eq. (3.1) is in excellent agreement with the solution of a numerical analysis of adhesive line contacts based on the L-J potential (Wu, 2009) and shows a gradual transition from the 2D Bradley solution to the 2D JKR solution. Moreover, Eq. (3.1) has been proven to hold for $R/\varepsilon >$ 50 (Chapter 2). Therefore, all simulation results of the present study are for $R/\varepsilon \approx 200$.

Adhesion between the moving asperity and the half-space surface is modeled by nonlinear springs, obeying a force-distance constitutive relation given by Eq. (3.1). Each spring is attached to the center of the asperity and a surface node of the half-space mesh. A total of 911 nonlinear spring elements are used to connect the asperity with surface nodes between $x = -1.8R$ and $x = 1.8R$. The springs remain attached to the moving asperity and the surface nodes of the mesh for the entire sliding phase of each simulation cycle. Friction and normal forces are obtained as the sum of all spring forces applied to the asperity in the x- and y-direction, respectively. All simulations were performed with the FEM code ABAQUS/Standard (version 6.9-EF2).

3.2.3 Material properties and plasticity models

Two different constitutive models are examined in the present analysis: elastic-perfectly plastic (EPP) and elastic-linear kinematic hardening plastic (ELKP) with a plastic modulus $E_p = 0.1E$, where E is the elastic modulus of the half-space. Yielding is determined by the standard von Mises yield criterion, expressed as

$$\sigma_M = \left[\frac{3}{2}(S_{ij}-\alpha_{ij})(S_{ij}-\alpha_{ij})\right]^{1/2} = Y \tag{3.2}$$

where σ_M is the von Mises equivalent stress, S_{ij} are components of the deviatoric stress tensor, and α_{ij} are components of the deviatoric internal (or back) stress tensor. Plastic deformation is modeled by the usual associated flow rule, assuming negligible plastic volume change. The evolution of plasticity is tracked by the equivalent plastic strain $\overline{\varepsilon}_p$, defined as

$$\bar{\varepsilon}_p = \int_\Omega \left[\frac{2}{3} d\varepsilon_{ij}^p d\epsilon_{ij}^p\right]^{1/2} \tag{3.3}$$

where Ω is the strain path and $d\epsilon_{ij}^p$ represents plastic strain increment. The plastic flow rule is applied for yielding material ($\sigma_M = Y$), whereas standard elastic constitutive equations are applied when $\sigma_M < Y$. For EPP material behavior, $\alpha_{ij} = 0$, while for ELKP material behavior, the back stress evolution law is given by

$$d\alpha_{ij} = \frac{E_p}{Y}\left(S_{ij} - \alpha_{ij}\right) d\bar{\varepsilon}_p \tag{3.4}$$

3.3 Numerical results and discussion

Numerical results of the normal and friction force, stress/strain history, and residual plastic strain are presented in this section in dimensionless form. Force, distance, stress, and work parameters are normalized by $R\Delta\gamma$, ε, Y, and E^*R, respectively. Results are interpreted in terms of dimensionless quantities, such as interaction distance δ/ε, material parameters λ and S, and post-yield material behavior (EPP or ELKP). Numerical results are presented for λ and S in the range of 0.3–0.5 and 0.25–1.5, respectively.

3.3.1 Elastic-perfectly plastic material

For EPP material behavior, steady-state sliding conditions were reached after the first or second sliding cycle, as evidenced by the evolution of the normal and friction force and the subsurface shear stress, in qualitative agreement with a previous FEM study of repeated rolling contact on an EPP half-space (Bhargava et al., 1985). Fig. 3.3 shows the friction and normal force, $F/R\Delta\gamma$ and $L/R\Delta\gamma$, respectively, and shear stress τ_{xy}/Y at depth $y/\varepsilon = 9.3$ as functions of sliding distance x/ε and sliding cycles N for $\lambda = 0.306$, $S = 1.38$, $\delta/\varepsilon = 0$, and EPP material behavior. The friction and normal force vary with sliding distance only at the start of each sliding cycle. After the first sliding cycle, both forces demonstrate insignificant variation with accumulating sliding cycles (Figs. 3.3(a) and 3.3(b)), while the shear stress below the surface reaches a steady state (Fig. 3.3(c)). A similar trend of the τ_{xy} stress was observed with different depths.

Fig. 3.4 shows the variation of the normal and shear stress, σ_{xx}/Y and τ_{xy}/Y, respectively, at the half-space surface ($y/\varepsilon = 0$) with sliding distance x/ε during the initial, transient, and steady-state stages of the first sliding cycle of the simulation case shown in Fig. 3.3. The center of the contact interface is under compression, while edge regions are under tension. Sliding (adhesion) distorts the symmetry of both stress distributions. This is particularly significant for the shear stress, which controls the magnitude of the friction force. Adhesion intensifies the surface shear stress at the center of contact, resulting in an asymmetric shear stress distribution at steady-state sliding, which explains the evolution of the friction force in the first sliding cycle (Fig. 3.3(a)). Because steady-state contact forces and surface stresses are reached in each cycle when the asperity is at $x/\varepsilon = 0$, the steady-state responses of each cycle are used hereafter to examine the effects of adhesion and material constitutive law on contact deformation.

Fig. 3.5 illustrates the effect of plasticity parameter S on contact deformation for $\lambda = 0.306$, $\delta/\varepsilon = 0$, and EPP material behavior. Plots of shear stress τ_{xy}/Y versus shear strain γ_{xy} are shown at the location of maximum plastic strain (point (0, 8.4) in Figs. 3.5(a) and 3.5(d) and point (0, 9.3) in Fig. 3.5(g)). The stable and linear stress-strain response obtained after the first sliding cycle for $S = 0.907$ (Fig. 3.5(a)) indicates the occurrence of elastic shakedown. Figs. 3.5(b) and 3.5(c) show corresponding depth distributions of residual plastic shear strain γ_{xy}^{p} and increment of plastic shear strain $\Delta\gamma_{xy}^{p}$ for $N = 1$–6. It is noted that the plastic zone is fully confined in the subsurface and $\gamma_{xy}^{p} > 0$, implying forward shearing within a subsurface layer ($6 < y/\varepsilon < 12$). The invariance of γ_{xy}^{p} and the fact that $\Delta\gamma_{xy}^{p} = 0$ after the first sliding cycle is further evidence of the occurrence of elastic shakedown after the first sliding cycle in the EPP half-space characterized by a relatively low plasticity parameter ($S = 0.907$).

Fig. 3.5(d) shows the development of a stable, narrow hysteresis in an EPP half-space with $S = 0.936$ after the first sliding cycle, indicative of plastic shakedown. This result is supported by the invariance of γ_{xy}^{p} (Fig. 3.5(e)) and that $\Delta\gamma_{xy}^{p} = 0$ (Fig. 3.5(f)) after the first sliding cycle. Thus, the increase of the plasticity parameter changes the steady-state mode of deformation form elastic shakedown to plastic shakedown. Similar with the elastic shakedown case, plasticity is confined in the subsurface and the maximum γ_{xy}^{p} arises at the same depth ($y/\varepsilon = 8.4$). However, the slight increase (~3.2%) of the plasticity parameter produces much higher γ_{xy}^{p} strains and forward shearing within a thicker subsurface layer ($6 < y/\varepsilon < 14$).

A profoundly different material behavior is encountered with a much higher plasticity parameter. For example, in the case of an EPP half-space with $S = 1.38$, the shear stress-strain response demonstrates ratcheting (Fig. 3.5(g)), γ_{xy}^{p} increases continuously with repeated sliding (Fig. 3.5(h)), and $\Delta\gamma_{xy}^{p}$ reaches a steady state in the second sliding cycle. In addition to the increase of γ_{xy}^{p} with sliding cycles, the size of the plastic zone and extent of plastic shearing are also affected significantly by the increase of the plasticity parameter. The elastic core between the plastic zone and the surface, observed in the previous simulation cases (Figs. 3.5(b) and 3.5(e)), does not exist in Fig. 3.5(h), and the depth profile of γ_{xy}^{p} reveals the formation of surface and subsurface layers of backward plastic shearing ($0 < y/\varepsilon < 2$ and $8 < y/\varepsilon < 14$, respectively) separated by a layer of forward plastic shearing ($2 < y/\varepsilon < 8$). Large plastic strain gradients between subsurface layers exhibiting backward and forward plastic shearing may act as precursors of delamination wear in repeated sliding.

The results shown in Fig. 3.5 provide insight into the effects of subsurface plasticity (deformation effect) and work of adhesion (adhesion effect) on the deformation response of EPP half-spaces due to repeated surface sliding. For a given yield strength, the increase of the plasticity parameter may be interpreted as an increase of the work of adhesion. As shown by Eq. (3.1), the adhesive pressure is proportional to $\Delta\gamma$. Because all simulation cases were performed in displacement-control mode, the increase of the work of adhesion enhanced both normal and friction forces. Thus, plasticity intensification leading to the transition from elastic shakedown ($S = 0.907$) to plastic shakedown ($S = 0.936$) to ratcheting ($S = 1.38$) may be attributed to the increase of the normal and shear surface tractions. Similarly, for fixed work of adhesion, an increase of the plasticity parameter may be interpreted as a decrease of the half-space yield

strength. Lower yield strength is conducive to higher subsurface plasticity and the evolution of a more damaging deformation mode at steady state.

Fig. 3.6 shows the effect of plasticity parameter S on friction force $F/R\Delta\gamma$, normal force $L/R\Delta\gamma$, and increment of maximum equivalent plastic strain $\Delta\bar{\varepsilon}_p^{\max}$ in the first sliding cycle and at steady-state sliding for $\lambda = 0.306$, $\delta/\varepsilon = 0$, and EPP material behavior. (Hereafter, first-cycle and steady-state parameters are designated by subscript 1 and ss, respectively.) As discussed earlier, a high plasticity parameter may be associated with a low-yield strength half-space or a sliding system characterized by high work of adhesion. Since the friction force is indicative of the energy dissipated during sliding in the form of plastic deformation, the similar increase of F_1 and F_{ss} (Fig. 3.6(a)) may be interpreted as the increase of plasticity with decreasing yield strength or the increase of surface traction with work of adhesion. In addition, the nonlinear increase of F_{ss}/F_1 with S indicates more energy dissipation during steady-state sliding of low-strength materials exhibiting high adhesion. The asymptotic trend of $F_{ss}/F_1 \rightarrow 1.0$ indicates similar energy dissipation (plasticity) in each sliding cycle for relatively high S (e.g., $S > 1.4$), consistent with ratcheting behavior (Figs. 3.5(g)–3.5(i)). The decrease of the normal force during the first sliding cycle and at steady-state sliding, L_1 and L_{ss}, respectively, with the increase of S (Fig. 3.6(b)) is attributed to the lower normal force required to achieve the same interaction distance for a lower strength material or the greater contribution of the attractive component of the adhesive pressure to the total normal force with higher work of adhesion. The fact that L_{ss}/L_1 is consistently less than 1.0 and shows a decreasing trend with increasing S indicates more sinking of the half-space due to plastic deformation in the first sliding cycle, especially for a weaker half-space.

The friction force trends shown in Fig. 3.6(a) correlate well with the plastic strain trends shown in Fig. 3.6(c). The variation of the increment of maximum equivalent plastic strain in the first sliding cycle and at steady-state sliding, $\Delta\bar{\varepsilon}_{p,1}^{\max}$ and $\Delta\bar{\varepsilon}_{p,ss}^{\max}$, respectively, and the increment of maximum equivalent plastic strain ratio, $\Delta\bar{\varepsilon}_{p,ss}^{\max}/\Delta\bar{\varepsilon}_{p,1}^{\max}$, with plasticity parameter reveal a strong correlation between friction and plasticity. It is noted that below a threshold $S \approx 0.9$, the friction force is zero and plastic deformation does not occur. This suggests that practically frictionless sliding may be possible for a certain combination of surface and bulk properties, such as high-strength materials demonstrating low affinity for the countersurface material (Komvopoulos, 2012).

The material response to normal and shear surface tractions arising in adhesive sliding contacts can be further interpreted in terms of the correlation of the friction force with plastic deformation. In the case of elastic shakedown, F_1 is very low because plastic deformation is localized and minimal (Fig. 3.5(b)), while $F_{ss} = 0$ because $\Delta\gamma_{xy}^p = 0$ after the first sliding cycle (Fig. 3.5(c)). Plastic shakedown is characterized by a slightly higher F_1 force because more plastic deformation accumulates initially (Fig. 3.5(e)), $F_{ss} \approx 0$ (very narrow stress-strain hysteresis (Fig. 3.5(d)), and $\Delta\gamma_{xy}^p = 0$ after the first sliding cycle (Fig. 3.5(f)). In contrast to elastic and plastic shakedown, conditions conducive to ratcheting yield significantly higher F_1 and F_{ss} forces, with $F_{ss}/F_1 \rightarrow 1.0$ as S increases above 1.4, because of the increase of γ_{xy}^p with sliding cycles (Fig. 3.5(h)) and the constancy of $\Delta\gamma_{xy}^p$ at steady-state sliding (Fig. 3.5(i)).

Fig. 3.7 shows the effect of the Maugis parameter λ on the friction force $F/R\Delta\gamma$, normal force $L/R\Delta\gamma$, and increment of maximum equivalent plastic strain $\Delta\bar{\varepsilon}_p^{\max}$ in the first sliding cycle and at steady-state sliding for S = 1.46, δ/ε = 0, and EPP material behavior. High λ may be interpreted as a sliding system with a high interfacial adhesion (high $\Delta\gamma$) and/or a compliant half-space (low E). Thus, the lower F_1 and F_{ss} forces obtained with higher λ (Fig. 3.7(a)) may be attributed to less plasticity due to the lower surface tractions developing on more compliant half-spaces, for a given interaction distance. In addition, the decreasing trend of F_{ss}/F_1 indicates a lower steady-state friction force for higher λ. The decrease of the friction force with increasing λ reveals the existence of a threshold $\lambda \approx 0.5$ above which energy dissipation diminishes, implying purely elastic deformation. This is supported by results of $\Delta\bar{\varepsilon}_{p,1}^{\max}$, $\Delta\bar{\varepsilon}_{p,ss}^{\max}$, and $\Delta\bar{\varepsilon}_{p,ss}^{\max}/\Delta\bar{\varepsilon}_{p,1}^{\max}$ shown in Fig. 3.7(c). The decrease of L_1 and L_{ss} with increasing λ is associated with the decrease of the half-space penetration resistance (stiffness), while the asymptotic trend of $L_{ss}/L_1 \rightarrow 1.0$ with $\lambda \rightarrow \sim 0.5$ indicates the approach toward purely elastic sliding conditions.

Fig. 3.8 shows the effect of the work of adhesion $\Delta\gamma/E^*R$ on the friction force $F/R\Delta\gamma$, normal force $L/R\Delta\gamma$, and increment of maximum equivalent plastic strain $\Delta\bar{\varepsilon}_p^{\max}$ in the first sliding cycle and at steady-state sliding for E^*/Y = 110, δ/ε = 0, and EPP material behavior. (E^*/Y is fixed in this simulation because both λ and S are functions of $\Delta\gamma$.) As expected, the friction force increases with the work of adhesion (Fig. 3.8(a)), in agreement with phenomenological observations. This trend can be explained by considering that a higher $\Delta\gamma$ produces higher surface tractions (Eq. (3.1)), implying more plastic deformation, as evidenced by plastic strain results (Fig. 3.8(c)). The normal force consists of attractive and repulsive components, which depend on the work of adhesion and material properties, respectively. The attractive force component increases with $\Delta\gamma$, while the repulsive force component remains constant, because E^* and Y are fixed in this simulation. This explains the decrease of both L_1 and L_{ss} with increasing $\Delta\gamma$ (Fig. 3.8(b)). The decreasing trend of L_{ss}/L_1 suggests more plasticity accumulation in the first sliding cycle than at steady state with increasing $\Delta\gamma$, for fixed interaction distance.

Fig. 3.9 shows the friction force $F/R\Delta\gamma$, normal force $L/R\Delta\gamma$, and increment of maximum equivalent plastic strain $\Delta\bar{\varepsilon}_p^{\max}$ versus interaction distance δ/ε in the first sliding cycle and at steady-state sliding for λ = 0.306, S =1.17, and EPP material behavior. The non-zero friction force in the presence of a negative normal force, observed in the range of $\delta/\varepsilon < -0.6$, is characteristic of adhesive contacts. The increase of both friction and normal forces with δ/ε (Figs. 3.9(a) and 3.9(b)) is due to the enhancement of surface repulsion and the invariance of surface attraction. The leads to intensification of both normal and shear surface tractions, resulting in the increase of plastic deformation with δ/ε (Fig. 3.9(c)). F_{ss}/F_1, L_{ss}/L_1, and $\Delta\bar{\varepsilon}_{p,ss}^{\max}/\Delta\bar{\varepsilon}_{p,1}^{\max}$ approach steady state for $\delta/\varepsilon > 0$, suggesting that for relatively large interaction distance (small interfacial gap), steady-state conditions are established after the first sliding cycle. Similar to previous simulation cases, below threshold $\delta/\varepsilon \approx -0.75$ deformation is purely elastic, as indicated by the zero friction force (Fig. 3.9(a)) and increment of maximum plastic strain (Fig. 3.9(c)). The trends for $F_{ss}/F_1 \rightarrow 1.0$ and $\Delta\bar{\varepsilon}_{p,ss}^{\max}/\Delta\bar{\varepsilon}_{p,1}^{\max} \rightarrow 1.0$ for $\delta/\varepsilon > 1.0$ are indicative of ratcheting.

The results of representative simulation cases discussed above indicate a strong dependence of contact deformation due to repeated adhesive sliding on both surface and bulk properties, such

as work of adhesion and elastic-plastic material properties, respectively, and interaction distance (interfacial gap). The increase of the plastic strain increment per sliding cycle leads to the transition from elastic to elastic-plastic deformation, resulting in elastic or plastic shakedown or ratcheting at steady-state sliding. Because S and λ are functions of surface and bulk properties, they can be used to construct a deformation map of adhesive sliding contacts.

Fig. 3.10 shows a deformation map obtained from several FEM simulations of repeated adhesive sliding on EPP half-spaces with different S and λ values for $\delta/\varepsilon = 0$ and 0.466. Line fits through data points represent boundaries between different deformation modes. Narrow domains of elastic and plastic shakedown are shown between wide domains of purely elastic deformation and ratcheting. A downward shift of deformation boundaries is observed with increasing interaction distance, indicating an enhancement of plasticity modes with decreasing interfacial gap. This can be attributed to the increase of plasticity due to intensification of the normal and shear surface tractions with decreasing interfacial gap. The most important finding is the strong dependence of the steady-state mode of deformation on both λ and S. Adhesive sliding systems with high λ and low S demonstrate high elastic limits. The size of the elastic deformation domain decreases with increasing S and decreasing λ, while the opposite trend is observed with the ratcheting domain. The deformation map shown in Fig. 3.10 can be further interpreted by considering that higher S implies lower Y and/or higher $\Delta\gamma$, whereas higher λ may be associated with lower E^* and/or higher $\Delta\gamma$. Therefore, for fixed interaction distance and work of adhesion, adhesive sliding systems characterized by high S and λ values may be considered to represent low-strength and high-compliance contact systems, respectively. Consequently, low-strength (high S) half-spaces exhibit more plasticity because yielding is enhanced (low elastic limit), whereas high-compliance (high λ) half-spaces demonstrate less plasticity because yielding is retarded (high elastic limit) due to the decrease of surface tractions with material stiffness.

3.3.2 Elastic-linear kinematic hardening plastic material

Strain hardening resulted in significantly different deformation characteristics. One of the main differences is that steady-state deformation in ELKP half-spaces was reached after the third or fourth sliding cycle, as opposed to the first cycle for EPP half-spaces. Fig. 3.11 shows the shear stress τ_{xy}/Y versus sliding distance x/ε or shear strain γ_{xy} at the depth of maximum plastic strain $y/\varepsilon = 9.3$, and depth distributions of γ_{xy}^{p} and $\Delta\gamma_{xy}^{p}$ at $x/\varepsilon = 0$ for N = 1–6, $\lambda = 0.306$, S = 1.38, $E_p/E = 0.1$, $\delta/\varepsilon = 0$, and ELKP material behavior. Although the depth of maximum plastic strain ($y/\varepsilon = 9.3$) is identical to that for EPP materials, the shear stress τ_{xy}/Y at this location stabilizes after the third sliding cycle (Fig. 3.11(a)), different from EPP materials showing a stable response after the first sliding cycle (Fig. 3.3(c)).

The effect of strain hardening on the deformation response to repeated adhesive sliding can be interpreted by contrasting results for identical parameters, such as those shown in Figs. 3.5(g)–3.5(i) and 3.11(b)–3.11(d). Fig. 3.11(b) shows that the shear stress-strain response at the location of maximum plastic strain ($x/\varepsilon = 0$ and $y/\varepsilon = 9.3$) reaches a stable closed-loop response after three sliding cycles. Thus, despite the identical values of λ, S, and δ/ε, hardening leads to plastic shakedown at steady-state sliding, as opposed to ratcheting for non-hardening material (Fig. 3.5(g)). The effect of the post-yield behavior on steady-state deformation can be further

examined in light of results showing the evolution of plasticity during repeated sliding. Although the depth distributions of γ_{xy}^{p} and $\Delta\gamma_{xy}^{p}$ (Figs. 3.11(c) and 3.11(d), respectively) demonstrate similarities with those of the EPP material (Figs. 3.5(h) and 3.5(i)), strain hardening results in significantly less plastic deformation (by an order of magnitude) and predominantly backward plastic shearing. For example, hardening decreases the maximum $\Delta\gamma_{xy}^{p}$ in the first sliding cycle by a factor of ~2 and the maximum γ_{xy}^{p} in the sixth sliding cycle by a factor of ~12. In addition, hardening stabilizes the γ_{xy}^{p} distribution, resulting in $\Delta\gamma_{xy}^{p} = 0$ after three sliding cycles (Fig. 3.11(d)), while non-hardening results in continuously increasing γ_{xy}^{p} (Fig. 3.5(h)) and non-zero $\Delta\gamma_{xy}^{p}$ at steady-state sliding (Fig. 3.5(i)). Another significant difference is the effect of strain hardening on the size of the plastic zone forming under conditions conducive to plastic shakedown. The plastic zone in the EPP half-space is confined in the subsurface (Fig. 3.5(e)), while the plastic zone in the ELKP half-space reaches the surface at steady-state sliding (Fig. 3.11(c)). Despite the evolution of surface plasticity, the results shown in Figs. 3.5(g)–3.5(i) and 3.11(b)–3.11(d) indicate that the reason for the disappearance of ratcheting is the significant decrease of plasticity due to strain hardening.

Fig. 3.12 shows a deformation map obtained from FEM simulations of repeated adhesive sliding over ELKP half-spaces with different S and λ values for $\delta/\varepsilon = 0$ and 0.466. Although the elastic shakedown limit demonstrates a similar trend with that observed with non-hardening materials (Fig. 3.10), the domain of plastic shakedown is dramatically larger and the S values corresponding to the elastic shakedown limit are higher than those obtained with non-hardening materials. The significantly larger domain of plastic shakedown for ELKP material behavior is a due to the much smaller $\Delta\gamma_{xy}^{p}$ in the presence of hardening. Another significant difference is the absence of ratcheting from the deformation map shown in Fig. 3.12, for the same range of λ and S parameters shown in Fig. 3.10. In fact, ratcheting was not encountered with ELKP half-spaces even for very high S values (e.g., $S = 30$), for both $\delta/\varepsilon = 0$ and 0.466. The elastic and elastic shakedown limits decrease slightly with increasing interaction distance, similar to EPP materials. The aforementioned differences between EPP and ELKP material responses to repeated adhesive sliding are consistent with 3D FEM results of repeated rolling contact (Kulkarni et al., 1991).

3.4 Conclusions

In this chapter, repeated adhesive sliding of a rigid asperity over an elastic-plastic half-space was examined in the context of FEM results. Surface adhesion was modeled by nonlinear springs obeying a constitutive force-displacement relation derived from the LJ potential. The half-space was modeled as a homogeneous, isotropic, semi-infinite medium characterized by EPP or ELKP constitutive laws. Results of the friction and normal force and subsurface stress/strain fields were obtained in terms of dimensionless parameters, such as plasticity parameter (representing the ratio of the work of adhesion to the yield strength of the half-space), Maugis parameter, and interaction distance normalized by the equilibrium interatomic distance.

Depending on material behavior, steady-state sliding conditions (indicated by the invariance of the friction and normal force and subsurface stresses) were achieved after the first sliding cycle (EPP) or after the third or fourth sliding cycle (ELKP). Stress-strain responses and subsurface plastic strain distributions revealed the evolution of different deformation modes.

Elastic-plastic properties, material hardening, and work of adhesion affected the occurrence of elastic or plastic shakedown and ratcheting at steady-state sliding. The increase of the plasticity parameter and, to a lesser extent, the interaction distance or the decrease of the Maugis parameter changed the steady-state deformation mode in the sequence: elastic, elastic shakedown, plastic shakedown, and ratcheting. However, hardening decreased significantly the accumulation of plasticity in each sliding cycle, leading to the disappearance of ratcheting, even for very low-strength materials, in qualitative agreement with results of earlier studies.

The increase of plastic deformation with increasing plasticity parameter and interaction distance and decreasing Maugis parameter was indicated by the increase of the friction force and the decrease of the steady-state/first-cycle normal force ratio. Deformation maps showed slightly larger elastic shakedown and dramatically larger plastic shakedown domains for ELKP than EPP material behaviors, and a decrease of the elastic limit with increasing interaction distance (decreasing interfacial gap).

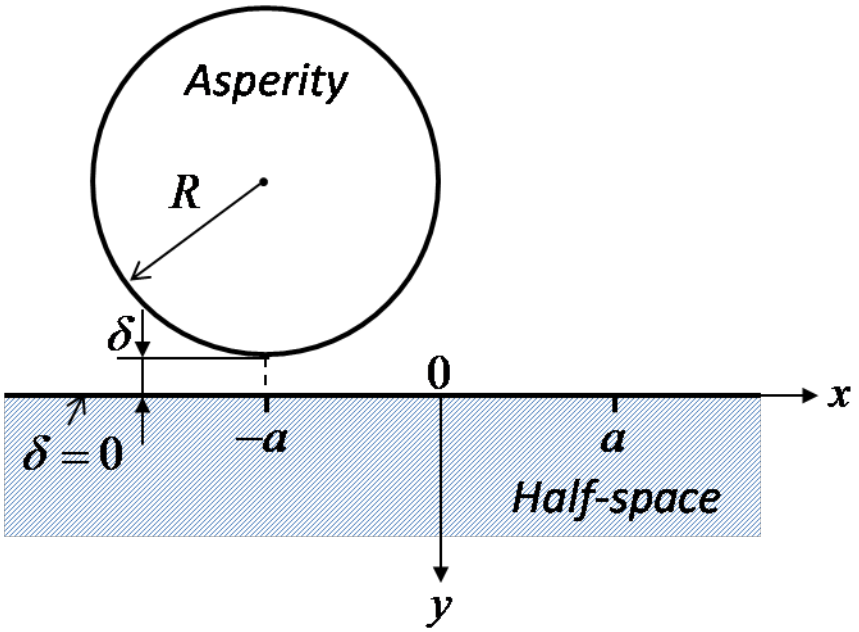

(a)

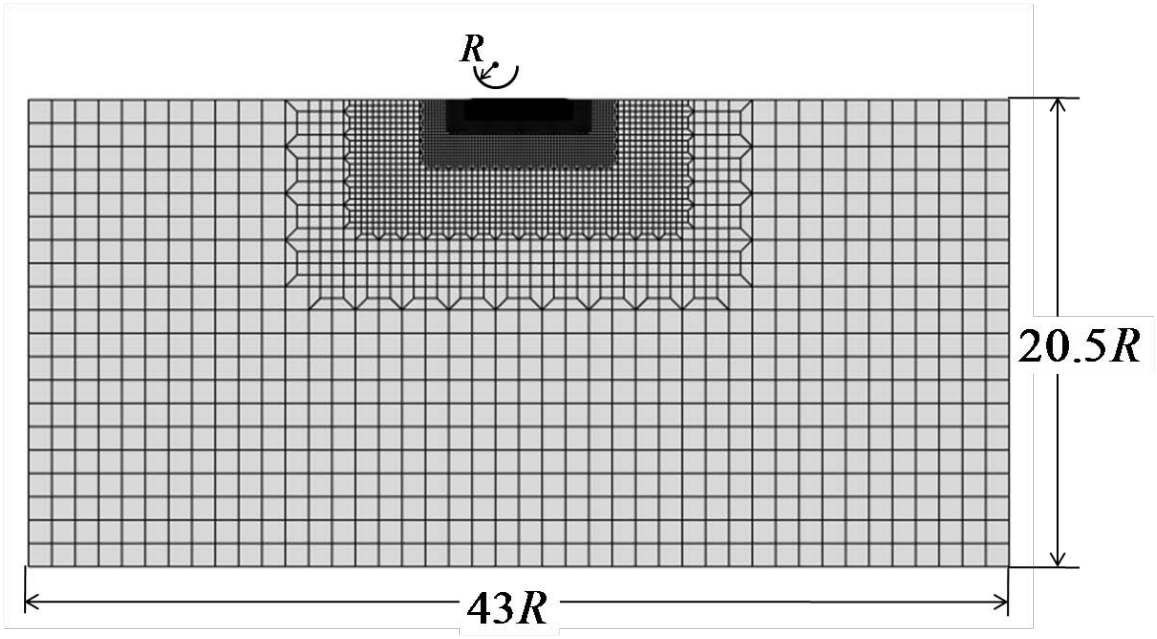

(b)

Figure 3.1 (a) Schematic of a cylindrical asperity of radius R at an interaction distance δ from a half-space and (b) finite element mesh of the half-space.

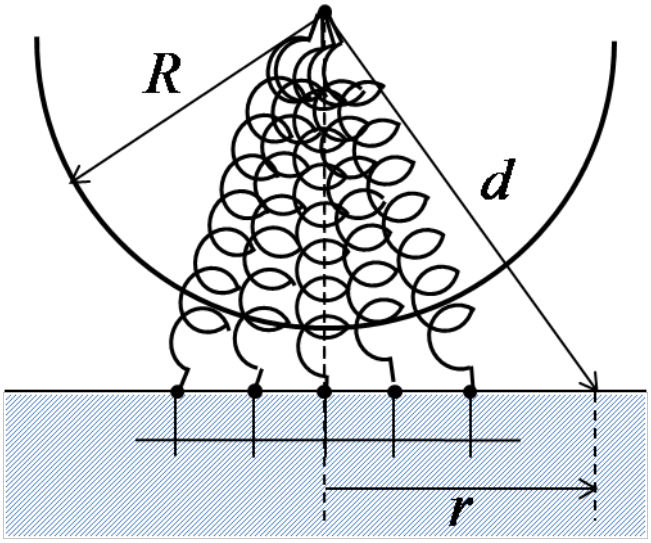

Figure 3.2 Schematic of adhesion contact model. Surface (adhesion) forces between a cylindrical asperity and a half-space are represented by nonlinear springs attached to the center of the asperity and surface nodes of the half-space mesh.

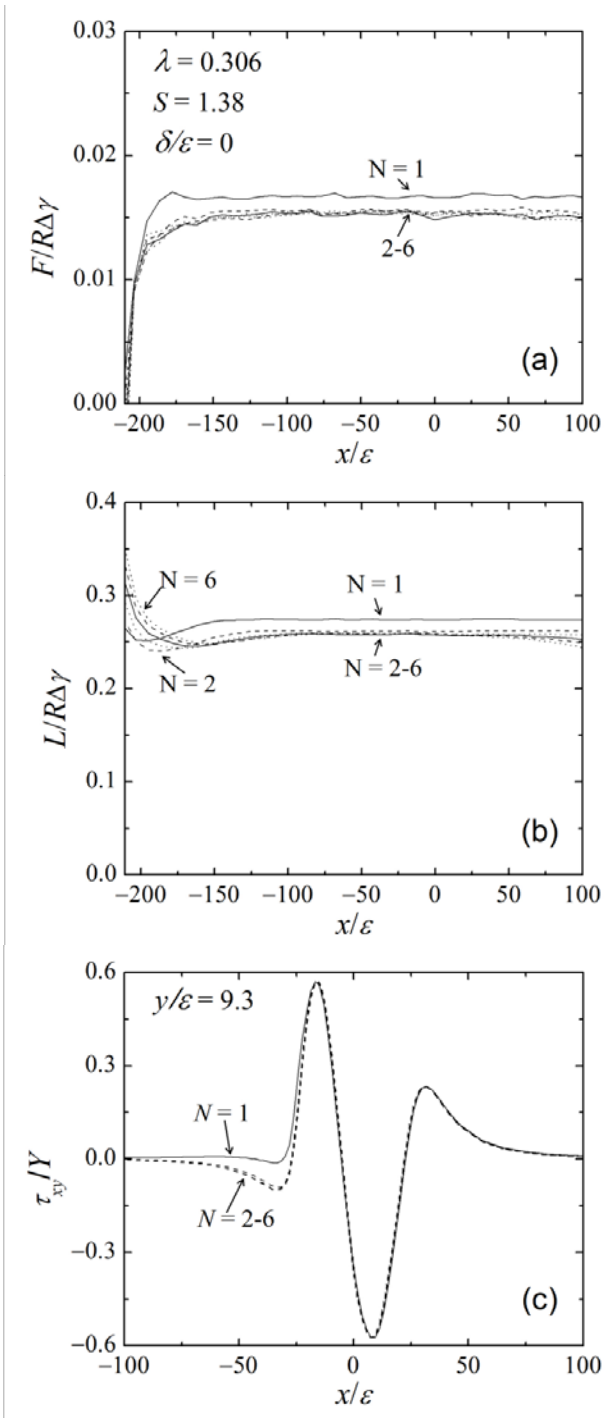

Figure 3.3 (a) Friction force $F/R\Delta\gamma$, (b) normal force $L/R\Delta\gamma$, and (c) shear stress τ_{xy}/Y at depth y/ε = 9.3 versus sliding distance x/ε and sliding cycles N for λ = 0.306, S = 1.38, δ/ε = 0, and EPP material behavior.

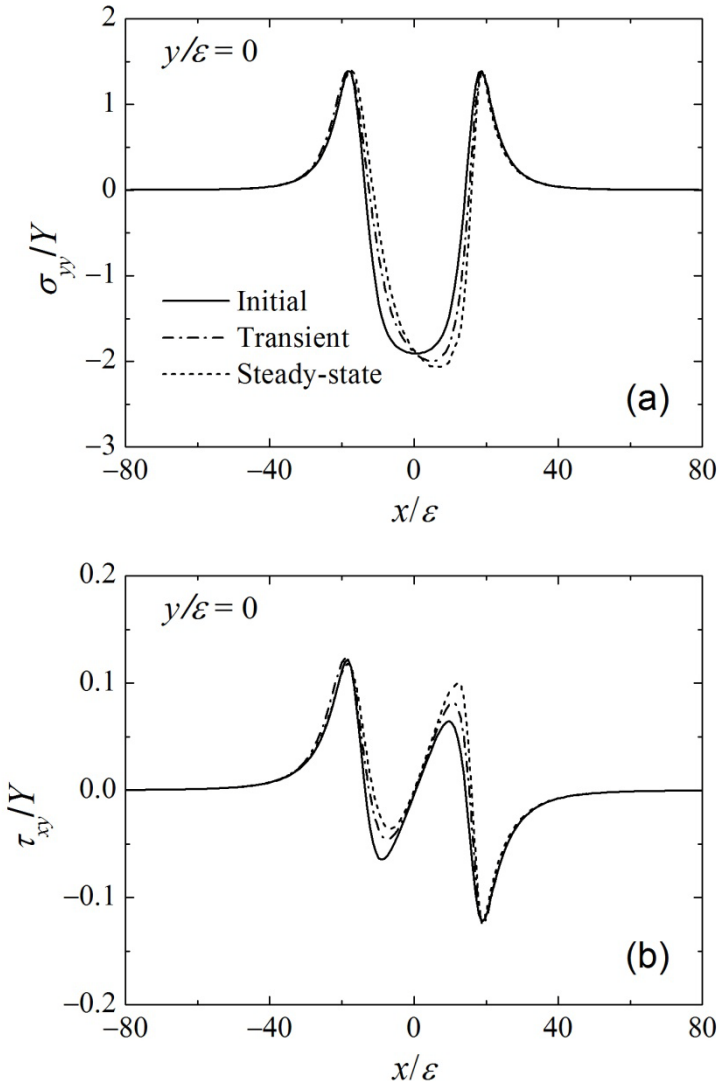

Figure 3.4 Variation of (a) normal stress σ_{yy}/Y and (b) shear stress τ_{xy}/Y at $y/\varepsilon = 0$ with sliding distance x/ε during the initial, transient, and steady-state stages of the first sliding cycle for $\lambda = 0.306$, $S = 1.38$, $\delta/\varepsilon = 0$, and EPP material behavior.

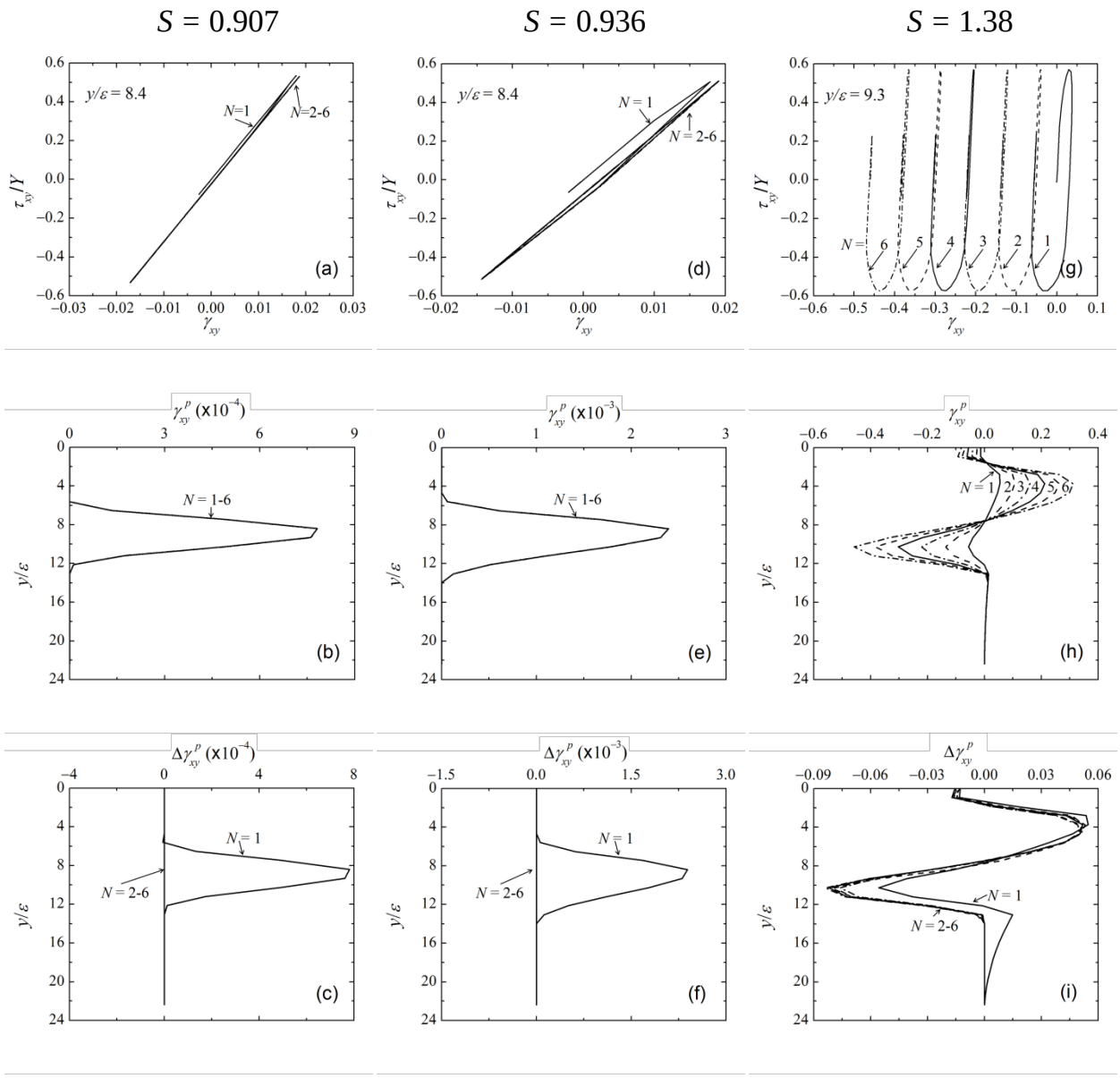

Figure 3.5 Effect of plasticity parameter S on deformation behavior for N = 1–6, λ = 0.306, δ/ε = 0, x/ε = 0, and EPP material behavior: (a), (d), and (g) shear stress τ_{xy}/Y versus shear strain γ_{xy} at the location of maximum plastic strain, (b), (e), and (h) depth distributions of residual plastic shear strain γ_{xy}^p, and (c), (f), and (i) depth distributions of residual plastic shear strain increment $\Delta\gamma_{xy}^p$.

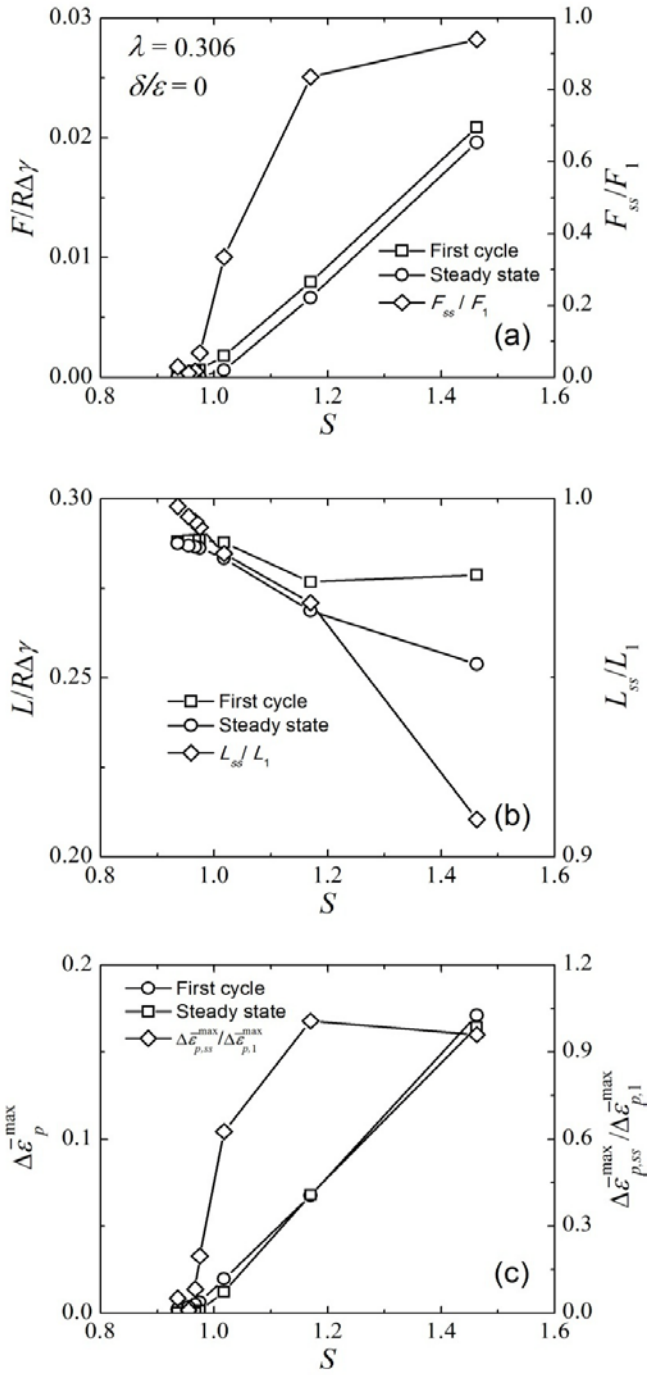

Figure 3.6 (a) Friction force $F/R\Delta\gamma$, (b) normal force $L/R\Delta\gamma$, and (c) increment of maximum equivalent plastic strain $\Delta\bar{\varepsilon}_p^{\max}$ versus plasticity parameter S for first sliding cycle and steady-state sliding, $\lambda = 0.306$, $\delta/\varepsilon = 0$, and EPP material behavior. The steady-state/first-cycle ratio of each parameter is also shown in each graph.

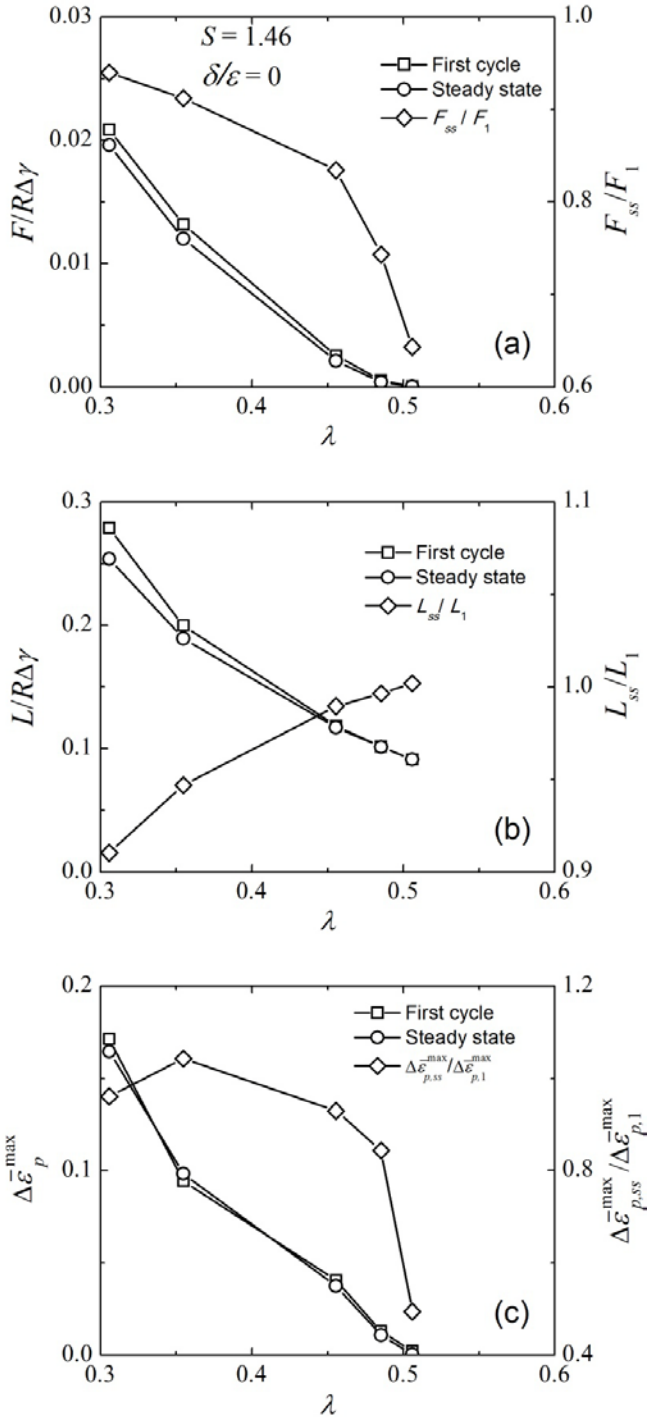

Figure 3.7 (a) Friction force $F/R\Delta\gamma$, (b) normal force $L/R\Delta\gamma$, and (c) increment of maximum equivalent plastic strain $\Delta\bar{\varepsilon}_p^{\max}$ versus Maugis parameter λ for first sliding cycle and steady-state sliding, S = 1.46, δ/ε = 0, and EPP material behavior. The steady-state/first-cycle ratio of each parameter is also shown in each graph.

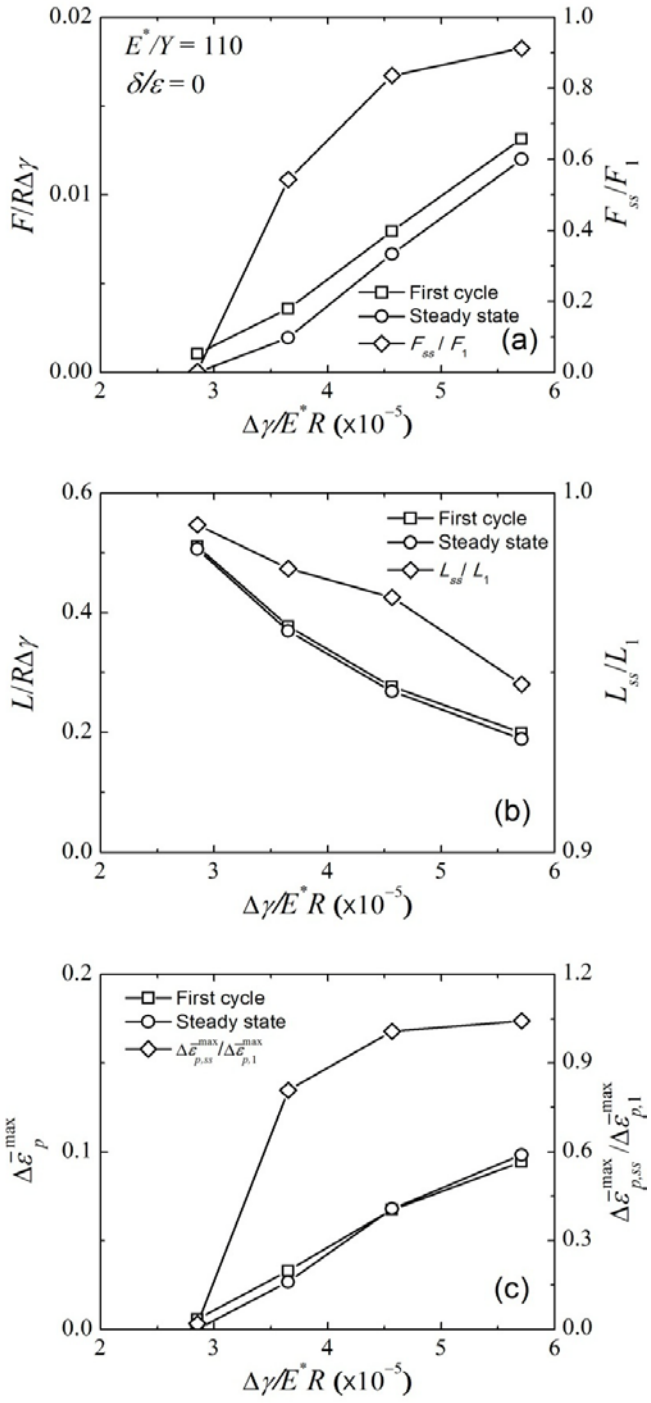

Figure 3.8 (a) Friction force $F/R\Delta\gamma$, (b) normal force $L/R\Delta\gamma$, and (c) increment of maximum equivalent plastic strain $\Delta\bar{\varepsilon}_p^{\max}$ versus work of adhesion $\Delta\gamma/E^*R$ for first sliding cycle and steady-state sliding, $E^*/Y = 110$, $\delta/\varepsilon = 0$, and EPP material behavior. The steady-state/first-cycle ratio of each parameter is also shown in each graph.

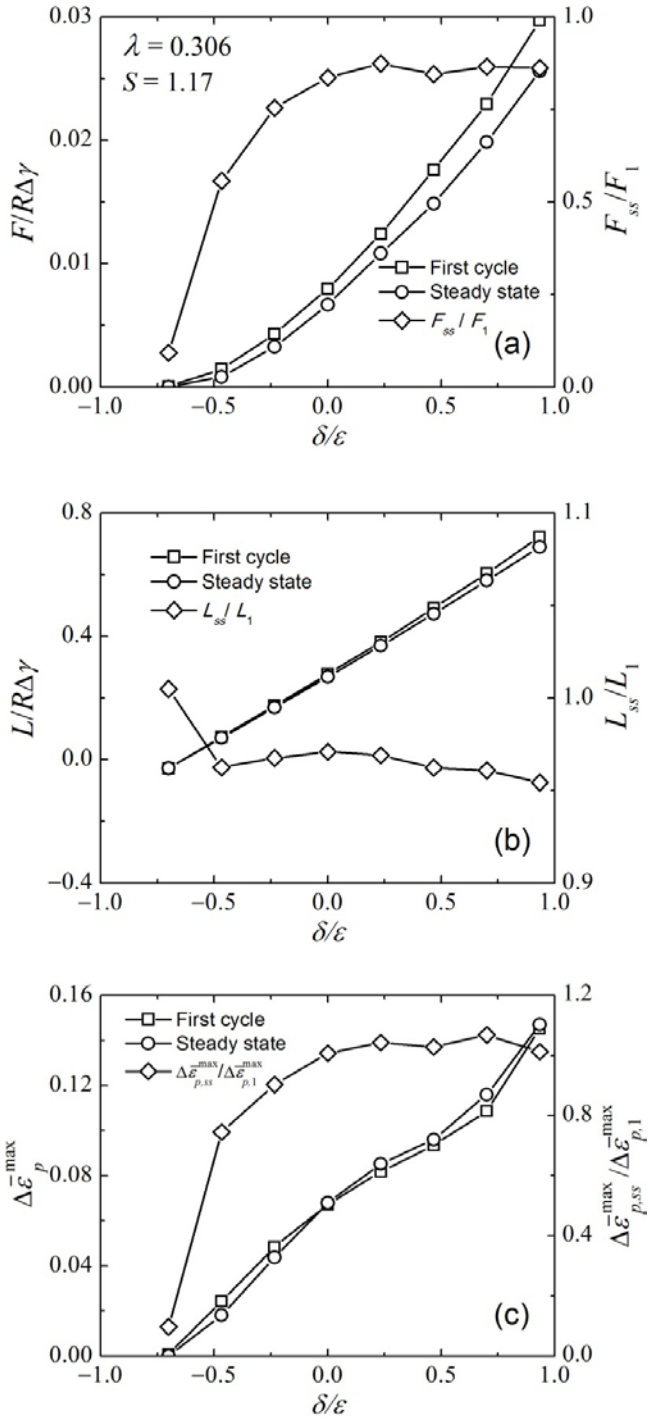

Figure 3.9 (a) Friction force $F/R\Delta\gamma$, (b) normal force $L/R\Delta\gamma$, and (c) increment of maximum equivalent plastic strain $\Delta\bar{\varepsilon}_p^{\max}$ versus interaction distance δ/ε for first sliding cycle and steady-state sliding, $\lambda = 0.306$, $S = 1.17$, and EPP material behavior. The steady-state/first-cycle ratio of each parameter is also shown in each graph.

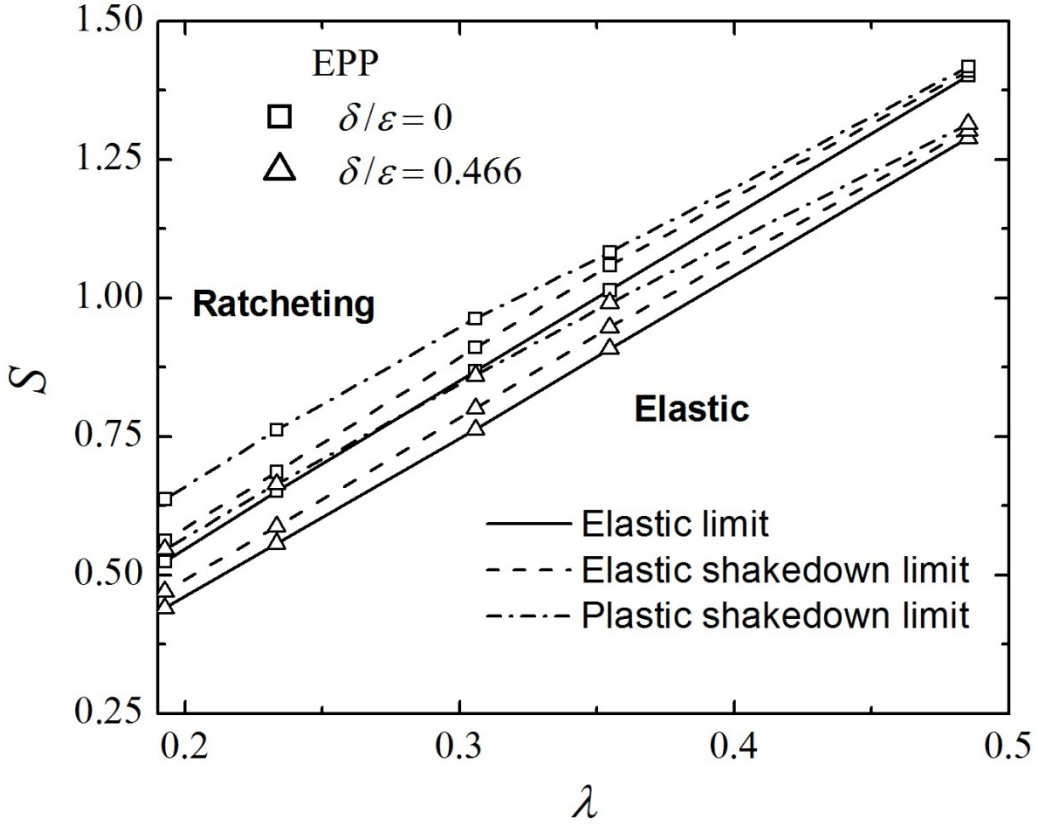

Figure 3.10 Deformation map of EPP half-spaces subjected to repeated adhesive sliding showing the effects of plasticity parameter S and Maugis parameter λ on steady-state mode of deformation for $\delta/\varepsilon = 0$ and 0.466.

ELKP

$\lambda = 0.306$, $S = 1.38$, $E_p/E = 0.1$, $\delta/\varepsilon = 0$

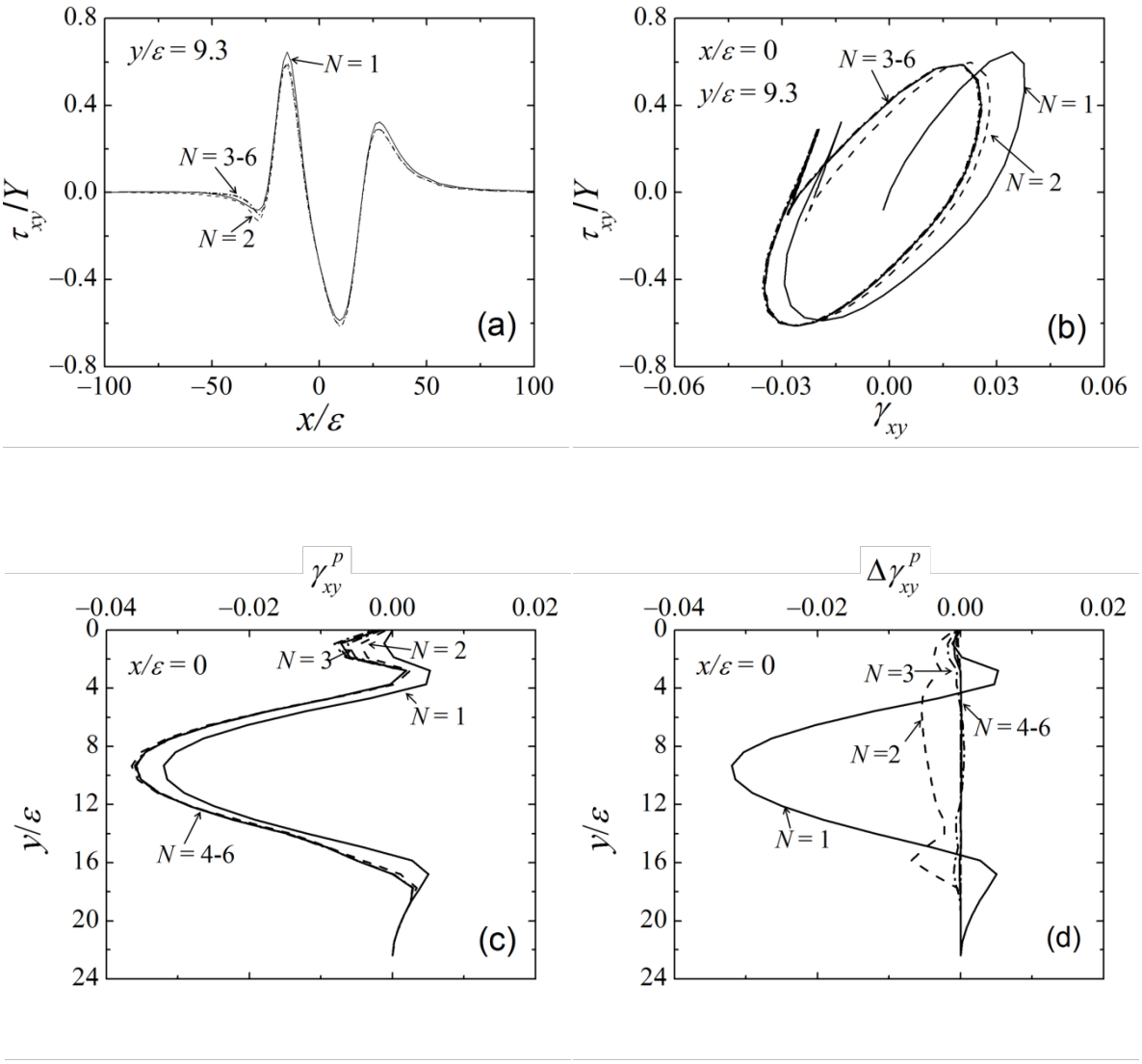

Figure 3.11 (a) Shear stress τ_{xy}/Y versus sliding distance x/ε and (b) shear stress τ_{xy}/Y versus shear strain γ_{xy} at $x/\varepsilon = 0$, both at the depth of maximum plastic strain $y/\varepsilon = 9.3$, (c) depth distributions of residual plastic shear strain γ_{xy}^{p} at $x/\varepsilon = 0$, and (d) depth distributions of residual plastic shear strain increment $\Delta\gamma_{xy}^{p}$ at $x/\varepsilon = 0$ for $N = 1$–6, $\lambda = 0.306$, $S = 1.38$, $E_p/E = 0.1$, $\delta/\varepsilon = 0$, and ELKP material behavior.

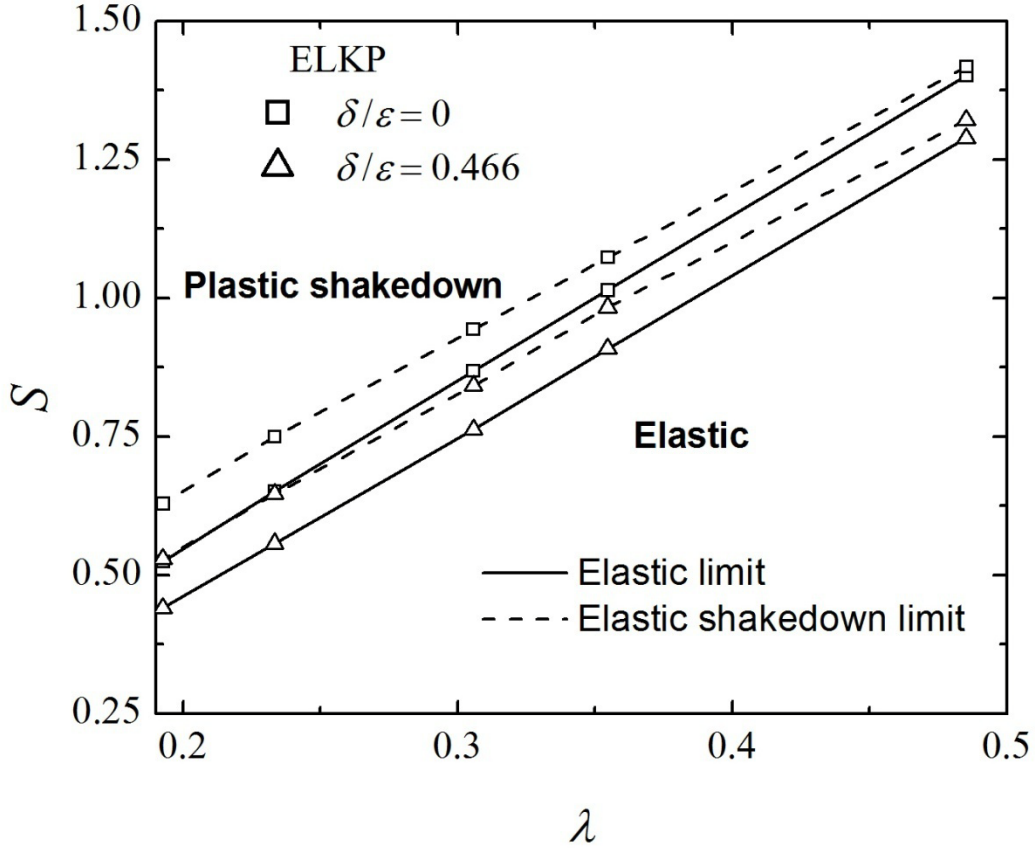

Figure 3.12 Deformation map of ELKP half-spaces with E_p/E = 0.1 subjected to repeated adhesive sliding showing the effects of plasticity parameter S and Maugis parameter λ on steady-state mode of deformation for δ/ε = 0 and 0.466.

Chapter 4
Finite element analysis of subsurface crack growth of layered media due to adhesive sliding contacts

4.1 Introduction

Coatings or thin films were commonly used in nano- (Deng, et al., 2004), micro- (Komvopoulos, 1996) and macro- scales mechanical, electronic, magnetic and optical devices due to their perfect modifications and improvements in various properties. The hard coatings (Paldley and Deevi, 2003) were always applied on the contact-mode components to improve the wear resistance properties and elongate the longevity of the devices. For instance, the carbides, nitrides and oxides hard coatings were deposited on the cutting tools to improve the wear-resistance properties through the chemical or physical deposition methods (Georges and Rabinowicz, 1996; Hintermann, 1984; Cho and Komvopoulos, 1997a). Nano-scale Al_2O_3 thin films were deposited on the micro-electro-mechanical devices by using atomic-layer deposition method to reduce the friction and wear in the sliding contacts (Mayer et al., 2003; Hoivik et al., 2003). The diamond-like carbon films were deposited on the sliders and disk media to improve the wear durability of the head-disk-interface in the hard disk drives (Bogy et al., 1994; Prabhakaran and Talke, 2000; Komvopoulos, 2000).

The improvement on wear resistance of layer media was realized by reducing friction and wear with the hard coating withstanding higher stresses without plastic deformation and minimizing the plowing and plastic deformation, and was of great dependence on the coating thickness (Komvopoulos et al., 1987). Besides, the studies of previous finite element analysis illustrated that the surface deformation and profiles, the initial yielding point and the shear stresses and strains for the two-layer elastic-plastic media were strongly affected by the surface friction (Tian and Saka, 1991), and the stresses and the plastic zone size and position were of great dependence on the existence and stiffness of the hard layer of the elastic-plastic layered media (Kral and Komvopoulos, 1997).

Among various wear mechanisms (Archard, 1953; Suh, 1973; Dwyer-Joyce et al., 1994) proposed in previous studies, such as abrasion, delamination, corrosion, and erosion, the delamination wear was a common failure mechanism or material removal process existing on the sliding contacts. Wear particle formation due to the normal and tangential traction forces in the sliding contacts often started from the plastic deformation and nucleation of voids, which subsequently coalesced to form subsurface cracks or surface cracks (Suh, 1977; Jahanmir and Suh, 1977). The wear particles were generated as the cracks crashed after the cracks had grown to a certain critical length under the driving force provided by the stresses resulting from asperity contact. The previous studies have shown that the crack growth occurred due to either the tensile or shear mechanism (Otsuka et al., 1975). Shear mode crack growth initiated in the plane with the maximum shear stress, whereas the tensile mode crack growth commenced at the plane perpendicular to the direction with the maximum tensile stress. Usually, the tensile and shear stresses at the crack tips due to asperity contact were characterized by the mode I and mode II

stress intensity factor (SIF), K_I and K_{II}, respectively. Among various methods for estimating the crack propagation direction under mixed mode I and mode II loadings, the most common criteria were the maximum tensile stress (Erdogan and Sih, 1963) and strain energy density (Sih, 1974; Sih and Erdogan, 1963), which predicted fairly accurate crack propagation direction under mixed mode static loading.

For the fatigue crack growth under cyclic loading, the directions and rates of the shear or tensile dominated mode crack propagation were determined by the corresponding maximum SIF ranges according to Paris' law (Paris and Erdogan, 1963). According to the experiments done by Mageed and Pandey (Mageed and Pandey, 1992), the crack growth path due to cyclic stresses was not accurately predicted by the maximum tensile stress and strain energy density criteria but it was in a better agreement with the results predicted by the maximum tensile stress criteria based on SIF ranges ΔK_I and ΔK_{II} with the consideration of the closure effect. Ko et al. (2001) analyzed the crack growth and wear particle formation in sliding contacts numerically based on SIFs criteria and discovered that the predicted particle size and wear volume were in reasonable agreement with their experimental results. Komvopoulos et al. (Komvopoulos and Cho, 1997; Gong and Komvopoulos, 2005; Cho and Komvopoulos, 1997b) have performed the numerical studies of subsurface cracking in homogeneous half-space and multi-layered media due to the contact with a moving asperity and the thermo-mechanical surface traction, and estimated the directions and rates of crack propagation based on the tensile and shear stress intensity factor ranges, ΔK_σ and ΔK_τ.

For nano- and micro- scales devices, the adhesion plays an important role in wear particle formation and crack growth, which was seldom involved in previous studies. The objective of this chapter was to analyze subsurface crack growth of the layered media in the adhesive sliding contacts due to fatigue and fracture. The subsurface cracking due to the adhesive sliding contacts between a rigid cylinder and an elastic- plastic layered media were elucidated by using finite element method based on Lennard-Jones potential law and analyzing stress intensity factors and stress intensity factor ranges in terms of interaction depth, film thickness, crack position, crack length, and material properties.

4.2 Analysis

4.2.1 State of the problem

To study the wear-resistance of the hard coatings for nano- and micro- scales devices, the problem is simplified to the analysis of crack growth in the adhesive sliding contact of a rigid cylinder over an elastic- plastic layered half-space, as shown by Fig. 4.1. The layered medium is composed of two layers, the hard coating and substrate. The substrate is homogeneous elastic-perfectly plastic and the top layer is treated as purely elastic material because of the significantly higher hardness of hard coating compared with the substrate. An initial horizontal crack is positioned in the top elastic layer to simulate the particle formation of delamination wear since the wear usually starts from the hard coating.

As shown by Fig. 4.1, the interaction depth δ represents the distance between the bottom point of the asperity surface and the undeformed surface of the layered medium. δ is positive for

the asperity below the undeformed surface and δ is negative for the asperity above the undeformed surface. The sliding displacement is defined upon the *x*-*y* coordinate system as shown by Fig. 4.1. The sliding displacement *x* is equal to 0 as the asperity reaches the center of the initial crack in horizontal direction. The displacement controlled sliding simulations of the adhesive sliding contacts are performed by positioning the asperity over the layered medium ($x = -a$) at a distance resulting in negligible adhesion force, displacing the asperity in the *y*-direction by a given interaction depth δ and, finally, displacing the asperity passing through the initial crack in the *x*-direction by a total distance $2a$ to the final position (x = *a*). The length of initial horizontal crack in the hard layer is defined as $2c$ and the position of the initial crack *d* is defined as the vertical distance from the crack to surface.

Due to the important effect of adhesion for the micro- and nano-scale contact components, the adhesive properties of two surfaces, such as the work of adhesion between two surfaces $\Delta\gamma$ and intermolecular distance ε, are of great importance to be analyzed in this model. Except for the adhesive properties of two surfaces, the effects of the thickness of hard layer *h*, the crack position *d* and length $2c$, and the material properties of the hard layer (elastic modulus E_l, Poisson's ratio ν_l) and the substrate (elastic modulus E_s, yield strength Y_s, Poisson's ratio ν_s), are discussed in the model. To obtain generalized solutions, the normalized parameters are used in present study, such as Maugis parameter λ and plasticity parameter *S*, which are expressed by Eq. (4.1) and Eq. (4.2), respectively. E_l^* is the equivalent Young's modulus given by $1/E_l^* = (1-\nu_l^2)/E_l + (1-\nu_c^2)/E_c$, where E_c and ν_c are the Young's modulus and the Poisson ratio of the asperity.

$$\lambda = \frac{9\sqrt{3}}{16}\left(\frac{R\Delta\gamma^2}{E_l^{*2}\varepsilon^3}\right)^{1/3} \tag{4.1}$$

$$S = \frac{\Delta\gamma}{\varepsilon Y_s} \tag{4.2}$$

4.2.2 Finite element model

In this chapter, finite element method was used to simulate the adhesive sliding contacts between the rigid cylindrical asperity and the layered elastic-plastic half-space. The radius of asperity is equal to *R*, whereas the width and height of the half space are $38.9R$ and $18.4R$, respectively as shown by Fig. 4.2(a). The mesh consists of about 35588 isoparametric, eight-node, quadrilateral, plane-strain elements having a total of 105296 nodes. The nodes at the bottom boundary of the mesh were constrained in the *x*-direction and *y*-direction. In all simulations, the total sliding distance and maximum sliding increment are equal to $2R$ ($a = R$) and $0.02R$, respectively.

Surface adhesion between the moving asperity and layered half-space is modeled by nonlinear springs, which are attached to the asperity center and surface nodes of the layered half-space, as shown by Fig. 4.3. The forces applied on springs obey a constitutive relation derived from the L-J potential. The adhesive force per unit area $p(D)$ between the moving asperity and a small segment of layered half-space surface, which is at the distance *r* away from center of asperity, as shown by Fig. 4.3, is expressed by the following equation (Chapter 2):

$$p(D) = \frac{2\Delta\gamma}{3\varepsilon}\frac{\left(\frac{\varepsilon}{D}\right)^3}{\left(1+\frac{D}{R}\right)^{1/2}}\left[4 - \frac{D}{R} - (4 - \frac{D}{4R})\left(\frac{\varepsilon}{D}\right)^6\right], \quad (4.3)$$

where $D = d(r) - R$, $d(r)$ is the distance between the center of asperity and the small segment and R is the radius of the asperity. Since the force direction is at the direction of $d(r)$, the force obtained by Eq. (4.3) included both the vertical and horizontal components. A total of 1001 nonlinear springs are attached to surface nodes of the finite element mesh from $x = -2R$ to $x = 2R$. The total force between the rigid asperity and layered half-space is determined as the sum of the forces transferred in all springs. The springs remain attached to the moving asperity and surface nodes of the mesh during the entire sliding process of a simulation.

The mesh around the crack is refined in order to obtain more accurate results for the stress distribution around the crack, as shown by Fig. 4.2(b). The mesh at each crack tip (left and right) consists of 32 isoparametric, eight-node, collapsed quadrilateral, plane-strain elements with their mid-side nodes displaced to the quarter-point distance to simulate the square root singularity of the crack-tip stress field and their crack-tip nodes constrained to move together in order to prevent crack-tip blunting. The simulations are performed with the FEM code ABAQUS (version 6.9-EF2).

4.2.3 Stress intensity factors

In linear elastic fracture mechanics, the mode I and mode II stress intensity factors (SIFs), K_I and K_{II}, respectively, are defined as

$$\mathrm{K_I} = \lim_{\mathrm{r}\to 0}\sqrt{2\pi \mathrm{r}}\,\tau_{\mathrm{xy}}(\mathrm{r}, \theta = 0), \quad (4.4a)$$

and

$$\mathrm{K_{II}} = \lim_{\mathrm{r}\to 0}\sqrt{2\pi \mathrm{r}}\,\tau_{\mathrm{xy}}(\mathrm{r}, \theta = 0), \quad (4.4b)$$

where (r, θ) and (x, y) are polar and local Cartesian coordinates centered at the crack tip, respectively, as shown by Fig. 4.1. θ is positive at left and crack tips as the plane of θ goes toward the surface. K_I and K_{II} are obtained from the stresses at nine nodes adjacent to the crack tip and along the crack plane ($\theta = 0$) using linear extrapolation of a least-square line fit through the SIF data (Chan et al., 1970). To obtain generalized solutions, the SIF data are normalized by $E_l c^{1/2}$.

Since the stresses around the crack tip are subjected to K_I and K_{II}, which depend on the sliding displacement of asperity, therefore, at a given plane with angle θ (shown by Fig. 4.1) and a given sliding displacement x (from $-a$ to a), the tensile and shear SIFs, represented by K_σ and K_τ, respectively, are given by

$$\mathrm{K_\sigma}(\theta, \mathrm{x}) = \sigma_{\theta\theta}\sqrt{2\pi \mathrm{r}} = \cos\frac{\theta}{2}\left[\mathrm{K_I}\cos^2\frac{\theta}{2} - \frac{3}{2}\mathrm{K_{II}}\sin\theta\right], \quad (4.5a)$$

and

$$K_\tau(\theta, x) = \tau_{r\theta}\sqrt{2\pi r} = \frac{1}{2}\cos\frac{\theta}{2}[K_I \sin\theta + K_{II}(3\cos\theta - 1)]. \quad (4.5b)$$

For the fracture process, shear mode crack propagation starts in the plane with the maximum shear stress, whereas the tensile mode crack propagation commences at the plane with the maximum tensile stress. The maximum tensile and shear stresses at the crack tips for an instance or a given sliding position are characterized by the maximum shear mode and tensile mode stress intensity factors (SIFs), K_σ^{max} and K_τ^{max}, which are expressed by

$$K_\sigma^{max}(x) = max[K_\sigma(\theta, x)] \ (-180^\circ \le \theta \le 180^\circ), \quad (4.6a)$$

and

$$K_\tau^{max}(x) = max[|K_\tau(\theta, x)|] \ (-180^\circ \le \theta \le 180^\circ). \quad (4.6b)$$

The sign of K_τ is only related to crack slipping direction and does not change the crack propagation direction, therefore, K_τ^{max} is the maximum value of absolute K_τ. Once the value of K_σ^{max} or K_τ^{max} exceeded the critical value, the crack propagates at the corresponding direction.

However, for the fatigue crack growth, the driving force for the crack propagation is the SIF ranges. For a given plane with $\theta = \theta^*$, the tensile and shear SIF ranges for a cycle, ΔK_σ and ΔK_τ, respectively, are expressed as

$$\Delta K_\sigma(\theta = \theta^*) = K_{\sigma,max}(\theta = \theta^*, x) - max[K_{\sigma,min}(\theta = \theta^*, x), 0], \quad (4.7a)$$

and

$$\Delta K_\tau(\theta = \theta^*) = K_{\tau,max}(\theta = \theta^*, x) - K_{\tau,min}(\theta = \theta^*, x). \quad (4.7b)$$

The closure effect is considered to calculate the tensile SIF range ΔK_σ, therefore, the part for K_σ less than zero is not counted for ΔK_σ.

The crack growth direction for tensile or shear dominant mode of fatigue crack growth is determined under the assumption that tensile mode crack propagation occurs in the plane with maximum tensile SIF range, ΔK_σ^{max}, whereas shear mode crack propagation commences at the plane with maximum shear SIF range, ΔK_τ^{max} (Komvopoulos and Cho, 1997; Gong and Komvopoulos, 2005; Cho and Komvopoulos, 1997b). The magnitudes of ΔK_σ^{max} and ΔK_τ^{max} are calculated by

$$\Delta K_\sigma^{max} = max[\Delta K_\sigma(\theta)] \ (-180^\circ \le \theta \le 180^\circ), \quad (4.8a)$$

and

$$\Delta K_\tau^{max} = max[\Delta K_\tau(\theta)] \ (-180^\circ \le \theta \le 180^\circ). \quad (4.8b)$$

The dominant mode of crack growth is determined by the magnitudes of ΔK_σ^{max} and ΔK_τ^{max}. The crack growth is dominated by tensile mode as $\Delta K_\sigma^{max} > \Delta K_\tau^{max}$, whereas the crack growth is

dominated by shear mode for $\Delta K_{\tau}^{max} > \Delta K_{\sigma}^{max}$. The crack propagation angle θ is corresponded to the crack propagation plane with the maximum SIF range ΔK_{σ}^{max} or ΔK_{τ}^{max}.

4.3 Results and discussion

Figure 4.4 shows the variations of dimensionless K_I and K_{II} at the left and right crack tips as functions of the sliding displacement or asperity position x as $\lambda = 0.49$, $S = 46.8$, $\delta/\varepsilon = 0$, $E_l/E_s = 5$, $h/c = 4$ and $d/c = 2$. As the asperity moving against the half-space, the center interface is under compression (repulsive force), while regions near the interface edges are under tension (attractive force). Therefore, K_I reaches two maximum values as the moving asperity arrives at the positions aside the left or right crack tips due to high tension on crack tips at these instances, and the value of K_I at left or right crack tip achieves the minimum value due to the high compression on crack tips as the moving asperity is on top of the left or right crack tip, respectively. K_{II} exhibits a cyclic variation with the increase of x, with the maximum and minimum values occurring before and after the asperity reaching the left or right crack tip, respectively. The curves reflecting the fluctuations of K_I or K_{II} at left crack tip are parallel to those at right crack tip. The results of current study is different with those obtained by the study of by Komvopoulos and Cho (1997) on analyzing subsurface cracking under the sliding contact without adhesion, which showed that the magnitude of K_I was almost equal to zero before the asperity moving away from the right crack tip and the maximum value of K_I was quite small compared with that of K_{II}, which played a much more important role on crack growth of non-adhesive sliding contact. The discrepancy is because of the introduction of the adhesion in the interface of moving asperity and half space in present study and the adhesion produces high attraction and significant tensile stress fields during the sliding contact and achieves high values of K_I. This difference also illustrates the importance of adhesion on crack growth.

Even though the stress fields around crack tips are determined by the external forces, the external forces are also affected by the crack tips. Figure 4.5 shows the variations of normal force F_N and lateral force F_L under the effect of asperity position x. To obtain generalized solutions, the forces are normalized by YR. The values of F_N and F_L are constant as the moving asperity is far away from the crack. However, the fluctuations of F_N and F_L due to the asperity moving closer to the crack especially the crack tips, reveal the significant effects of the stress fields around the crack tips on F_N and F_L.

4.3.1 Fracture crack propagation

Crack propagation of fracture occurs in shear mode or tensile mode once the shear mode or tensile mode stress intensity factor reaches the critical value, respectively. Shear mode crack propagation commences at the plane with K_{τ}^{max} reaching the critical shear mode SIF K_{IIC}, whereas the tensile mode crack growth occurs at the plane with K_{σ}^{max} achieving the critical tensile mode SIF K_{IC}. The dominant crack growth mode is shear mode if K_{τ}^{max} reached the critical value earlier than K_{σ}^{max}, and vice versa.

Figures 4.6 reveal the effect of interaction depth δ on K^{max} and the corresponding angles θ for K^{max} at left crack tip as functions of sliding displacement x as $\lambda = 0.49$, $S = 46.8$, $E_l/E_s = 5$, $h/c = 4$, $d/c = 2$, and $\delta/\varepsilon = -0.466$, 0 and 0.466. The solid line represents the maximum tensile

mode SIF K_σ^{max}, whereas the dashed line represents the maximum shear mode SIF K_τ^{max}. Since the compressive force component is applied on the central zone of interface and the attractive force component is applied on edges of interface as the asperity interacting with layered medium, the stress around the left crack tip transits in a sequence of tensile, compressive and tensile modes as the asperity moving across the left crack tip from left to right, similar as in right crack tip. Therefore, both K_σ^{max} and K_τ^{max} exhibit the cyclic variations with increasing value of x and have two maximum peaks as the rigid asperity is on two sides of left or right crack tip. Since the tensile mode SIF K_σ is increased by enhancing tensile stress fields around crack tip and the shear mode SIF K_τ is enlarged by enhancing shear stress fields around crack tip, the asperity positions with K_σ^{max} reaching maximum values at left crack tip are further away from left crack tip compared with those for K_τ^{max}. Once the rigid asperity is on top of the crack tip, the values of K_σ^{max} and K_τ^{max} are almost equal to zero due to the closure of crack tip and no relative slipping of crack. The values of θ corresponding to K_σ^{max} are different with those of K_τ^{max}, for examples, the values of θ with maximum K_σ^{max} are around 70^o or -70^o, whereas, the values of θ with maximum K_τ^{max} are around 0^o. For the given conditions shown by Figs. 4.6, the magnitudes of K_σ^{max} are larger than those of K_τ^{max}. The magnitudes of K_σ^{max} and K_τ^{max} are enhanced together with the higher propensity of crack propagation by increasing interaction depth due to stronger stress fields around the crack tip. Besides, it also causes the asperity position with maximum K_σ^{max} or K_τ^{max} further away from the crack tip due to the enhancement of compressive effect.

Figures 4.7 have shown the differences of K_σ^{max} and corresponding angle θ at the left and right crack tips as a function of sliding displacement x as λ = 0.49, S = 46.8, E_l/E_s = 5, h/c = 4, d/c = 2, and δ/ε = -0.466, 0 and 0.466. The solid line represents left crack tip, whereas the dashed line represents right crack tip. Due to the variation of stress fields around crack tips, the variation of K_σ^{max} at right crack tip exists with the increase of x, similar as that at left crack tip. However, A right shift is observed for the curves of K_σ^{max} at right crack tip compared with those at left crack tip due to the different effective regions for left and right crack tips. Except for a shift in x-direction, the curves of θ corresponding to K_σ^{max} at right crack tip are mirror symmetric to those at left crack tip due to the different definitions of θ. Since the propensity of crack propagation is highest as K_σ^{max} or K_τ^{max} reaching the maximum value in one sliding cycle ($x = -a \sim a$), it is of great importance and usefulness to analyze the magnitudes and corresponding angle θ of $max(K_\sigma^{max})$ and $max(K_\tau^{max})$ of one sliding cycle.

Figures 4.8 reveal the effect of Maugis parameter λ on the magnitudes of $max(K_\sigma^{max})$ and $max(K_\tau^{max})$, and the corresponding angle θ as S = 46.8, E_l/E_s = 5, h/c = 4, d/c = 2, and δ/ε = 0. According to Eq. (4.1), a higher value of Maugis parameter λ can be interpreted as higher work of adhesion $\Delta\gamma$ and/or lower elastic modulus E. As shown by Fig. 4.8(a), the normalized values of $max(K_\sigma^{max})$ and $max(K_\tau^{max})$ increase with λ due to the enhancement of stress fields under the increase of the work of adhesion between the rigid asperity and layered medium or the reduction of hard layer stiffness. The increment of $max(K_\sigma^{max})$ is more significant than that of $max(K_\tau^{max})$ with increasing λ. This phenomenon represents that the propensity of tensile mode dominated crack propagation can be enhanced by the increase of λ with higher work of adhesion $\Delta\gamma$ and/or lower elastic modulus E of hard coating. Besides, the tensile mode crack propagation is dominant

in the given conditions of Figs. 4.8 since the magnitudes of $max(K_\sigma^{max})$ is larger than that of $max(K_\tau^{max})$.

As shown by Fig. 4.8(b), at low value of λ, the angle θ for $max(K_\sigma^{max})$ at left crack tip is 70^o whereas the angle θ for $max(K_\sigma^{max})$ at right crack tip is -70^o, indicating that the crack propagates toward the surface at the left crack tip and downward into the subsurface at the right crack tip for tensile mode dominated crack propagation, in agreement with the experimental evidence of sheet like fragment formation of delamination wear (Suh, 1977). However, with the enhancement of attraction effect by increasing λ, the angle θ corresponding to $\max(K_\sigma^{max})$ transits from 70^o to -70^o at left crack tip and from -70^o to 70^o at right crack tip. Therefore, with increasing λ, the crack propagation for tensile mode dominated fracture process transits in the sequence of three out-of-plane modes shown by Figs. 4.9(a)-(c), representing left upward and right downward, left and right upward, and left downward and right upward, respectively. The angle θ corresponding to $\max(K_\tau^{max})$ is equal to zero at both the left and right crack tips. This represents that the crack propagates in the horizontal direction if the shear mode crack propagation is dominated for fracture process, as shown by Fig. 4.9(d).

Figures 4.10 reveal the effect of Maugis parameter λ on the magnitudes of $max(K_\sigma^{max})$ and $max(K_\tau^{max})$, and the corresponding angle θ at same conditions as Figs. 4.8 except for $d/c = 1$. The increment of the magnitude of $\max(K_\sigma^{max})$ due to the increase of λ for $d/c = 1$ is much more significant than that for $d/c = 2$ shown by Fig. 4.8(a) because the enhancement of tensile stress fields around crack tips is more significant due to closer distance of crack to surface. Besides, according to Eqs. (4.5) and (4.6), as K_I is zero, the angle θ corresponding to K_σ^{max} and K_τ^{max} are equal to $\pm 70^o$ and 0^o respectively, therefore, the enhancement of tensile stress fields by increasing λ, induces the decrease of absolute value of angle θ corresponding to $\max(K_\sigma^{max})$ and the existence of non-zero value of θ corresponding to $\max(K_\tau^{max})$ due to the enlargement of K_I, and consequently causes the tensile mode in-plane crack propagation (Fig. 4.9(d)) and the shear mode out-of-plane crack propagation as shown by Fig. 4.9(c).

Figures 4.11 show the effect of relative crack position d/c on the magnitudes of $max(K_\sigma^{max})$ and $max(K_\tau^{max})$, and the corresponding angle θ as $\lambda = 0.49$, $S = 46.8$, $E_l/E_s = 5$, $h/c = 4$ and $\delta/\varepsilon = 0$. Both the tensile and the shear stress fields around the crack tips are enhanced as the crack is closer to the surface, but the enhancement of the tensile stress field is more significant due to the effect of interfacial attraction. Besides, the magnitude of $max(K_\sigma^{max})$ is increased by the enhancement of tensile stress field whereas the magnitude of $max(K_\tau^{max})$ is increased by the enhancement of shear stress field but reduced by the enhancement of tensile stress field. Therefore, with crack closer to the surface, the magnitude of $max(K_\sigma^{max})$ increases and the magnitude of $max(K_\tau^{max})$ firstly increases due to the enhancement of shear stress field but then decreases due to the stronger enhancement of tensile stress field. The crack has the highest propensity to propagate with $d/c \approx 1.5$ if the shear mode crack growth is dominant. Besides, the propensity of tensile mode dominated crack propagation is enhanced as the crack closer to surface and the tensile mode fracture process is more dominant at conditions given by Figs. 4.11 since $\max(K_\sigma^{max}) > \max(K_\tau^{max})$.

Figures 4.12 summarize the effect of relative interaction depth δ/ε on the magnitudes of $max(K_\sigma^{max})$ and $max(K_\tau^{max})$, and the corresponding angle θ as $\lambda = 0.49$, $S = 46.8$, $E_l/E_s = 5$, $h/c = 4$ and $d/c = 1$. The increase of δ/ε enhances the plowing effect during the sliding contact and the shear stress fields around the crack tips, and induces the increases of the magnitudes of $max(K_\sigma^{max})$ and $max(K_\tau^{max})$ at crack tips, but the increment of $max(K_\tau^{max})$ is more significant due to stronger enhancement of shear stress fields. The angle θ corresponding to $\max(K_\sigma^{max})$ slightly increases with the increase of δ/ε due to the enhancement of shear stress fields whereas the effect of δ/ε on the angle θ corresponding to $\max(K_\tau^{max})$ is secondary. The tensile mode fracture process is more dominant at conditions shown by Figs. 4.12 since $\max(K_\sigma^{max}) > \max(K_\tau^{max})$.

Figures 4.13 illustrate the effect of relative hard coating thickness h/c on the magnitudes of $max(K_\sigma^{max})$ and $max(K_\tau^{max})$, and the corresponding angle θ as $\lambda = 0.49$, $S = 46.8$, $E_l/E_s = 5$, $d/c = 1$ and $\delta/\varepsilon = 0$. The substrate effect becomes less significant with thicker hard coating, subsequently the friction force is reduced since less plastic deformation energy dissipates during the sliding contact and the shear and tensile stress fields around the crack tips are weakened due to less friction force, but the reduction of the tensile stress field is less significant. Therefore, the magnitudes of $max(K_\sigma^{max})$ and $max(K_\tau^{max})$ decrease with the increase of h/c and achieve low limits as $h/c > 8$ when the substrate effect is negligible. Besides, the reduction of shear stress field with increasing h/c induces a higher decrease of $max(K_\tau^{max})$ than that of $max(K_\sigma^{max})$ and the reduction of angle θ corresponding to $\max(K_\sigma^{max})$ from 60^o to 20^o at both crack tips. The propensity of fracture crack propagation is weakened by increasing the thickness of hard coating especially for shear mode crack propagation.

Above all, the fact of $\max(K_\sigma^{max}) > max(K_\tau^{max})$ indicates that the tensile mode crack propagation is more dominant mode in the fracture process if the critical values for tensile and shear mode crack propagations are the same. The propensity of crack propagation due to fracture is reduced for higher thickness or stiffness of hard coating, lower interfacial adhesion or interaction depth, and further distance of crack to surface.

4.3.2 Fatigue crack growth

The driving forces for fatigue crack growth are the tensile mode and shear mode SIF ranges, ΔK_σ^{max} and ΔK_τ^{max}. The tensile mode crack propagation occurs in the plane with maximum tensile SIF range, ΔK_σ^{max}, whereas shear mode crack propagation commences at the plane with maximum shear SIF range, ΔK_τ^{max}. The tensile mode crack propagation is more dominant as $\Delta K_\sigma^{max} > \Delta K_\tau^{max}$, and the shear mode crack propagation is more dominant as $\Delta K_\sigma^{max} < \Delta K_\tau^{max}$.

Figures 4.14 have shown the effect of Maugis parameter λ on the magnitudes and corresponding angle θ for the maximum SIF ranges ΔK_σ^{max} and ΔK_τ^{max} at left and right crack tips as $S = 46.8$, $E_l/E_s = 5$, $h/c = 4$, $d/c = 1$, and $\delta/\varepsilon = 0$. As mentioned in previous, higher λ represents higher interfacial adhesion or softer hard coating. The values of dimensionless ΔK_σ^{max} and ΔK_τ^{max} increase with λ due to the enhancement of tensile and shear stress fields around crack tips caused by stronger interfacial adhesion between asperity and hard coatings. Since the enhancement of tensile stress fields is more significant, the increment of ΔK_σ^{max} is higher than that of ΔK_τ^{max} and the propensity of tensile mode dominated crack propagation is enhanced with

the increase of λ. As shown in Fig. 4.14(a), $\Delta K_{\sigma}^{max} < \Delta K_{\tau}^{max}$ at small values of λ, whereas $\Delta K_{\sigma}^{max} > \Delta K_{\tau}^{max}$ at large values of λ. If the shear mode crack growth was dominant, the corresponding angles θ at left and right crack tips are almost the same and around 0^o and only in-plane crack growth occurs, in good agreement with the results of non-adhesive sliding contacts obtained by Komvopoulos and Cho (1997). If the tensile mode crack growth was dominant, the corresponding angles θ reduces with increasing λ due to the enhancement of attraction effect and the out-of-plane crack growth occurs with the crack propagating toward surface at both left and right crack tips as shown by Fig. 4.9(b) or even more the in-plane crack growth commences with high value of λ, which is different with the results for non-adhesive sliding contacts (Komvopoulos and Cho, 1997) showing the crack propagating toward surface at left crack tip and downward into subsurface at right crack tip as shown by Fig. 4.9(a). The discrepancies are caused by the interfacial adhesion considered in current study, which strongly influences the tensile stress fields around the crack tips and affects the tensile mode fatigue crack propagation direction especially for the case with $d/c = 1$. However, if the adhesion was not high or the crack was far away from the surface, such as at small values of λ with $d/c = 2$, the crack propagates toward the surface at left crack tip and downward into subsurface at the right crack tip for tensile mode crack propagation, similar as the results for non-adhesive sliding contacts.

Figures 4.15 illustrate the effect of relative crack position d/c on the magnitudes and corresponding angle θ for the maximum SIF ranges ΔK_{σ}^{max} and ΔK_{τ}^{max} at left and right crack tips as $\lambda = 0.49$, $S = 46.8$, $E_l/E_s = 5$, $h/c = 4$ and $\delta/\varepsilon = 0$. As the crack closer to the surface, both the tensile and shear stress fields around crack tips are intensified but the enhancement of tensile stress field is more significant. The magnitude of ΔK_{τ}^{max} firstly increases and then decreases as the crack closer to the surface since the magnitude of ΔK_{τ}^{max} is enhanced by the shear stress field but weakened by tensile stress field; the magnitude of ΔK_{σ}^{max} increases due to the enhancement of tensile stress fields and the propensity of tensile mode crack growth is enhanced. Therefore, the crack growth switches from shear mode to tensile mode with decreasing d/c. The crack growth angles θ are equal to zero and independent on the crack position if the shear mode crack growth was dominant, whereas the crack growth angles θ decreases from 70^o to 30^o with decreasing d/c due to the enhancement of stress tensile fields if the tensile mode crack growth was dominant.

Figures 4.16 illustrate the effect of relative interaction depth δ/ε on the magnitudes and corresponding angle θ for the maximum SIF ranges ΔK_{σ}^{max} and ΔK_{τ}^{max} at left and right crack tips as $\lambda = 0.49$, $S = 46.8$, $E_l/E_s = 5$, $h/c = 4$ and $d/c = 1$. The increase of δ/ε enhances the plowing effect of sliding contact and intensifies the stress fields around crack tips especially the shear stress field. This enlarges the magnitudes of ΔK_{σ}^{max} and ΔK_{τ}^{max} but the intensification of ΔK_{τ}^{max} is more significant. Therefore, the crack growth is dominated by tensile mode at small δ/ε since $\Delta K_{\sigma}^{max} > \Delta K_{\tau}^{max}$ due to higher attraction effect, whereas the shear mode crack propagation is more dominant at large values of δ/ε since $\Delta K_{\sigma}^{max} < \Delta K_{\tau}^{max}$ due to high plowing effect. The increase of δ/ε not only makes the dominant crack growth mode transit from tensile mode to shear mode but also slightly increases the value of θ corresponding to ΔK_{σ}^{max} due to stronger shear stress fields around crack tips. The crack propagates toward the surface at both the left and right crack tips for tensile mode crack growth. The effect of δ/ε on the value of θ corresponding to ΔK_{τ}^{max} is secondary and only in-plane crack propagation occurs for shear mode crack growth.

Figures 4.17 show the effect of relative hard coating thickness *h/c* on the magnitudes and corresponding angle θ for the maximum SIF ranges ΔK_{σ}^{max} and ΔK_{τ}^{max} at left and right crack tips as λ = 0.49, S = 46.8, E_l/E_s = 5, d/c = 1 and δ/ε = 0. As mentioned in previous, the shear stress fields around crack tips are reduced with thicker hard coating due to the less significant substrate effect and less friction. Furthermore, the magnitudes of ΔK_{σ}^{max} or ΔK_{τ}^{max} are reduced but the reduction of ΔK_{τ}^{max} is more significant. Therefore, the crack growth mode transits from shear mode to tensile mode with the increase of *h/c*. Besides, the magnitudes of ΔK_{σ}^{max} or ΔK_{τ}^{max} becomes stable when the substrate effect is negligible as *h/c* reaches a critical value, such as *h*/*c* = 8. The effect of hard coating thickness on shear mode crack growth direction is secondary and only the in-plane crack propagation occurs for shear mode crack growth. For tensile mode crack growth, the crack propagates toward the surface at both the left and right crack tips and the angles decreases from 60^o to 20^o due to the reduction of shear stress fields.

In general, for fatigue crack growth under adhesive sliding contacts, the magnitudes of ΔK_{σ}^{max} or ΔK_{τ}^{max} are almost same at the left and right crack tips and both the tensile mode and shear mode crack growth occurs. The propensity of tensile mode dominated crack growth is enhanced with larger thickness or smaller stiffness of hard coating, higher interfacial adhesion, smaller interaction depth, and closer distance of crack to surface. The tensile mode crack growth direction is similar as that for fracture process under the same condition. Only in-plane shear mode crack growth occurs for fatigue whereas out-of-plane shear mode crack growth also occurred for fracture process.

4.4 Conclusions

In this chapter, by using linear elastic fracture mechanics and the finite element method (FEM) based on Lennard-Jones law, subsurface cracking in layered medium due to adhesive sliding contact with a rigid asperity was analyzed. The shear mode and tensile mode crack propagation directions and propensities were obtained under the analysis of fracture and fatigue by considering the effects of relative interaction depth, hard coating thickness, crack position, and Maugis parameter. Based on the presented results and discussion, the following main conclusions can be drawn from this chapter.

1. The interfacial adhesion between rigid asperity and layered medium intensifies the stress fields around crack tips, producing the cyclic variations for both K_I and K_{II}. Besides, the normal and friction forces are affected by the stress fields around crack tips and fluctuate when the rigid asperity moves close to the crack tips.

2. The tensile and shear mode crack propagation direction for fracture are determined based on K_{σ}^{max} and K_{τ}^{max}, respectively. Both in-plane and out-of-plane crack propagations occur for the shear mechanism or tensile mechanism with the assumption that the crack initiates at instances with max(K_{σ}^{max}) or max(K_{τ}^{max}) in sliding contact. In general, the tensile mode crack propagation is more dominant for the fracture process. The propensity of fracture is enhanced due to the increase of magnitudes of K_{σ}^{max}, by increasing interaction depth, Maugis parameter, decreasing the hard coating thickness or making the crack position closer to the surface.

3. The tensile and shear mode crack propagation directions for fatigue are determined based on ΔK_{σ}^{max} and ΔK_{τ}^{max}. Only in-plane crack growth occurs due to the shear mechanism whereas both out-of-plane and in-plane crack growth commences due to tensile mechanism. The increase of Maugis parameter and hard coating thickness, the decrease of interaction depth or the closer distance of the crack to the surface make the dominant crack growth mode switching from shear mode to tensile mode and induce the transition from out-of-plane to in-plane tensile mode crack growth due to the enhancement of tensile stress fields around crack tips. With the increases of interaction depth and Maugis parameter, or the decrease of hard coating thickness, the magnitudes of ΔK_{σ}^{max} and ΔK_{τ}^{max} are enhanced, indicating higher fatigue crack growth velocity.

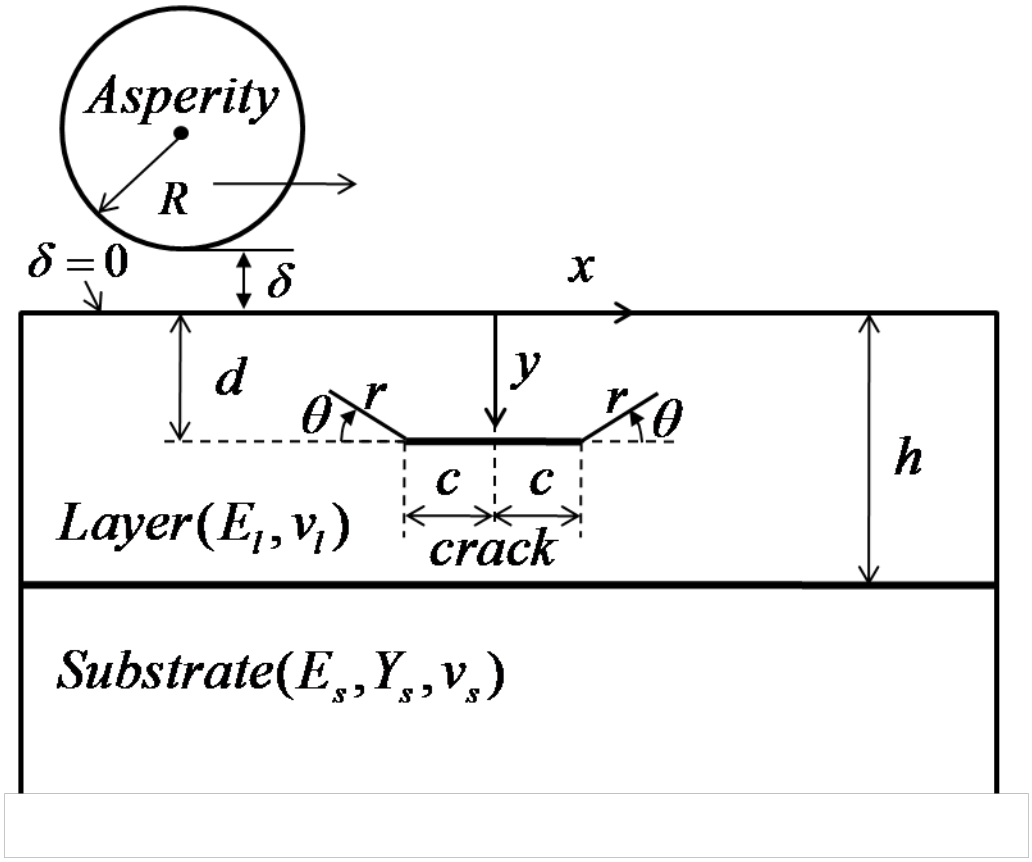

Figure 4.1 Schematic of adhesive sliding contact of asperity over layered medium including an initial horizontal subsurface crack with pertinent nomenclature.

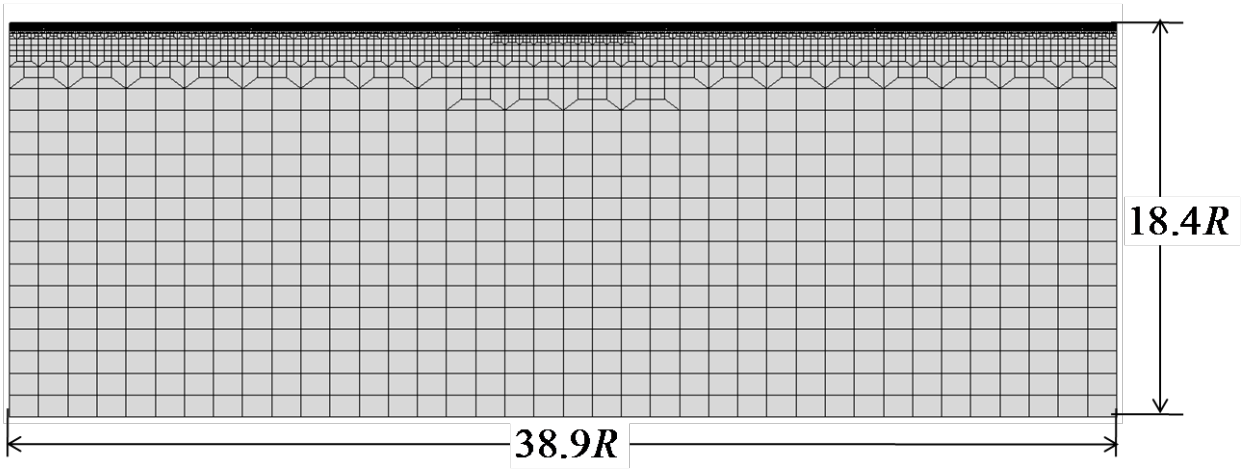

(a)

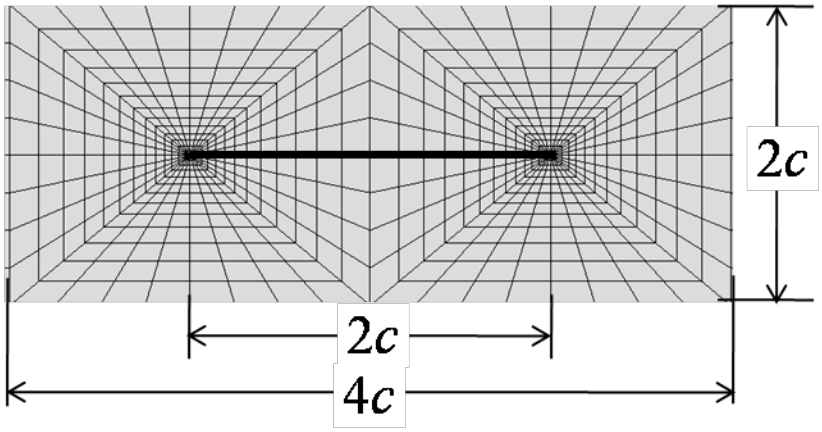

(b)

Figure 4.2 (a) Finite element mesh of the layered medium, and (b) detail of the refined mesh around the crack.

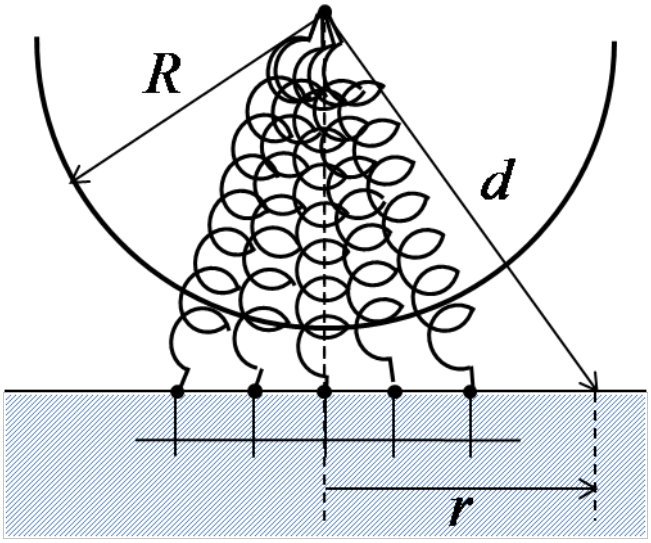

Figure 4.3 Schematic of an asperity in close proximity with a half-space. Adhesive forces are modeled by nonlinear springs connecting surface nodal points of the half-space with the center of the asperity.

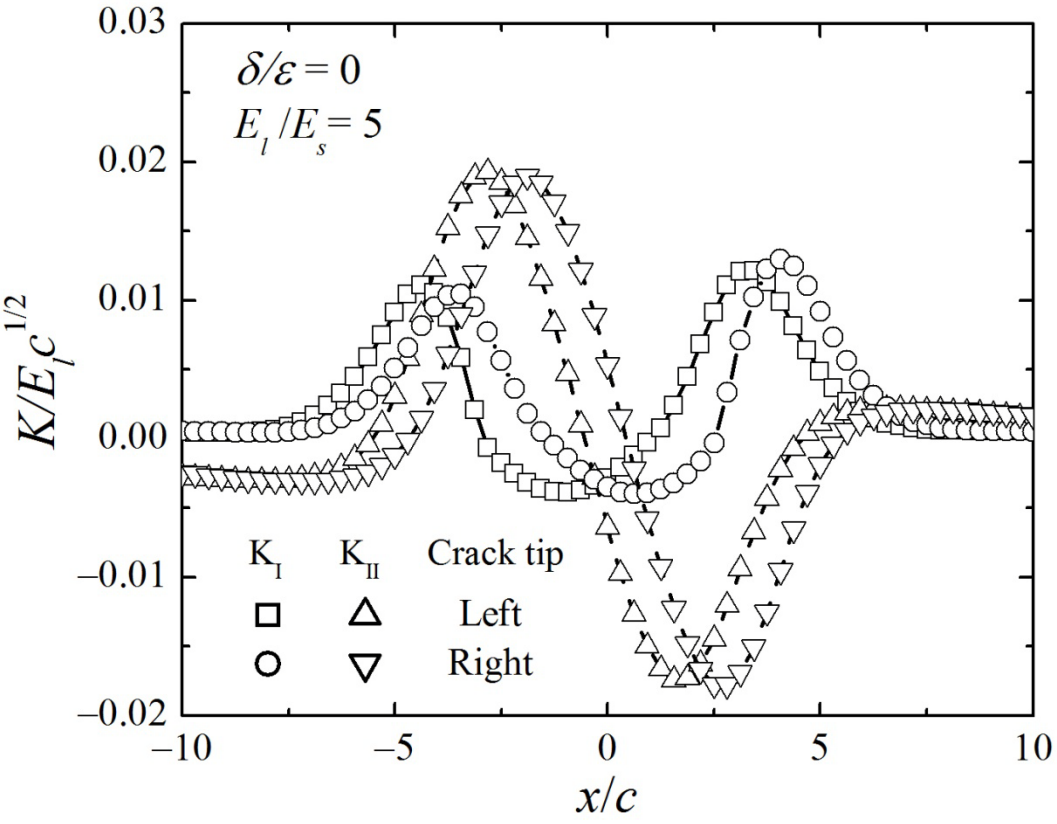

Figure 4.4 Variations of dimensionless K_I and K_{II} with sliding distance x/c at left and right crack tips for $\lambda = 0.49$, $S = 46.8$, $\delta/\varepsilon = 0$, $E_l/E_s = 5$, $h/c = 4$ and $d/c = 2$.

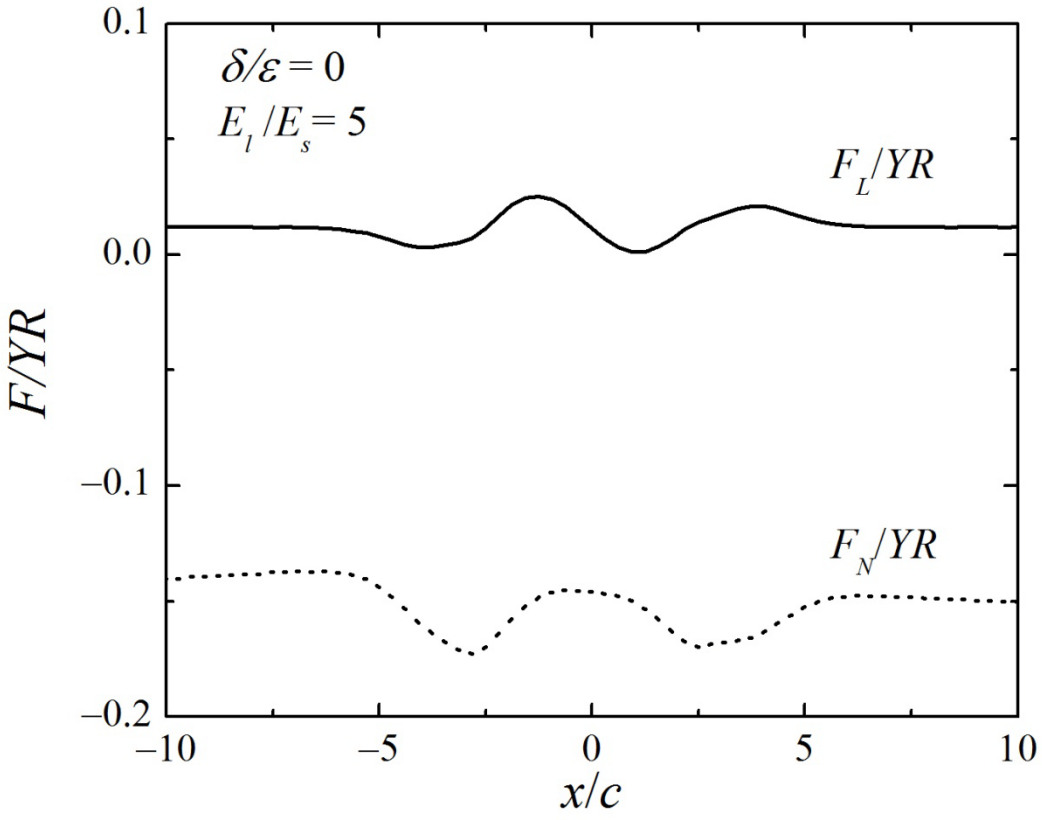

Figure 4.5 Variations of friction force F_L/EY and normal force F_N/EY with sliding distance x/c for $\lambda = 0.485$, $S = 46.8$, $\delta/\varepsilon = 0$, $E_l/E_s = 5$, $h/c = 4$ and $d/c = 2$.

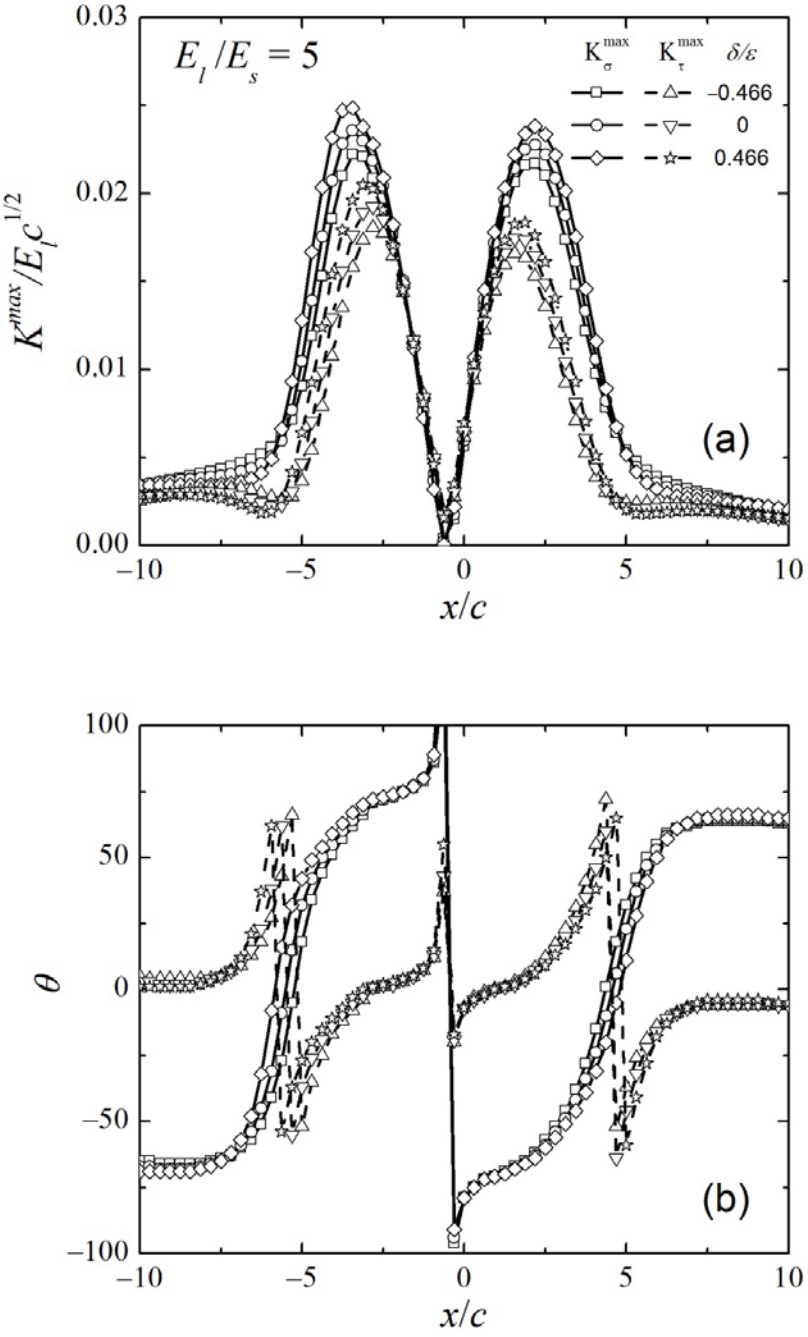

Figure 4.6 Variations of (a) dimensionless K_σ^{max} and K_τ^{max} and (b) the corresponding angle θ with sliding distance x/c at left crack tip for λ = 0.49, S = 46.8, E_l/E_s = 5, h/c = 4, d/c = 2 and δ/ε = -0.466, 0 and 0.466.

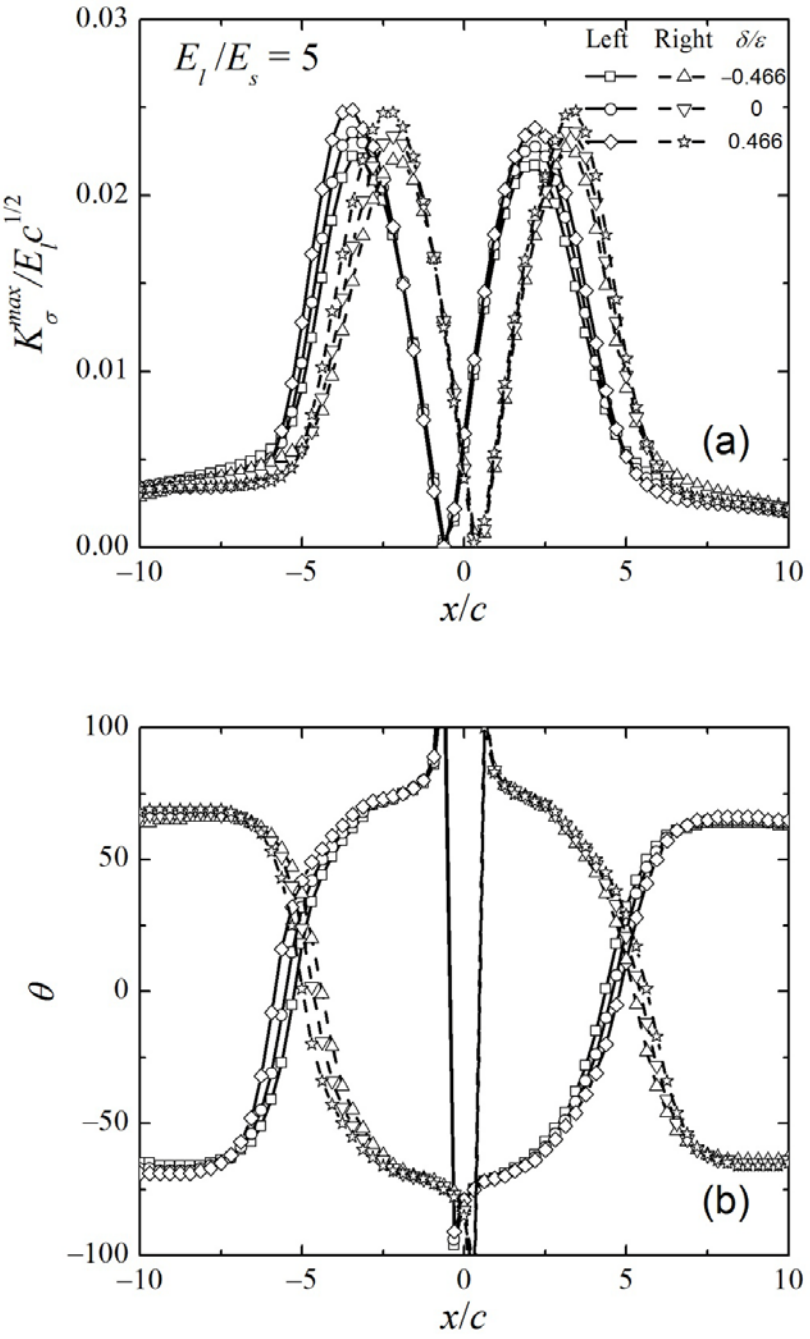

Figure 4.7 Variations of (a) dimensionless K_σ^{max} and (b) the corresponding angle θ with sliding distance x/c at left and right crack tips for λ = 0.49, S = 46.8, E_l/E_s = 5, h/c = 4, d/c = 2 and δ/ε = -0.466, 0 and 0.466.

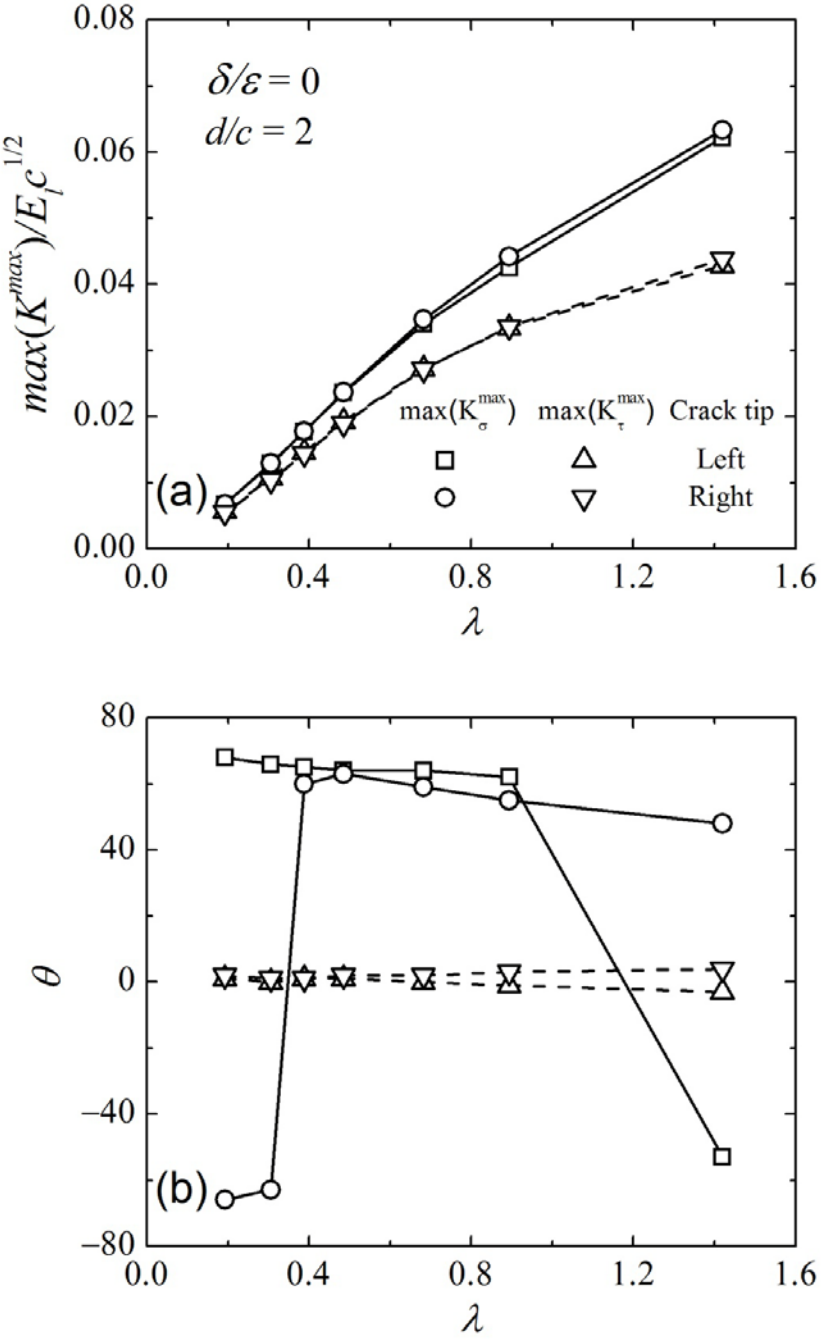

Figure 4.8 Effects of Maugis parameter λ on (a) dimensionless max(K_σ^{max}) and max(K_τ^{max}), and (b) the corresponding sliding distance x/c and (c) angle θ at left and right crack tips for S = 46.8, δ/ε = 0, h/c = 4, d/c = 2.

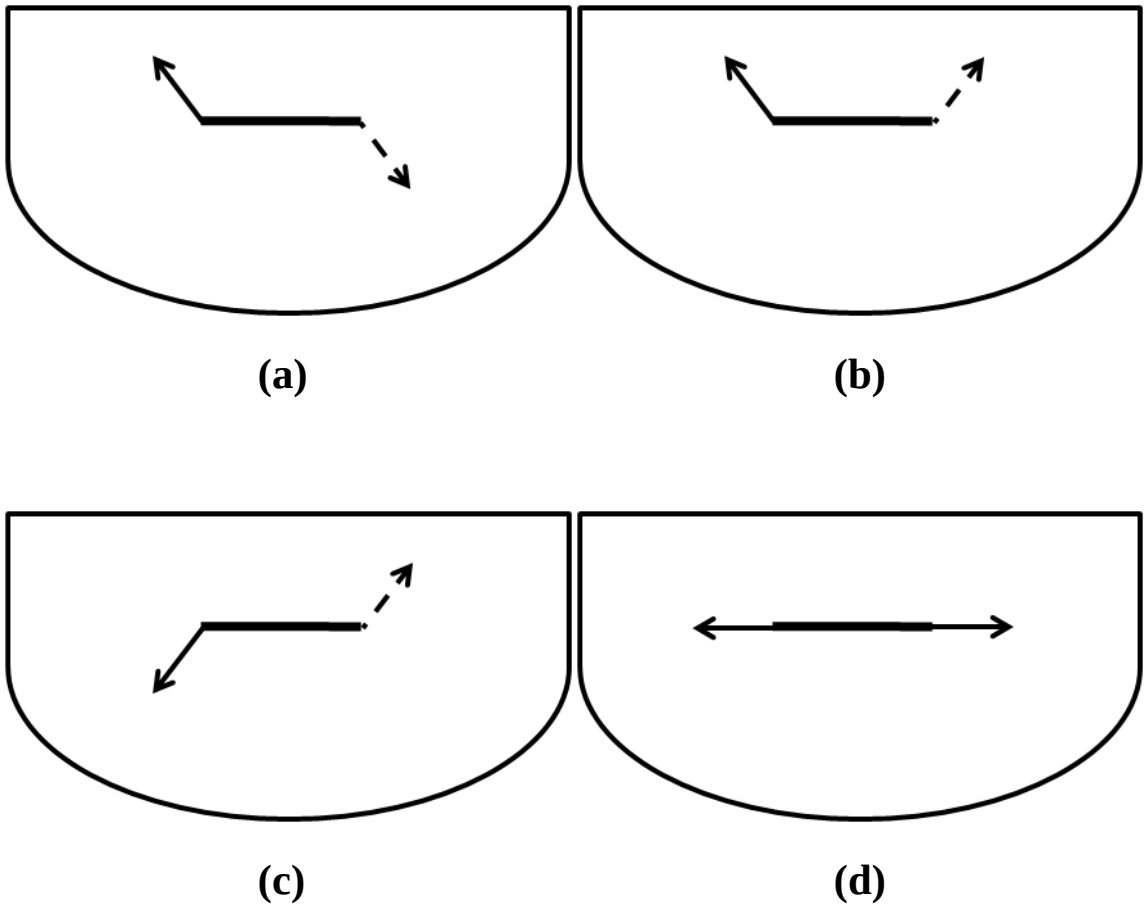

Figure 4.9 Schematic representation of (a)-(c) three cases of out-of-plane crack propagation and (d) in-plane crack propagation.

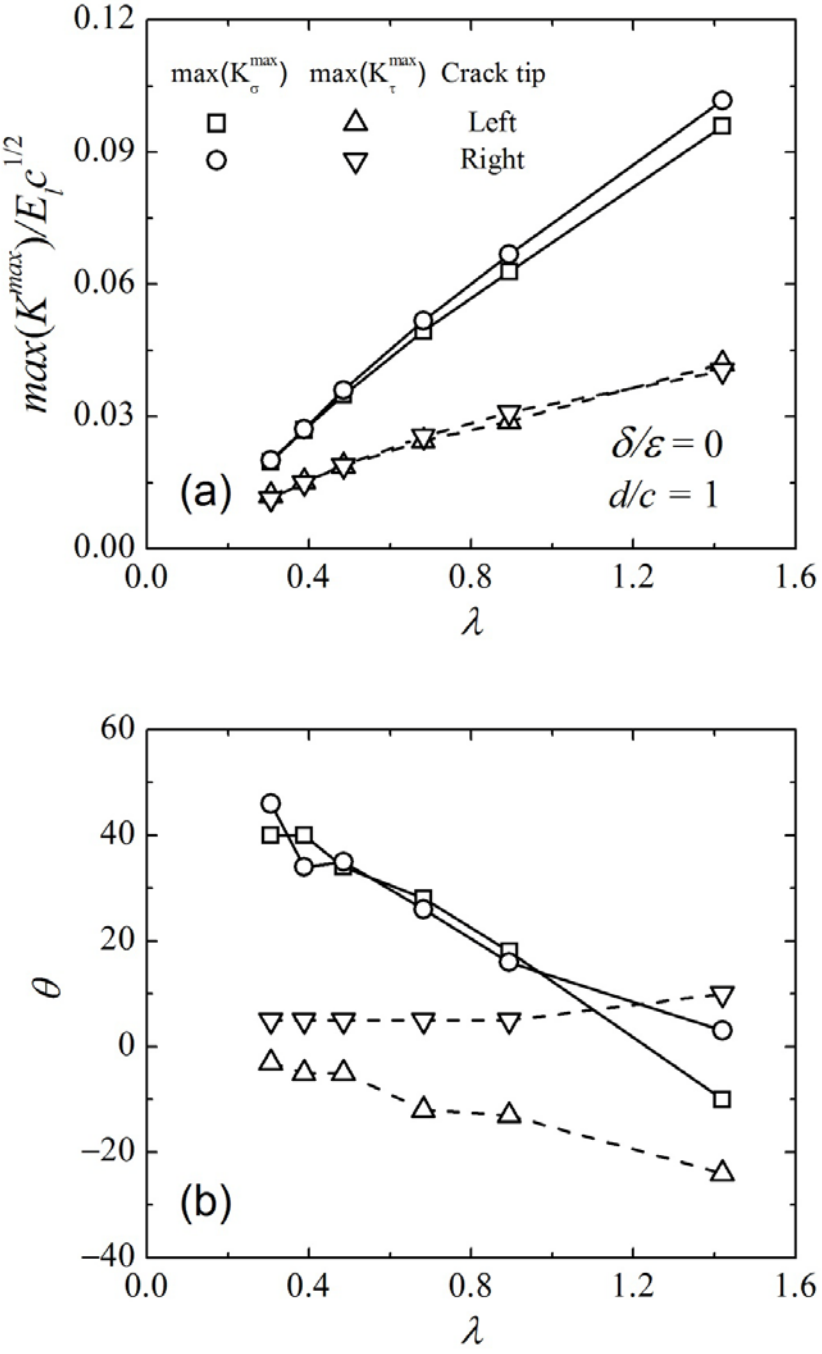

Figure 4.10 Effects of Maugis parameter λ on (a) dimensionless max(K_σ^{max}) and max(K_τ^{max}), and (b) the corresponding sliding distance x/c and (c) angle θ at left and right crack tips for S = 46.8, δ/ε = 0, h/c = 4, d/c = 1.

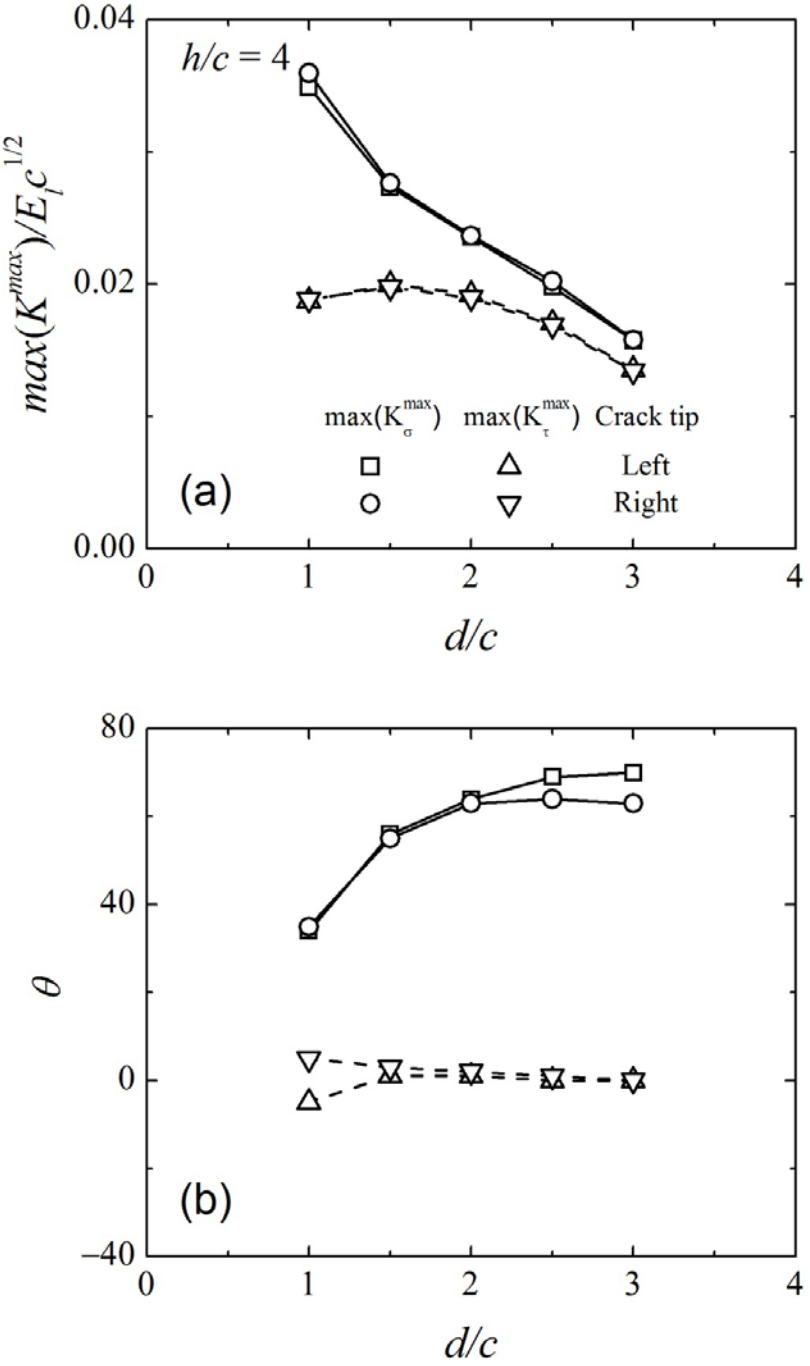

Figure 4.11 Effects of relative crack position d/c on (a) dimensionless max(K_σ^{max}) and max(K_τ^{max}), and (b) the corresponding sliding distance x/c and (c) angle θ at left and right crack tips for $\lambda = 0.49$, $S = 46.8$, $E_l/E_s = 5$, $h/c = 4$, $\delta/\varepsilon = 0$.

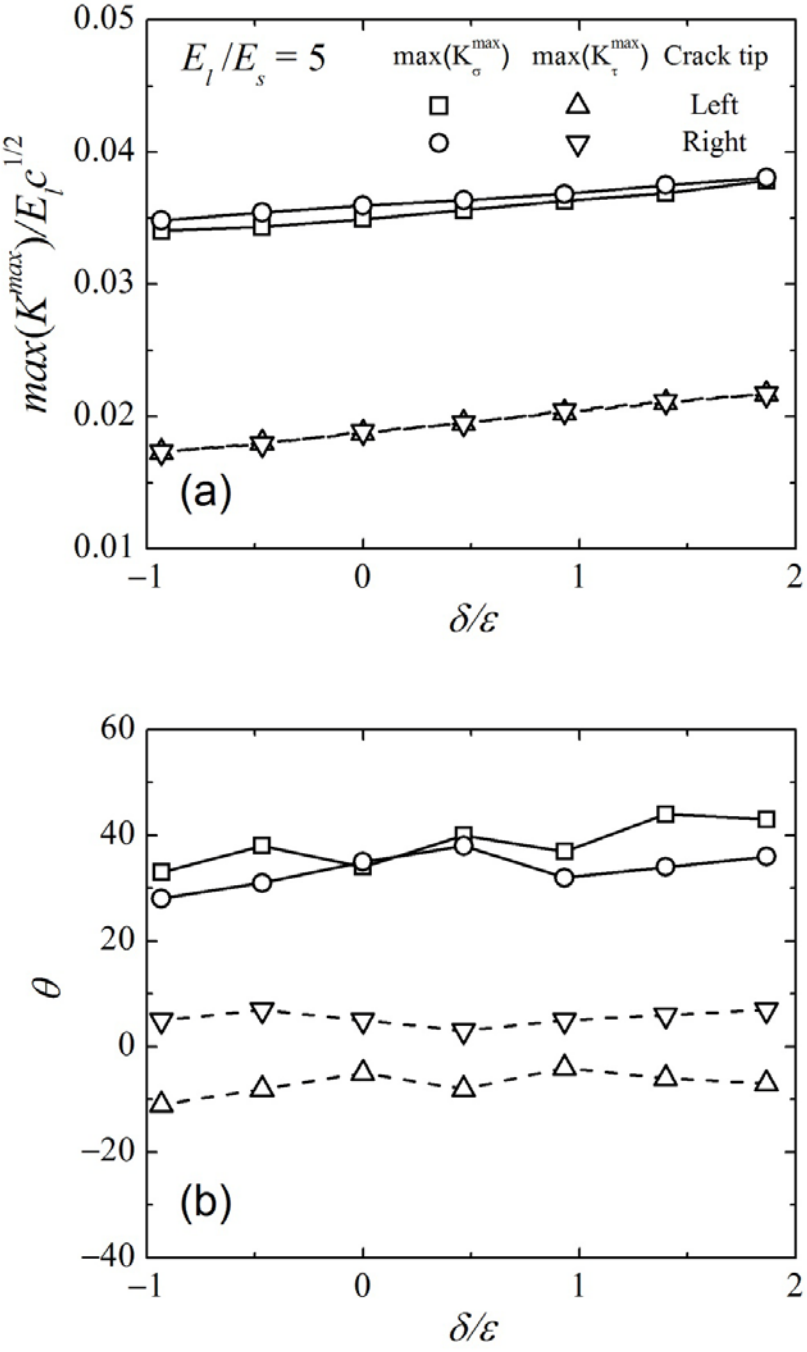

Figure 4.12 Effects of interaction distance δ/ε on (a) dimensionless max(K_σ^{max}) and max(K_τ^{max}), and (b) the corresponding sliding distance x/c and (c) angle θ at left and right crack tips for λ = 0.49, S = 46.8, E_l/E_s = 5, h/c = 4, d/c = 1.

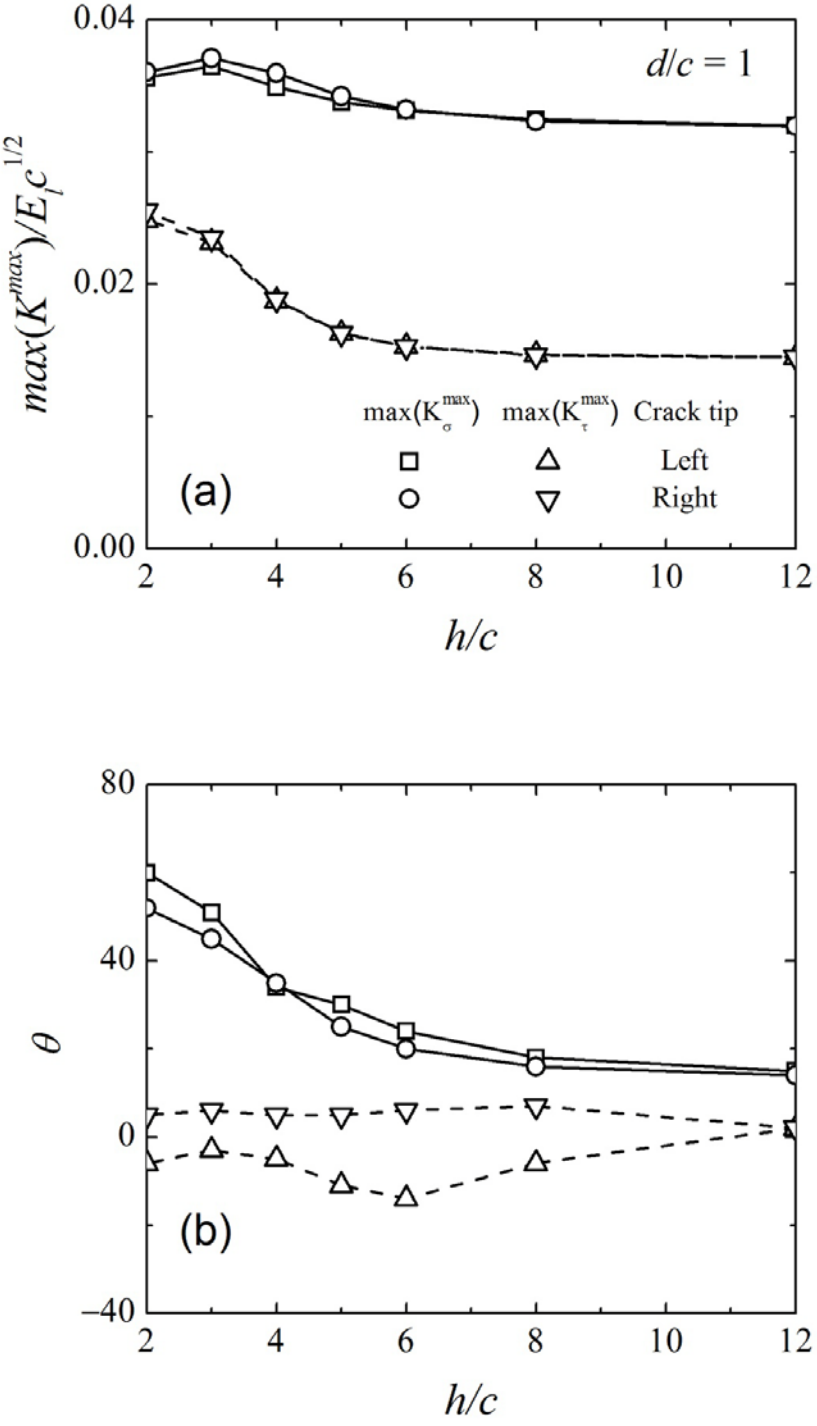

Figure 4.13 Effects of relative hard coating thickness h/c on (a) dimensionless max(K_σ^{max}) and max(K_τ^{max}), and (b) the corresponding sliding distance x/c and (c) angle θ at left and right crack tips for $\lambda = 0.49$, $S = 46.8$, $E_1/E_2 = 5$, $d/c = 1$, $\delta/\varepsilon = 0$.

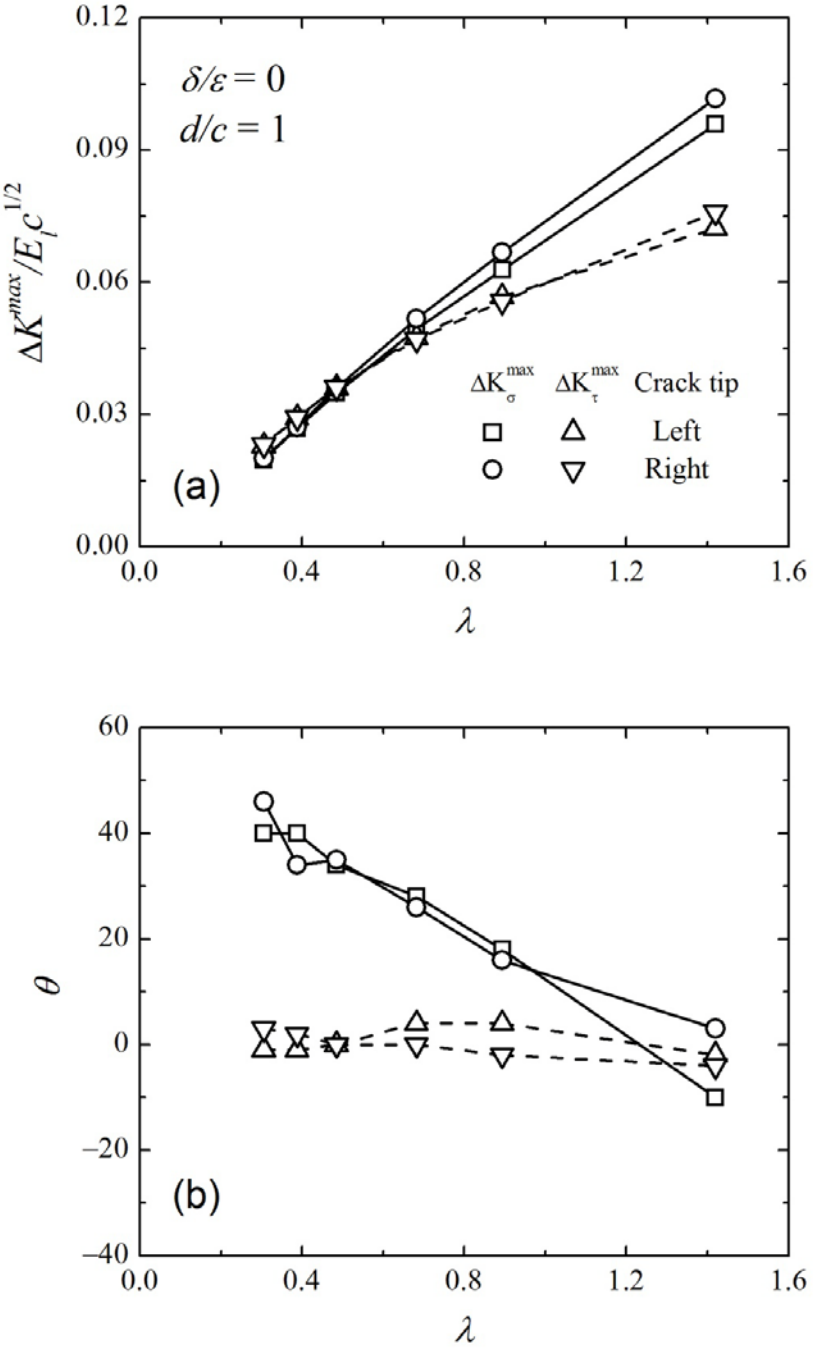

Figure 4.14 Effects of Maugis parameter λ on (a) dimensionless ΔK_σ^{max} and ΔK_τ^{max} and (b) the corresponding angle θ at left and right crack tips for S = 46.8, δ/ε = 0, h/c = 4 and d/c = 1.

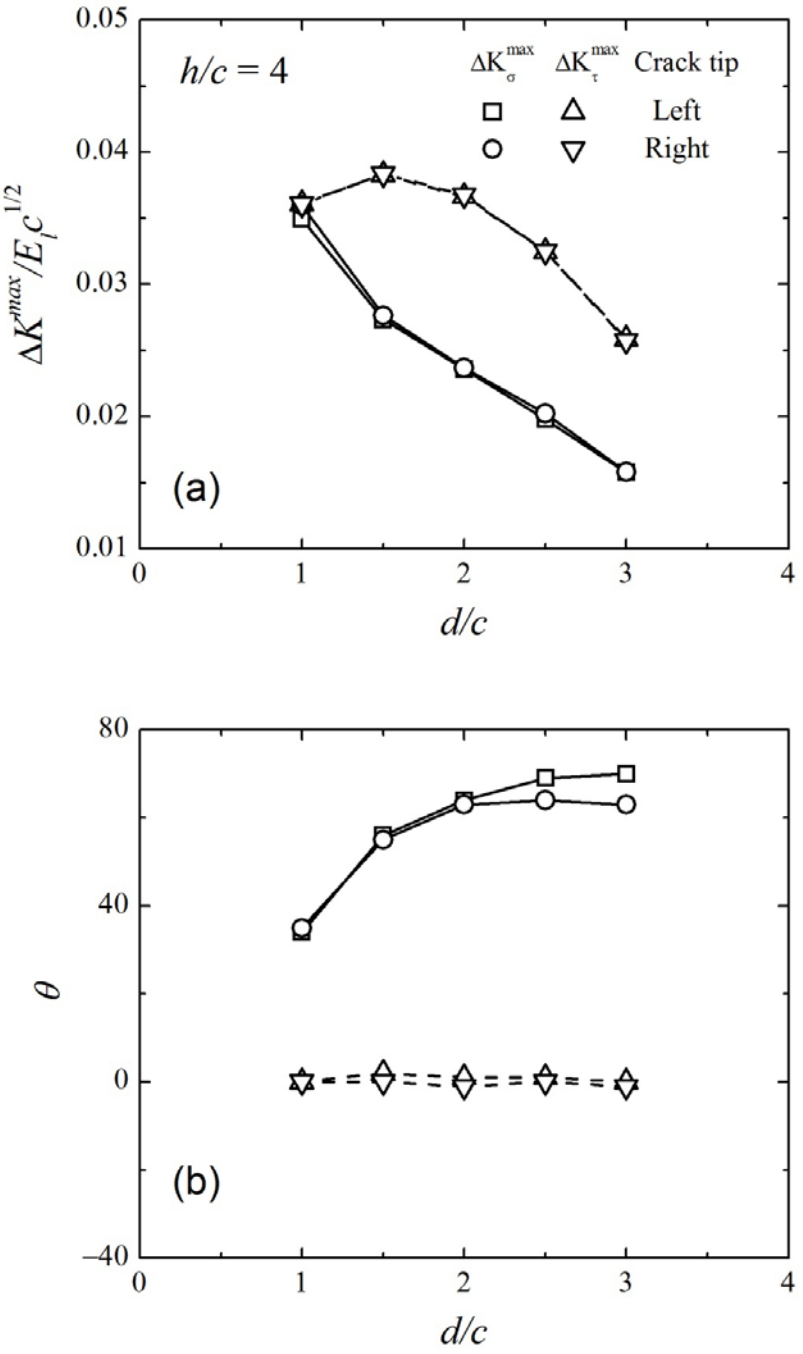

Figure 4.15 Effects of relative crack position d/c on (a) dimensionless ΔK_{σ}^{max} and ΔK_{τ}^{max} and (b) the corresponding angle θ at left and right crack tips for $\lambda = 0.49$, $S = 46.8$, $E_l/E_s = 5$, $h/c = 4$ and $\delta/\varepsilon = 0$.

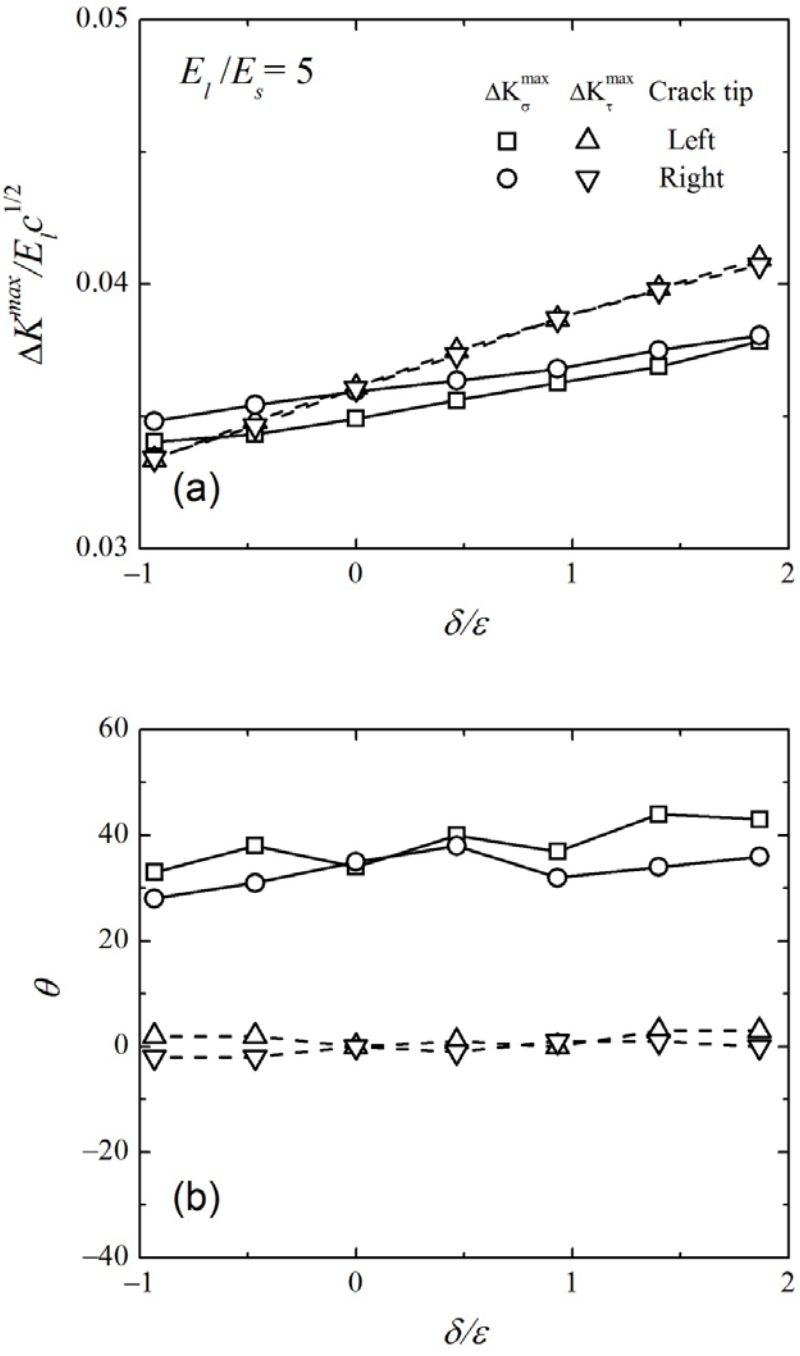

Figure 4.16 Effects of interaction distance δ/ε on (a) dimensionless ΔK_σ^{max} and ΔK_τ^{max} and (b) the corresponding angle θ at left and right crack tips for S = 46.8, E_l/E_s = 5, h/c = 4, d/c = 1.

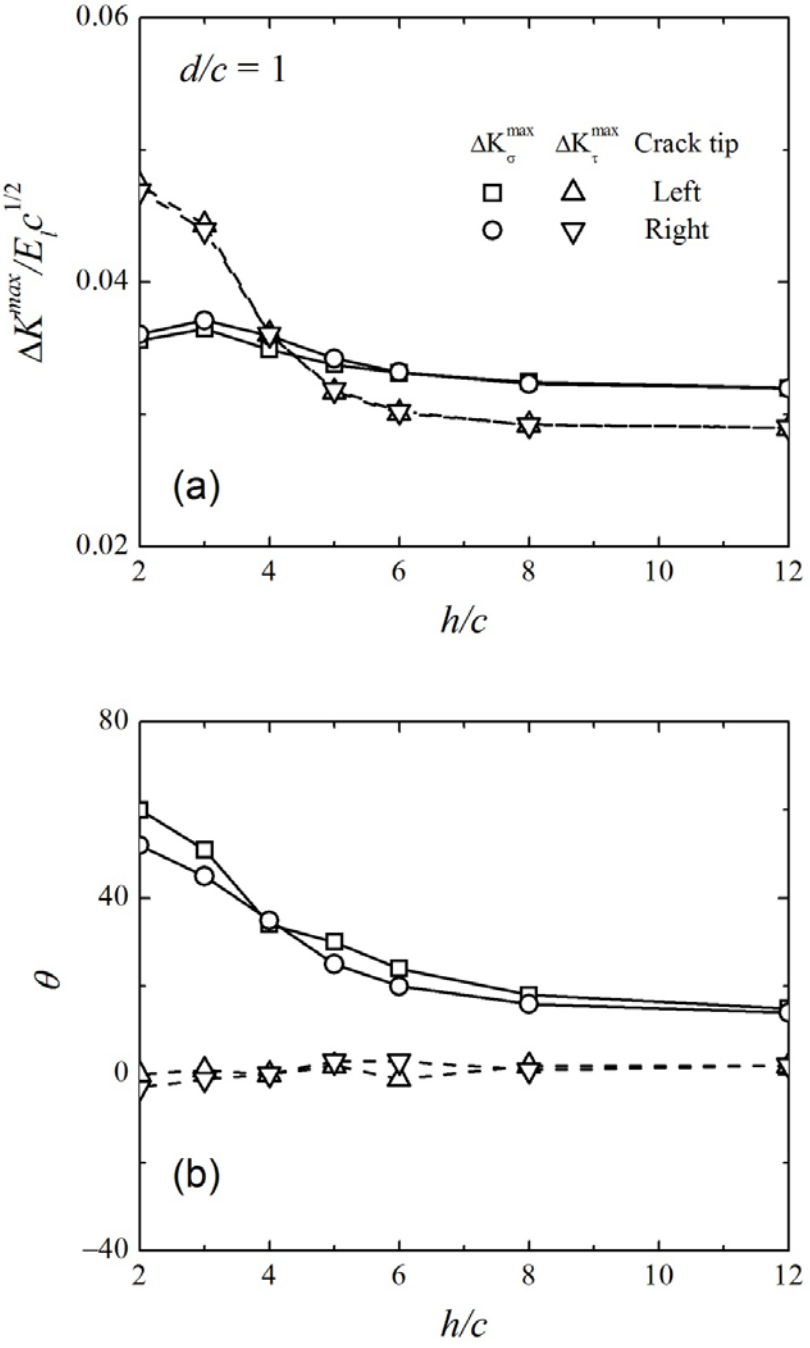

Figure 4.17 Effects of relative hard coating thickness h/c on (a) dimensionless ΔK_{σ}^{max} and ΔK_{τ}^{max} and (b) the corresponding angle θ at left and right crack tips for $\lambda = 0.49$, $S = 46.8$, $E_l/E_s = 5$, $d/c = 1$ and $\delta/\varepsilon = 0$.

Chapter 5
Fracture mechanics analysis of asperity cracking due to adhesive normal contact

5.1 Introduction

Among the various wear processes resulting in the removal of material from interacting surfaces (Archard, 1953; Suh, 1973; Dwyer-Joyce et al., 1994), the most often encountered wear process is adhesive wear (Burwell and Strang, 1952; Lisowski and Stolarski, 1981). Surface property modification or damage caused by adhesive wear is considered to be one of the main precursors of failure in micro/nano-scale applications (Bassani and D'Acunto, 2000), such as micro-electromechanical systems, hard-disk drives, chemomechanical polishing of semiconductor devices, and lapping of magnetic recording heads. Therefore, understanding adhesion-induced material removal is of great importance to the endurance of mechanical systems and effectiveness of surfacing processes.

Wear particle formation due to asperity-asperity interaction is often a consequence of cumulative surface damage comprising the sequential stages of plastic deformation, void nucleation, crack initiation, and crack propagation (Suh, 1977; Jahanmir and Suh, 1977). Asperity fracture occurs when the dominant crack in a damaged asperity reaches a critical length corresponding to the maximum values of the stress intensity factor (SIF), known as the fracture toughness. The driving force for crack growth in the cracked asperity generated by the normal and shear surface tractions depends on the mode I and mode II SIFs, K_{I} and K_{II} , respectively. The maximum tensile stress (Erdogan and Sih, 1963) and the strain energy density (Sih, 1974) are traditional criteria of the crack growth direction for mixed mode loading. However, the direction and the rate of crack growth predominantly in tensile or shear mode strongly depended on the corresponding maximum SIF ranges $\Delta K_{\sigma}^{\max}$ and $\Delta K_{\tau}^{\max}$, which are functions of the mode I and mode II SIF ranges ΔK_{I} and ΔK_{I}, respectively (Paris and Erdogan, 1963). Experimental observations (Mageed and Pandey, 1992) suggest that the criterion based on $\Delta K_{\sigma}^{\max}$ yields more accurate predictions of the crack growth path under cyclic loading than the criteria of maximum tensile stress and strain energy density. A numerical analysis of crack growth and wear particle formation due to sliding contact has shown that the predicted wear particle size and wear volume were in fair agreement with experimental results (Ko et al., 2001). The direction and rate of subsurface crack growth in homogeneous half-spaces (Komvopoulos and Cho, 1997) and layered media (Gong and Komvopoulos, 2005) due to asperity sliding have been analyzed in terms of the SIF ranges ΔK_{σ} and ΔK_{τ}. However, the effect of adhesion on surface cracking was not considered in the former studies.

According to the primitive model of adhesive spherical contact introduced by Bradley (1932), the force needed to separate two adhering rigid spheres (referred to as the pull-off force) is equal to $2\pi R\Delta\gamma$, where $R = [1/R_1 + 1/R_2]^{-1}$ is the equivalent radius of curvature (R_1 and R_2 are the radii of curvature of the two spheres) and $\Delta\gamma = \gamma_1 + \gamma_2 - \gamma_{12}$ is the work of adhesion (γ_1 and γ_2 are the surface energies of the two spheres and γ_{12} is the surface energy of the

interface). The same relation of the pull-off force is given by the DMT model developed by Derjaguin et al. (1975), who neglected the effect of adhesion on the contact area predicted by Hertz theory, whereas the JKR model of Johnson et al. (1971), which accounts for adhesion only within the contact region of the two elastic spheres, yields a pull-off force equal to $(3/2)\pi R\Delta\gamma$. Tabor (1977) interpreted the differences between the DMT and JKR models in terms of a dimensionless parameter, known as the Tabor parameter, defined as

$$\mu = \left(\frac{R\Delta\gamma^2}{E^{*2}\varepsilon^3}\right)^{1/3}, \tag{5.1}$$

where $E^* = [(1-\nu_1^2)/E_1 + (1-\nu_2^2)/E_2]^{-1}$ is the effective elastic modulus (E_1, E_2 and ν_1, ν_2 are the elastic modulus and Poisson's ratio of the two spheres, respectively) and ε is the equilibrium interatomic distance, arguing that the DMT and JKR models represent significantly different contact systems with $\mu < 0.1$ and $\mu > 3$, respectively. Using the Dugdale approximation, Maugis (1992) obtained an analytical solution of the pull-off force in the range $0.1 < \mu < 3$. Johnson and Greenwood (1997) introduced an adhesion map that determines the applicability of the previous models including the Hertzian model in terms of the applied normal load and the Tabor parameter. Muller et al. (1980), Attard and Parker (1992), and Greenwood (1997) used a different approach to model adhesive contact of elastic spheres. They assumed that surface interaction is governed by the Lennard-Jones (L-J) potential (Israelachvili, 1992), and examined the variation of the pull-off force in the transition range of the Tabor parameter bounded by the solutions of the Bradley (DMT) model and the JKR model.

Contrary to spherical adhesive contacts, the pull-off force of two-dimensional (2D) adhesive contacts depends on the effective elastic modulus and, according to the modified JKR model of Chaudhury et al. (1996), is equal to $(3/4)(4\pi RE^*\Delta\gamma^2)^{1/3}$. Leng et al. (2000) and Johnson and Greenwood (2008) used the Maugis method to analyze 2D adhesive contact and obtained a solution of the pull-off force in the range of the Maugis parameter $\lambda = (9\sqrt{3}/16)\mu$ bounded by the solutions of the 2D JKR model to 2D DMT model. Wu (2009) used the L-J potential to model the adhesion of a cylinder with a half-space and obtained a semi-empirical relation of the pull-off force in the transitions range of the Maugis parameter bounded by the solutions of the 2D JKR model and the 2D Bradley model.

Although the aforementioned studies have yielded important insight into the effect of adhesion on elastic contact deformation, they cannot elucidate the effect of adhesion on contact-induced cracking at asperity contacts. Thus, the objective of this chapter was to perform a comprehensive fracture mechanics analysis of asperity cracking due to repetitive adhesive contact. The direction and rate of crack growth in a cyclic loaded and unloaded elastic asperity were determined in terms of the maximum SIF ranges obtained from a liner elastic fracture mechanics analysis and the FEM. The crack propagation direction and the dominant crack mechanisms are discussed in terms of the maximum surface interaction (minimum surface gap), initial crack position, crack-face friction, asperity elastic properties, and work of adhesion.

5.2 Numerical model

5.2.1 Problem definition

It is well known that contact of rough surfaces is confined at asperity microcontacts where the development of normal and shear tractions results in energy dissipation. The distribution of asperity microcontacts depends on the roughness and material properties of the interacting surfaces and the applied normal load. In the present study, normal contact of two elastic asperities is modeled by the equivalent contact system of a rigid plane and an elastic asperity of equivalent radius of curvature R and effective elastic modulus E^*, shown schematically in Fig. 5.1. This contact model is representative of materials undergoing elastic deformation in the loading range of interest, ductile materials exhibiting elastic shakedown, or brittle (hard) materials demonstrating purely elastic deformation. The elastic asperity is modeled as a homogeneous and isotropic medium with a very small surface crack, defined by an angle α measured from the horizontal direction.

Cartesian and polar coordinates fixed at the crack tip (x, y) and (r, θ), respectively, and surface distance δ (defined as the distance between the rigid plane and the top of the undeformed asperity) are shown in Fig. 5.1. The reference plane (dashed line) corresponds to $\delta = 0$; thus, $\delta < 0$ implies that the rigid plane is above the top of the undeformed asperity configuration. A full contact cycle consists of incrementally displacing the rigid plane toward the elastic asperity from a distance sufficiently large for surface adhesion to be insignificant to a maximum surface distance $\delta_{\max}$ (or minimum surface gap) and then retracting the rigid plane following the same incremental path.

5.2.2 Finite element model

Figure 5.2(a) shows the FEM mesh of a semi-infinite elastic half-space with an asperity of radius R interacting with a rigid plane. Normal to the asperity surface is a crack of length $c = 0.04R$. The width and height of the half-space are equal to $20R$ and $10R$, respectively. The mesh consists of 5,332 isoparametric, eight-node, quadrilateral, plane-strain elements, comprising a total of 16,572 nodes. Nodes at the bottom boundary of the FEM mesh are constrained against displacement in both in-plane directions.

From the L-J potential, the adhesive force per unit area (pressure) p acting between two infinite planes is given by

$$p = \frac{8\Delta\gamma}{3\varepsilon}\left[\left(\frac{\varepsilon}{h}\right)^3 - \left(\frac{\varepsilon}{h}\right)^9\right], \tag{5.2}$$

where h is the gap between the two infinite planes. According to the Derjaguin approximation (Derjaguin, 1934), the interaction energy between small areas of solids, which may be curved and slightly inclined to each other, is the same as the energy per unit area between infinite planar solids, while the equivalent approximation for surface forces is also tenable. Therefore, similar to previous studies (Muller et al., 1980; Attard and Parker, 1992; Greenwood, 1997; Wu, 2009), the two solid surfaces are discretized into numerous small segments, and the total adhesive force is determined as the sum of the forces corresponding to each segment using Eq. (5.2).

Consequently, in the present FEM model, adhesion between the rigid plane and the elastic asperity is modeled by nonlinear springs attached to nodal points on the asperity surface and rigid plane, as shown in Fig. 5.2(b). The present FEM model contains a total of 125 nonlinear springs at a fixed lateral distance of ~1.2R are symmetrically distributed about the asperity center.

To enhance the accuracy, the FEM mesh is refined around the crack tip as shown in Fig. 5.2(c). The mesh at the crack tip consists of 30 isoparametric, eight-node, collapsed quadrilateral, plane-strain elements with their mid-side nodes displaced to the quarter-point distance to simulate the singularity of the crack-tip stresses. In addition, to prevent crack-tip blunting, the crack-tip nodes are constrained to move together. To prevent overlapping of the crack faces and to allow the transmission of traction across the crack interfaces, self-contact with a hard overclosure (i.e., no displacement of a crack-face node into the opposed crack face) is specified for the entire crack interface. All simulations were performed with the FEM code ABAQUS/Standard (version 6.9-2).

5.3 Results and discussion

In this section, FEM results of the normalized SIFs and their ranges, crack propagation direction, and crack-face mechanisms are discussed in terms of dimensionless parameters, such as surface distance δ/ε, maximum surface distance $\delta_{\max}/\varepsilon$(or minimum surface gap), crack-face coefficient of friction μ_c, Maugis parameter λ, crack position (defined by angle α), crack-interface position x_c/c (where c is the crack length) and angle θ. To obtain general solutions, the SIFs and their ranges are normalized by $Ec^{1/2}$ (where E is used to represent the effective elastic modulus for simplicity).

5.3.1 Stress intensity factors

In linear elastic fracture mechanics, the driving force for cracking is the maximum stress intensity factor range $\Delta K^{\max}$, which is a function of K_{I} and K_{II}, defined as

$$K_{\mathrm{I}} = \lim_{r\to 0} \sqrt{2\pi r}\, \sigma_{yy}(r, \theta = 0), \tag{5.3a}$$

and

$$K_{\mathrm{II}} = \lim_{r\to 0} \sqrt{2\pi r}\, \tau_{xy}(r, \theta = 0), \tag{5.3b}$$

where $\theta > 0$ in the counter-clockwise direction. K_{I} and K_{II} are calculated from the stresses at nine nodes adjacent to the crack tip along the crack plane (θ = 0) using a linear extrapolation of a least-square line fit through the SIF data (Chan et al., 1970).

Figure 5.3 shows the variation of the normalized mode I and mode II SIFs, $K_{\mathrm{I}}/Ec^{1/2}$ and $K_{\mathrm{II}}/Ec^{1/2}$, respectively, with the surface distance δ/ε during loading and unloading for μ_c = 0, α = 36$^{\mathrm{o}}$, and λ = 0.121, 0.306, and 0.563. It is well known that both attractive and repulsive force components play important roles in adhesive contacts (Luan and Robbins, 2005). As shown in Fig. 5.3(a), for δ/ε < 0, K_{I}> 0 because the attractive force component is dominant; however, the increase of δ/ε (i.e., decrease of surface gap) leads to K_{I} < 0 because it results in the dominance

of the repulsive force component. Considering Eq. (5.1) and that $\lambda \sim \mu$, a higher λ may be interpreted as a higher work of adhesion and/or a lower effective elastic modulus. Thus, the increase of K_{I} with λ can be attributed to the increase of the attractive force component due to the increase of the work of adhesion. This trend is more apparent in the low range of δ/ε (e.g., δ/ε < 0), where surface attraction is more dominant than surface repulsion. Significant differences between the loading and unloading paths and clear evidence of contact instabilities (jump-in and jump-out) are observed for a relatively high λ value (e.g., λ = 0.563). However, as λ decreases, the elastic contact asymptotically approaches the condition of rigid contact, which is not conducive to contact instabilities surface contact (loading) and surface separation (unloading) occur smoothly, as shown by the merely overlapped loading and unloading curves for λ = 0.121. Similar adhesion-induced contact instabilities have been observed for 3D elastic contacts (Song and Komvopoulos, 2011), but for a different critical λ value because of the difference between 3D (point) and 2D (line) contacts mentioned previously. Similar to mode I, significantly different loading and unloading paths and contact instabilities can be seen for mode II when λ assumes a relatively high value (Fig. 5.3(b)). The dependence of K_{II} on λ diminishes with the increase of δ/ε, eventually disappearing in the range of δ/ε > 1 (because the dominance of repulsion does not depend on adhesion) and with the decrease of λ, similar to K_{I}.

5.3.2 Stress intensity factor ranges and crack propagation direction

Cracking under both mode I and mode II loading conditions is controlled by the tensile and shear SIFs, K_σ and K_τ, respectively, are given by

$$K_\sigma(\theta,\delta) = \sigma_{\theta\theta}\sqrt{2\pi r} = \cos\frac{\theta}{2}\left[K_{\mathrm{I}}\cos^2\frac{\theta}{2} - \frac{3}{2}K_{\mathrm{II}}\sin\theta\right], \tag{5.4a}$$

and

$$K_\tau(\theta,\delta) = \tau_{r\theta}\sqrt{2\pi r} = \frac{1}{2}\cos\frac{\theta}{2}[K_{\mathrm{I}}\sin\theta + K_{\mathrm{II}}(3\cos\theta - 1)]. \tag{5.4b}$$

For a given plane with $\theta = \theta^*$, the tensile and shear SIF ranges, ΔK_σ and ΔK_τ, respectively, can be expressed as

$$\Delta K_\sigma(\theta=\theta^*) = K_{\sigma,\max}(\theta=\theta^*,\delta) - \max\left[K_{\sigma,\min}(\theta=\theta^*,\delta), 0\right], \tag{5.5a}$$

and

$$\Delta K_\tau(\theta=\theta^*) = K_{\tau,\max}(\theta=\theta^*,\delta) - K_{\tau,\min}(\theta=\theta^*,\delta). \tag{5.5b}$$

Since only $K_\sigma > 0$ is physically significant, in the calculation of ΔK_σ all negative values of K_σ were nullified.

Figure 5.4 shows the dimensionless tensile and shear SIF ranges $\Delta K_\sigma/Ec^2$ and $\Delta K_\tau/Ec^2$ as functions of θ for μ_c = 0, α = 36°, $\delta_{\max}/\varepsilon$ = 23.3, and λ = 0.066–1.419. As explained earlier, an increase of λ may be interpreted as an increase of the work of adhesion. Consequently, the increases of ΔK_σ and ΔK_τ with λ can be attributed to the increases of the attractive and repulsive force components, respectively, due to the increase of the work of adhesion. However, the

enhancement of attractive force component is much more pronounced than that of repulsive force component, therefore, the increment of ΔK_σ is higher than that of ΔK_τ with the increase of λ. Figure 5.4(a) shows that the maximum value of ΔK_σ occurs at $\theta \approx 0^o$, while Fig. 5.4(b) shows that ΔK_τ has two local maxima at $\theta \approx \pm 70.4^o$.

Tensile-mode crack growth occurs in the plane of $\Delta K_\sigma^{\max}$, while shear-mode crack growth commences on the plane of $\Delta K_\tau^{\max}$ (Komvopoulos and Cho, 1997; Gong and Komvopoulos, 2005; Cho and Komvopoulos, 1997b). These maximum SIF ranges are obtained as

$$\Delta K_\sigma^{\max} = \max[\Delta K_\sigma(\theta)] \qquad (-180^\circ \le \theta \le 180^\circ), \tag{5.6a}$$

and

$$\Delta K_\tau^{\max} = \max[\Delta K_\tau(\theta)] \qquad (-180^\circ \le \theta \le 180^\circ). \tag{5.6b}$$

The dominant mode of crack growth depends on the magnitudes of $\Delta K_\sigma^{\max}$ and $\Delta K_\tau^{\max}$. Crack growth is dominated by the tensile mode when $\Delta K_\sigma^{\max} > \Delta K_\tau^{\max}$ or shear mode when $\Delta K_\sigma^{\max} < \Delta K_\tau^{\max}$. Hence, the crack growth rate can be expressed as (Paris and Erdogan, 1963)

$$\frac{dc}{dN} = A(\Delta K_i^{\max})^n, \tag{5.7}$$

where $\Delta K^{\max} = \max[\Delta K_\sigma^{\max}, \Delta K_\tau^{\max}]$, A and n are material constants, and N is the number of loading cycles.

The size of the wear particle produced from asperity cracking significantly depends on the crack growth angle θ and the crack position, i.e., angle α (Fig. 5.1). A larger wear particle will be produced if the crack grows toward the half-space (i.e., $\theta > 0$). Thus, the rate of wear particle formation depends on the crack-growth rate (Eq. (5.7)), the crack growth direction, and the crack position.

5.3.3 Effect of the Maugis parameter

Figure 5.5(a) shows the maximum tensile and shear SIF ranges, $\Delta K_\sigma^{\max}/Ec^2$ and $\Delta K_\tau^{\max}/Ec^2$, respectively, as functions of the Maugis parameter λ for $\mu_c = 0$, $\alpha = 36^o$, and $\delta_{\max}/\varepsilon = 23.3$. Both SIF ranges monotonically increase with λ. As mentioned earlier, a higher λ value indicates a higher work of adhesion, producing stronger attractive and repulsive effects. However, the enhancement of attraction is much more pronounced than that of repulsion, leading to the increase of $\Delta K_\sigma^{\max}$, while the enhancement of repulsion leads to a marginal increase of $\Delta K_\tau^{\max}$. Therefore, although both $\Delta K_\sigma^{\max}$ and $\Delta K_\tau^{\max}$ increase with λ, the increase of $\Delta K_\sigma^{\max}$ is much higher than that of $\Delta K_\tau^{\max}$, suggesting that the most likely mode of crack growth is the tensile mode. This is demonstrated by the transition from shear to tensile dominant mode of crack growth at $\lambda \approx 0.6$.

Figure 5.5(b) illustrates the effect of the Maugis parameter λ on the crack growth direction θ predicted by $\Delta K_\sigma^{\max}$ and $\Delta K_\tau^{\max}$ for $\mu_c = 0$, $\alpha = 36^o$, and $\delta_{\max}/\varepsilon = 23.3$. It can be seen that the effect of the Maugis parameter on the crack growth direction is secondary. The crack growth

angle corresponding to $\Delta K_{\sigma}^{\max}$ is almost constant and equal to zero, i.e., mode I crack growth. This indicates a significant effect of surface attraction. Eqs. (5.4b) and (5.5b) show that $\theta = \pm 70.4^{o}$ when $K_{\mathrm{II}} = 0$ and that the absolute value of θ corresponding to $\Delta K_{\tau}^{\max}$ decreases with the increase of K_{II}. Therefore, shear mode crack growth is predicted to occur at an angle θ between –57^{o} and –64^{o} with the increase of λ because the repulsion effect is less significant.

The occurrence of opening, slip, and stick between the crack faces during loading and unloading are closely related to the dominant mode of crack growth. Figure 5.6 shows crack mechanism maps demonstrating the effect of the Maugis parameter on the evolution of crack-face mechanisms during loading and unloading for $\mu_c = 0$, $\alpha = 36^{o}$, and $\delta_{\max}/\varepsilon = 23.3$. The vertical axis of the maps indicates the surface distance (i.e., the displacement of the rigid plane) and the horizontal axis indicates the crack interface (x_c/c = 0 denotes the crack tip and x_c/c = 1 denotes the crack mouth). The crack mechanisms strongly depend on the intensity of surface interaction. When the surfaces are appreciably apart, the crack faces stick to each other in the absence of any traction to induce relative movement. As the rigid plane moves closer to the elastic asperity, crack-face opening becomes more significant because of the increasing effect of interfacial attraction. Further decreasing the surface gap leads to a transition from crack-face opening to slip because the intense surface interaction causes the contact force to change from attractive (tensile) to repulsive (compressive). Thus, an attractive contact force promotes crack opening, as opposed to a repulsive contact force that enhances crack-face slip.

The intensification of surface attraction caused by the increase of λ, reflected by the enhancement of crack-face opening in Fig. 5.6, indicates a higher propensity for crack growth predominantly in the tensile mode. For very low λ values (e.g., $\lambda = 0.306$), crack-face slip becomes dominant because the low work adhesion yields a weak attraction effect. Differences in crack-face opening during loading and unloading are attributed to differences in critical surface distance for the occurrence of contact instabilities.

5.3.4 Effect of crack-face friction

Figure 5.7 shows the dependence of $\Delta K_{\sigma}^{\max}/Ec^{2}$, $\Delta K_{\tau}^{\max}/Ec^{2}$, and θ on the crack-face coefficient of friction μ_c for λ = 0.563, $\alpha = 36^{o}$, and $\delta_{\max}/\varepsilon = 23.3$. The increase of the slip resistance of the crack faces with the increase of μ_c lowers the propensity of shear-mode crack growth by reducing the shear stresses at the crack tip. However, the effect of μ_c in adhesive normal contact is secondary. As shown in Fig. 5.7(a), the tensile mode is the most likely mode of asperity cracking despite the significant variation of crack-face friction. In addition, Fig. 5.7(b) shows that the crack-growth direction is also not affected by the variations in crack-face friction.

5.3.5 Effect of maximum surface distance

Figure 5.8 shows $\Delta K_{\sigma}^{\max}/Ec^{2}$, $\Delta K_{\tau}^{\max}/Ec^{2}$, and θ as functions of the maximum surface distance $\delta_{\max}/\varepsilon$ (or minimum surface gap) for $\mu_c = 0$, $\alpha = 36^{o}$, and λ = 0.563. While the compression of the elastic asperity by the rigid plane increases with the $\delta_{\max}$, the effect on attraction is negligible. Therefore, the effect of $\delta_{\max}$ on $\Delta K_{\sigma}^{\max}$ and corresponding θ is secondary. However, $\Delta K_{\tau}^{\max}$ increases with $\delta_{\max}$ and the corresponding θ changes from –68^{o} to –59^{o}. This suggests an increased propensity for shear mode dominant crack growth. Figure 5.8(a)

shows that a transition from tensile-to-shear mode of crack growth occurs at $\delta_{\max}/\varepsilon \approx 25$. This transition of the dominant mode of crack growth can be interpreted in the context of the crack-mechanism map shown in Fig. 5.6. It can be seen that slip between the crack faces is enhanced for large δ/ε (i.e., small surface gap) while there is no effect on crack-face opening, which is consistent with the tension-to-shear mode transition observed in Fig. 5.8(a).

5.3.6 Effect of crack position

Figure 5.9 shows the effect of the crack position, indicated by angle α, on $\Delta K_\sigma^{\max}/Ec^2$, $\Delta K_\tau^{\max}/Ec^2$, and corresponding angle θ for $\mu_c = 0$, $\delta_{\max}/\varepsilon = 23.3$, and λ = 0.306, 0.563 and 1.419. Because of the small crack size, the change of the crack position is not expected to affect the repulsive and attractive force components at the interface of the rigid plane and the elastic asperity. The decrease of α leads to lower stresses around crack tip due to the increase of the distance between the surface traction and the crack tip. However, Eqs. (5.4)–(5.6) indicate that $\Delta K_\sigma^{\max}$ and $\Delta K_\tau^{\max}$ are strongly affected by K_{I}, which increases as the crack tends to become parallel to the horizontal direction with the decrease of α. Consequently, $\Delta K_\sigma^{\max}$ and $\Delta K_\tau^{\max}$ first decrease and then increase with increasing α. Moreover, the increase of θ corresponding to $\Delta K_\tau^{\max}$ with the decrease of α reveals an enhancement of crack-face slip and an increase of K_{II} during loading and unloading. This is a consequence of the intensified shear stress field induced by the half-space when the crack is close to edge of the asperity. This effect becomes more pronounced with the decrease of λ due to the more pronounced half-space effect caused by the increase elastic modulus as indicated by the decrease of λ.

5.4 Conclusions

In this chapter, a linear elastic fracture mechanics analysis of a pre-cracked asperity in adhesive normal contact with a rigid plane was performed with the FEM, using the Lennard-Jones potential and the Derjaguin approximation to model surface adhesion. Simulation results demonstrated the effects of the initial crack position, crack-face friction, maximum surface distance (minimum surface gap), and Maugis parameter (a function of the effective elastic modulus, asperity radius, work of adhesion, and intermolecular equilibrium distance) on the crack growth direction (angle θ) and the rate of crack growth controlled by $\Delta K_\sigma^{\max}$ or $\Delta K_\tau^{\max}$, depending on the dominant mode of crack growth. Based on the presented results and discussion, the following main conclusions can be drawn from this chapter.

1. In the high range of the Maugis parameter, the variation of SIFs with the surface distance during loading differs from that during unloading due to differences in the critical surface distance for the occurrence of contact instabilities. In the low range of the Mauguis parameter, contact instabilities are not apparent in the SIF responses and the loading and unloading paths almost coincide.

2. The effects of the Maugis parameter and the maximum surface distance on $\Delta K_\sigma^{\max}$, $\Delta K_\tau^{\max}$, and the corresponding crack growth angle θ are more significant than those of the crack-face friction and the initial crack position.

3. Although both $\Delta K_{\sigma}^{\max}$ and $\Delta K_{\tau}^{\max}$ increase with the Maugis parameter, the increase of $\Delta K_{\sigma}^{\max}$ is much more significant. This increases the crack growth rate and the propensity for tensile mode cracking, as evidenced by the enhancement of the crack-face opening mechanism under both loading and unloading conditions. While the increase of the Maugis parameter does not affect the direction of tensile-mode crack growth, it decreases the angle of shear-mode crack growth.

4. Although $\Delta K_{\sigma}^{\max}$ and the corresponding crack growth angle θ are insensitive to the variations of the surface distance, $\Delta K_{\tau}^{\max}$ and the corresponding crack growth angle θ increase with the maximum surface distance (minimum surface gap), implying an increased propensity for shear-mode crack growth, as evidenced by the enhancement of crack-face slip.

5. $\Delta K_{\sigma}^{\max}$ and $\Delta K_{\tau}^{\max}$ and corresponding crack growth angles θ are affected by the crack position at the asperity surface.

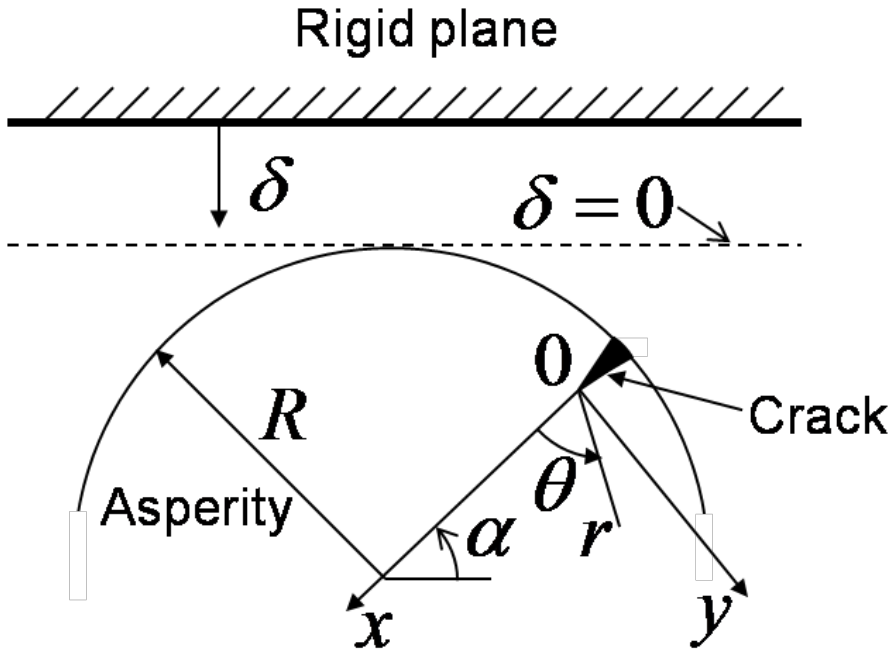

Figure 5.1 Schematics of the adhesive normal contact of a rigid plane over a deformable cylinder with an initial normal surface crack.

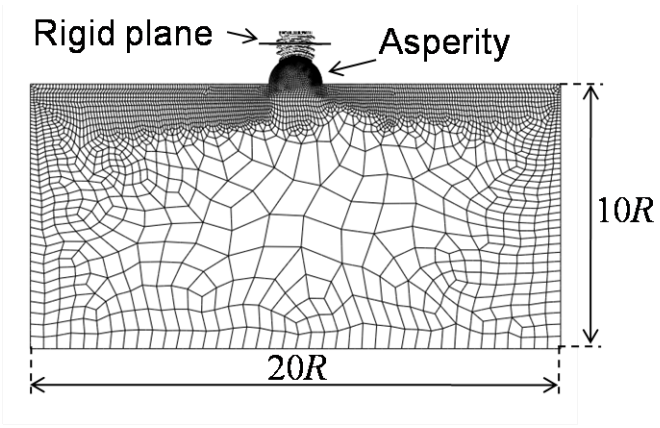

(a)

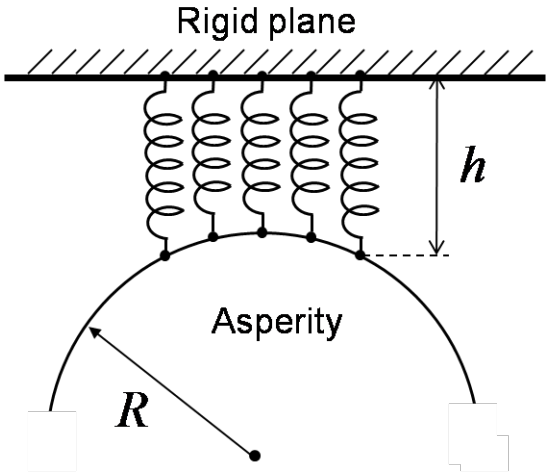

(b)

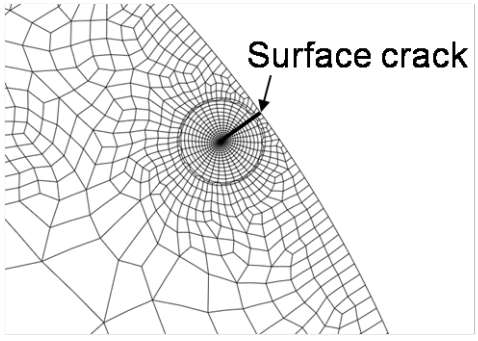

(c)

Figure 5.2 (a) Finite element mesh of the adhesive normal contact between a rigid plane and an elastic deformable asperity with an initial normal surface crack on half space, (b) schematics of nonlinear springs in FEM model used for modeling normal adhesive forces connecting surface nodal points of the asperity with the corresponding point on rigid plane, and (c) refined finite element mesh around surface crack.

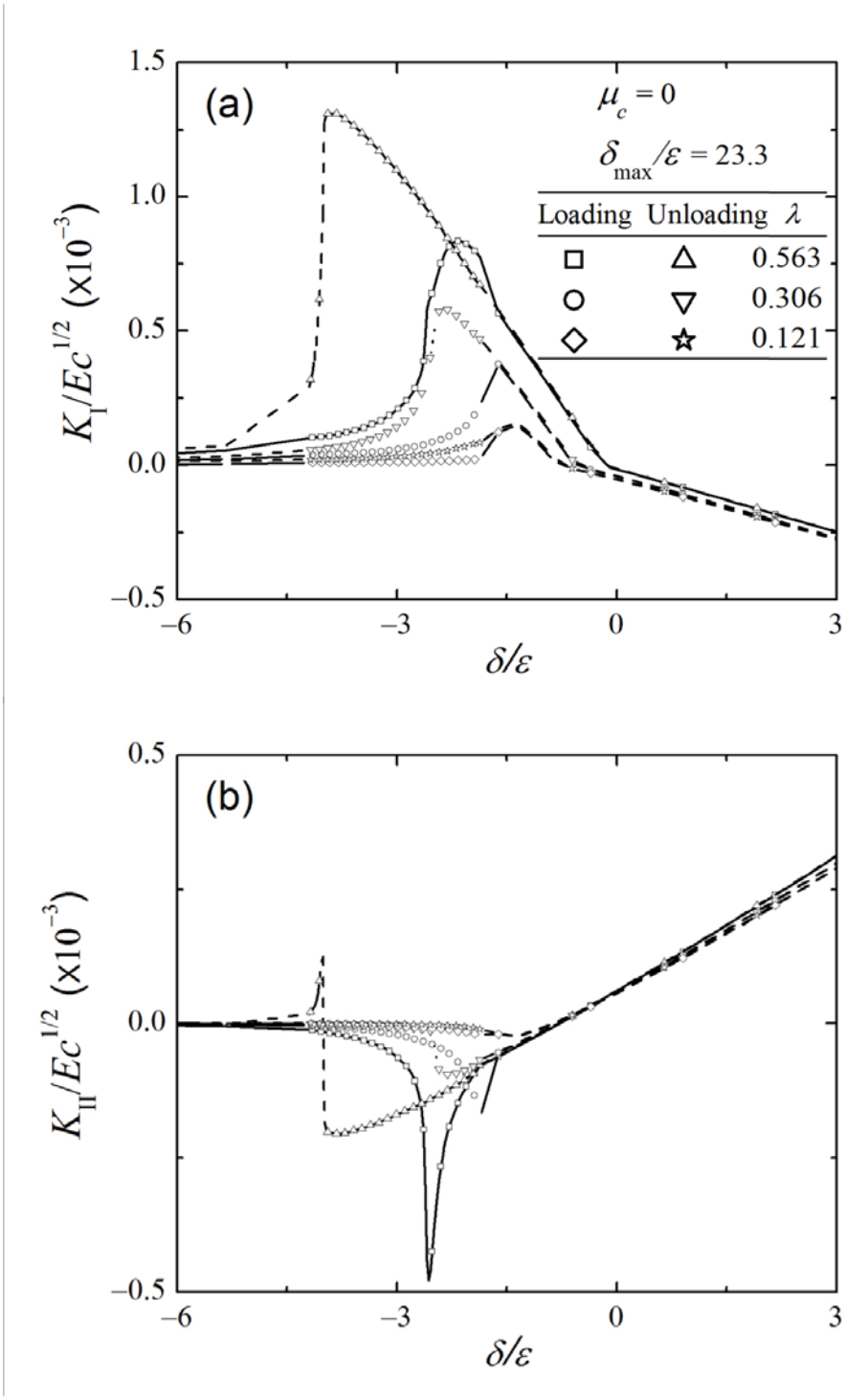

Figure 5.3 (a) Dimensionless K_I and (b) dimensionless K_{II} versus relative indentation displacement of rigid plane δ/ε for $\mu_c = 0$, $\alpha = 36^o$, $\delta_{max}/\varepsilon = 23.3$ and $\lambda = 0.121$, 0.306, and 0.563 under loading and unloading processes.

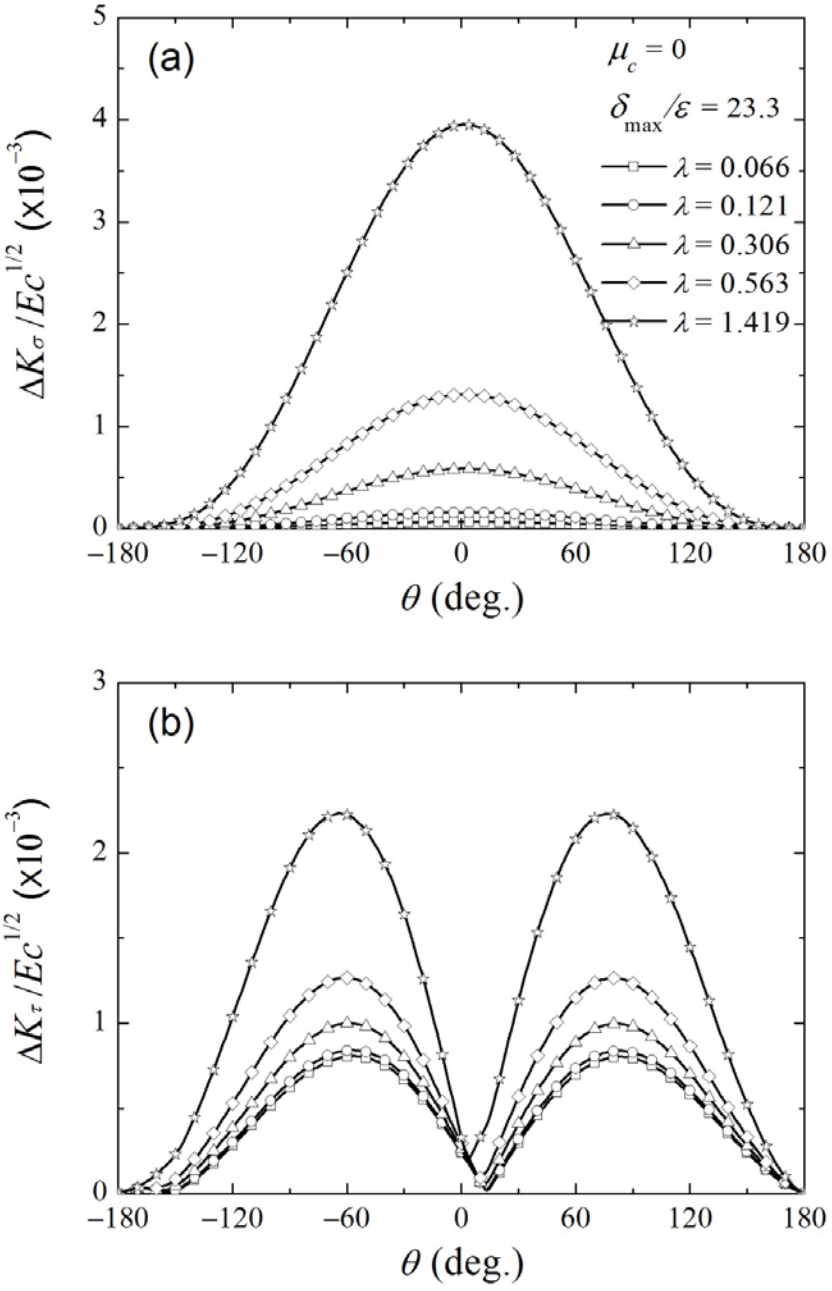

Figure 5.4 (a) Dimensionless ΔK_σ and (b) dimensionless ΔK_τ versus θ for $\mu_c = 0$, $\alpha = 36^o$, $\delta_{max}/\varepsilon = 23.3$ and $\lambda = 0.066$, 0.121, 0.306, 0.563 and 1.419.

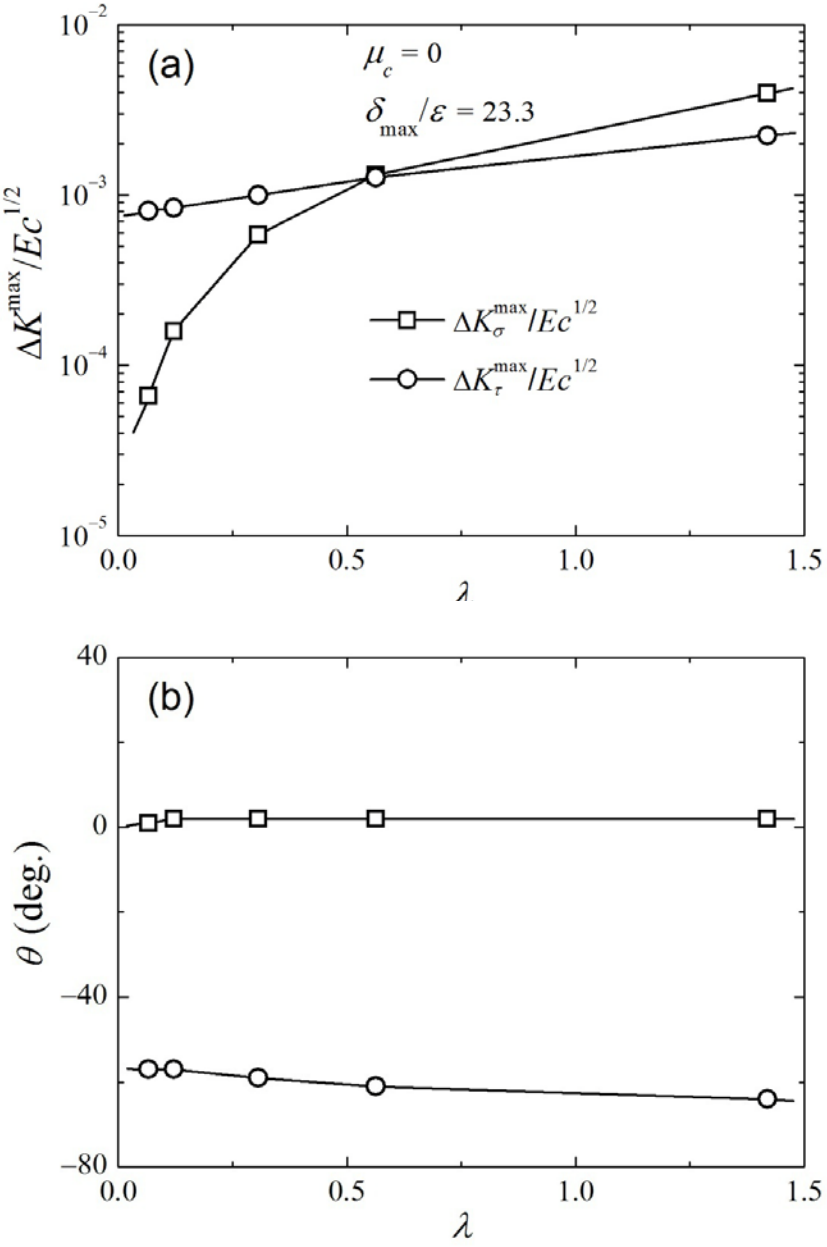

Figure 5.5 Effects of Maugis parameter λ on (a) dimensionless ΔK^{max} and (b) crack growth angle θ for $\mu_c = 0$, $\alpha = 36^o$, $\delta_{max}/\varepsilon = 23.3$.

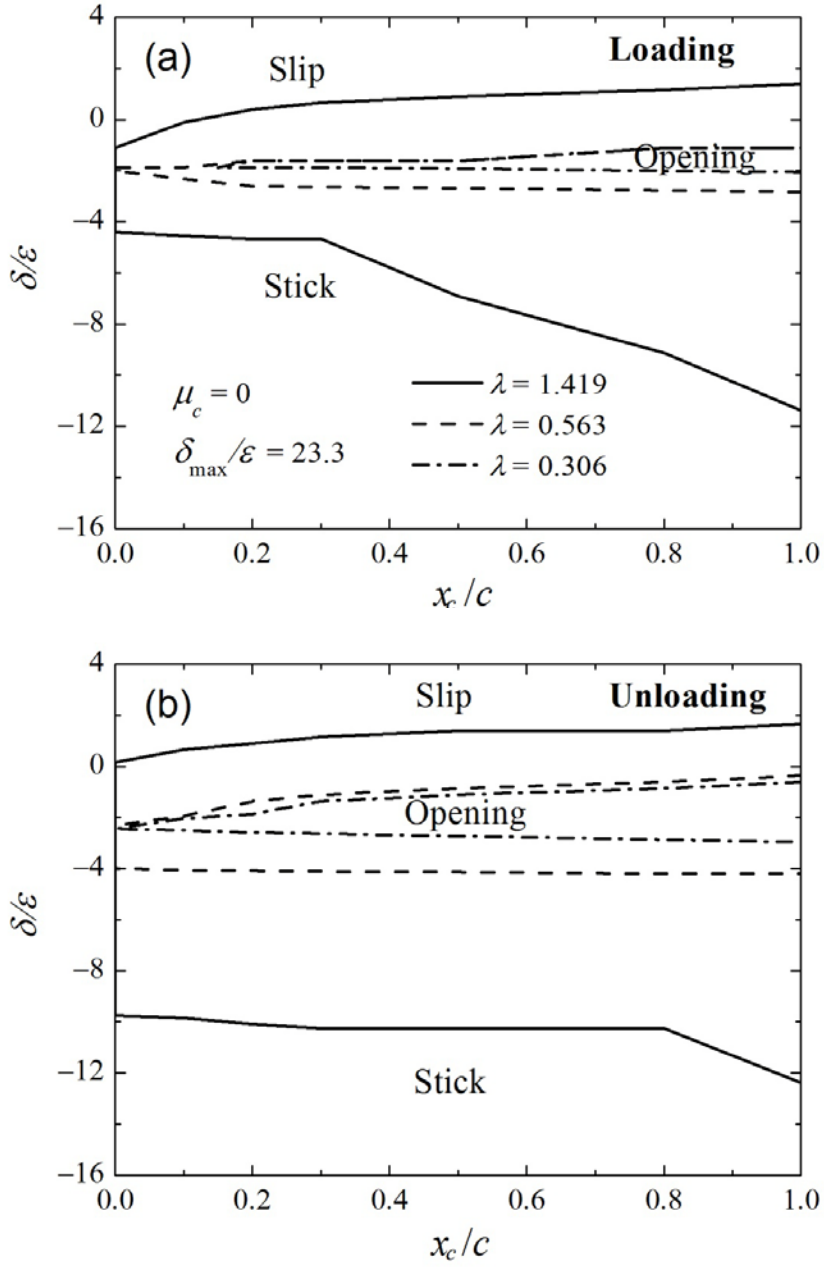

Figure 5.6 Crack mechanisms map as functions of relative indentation displacement of rigid plane δ/ε and relative crack interface position x_c/c at (a) loading process and (b) unloading process for $\mu_c = 0$, $\alpha = 36^o$, $\delta_{max}/\varepsilon = 23.3$ and $\lambda = 0.306$, 0.563 and 1.419 (OP: opening, SL: slip, ST: static).

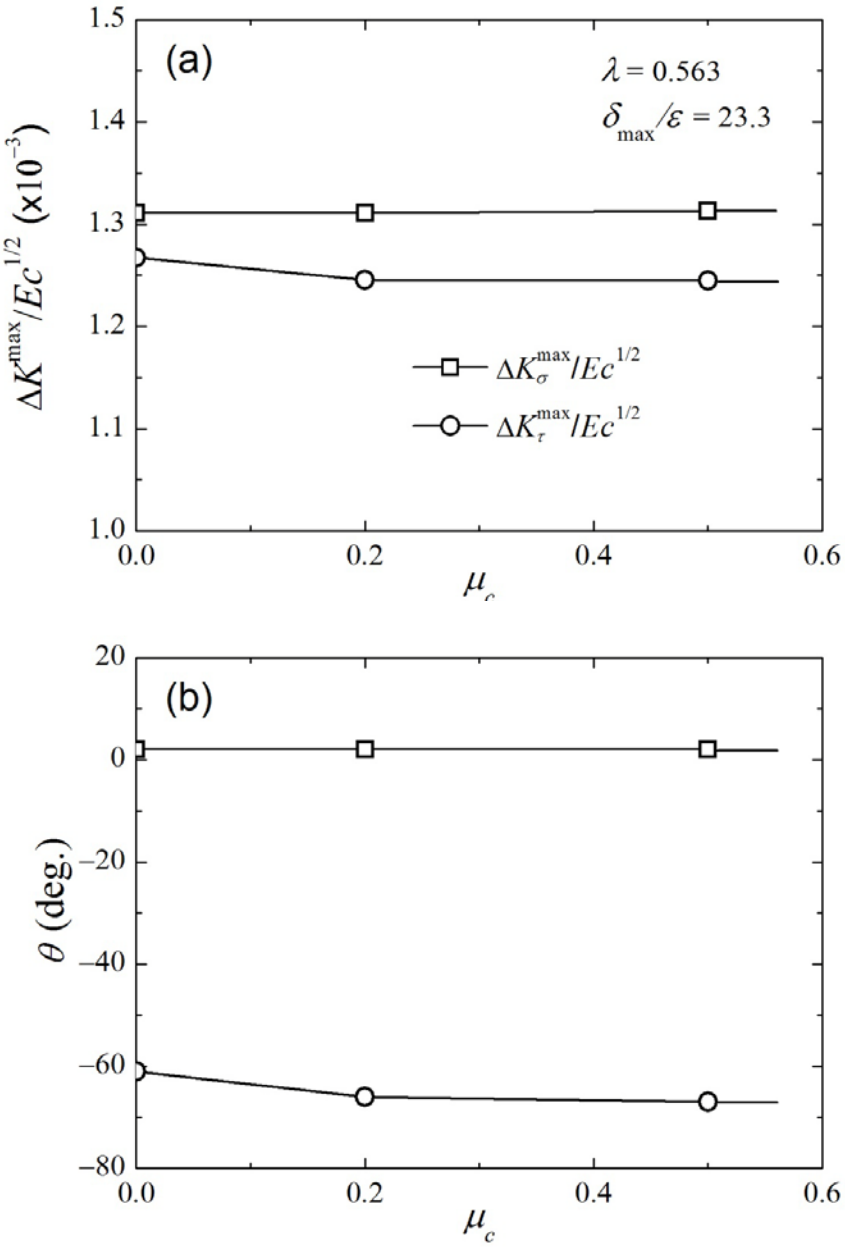

Figure 5.7 Effects of crack-face friction coefficient μ_c on (a) dimensionless ΔK^{max} and (b) crack growth angle θ for $\lambda = 0.563$, $\alpha = 36^o$ and $\delta_{max}/\varepsilon = 23.3$.

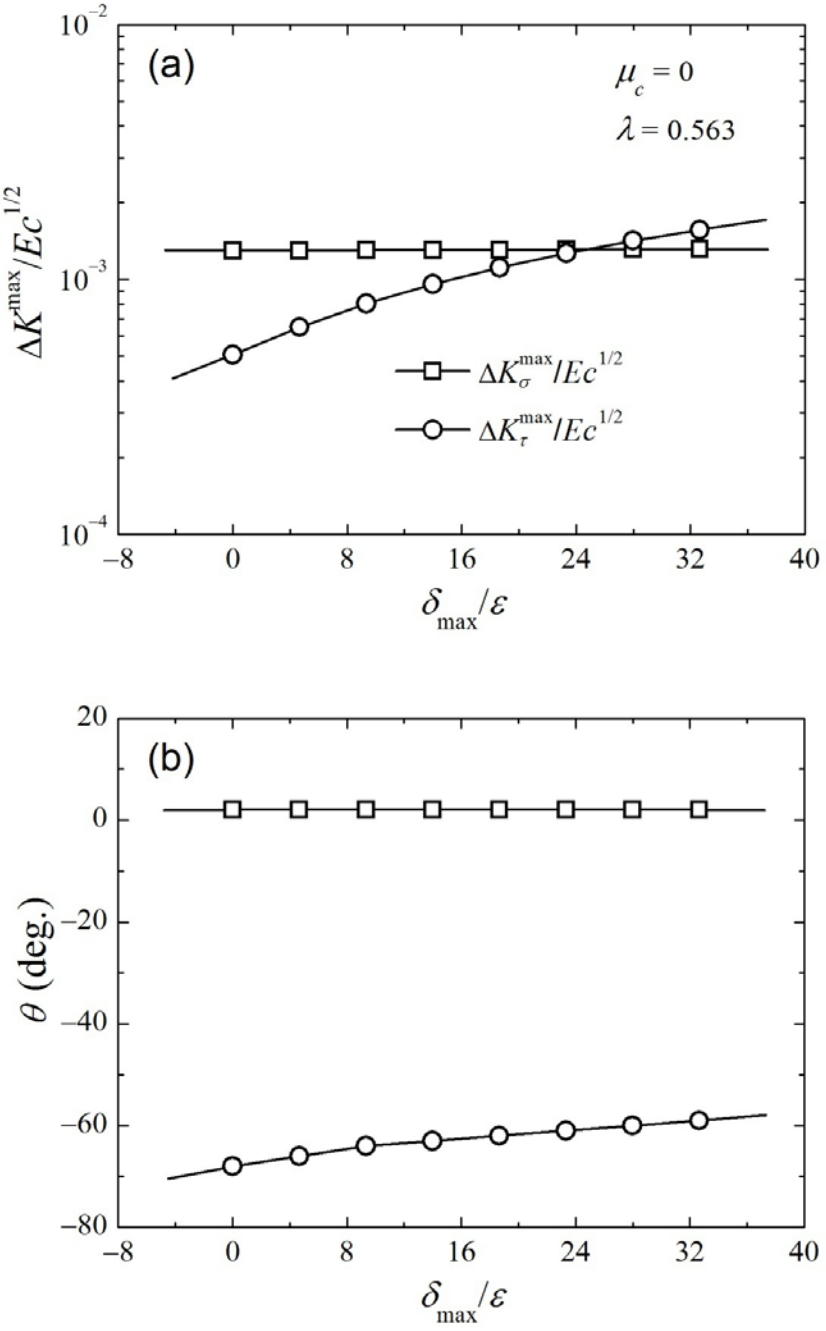

Figure 5.8 Effects of relative maximum indentation displacement of rigid plane δ_{max}/ε on (a) dimensionless ΔK^{max} and (b) crack growth angle θ for $\lambda = 0.563$, $\mu_c = 0$ and $\alpha = 36^o$.

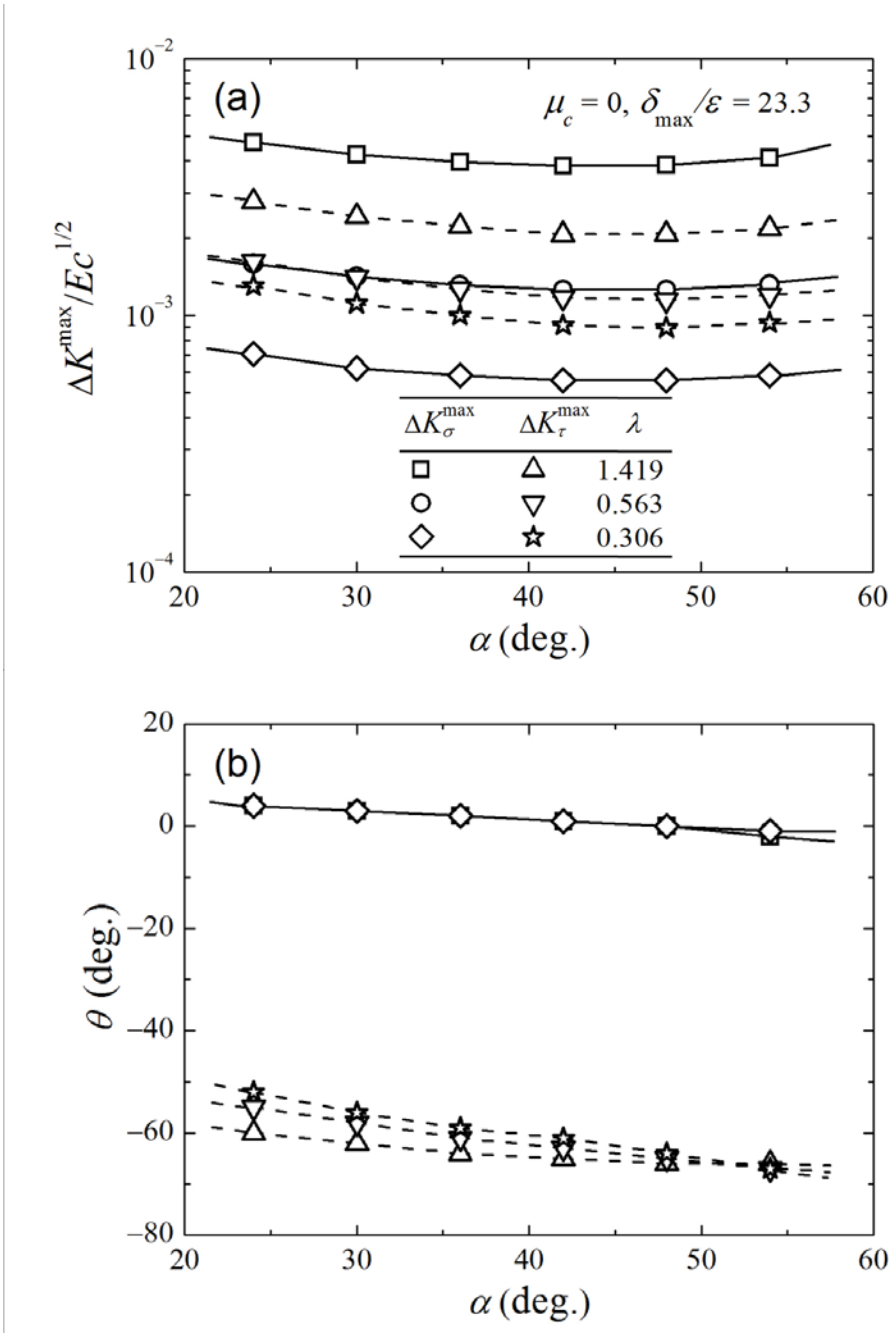

Figure 5.9 Effects of crack position α on (a) dimensionless ΔK^{max} and (b) crack growth angle θ for $\mu_c = 0$, $\delta_{max}/\varepsilon = 23.3$, and $\lambda = 0.306$, 0.563 and 1.419.

Chapter 6
Fracture mechanics analysis of asperity cracking due to repetitive sliding contacts

6.1 Introduction

Wear at contact interfaces due to relative surface movement is a common phenomenon in contact-mode components. Although the failure and collapse caused by wear particles are the dominant reliability issues of most devices with contact components, such as micro-electro-mechanical systems (Tanner, 2000), head-disk interface of hard disk drives (Liu et al., 1996), and bearings, control of wear particle formation was also critical to the fabrication processes to achieve ultra-smooth surfaces, such as traditional polishing, lapping process, and chemical-mechanical polishing (Larsen-Basse and Liang, 1999; Zhao and Chang, 2002), which are sensitive to the size and density of the abrasive particles used for polishing. Therefore, insight into mechanisms of wear particle formation is of great importance in the contact-mode devices and those manufacturing processes where final surface finish is of great dependence on accurate control of material removal.

Wear particle initiated from subsurface cracks or surface cracks which coalesced from plastic deformation and nucleation of voids (Suh, 1973 and 1977; Jahanmir and Suh, 1977), followed by the crack growth under the driving force provided by the stresses due to asperity contact, and was finally formatted once subsurface cracks propagated toward the surface or surface cracks grew back to the surface. The crack propagation direction under mixed mode static loading was predicted fairly accurately by the approaches based on the criteria of maximum tensile stress (Erdogan and Sih, 1963) and strain energy density (Sih, 1974). However, since the crack growth under cyclic load was due to fatigue, the determination of the rate, direction and dominant mode of crack propagation were commonly estimated by the corresponding maximum SIF ranges according to Paris' law (Paris and Erdogan, 1963).

Mageed and Pandey (1992) showed that the crack growth path due to cyclic stresses was not accurately predicted by the criteria of maximum tensile stress and strain energy density criteria, but it was in better agreement with the prediction estimated by the criterion based on stress intensity factor (SIF) ranges ΔK_I and ΔK_{II} with the consideration of the closure effect. K_I and K_{II} represented the mode I and mode II stress intensity factors, respectively. Komvopoulos and Cho (1997) performed a numerical study of subsurface cracking in a homogeneous half-space interacting with a moving asperity and predicted the crack propagation directions rate based on the tensile and shear stress intensity factor ranges, ΔK_σ and ΔK_τ. Gong and Komvopoulos (2005) used similar method to simulate the surface cracking process in a multi-layered media sliding against a rigid asperity. Ko et al. (2001) estimated the crack growth and wear particle formation in sliding contacts numerically based on stress intensity factor ranges and discovered that the predicted particle size and wear volume were in reasonable agreement with their experimental results.

The previous studies were focused on the analytical or experimental estimation of surface or subsurface crack propagation of a flat half-space with repetitive sliding contacts against a rigid asperity. However, microscopy observations (Berry and Lewis, 1980; Majumdar and Tien, 1990) indicated that most engineering surfaces exhibited fractal behavior, which were expressed as a superposition of a series of wavelengths (Yan and Komvopoulos, 1998a). Therefore, the real surface was not theoretically flat and was composed of many small asperities. It was of great importance to look into wear particle formation in the asperity-asperity contacts in addition to the contacts between asperity and flat half-space.

The objective of this chapter was to estimate the wear particle size and the wear rate due to repetitive asperity-asperity sliding contacts, which produced cyclic contact stresses providing the driving force of crack propagation to trigger the formation of wear particle. The wear rate was represented by the crack growth rate and the size of wear particle was estimated by the crack growth direction. The rate and direction of crack growth due to repetitive asperity-asperity sliding contacts were analyzed together with the elucidation of the crack propagation mechanisms based on linear elastic fracture mechanics and finite element method (FEM), in terms of asperity interaction depth, interfacial friction, initial crack position, crack-face friction, and material properties.

6.2 Analysis

6.2.1 State of the problem

The normal and shear tractions caused by the relative motion between two solids are transmitted through the asperity micro-contacts, which trigger the wear particle formation due to asperity failure. The distribution of micro-contacts depends on the surface topographies, normal load and material properties of the interacting solids. Besides, since the wear particle is easier to be generated in a soft solid with higher plastic deformation, the hard solid is more robust and treated as a rigid body. The soft solid is treated as homogenous elastic, because many materials under consideration, such as silicon wafer and ceramics, are brittle, and some ductile materials show purely elastic property after strain hardening to elastic shakedown deformation mode.

Thus, the problem of wear particle formation at interfaces undergoing repetitive sliding contacts is treated as that of a rigid asperity cyclic sliding against a homogenous elastic asperity containing a normal surface crack, as shown by Fig. 6.1. The two asperities have relatively equivalent sizes and the initial surface crack length is much smaller than the asperity size. The present study mainly analyzes the fatigue surface crack propagation in the homogeneous elastic asperity since the wear particle formation in the manufacturing processes or some devices for long term usage was mostly caused by fatigue due to repetitive interactions between solids.

Since the driving force for the fatigue crack growth is the stress intensity factor ranges, which are dependent on the stress fields around the crack tip, the rate and direction of crack growth are estimated based on the stress field around the crack tip by using linear elastic fracture mechanics, in terms of elastic modulus of the homogeneous elastic asperity E, crack position (defined by the crack angle α or initial crack edge position d_c), asperity interaction depth d_s (vertical distance of rigid asperity bottom point to top point of un-deformed elastic asperity, as shown by Fig. 6.1) and interfacial friction μ (i.e., sliding friction between the two asperities), and

crack-face friction μ_c. The crack mechanisms are also analyzed based on previous parameters. Three crack positions are modeled for comparison at α equal to 36^o, 42^o and 48^o while the relative interaction depth d_s/d_c varies from 0 to 1.5. The interfacial friction coefficient μ varies from 0 to 0.3 and the crack-face friction coefficient μ_c varies from 0 to 0.5. Each cycle of repetitive sliding contacts starts from the initial contact between two asperities and ends at the final detachment of two asperities with constant interaction depth d_s. Figure 6.1 shows the initial contact between two asperities and the rigid asperity moves from right to left. For each cycle of sliding, the relative position of rigid asperity x_s/x_l varies from −1 to 1. x_s was the rigid asperity position according to the Cartesian coordinate (x_s, y_s) and x_l is half of the sliding distance of the rigid asperity for each sliding cycle at a given interaction depth, as shown by Fig. 6.1.

6.2.2 Finite element model

In this chapter, finite element method was used to calculate the stress field caused by the sliding contact between two asperities. Fig. 6.2(a) shows a finite element mesh of an elastic half-space with an asperity interacting against a rigid asperity with equal radius *R*. The elastic asperity has a normal surface crack with length $c = 0.04R$. The width and height of the half space are $40R$ and $20R$, respectively. The mesh for $\alpha = 36^o$ consists of 4550 isoparametric, eight-node, quadrilateral, plane-strain elements having a total of 14150 nodes. The meshes for $\alpha = 42^o$ and 48^o are similar as that of $\alpha = 36^o$. The mesh around the crack is refined in order to obtain more accurate results for the stress distribution around the crack, as shown by Fig. 6.2(b). The mesh at the crack tip consists of 30 isoparametric, eight-node, collapsed quadrilateral, plane-strain elements with their mid-side nodes displaced to the quarter-point distance to simulate the square root singularity of the crack-tip stress field and their crack-tip nodes constrained to move together in order to prevent crack-tip blunting.

The simulations were performed with the FEM code ABAQUS (version 6.7-1). The nodes at the bottom boundary of the mesh were constrained in the vertical and horizontal directions. To prevent the overlapping on the two opposite crack faces and to allow the transmission of the contact forces, a self-contact was set up for the entire crack face with a hard overclosure (i.e., no displacement of a nodal point of a surface into another contact surface).

6.3 Results and discussion

6.3.1 Stress intensity factors

In linear elastic fracture mechanics, the driving force for fatigue crack growth is the maximum stress intensity factor range, ΔK^{max}, which is determined by the mode I and mode II stress intensity factors (SIFs), K_I and K_{II}, respectively, defined as

$$K_I = \lim_{r\to 0} \sqrt{2\pi r}\, \tau_{y'y'}(r, \theta = 0), \tag{6.1a}$$

and

$$K_{II} = \lim_{r\to 0} \sqrt{2\pi r}\, \tau_{x'y'}(r, \theta = 0), \tag{6.1b}$$

where (r, θ) and (x', y') are polar and Cartesian coordinates centered at the crack tip, respectively, as shown by Fig. 6.1. $\theta = 0$ at the crack plane and θ becomes positive at counter-clockwise direction. K_I and K_{II} are obtained from the stresses at nine nodes adjacent to the crack tip and along the crack plane ($\theta = 0$) using linear extrapolation of a least-square line fit through the SIF data (Chan et al., 1970). The SIF data are normalized by the parameter $Ec^{1/2}(\cos\alpha)^{1/2}(d_c/r')$ taking into consideration the material properties and the length and initial position of crack. As shown by Fig. 6.1, r' is defined as the horizontal distance between the initial crack and the center of the asperity.

Figures 6.3 show the variations of K_I and K_{II} as functions of relative rigid asperity position x_s/x_l for d_s/d_c = 0.75, μ_c = 0 and μ = 0, 0.15 and 0.3, respectively. As the interfacial friction coefficient μ is zero, the crack tip is closed and compressed, and K_I is negative during the entire sliding cycle without physical representation and K_{II} reaches the maximum value at x_s/x_l = 0, where the compressive force applied on asperity is maximum. With the increase of μ, K_I becomes positive due to the enhancement of the surface shear traction and the value of x_s/x_l with maximum K_I is closer to zero whereas the value of x_s/x_l with maximum K_{II} is further away from zero. Both K_I and K_{II} increase with the interfacial friction coefficient μ, attributed by the higher stresses arising at the crack tip due to the enhancement of the surface shear traction. However, the increase of K_I with higher interfacial friction is more significant than that of K_{II}, with the indication of the enhancement of propensity of tensile mode crack growth for higher interfacial friction.

6.3.2 Crack propagation direction and crack growth rate

Since the stresses in the crack tip are subjected to K_I and K_{II}, which depend on the rigid asperity position, therefore, for a given plane with angle θ (shown by Fig. 6.1) and a given rigid asperity position x_s, the tensile and shear SIFs, represented by K_σ and K_τ, respectively, are given by

$$\mathrm{K}_\sigma(\theta, \mathrm{x_s}) = \sigma_{\theta\theta}\sqrt{2\pi \mathrm{r}} = \cos\frac{\theta}{2}\left[\mathrm{K_I}\cos^2\frac{\theta}{2} - \frac{3}{2}\mathrm{K_{II}}\sin\theta\right], \tag{6.2a}$$

and

$$\mathrm{K}_\tau(\theta, \mathrm{x_s}) = \tau_{\mathrm{r}\theta}\sqrt{2\pi \mathrm{r}} = \frac{1}{2}\cos\frac{\theta}{2}[\mathrm{K_I}\sin\theta + \mathrm{K_{II}}(3\cos\theta - 1)]. \tag{6.2b}$$

For a given plane with $\theta = \theta^*$, the tensile and shear SIF ranges ΔK_σ and ΔK_τ for a sliding cycle with x_s/x_l varying from –1 to 1, are expressed as

$$\Delta\mathrm{K}_\sigma(\theta = \theta^*) = \mathrm{K}_{\sigma,\max}(\theta = \theta^*, \mathrm{x_s}) - \max\left[\mathrm{K}_{\sigma,\min}(\theta = \theta^*, \mathrm{x_s}), 0\right], \tag{6.3a}$$

and

$$\Delta\mathrm{K}_\tau(\theta = \theta^*) = \mathrm{K}_{\tau,\max}(\theta = \theta^*, \mathrm{x_s}) - \mathrm{K}_{\tau,\min}(\theta = \theta^*, \mathrm{x_s}). \tag{6.3b}$$

The closure effect is taken into consideration to calculate the tensile SIF range ΔK_σ which does not account for the part of $K_\sigma < 0$. Figures 6.4 show the dependence of ΔK_σ and ΔK_τ on θ for $d_s/d_c = 0.75$, $\mu_c = 0$ and $\mu = 0$, 0.15 and 0.3, respectively. For frictionless interface, the fact that ΔK_σ is almost equal to zero indicates the small propensity of tensile mode fatigue crack growth. The increase of interfacial friction enlarges both of the tensile and shear SIF ranges, ΔK_σ and ΔK_τ, and the increment of ΔK_σ is larger than that of ΔK_τ due to higher surface traction. This fact indicates the propensity of tensile mode fatigue crack growth is enhanced for higher interfacial friction. The maximum value of ΔK_σ occurs at θ close to 0^o, which is the angle for mode I crack propagation. There are two maximum and equivalent values of ΔK_τ occurring at θ around -70.4^o and 70.4^o, which are the angles for mode II crack propagation. The values of θ corresponding to maximum values of ΔK_σ or ΔK_τ are slightly affected by the interfacial friction.

The crack growth direction for tensile or shear dominant mode of fatigue crack growth is determined under the assumption that tensile mode crack propagation occurs in the plane with maximum tensile SIF range, ΔK_σ^{max}, whereas shear mode crack propagation commences at the plane with maximum shear SIF range, ΔK_τ^{max} (Cho and Komvopoulos, 1997a and 1997b; Gong and Komvopoulos, 2005; Komvopoulos and Cho, 1997). The magnitudes of ΔK_σ^{max} and ΔK_τ^{max} are calculated by

$$\Delta K_\sigma^{max} = \max[\Delta K_\sigma(\theta)] \ \ (-180^\circ \le \theta \le 180^\circ), \tag{6.4a}$$

and

$$\Delta K_\tau^{max} = \max[\Delta K_\tau(\theta)] \ \ (-180^\circ \le \theta \le 180^\circ). \tag{6.4b}$$

The dominant mode of crack growth depends on the magnitudes of ΔK_σ^{max} and ΔK_τ^{max}. The crack growth is dominated by tensile mode as $\Delta K_\sigma^{max} > \Delta K_\tau^{max}$, whereas the crack growth is dominated by shear mode as $\Delta K_\tau^{max} > \Delta K_\sigma^{max}$. The maximum SIF range ΔK^{max} is the higher value of ΔK_σ^{max} and ΔK_τ^{max}. The crack propagation angle θ is the angle of the plane with the maximum SIF range ΔK^{max}.

The crack growth rate due to cyclic loading depends on ΔK^{max} (Paris and Erdogan, 1963), and is expressed as

$$\frac{dc}{dN} = A(\Delta K^{max})^n, \tag{6.5}$$

where A and n are material constants and N was the number of loading cycles.

The wear particle size due to sliding contact between asperities significantly depends on the crack propagation angle θ. As shown by Fig. 6.1, as θ is larger, the crack goes downward to achieve a larger wear particle size. The wear rate is affected by both crack growth rate and crack propagation angle. Usually, larger crack growth rate due to higher maximum SIF range ΔK^{max} contributes to higher wear rate. Therefore, this study mainly analyzes maximum SIF range ΔK^{max} and crack propagation angle θ under the effects of the aforementioned parameters in consideration. Besides, in all the following figures related to ΔK^{max} and θ, dashed lines indicate

tensile mode-dominated crack growth, whereas solid lines represent shear mode-dominated crack growth.

Figures 6.5 show the effects of initial crack position α and relative interaction depth d_s/d_c on the dimensionless maximum SIF range, $\Delta K^{max}/ Ec^{1/2}(\cos\alpha)^{1/2}(d_c/r')$, and the crack propagation angle θ at $\mu_c = 0$ and $\mu = 0$. The value of $\Delta K_\sigma^{\max}$ is less than that of $\Delta K_\tau^{\max}$ due to high interfacial compression instead of shear traction at $\mu = 0$ and $\mu_c = 0$, so the crack growth is dominated by the shear mode indicated by the solid lines for the curves of Figs. 6.5. Besides, the curves of normalized $\Delta K^{\max}$ and θ as functions of relative interaction depth d_s/d_c almost overlap for three different crack positions ($\alpha = 36^o$, 42^o and 48^o).

As shown by Figs. 6.5, dimensionless $\Delta K^{\max}$ increases with the relative interaction depth d_s/d_c. This is because of the enhancement of the stress field around the crack tip due to the higher interference between asperities with increasing d_s/d_c. As $d_s/d_c < 1$, the crack propagation angle θ slightly increases with d_s/d_c. However, the value of θ jumps from around -60^o to about 0^o as $d_s/d_c > 1$. This indicates a significant increase of wear particle size due to the enormous enlargement of the crack growth angle once the rigid asperity sliding against the deformable asperity below the initial crack compared with the case above the initial crack at $\mu = 0$ and $\mu_c = 0$.

Figures 6.6 illustrate the effects of initial crack position α and relative interaction depth d_s/d_c on the dimensionless $\Delta K^{\max}$ and θ at $\mu_c = 0$ and $\mu = 0.30$. At $\mu = 0.30$ and $\mu_c = 0$, the shear maximum SIF range $\Delta K_\tau^{\max}$ is smaller than the tensile maximum SIF range $\Delta K_\sigma^{\max}$ and the crack growth is dominated by the tensile mode (dashed line in Figs. 6.6). The value of θ is independent on the value of d_s/d_c and is close to 0^o, which is the mode I crack growth angle. Similar as frictionless condition, dimensionless $\Delta K^{\max}$ also increases with the relative interaction depth d_s/d_c at $\mu = 0.30$. Besides, the curves of normalized $\Delta K^{\max}$ and θ as functions of d_s/d_c also overlap for three different crack positions ($\alpha = 36^o$, 42^o and 48^o). Therefore, based on results from Figs. 6.5 and 6.6, the dependences of dimensionless $\Delta K^{\max}$ and θ on d_s/d_c are independent on crack position due to suitable selection of normalization parameters. Thus, only the case for $\alpha = 36^o$ is discussed later to study the effects of crack-face friction and interfacial friction since it can represent other cases with different crack positions.

Figures 6.7 illustrate the effect of crack-face friction μ_c on the dimensionless $\Delta K^{\max}$ and θ at $\mu = 0$. The shear mode crack growth is dominated at $\mu = 0$ since the tensile maximum SIF range $\Delta K_\sigma^{\max}$ is smaller than the shear maximum SIF range $\Delta K_\tau^{\max}$. The effect of crack-face friction coefficient μ_c on the dimensionless $\Delta K^{\max}$ is secondary and the increase of μ_c slightly reduces the amplitude of the dimensionless $\Delta K^{\max}$ since the crack-face friction prevents the slip movement of crack. As the position of rigid asperity is above the crack, the increase of μ_c slightly reduces the value of θ, except for the big difference as μ_c varies from 0 to 0.05. As the position of rigid asperity below the crack, the value of θ decreases with the increase of μ_c. Therefore, the variation of crack-face friction modifies the stress field around the crack tip slightly due to the introduction of the crack-face shear stress and achieves differences in crack growth direction and crack growth rate, but the effect of crack-face friction is negligible compared with that of interaction depth.

Figures 6.8 show the dependences of dimensionless ΔK^{max} and θ on the interfacial friction coefficient μ at $\mu_c = 0$. As mentioned in previous, dashed lines indicate tensile mode-dominated crack growth, whereas solid lines represent shear mode-dominated crack growth. As μ is in the range of 0.10–0.15, a transition from shear to tensile mode-dominated crack growth occurs with the increase of d_s/d_c. The shear mode crack growth is dominated as μ <0.10 whereas the tensile mode crack growth is dominant as μ >0.15. Therefore, the increases of interfacial friction or relative interaction depth d_s/d_c enhance the propensity of tensile mode-dominated crack growth due to the enhancement of tensile stress field around crack tip caused by the increment of surface shear traction on asperity sliding contact.

Since the increase of μ enhances the tensile stress fields around crack tip and consequently enlarges the value of ΔK_σ^{max}, the dimensionless ΔK^{max} increases with μ if the tensile mode crack growth was dominant. However, the dimensionless ΔK^{max} decreases with the increase of μ if the shear mode crack growth was dominant because the increase of μ somehow reduces the shear stress field around crack tip thereafter decreases the magnitude of ΔK_τ^{max} especially at the range of low μ.

The crack propagation angle θ increases with μ as the rigid asperity above the initial crack and this trend is independent on the dominant mode of crack growth. The value of θ varies from -60^o (close to mode II crack propagation angle) to ~ 0^o (mode I crack propagation angle) with the increase of μ, and this variation also reflects the transition of dominated mode of crack growth from shear mode to tensile mode. The value of θ also increases with the increase of d_s/d_c and it has an upper limit value if the tensile mode crack growth is dominated. Especially as μ is high enough, such as μ = 0.3, the value of θ is independent on d_s/d_c and is equal to the upper limit, which is about 0^o.

Figures 6.9 compare the effects of sliding interfacial friction coefficient μ, crack-face friction coefficient μ_c and relative asperity interaction depth d_s/d_c on dimensionless ΔK^{max} and θ. Since the increase of μ enlarges the tensile stress field around the crack tip, and consequently increases the value of ΔK_σ^{max} but reduces the value of ΔK_τ^{max}. Besides, the increase of μ increases the crack propagation angle θ for both tensile and shear dominated modes of crack growth. The increase of d_s/d_c enhances stress fields around crack tip, therefore, it enlarges the values of ΔK^{max} and θ in both shear and tensile dominated modes crack growth. The increase of μ_c enlarges the resistance for the relative movement (slipping) between crack faces, so it reduces the magnitude of ΔK^{max} and θ at shear mode dominated crack growth. However, the effect of μ_c is negligible for tensile-mode dominated crack growth because the crack is open.

Figure 6.10 shows the effects of sliding interfacial friction coefficient μ and relative asperity interaction depth d_s/d_c on the dominant mode of crack growth for μ_c = 0 and 0.5. The transition from shear to tensile mode dominant crack growth is enhanced by the increase of μ and d_s/d_c, while the effect of μ_c is negligible with the evidence of two overlapped curves for different values of μ_c. Besides, when the value of μ is large enough, e.g., larger than 0.20, the crack growth is dominated by the tensile mode and independent on the value of d_s/d_c.

6.3.3 Crack mechanisms

The occurrence of opening, slip, and stick crack mechanisms during sliding of the rigid asperity against the elastic asperity are closely related to the dominant mode of crack growth. To further elucidate the crack behavior, crack mechanisms are studied for various asperity interaction depths, interfacial friction coefficients, and crack-face friction coefficients.

Figures 6.11 illustrate crack mechanism maps showing the effect of μ_c on the regions of the crack exhibiting opening, stick, and slip mechanisms for $\mu = 0$ and $d_s/d_c = 1.50$. The vertical axis of the maps indicates the relative value of the rigid asperity position relative to the stationary elastic asperity ($x_s/x_l = -1$ denotes the initial position and $x_s/x_l = 1$ denotes the ending position) and the horizontal axis indicates the crack interface ($x_c/c = 0$ denotes the crack tip and $x_c/c = 1$ denotes the crack mouth). A comparison of Figs. 6.11 (a)-(c) shows that crack-face friction promotes the stick mechanism between crack faces and causes the slip mechanism to disappear, and the effect of crack-face friction on opening mechanism is secondary. Since the opening region reveals the propensity of tensile mode dominated crack growth while the slipping and stick regions reflects the propensity of shear mode dominated crack growth, the effect of μ_c on crack growth dominant mode is secondary because of the constant opening region upon different values of μ_c. However, since the stiction between crack faces reduces the rate of shear mode dominated crack growth, the increase of μ_c decreases the $\Delta K^{\max}$ due to the promotion of stick mechanism as the crack growth dominated by shear mode.

Figure 6.12 shows the crack mechanism map revealing the effect of d_s/d_c on the regions of the crack exhibiting opening and slip mechanisms for $\mu_c = 0$ and $\mu = 0.10$. For $\mu = 0.10$, the opening region increases with d_s/d_c, suggesting a higher propensity of tensile mode dominated crack growth. At $d_s/d_c = 0.25$, the fact that the crack tip is closed and slipping during the entire sliding cycle, indicates that the crack growth is dominated by shear mode as shown by Figs. 6.8. At $d_s/d_c = 0.50$, the crack tip is open at the beginning of the sliding cycle but the dominant mode of crack growth is still shear mode since the opening region is not large enough during the entire sliding cycle; whereas the crack growth at $d_s/d_c = 0.75$ is dominated by tensile mode due to large opening region. Therefore, the dominant mode of crack growth is revealed by the competition between the opening region and the slip or stick regions in crack mechanism map.

Figure 6.13 illustrates the crack mechanism map revealing the effect of interfacial friction on the regions of the crack exhibiting opening and slip mechanisms for $\mu_c = 0$ and $d_s/d_c = 0.75$. The enlargement of the opening regions with the increase of μ indicates the enhancement of the propensity for crack growth predominantly by the tensile mode, which is verified by the transition from shear to tensile mode dominant crack growth shown by Figs. 6.8.

The opening region on crack mechanism map not only represents the propensity of tensile mode dominant crack growth but also indicates the variation of the crack propagation angle. At $d_s/d_c = 0.75$, the increase of μ enlarges the crack propagation angle (Fig. 6.8 (b)) with the increment of opening region. At $\mu = 0.10$, the increase of d_s/d_c also increases the crack propagation angle (Fig. 6.8 (b)) together with the increment of opening region. Besides, the fact that the opening region is almost constant and independent on the value of d_s/d_c at $\mu = 0.30$ is verified by the constant crack propagation angle shown by Fig. 6.8 (b).

6.4 Conclusions

In this chapter, a linear elastic fracture mechanics analysis of asperity cracking due to sliding contact was performed to examine the effects of the initial crack position, crack-face friction, asperity interaction depth, and interfacial friction on the direction and rate of crack growth, represented by the crack propagation angle and SIFs, respectively. Based on the presented results and discussion, the following main conclusions can be drawn from this chapter.

1. FEM results show that the effects of asperity interaction depth and interfacial friction coefficient are more significant than that of the crack-face friction. The effects of the initial crack position and the crack-face friction on the dimensionless ΔK^{max} and θ are secondary.

2. The dimensionless ΔK^{max} and θ increase with the relative asperity interaction depth d_s/d_c. The value of θ reaches an upper limit at the tensile mode dominated crack growth as the value of d_s/d_c is large enough.

3. With the increase of μ, the dimensionless ΔK^{max} decreases at the shear mode dominated crack growth whereas the dimensionless ΔK^{max} increases at the tensile mode dominated crack growth. The crack propagation angle θ increases with μ until it reaches an upper limit.

4. The transition from shear to tensile mode of crack growth is enhanced by the increase of μ and d_s/d_c, whereas the effect of μ_c is negligible.

5. Crack mechanisms are studied for various asperity interaction depths, interfacial friction coefficients, and crack-face friction coefficients to elucidate the crack behavior especially the crack growth mode. The propensity for crack growth predominantly by the tensile mode increases with the increases of d_s/d_c and μ, as indicated by the enlargement of the opening regions. The effect of μ_c on the crack growth mode is secondary, as revealed by the constant opening region. Besides, the increase of crack propagation angle for tensile mode dominant crack growth corresponds to the enlargement of opening region.

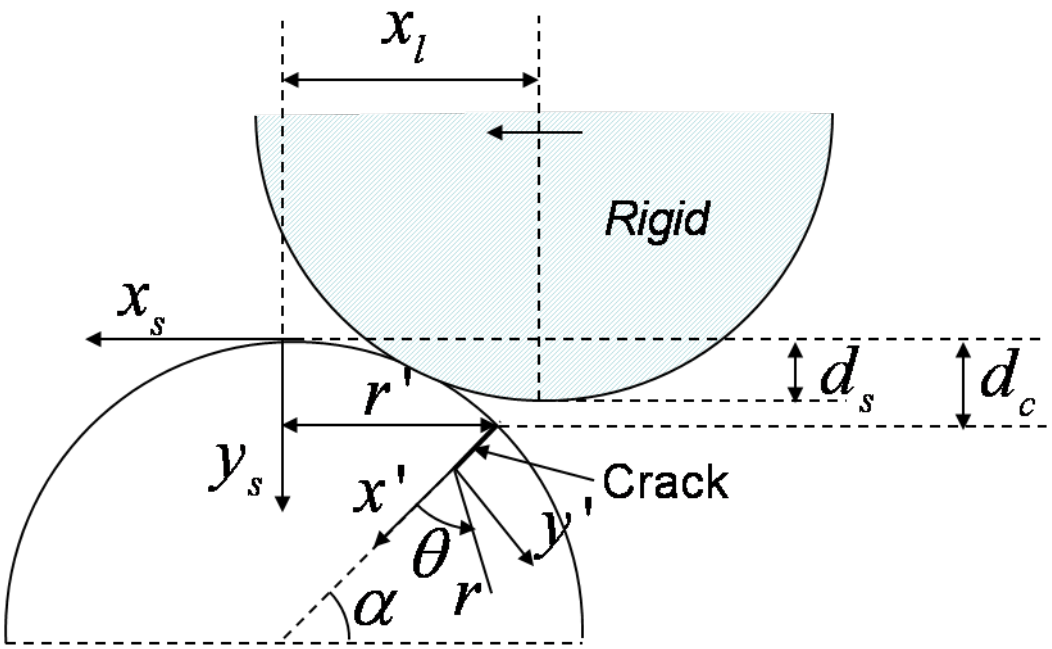

Figure 6.1 Schematic of a rigid cylindrical asperity sliding against a deformable cylindrical asperity including an initial normal surface crack with pertinent nomenclature.

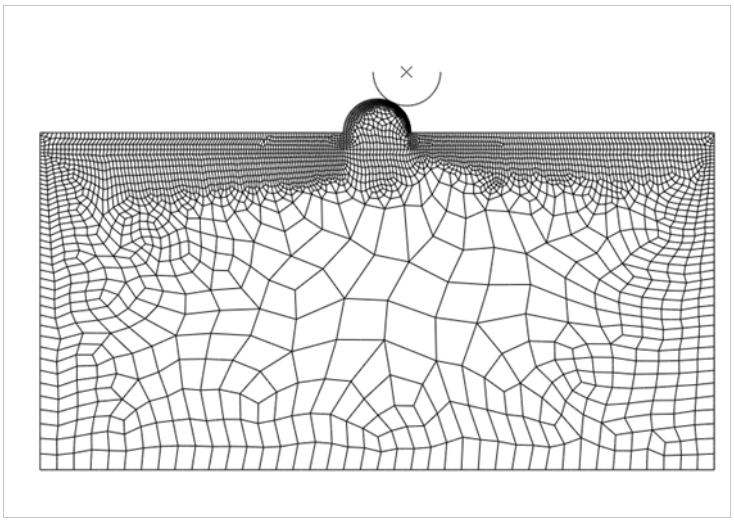

(a)

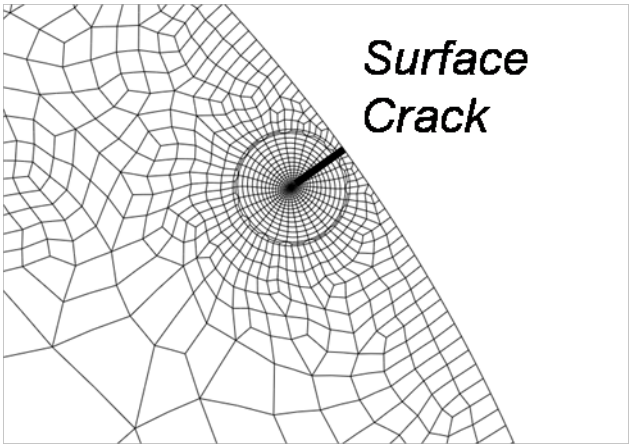

(b)

Figure 6.2 (a) Finite element mesh for a rigid asperity sliding against another deformable asperity on substrate and (b) refined finite element mesh around the surface crack.

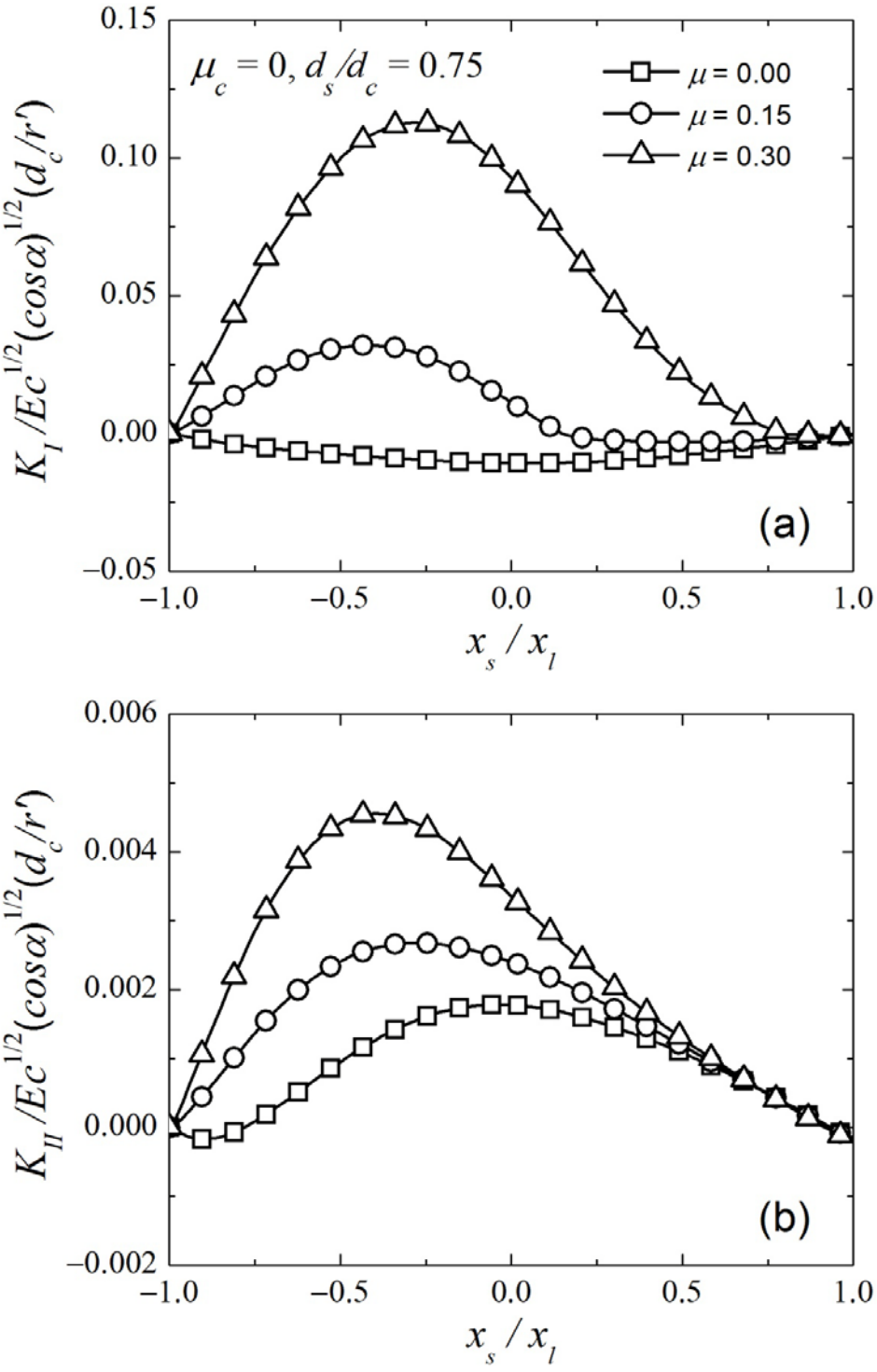

Figure 6.3 (a) Dimensionless K_I and (b) dimensionless K_{II} versus relative sliding distance x_s/x_l for $d_s/d_c = 0.75$, $\mu_c = 0$ and $\mu = 0$, 0.15 and 0.3.

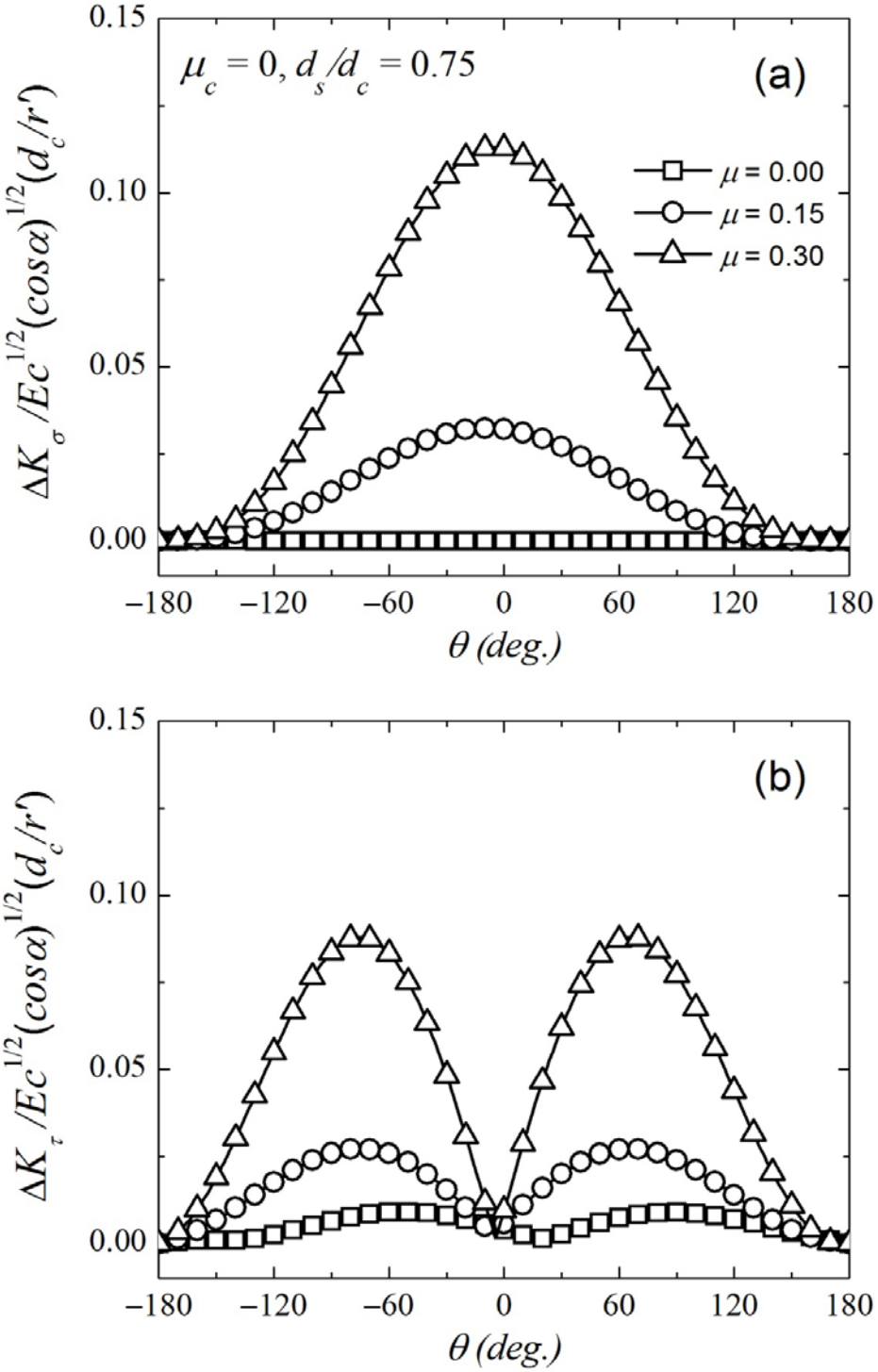

Figure 6.4 (a) Dimensionless ΔK_σ and (b) dimensionless ΔK_τ versus θ for d_s/d_c = 0.75, μ_c = 0 and μ = 0, 0.15 and 0.3.

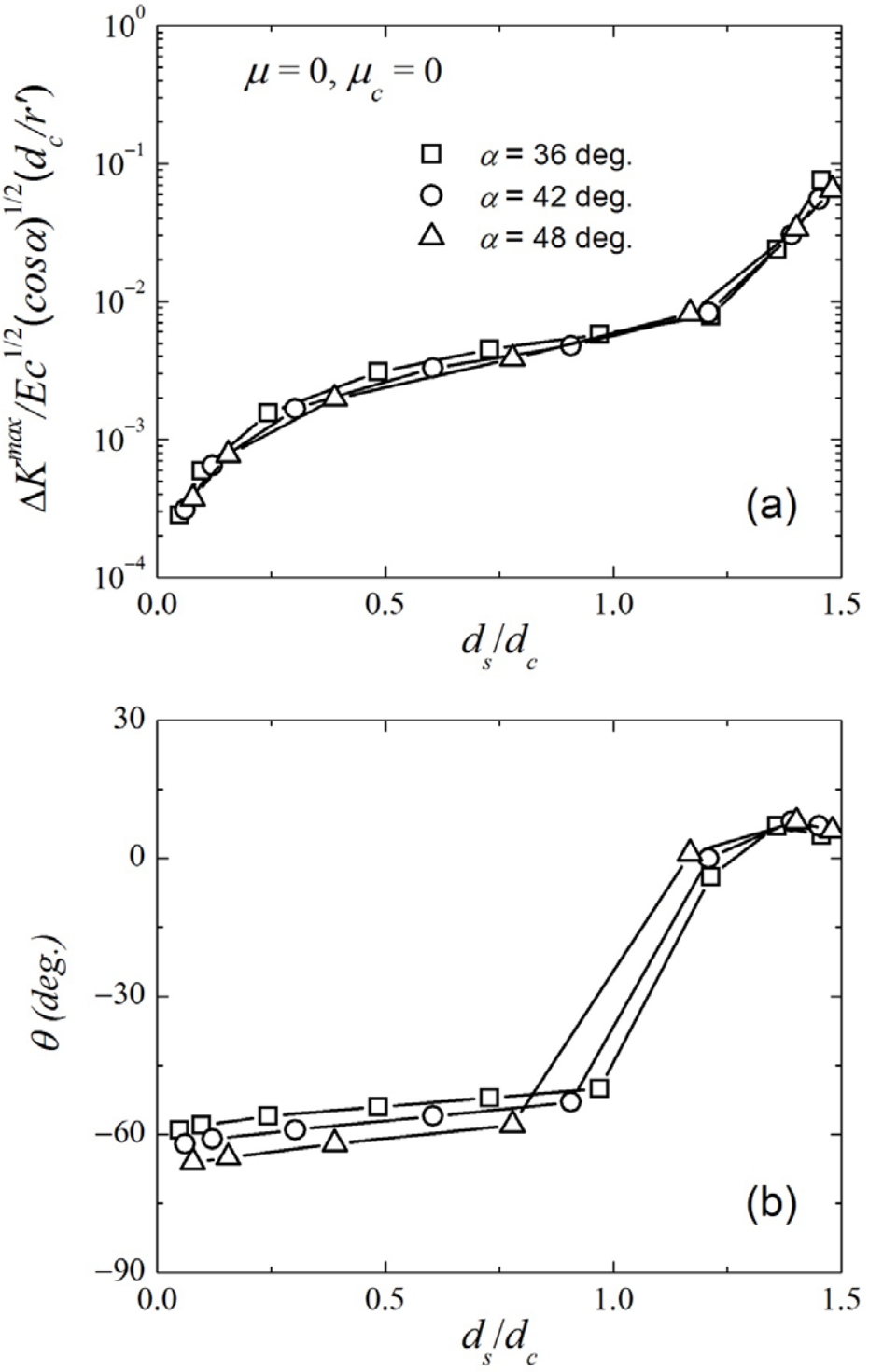

Figure 6.5 (a) Dimensionless ΔK^{max} and (b) crack growth angle θ for μ = 0, μ_c = 0 and α = 36°, 42° and 48°.

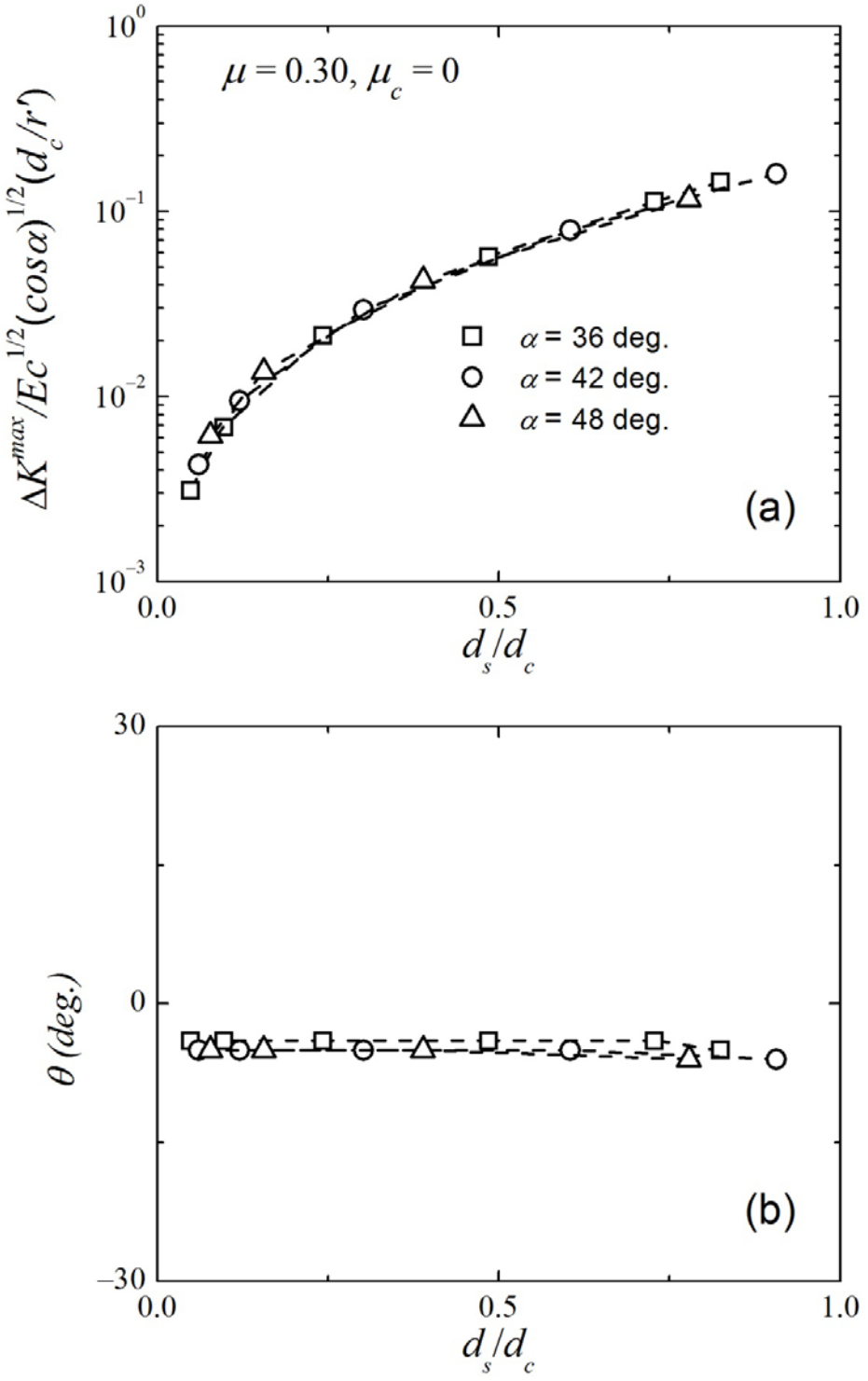

Figure 6.6 (a) Dimensionless ΔK^{max} and (b) crack growth angle θ versus relative interaction depth d_s/d_c for $\mu = 0.30$, $\mu_c = 0$ and $\alpha = 36^o$, 42^o and 48^o.

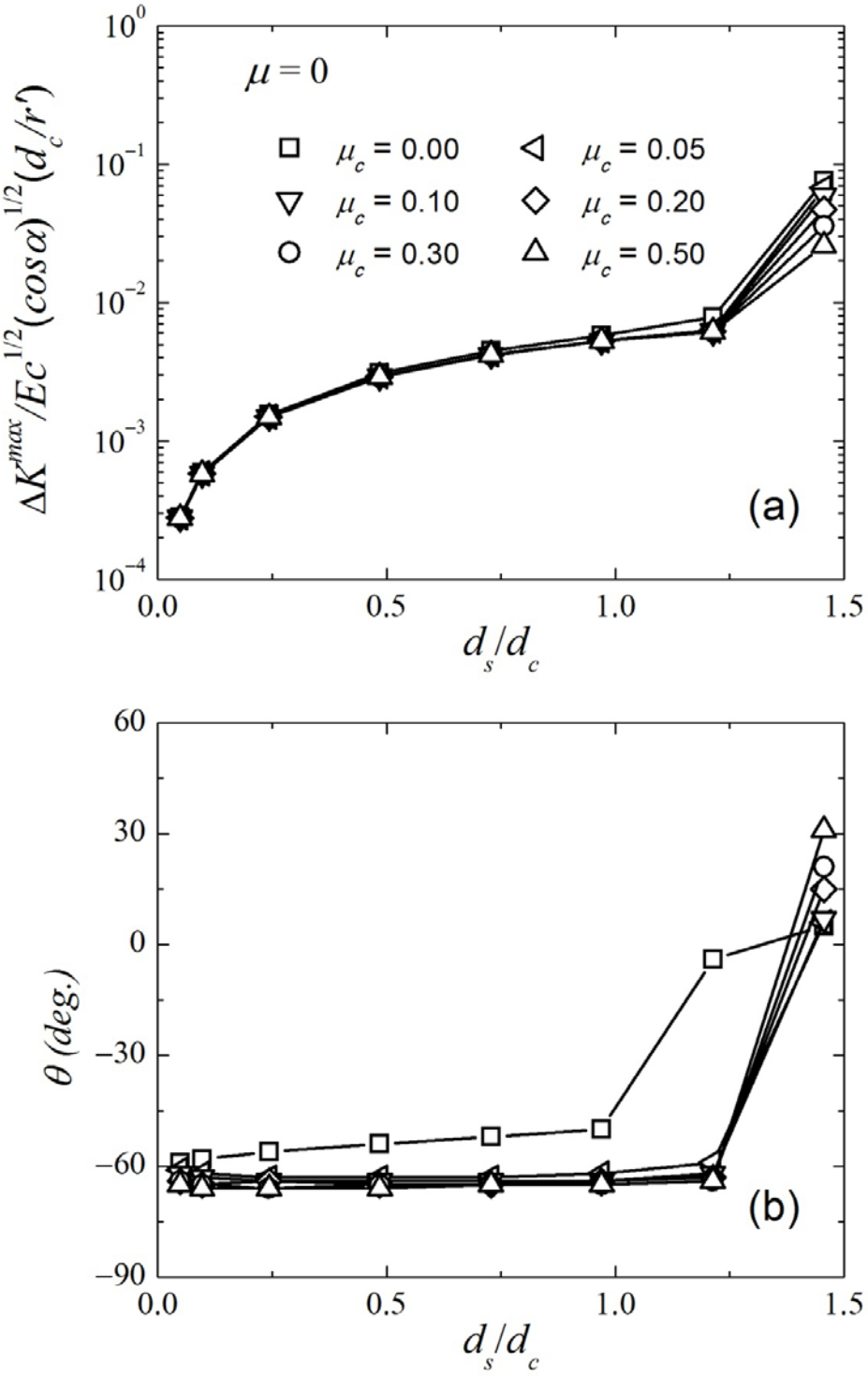

Figure 6.7 (a) Dimensionless ΔK^{max} and (b) crack growth angle θ versus relative interaction depth d_s/d_c for $\mu = 0$, $\alpha = 36^o$, and μ_c = 0, 0.05, 0.10, 0.20, 0.30 and 0.50.

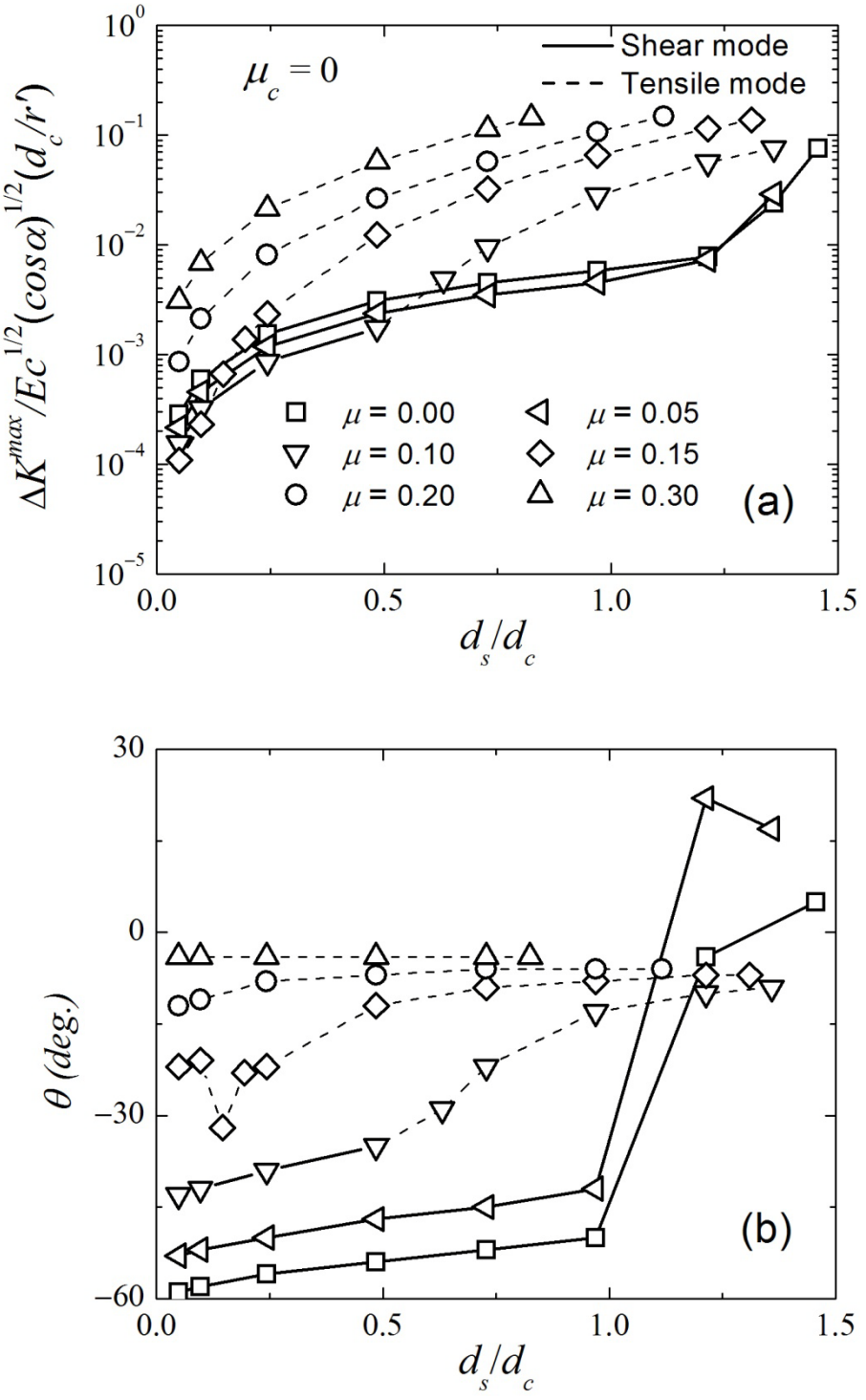

Figure 6.8 (a) Dimensionless ΔK^{max} and (b) crack growth angle θ versus relative interaction depth d_s/d_c for $\alpha = 36^o$, $\mu_c = 0$ and $\mu = 0$, 0.05, 0.10, 0.15, 0.20 and 0.30.

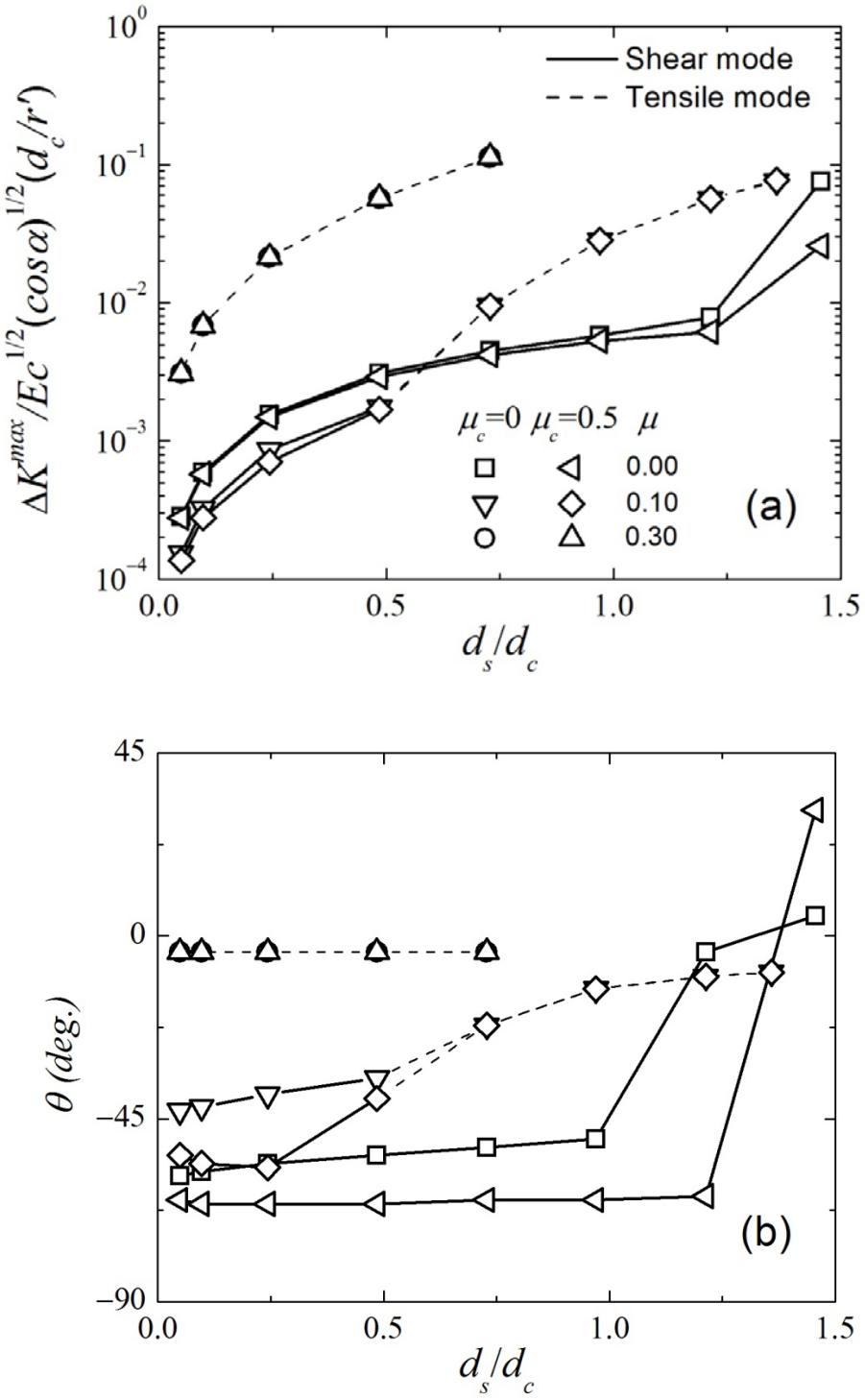

Figure 6.9 (a) Dimensionless ΔK^{max} and (b) crack growth angle θ versus relative interaction depth d_s/d_c for $\alpha = 36^o$, $\mu = 0$, 0.10 and 0.30, and $\mu_c = 0$ and 0.50.

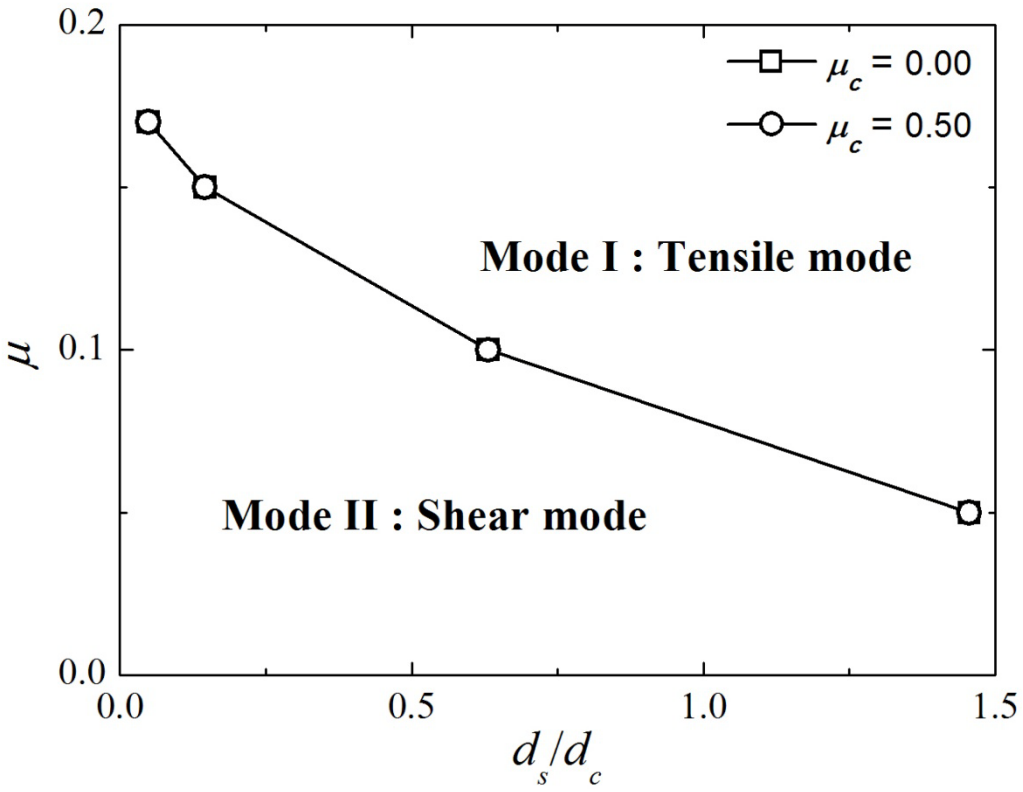

Figure 6.10 Crack growth transition map as functions of sliding interfacial friction coefficient μ and relative asperity interaction depth d_s/d_c for $\alpha = 36^o$, and $\mu_c = 0$ and 0.50.

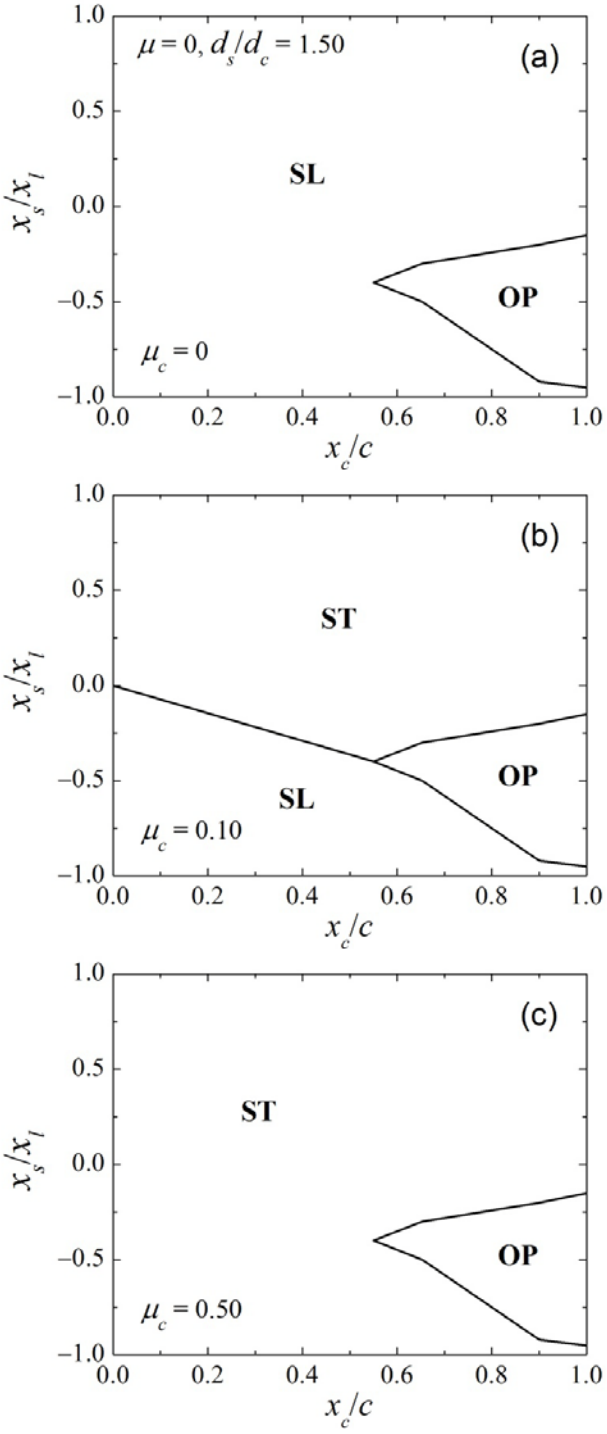

Figure 6.11 Crack mechanisms map as functions of relative sliding distance x_s/x_l and relative crack interface position x_c/c at (a) $\mu_c = 0$, (b) $\mu_c = 0.10$ and (c) $\mu_c = 0.50$ for $\alpha = 36^o$, $\mu = 0$, and $d_s/d_c = 1.50$ (OP: opening, SL: slip, ST: stick).

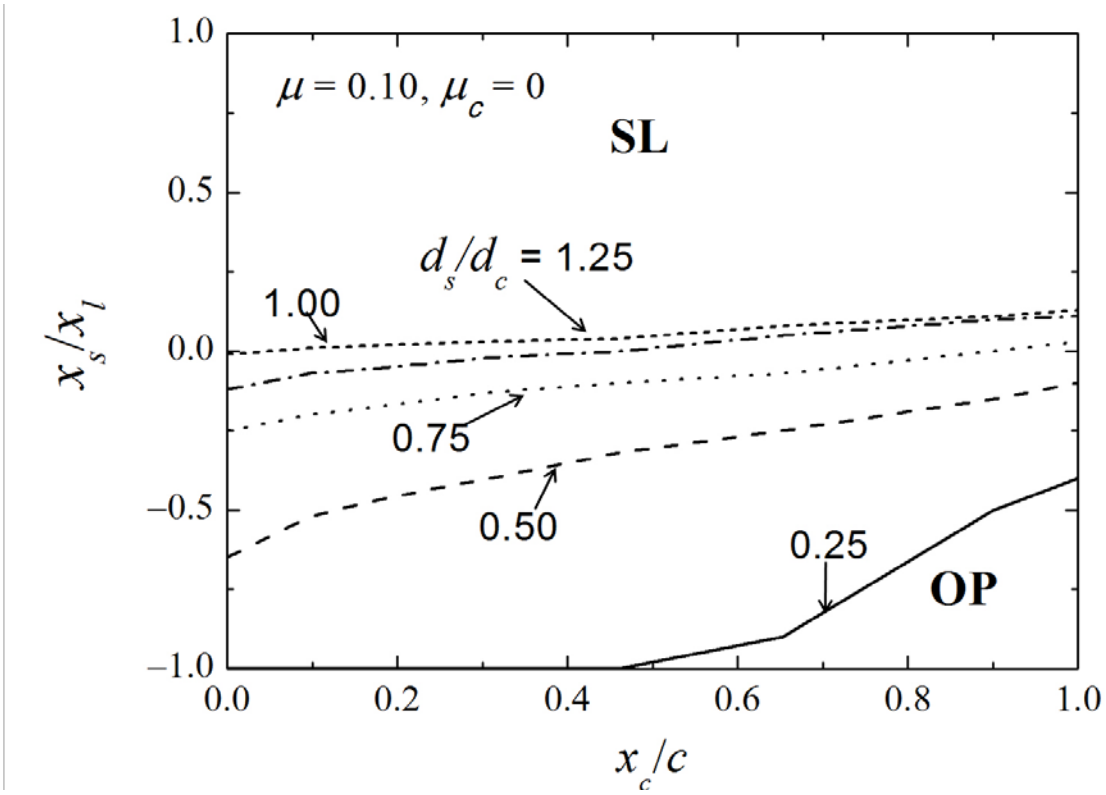

Figure 6.12 Crack mechanisms map as functions of relative sliding distance x_s/x_l and relative crack interface position x_c/c for α = 36^o, μ_c = 0, μ = 0.10, and d_s/d_c = 0.25, 0.50, 0.75, 1.00, and1.25 (OP: opening, SL: slip, ST: stick).

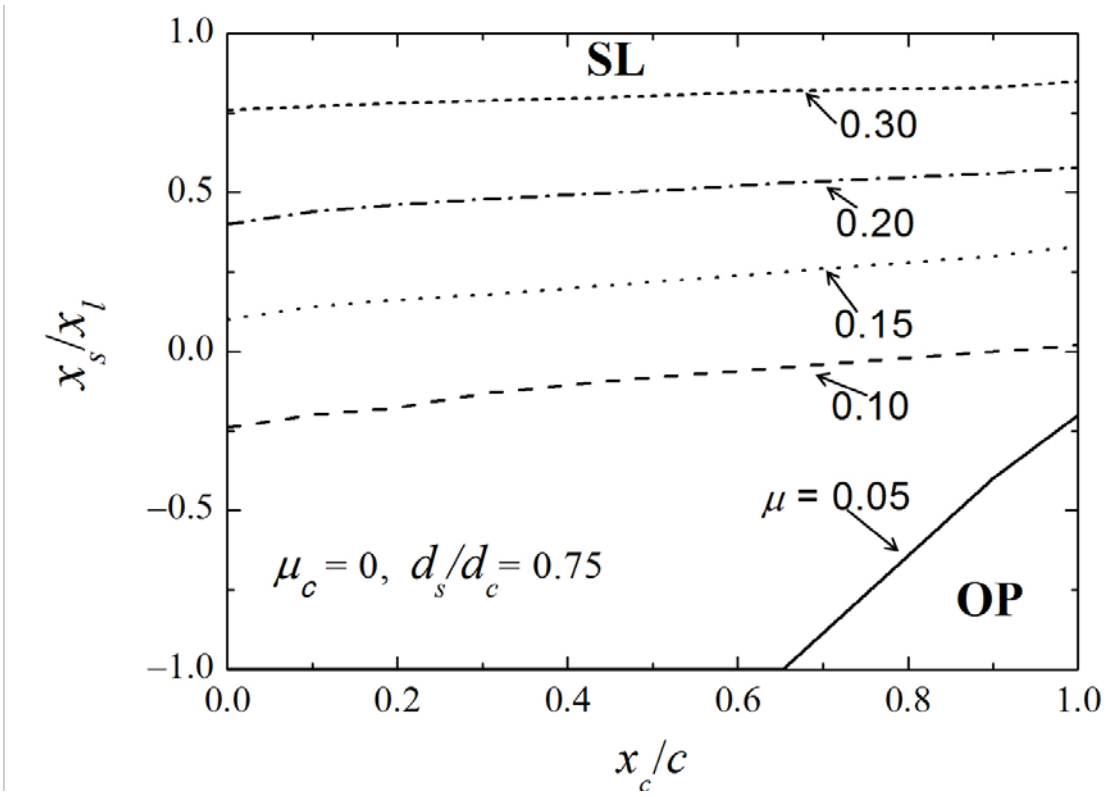

Figure 6.13 Crack mechanisms map as functions of relative sliding distance x_s/x_l and relative crack interface position x_c/c for $\alpha = 36^o$, $\mu_c = 0$, $d_s/d_c = 0.75$, and $\mu = 0.05$, 0.10, 0.15, 0.20 and 0.30 (OP: opening, SL: slip, ST: stick).

Chapter 7
A quasi-static mechanics analysis of three-dimensional nanoscale surface polishing

7.1 Introduction

Surface polishing at submicron scales is of paramount importance in many leading-edge technologies where precise surface planarization is of critical importance to product quality, such as chemical-mechanical polishing (CMP) of semiconductor wafers and fine-scale polishing (lapping) of magnetic recording heads. Basic understanding of the effects of important process parameters on surface quality (e.g., roughness) and material removal rate (MRR) is essential to the enhancement of the product performance and efficiency of nanoscale surface polishing.

The main emphasis in previous studies was on the MRR and final roughness of the polished surface. For example, Touge and Matsuo (1996) examined the effect of two-body and three-body abrasion conditions on the MRR and surface roughness of Mn–Zn ferrite; Preston (1927) introduced an empirical model that predicts the MRR of polished glass; Larsen-Basse and Liang (1999) studied the dominant wear mechanisms under CMP conditions; Zhao and Chang (2002) combined an elastic-plastic microcontact model with an abrasive wear theory to develop a CMP model for silicon; Tichy et al. (1999) used contact mechanics and elastohydrodynamic lubrication analyses to derive a CMP model; and Luo and Dornfeld (2003a) discussed chemical and mechanical surface effects on the MRR.

Despite useful information for the steady-state surface roughness and MRR obtained from earlier studies of surface polishing, most analyses provided semi-empirical models based on phenomenological observations. More importantly, multi-scale roughness and deformation at the asperity level (particularly, the evolution of surface topography) were not considered in previous analytical studies of the polishing process. Different microscale deformation and wear mechanisms may affect surface roughness and MRR when polishing occurs at microscopic levels. Therefore, changes in the surface topography of the polished surface due to the removal of material and plowing effects and smoothening and roughening mechanisms commencing at the asperity level must be included in the analysis of nanoscale surface polishing.

The present study is the first to develop a comprehensive quasi-static analysis of nanoscale surface polishing that integrates fundamental concepts from contact mechanics and multi-scale surface topography description by fractal geometry into a three-dimensional stochastic model. The analysis accounts for the evolution of the surface topography during polishing due to competing surface smoothening and roughening effects, resulting in the removal of material and irreversible localized deformation, respectively. Numerical results of the steady-state roughness, MRR, and wear coefficient of polished ceramic heads used in magnetic recording are discussed in terms of important parameters, such as polishing plate roughness, nanoparticle average size and density, initial roughness and mechanical properties of polished surface, and apparent contact pressure. To validate the analysis, simulation trends and numerical results are compared

with experimental observations and measurements obtained in this chapter as well as previous investigations of nanoscale surface polishing of magnetic recording ceramic heads.

7.2 Analysis

7.2.1 Model of nanoscale surface polishing

Figure 7.1(a) shows a cross-sectional schematic of the problem under consideration. Material is removed from the surface to be polished (hereafter referred to as the sample surface) by hard (rigid) nanoparticles embedded into a polishing plate rotated at a constant angular speed. The gap between the polishing plate and the sample surface is occupied by fluid (boundary lubricant). Figure 7.1(b) depicts the kinematics of the polishing process. The sample is pressed against the polishing plate and is oscillated back and forth in the radial direction at a constant speed. The relative speed between the moving surfaces and the applied pressure promote sliding in the boundary lubrication regime. Thus, the external load is transmitted through solid-solid contacts established between nanoparticles and asperities of the sample surface, whereas hydrodynamic effects are secondary. Surface roughness, nanoparticle distribution, and sample surface modification yield intermittent solid-solid contact. Surface movement and topography changes due to inelastic deformation (plowing) and material removal (polishing) mechanisms promote discontinuous asperity-nanoparticle interactions. Thus, surface polishing at the nanoscale is a random process affected by both local and global factors, such as surface roughness, nanoparticle average size and distribution (density), apparent contact pressure, and relative sliding speed. Therefore, a stochastic model that accounts for topography changes is used to analyze the removal of material during nanoscale surface polishing.

7.2.2 Surface description

Fractal geometry was first introduced by Mandelbrot (1967) to describe the behavior of the Earth's coastlines. Microscopy observations indicate that most engineering surfaces also exhibit fractal behavior, characterized by the properties of continuity, non-differentiability, and self-affinity (Berry and Lewis, 1980; Ausloos and Berman, 1985; Majumdar and Bhusha, 1990; Majumdar and Tien, 1990). Hence, the original topography of the sample surface was modeled as an isotropic, three-dimensional (3D) fractal surface with profile $z(x, y)$ given by a two-variable Weierstrass-Mandelbrot (W-M) function (Berry and Lewis, 1980; Ausloos and Berman, 1985). For dimensional consistency, the original W-M function is expressed as (Yan and Komvopoulos, 1998a)

$$z(x,y) = L\left(\frac{G}{L}\right)^{(D-2)}\left(\frac{\ln\gamma}{M}\right)^{1/2}\sum_{m=1}^{M}\sum_{n=0}^{n_{\max}}\gamma^{(D-3)n}\left\{\cos\phi_{m,n} - \cos\left[\frac{2\pi\gamma^{n}\left(x^{2}+y^{2}\right)^{1/2}}{L}\cos\left(\tan^{-1}\left(\frac{y}{x}\right) - \frac{\pi m}{M}\right) + \phi_{m,n}\right]\right\} \tag{7.1}$$

where L is the length over which the surface exhibits fractal behavior, G is the fractal roughness, D is the fractal dimension ($2 < D < 3$), γ is a scaling parameter, M is the number of superposed

ridges, n is a frequency index having an upper limit $n_{\max} = \text{int}[\log(L/L_s)/\log\gamma]$, where L_s is a cut-off length below which continuum description breaks down, and $\phi_{m,n}$ is a random phase used to prevent the coincidence of different frequencies at any point of the surface profile. Surface flatness and frequency distribution density considerations suggest that $\gamma = 1.5$ is a reasonable choice (Komvopoulos and Yan, 1997a). A sufficiently large number of ridges must be used in Eq. (7.1) (Yan and Komvopoulos, 1998a) to ensure surface homogeneity. An isotropic 3D fractal surface was obtained for M = 5000. Equation (7.1) indicates that the fractal surface profile is a superposition of cosine functions with highest and lowest frequencies $\omega_h = 1/L_s$ and $\omega_l = 1/L$, respectively. Since L_s is typically on the order of ~5-6 lattice distances (Yan and Komvopoulos, 1998a), it is assumed that $L_s = 1$ nm.

The scale-independent fractal parameters D and G can be determined from experimental measurements. For example, the fractal parameters of an isotropic 3D fractal surface can be estimated from the slope and the y-intercept, respectively, of the log-log plot of the power spectrum $P(\omega)$ of a two-dimensional (2D) profile of the 3D surface topography (Majumdar and Tien, 1990; Yang and Komvopoulos, 2005a),

$$P(\omega) = \frac{G_1^{2(D_1-1)}}{2\ln\gamma}\frac{1}{\omega^{(5-2D_1)}} \tag{7.2}$$

where G_1 and D_1 are the fractal parameters of the 2D fractal surface profile. For an isotropic 3D fractal surface, $G \approx G_1$ and $D = D_1 + 1$.

Fractal dimension D determines the contributions of high- and low-frequency components in the surface profile, whereas fractal roughness G controls the wavelength amplitudes and is independent of frequency (Komvopoulos and Ye, 2001). As shown by Eq. (7.1), the surface profile comprises a wide range of roughness structures of different wavelengths and amplitudes. For a fixed G, the amplitude ratios of the high-to-low frequency components increase with D. Thus, the surface topography appears rougher when the vertical scale is comparable to the amplitude of the lowest frequency component ω_l. However, for $G < L$, an increase in D produces a marked decrease of ω_l due to the significant decrease of $(G/L)^{D-2}$ (Eq. (7.1)). Since surface characterization by fractal geometry yields scale-independent topography parameters over the range of length scales where the surface exhibits fractal behavior, fractal geometry can be used to describe the surface topography over a wide range of length scales, not only that of the profilometry measurements.

7.2.3 Deformation modes

Since the material is removed from the sample surface by hard nanoparticles, it is necessary to consider surface deformation at the asperity level. The nanoparticles are assumed to be spherical and rigid relative to all other materials involved, e.g., polished surface and layer of the polishing plate. This assumption is reasonable because the nanoparticles usually consist of diamond. The material behavior at the nanoscale differs significantly from that at the macroscale.

For example, nanoscratching of macroscopically brittle materials (e.g., ceramics) has been observed to result in localized plastic deformation characterized by the formation of crack-free plowing marks (Lu and Komvopoulos, 2001). Indeed, high-magnification imaging of Al_2O_3-TiC samples scratched by a sharp diamond tip revealed the dominance of surface plowing and the absence of surface cracks despite the brittle behavior of the ceramic material in its bulk form. Therefore, the polished surface is modeled as an elastic-perfectly plastic material. Furthermore, the friction coefficient obtained from the same nanoscratching experiments was found to be equal to ~0.12. In view of this low friction coefficient of the diamond/Al_2O_3-TiC system and the use of a fluid in nanoscale polishing, contact between the rigid nanoparticles and deformable asperities of the polished surface is assumed to be frictionless for simplicity.

For elastic-perfectly plastic material behavior and frictionless (normal) contact, the mean contact pressure p_m and real contact area a_r at asperity-nanoparticle contacts (hereafter referred to as contacts for brevity) can be determined from the following relationships (Kogut and Komvopoulos, 2004):

(a) Elastic deformation ($\delta / r' < 1.78(E/Y)^{-1}$),

$$\frac{p_m}{Y} = \frac{4\sqrt{2}}{3\pi}\left(\frac{E\delta}{Yr'}\right), \quad \frac{a'}{a_r} = 2 \tag{7.3}$$

(b) Elastic-plastic deformation ($1.78(E/Y)^{-1} \le \delta / r' \le \left[1 + 0.037(E/Y)\right]^{-1}$),

$$\frac{p_m}{Y} = 0.839 + \ln\left[\left(\frac{E}{Y}\right)^{0.656}\left(\frac{\delta}{r'}\right)^{0.651}\right], \quad \frac{a'}{a_r} = 2.193 - \ln\left[\left(\frac{E}{Y}\right)^{0.394}\left(\frac{\delta}{r'}\right)^{0.419}\right] \tag{7.4}$$

(c) Fully-plastic deformation ($\delta / r' > \left[1 + 0.037(E/Y)\right]^{-1}$),

$$p_m = H, \quad \frac{a'}{a_r} = 1 \tag{7.5}$$

where δ is the local interference, r' is the radius of the truncated contact area a', and E, Y, and H are the elastic modulus, yield strength, and hardness of the polished surface. Equations (7.3)–(7.5) also hold for sliding contact conditions when the friction coefficient is ≤ 0.1, as in nanoscale surface polishing due to the relatively low adhesion of diamond with most materials and the presence of a fluid which also plays the role of a boundary lubricant. These relationships indicate that both the mean contact pressure and real contact area are functions of the elastic-plastic material properties of the polished surface and the dimensionless local interference δ / r'.

In earlier contact mechanics studies involving fractal surfaces, asperity deformation was assumed to be either elastic or fully plastic (Yang and Komvopoulos, 2005; Majumdar and Bhushan, 1991). However, elastic-plastic deformation yields a smooth transition from elastic to fully-plastic deformation and also contributes significantly to the load distribution and evolution

of the surface topography. Therefore, all three deformation modes described by Eqs. (7.3)–(7.5) are included in the present analysis.

7.2.4 Stochastic analysis of nanoscale surface polishing

A quasi-static stochastic analysis of the removal of material that accounts for the randomness of asperity-nanoparticle interactions is introduced in this section. Without loss of generality, the analysis is performed for a 1 × 1 μm^2 sample area with periodic boundary conditions, implying a fractal behavior of the original topography of the sample surface for $L = 1$ μm (Eq. (7.1)).

The quasi-static stochastic analysis is based on a numerical algorithm of the evolution of the polishing process that uses the following main steps in each sliding increment: (a) calculation of the global distance between the mean-height planes of the sample surface and the polishing plate; (b) calculation of the local interference at each asperity-nanoparticle contact; (c) determination of the deformation mode of each interacting asperity; (d) evaluation of the volume of material removed from fully-plastic contacts and the volume of material displaced at elastic-plastic contacts; and (e) construction of the new sample surface topography. To account for the effect of topography changes on the polishing process, the sample surface topography is modified at sliding increments d*s* = 1 μm, and the previously described iteration scheme are repeated until both the surface roughness of the polished surface and the material removal rate (wear coefficient) reach steady-state values.

Figure 7.2 shows a 2D schematic of the interface between the sample surface and the polishing plate. The global surface distance *h* is defined as the gap between the mean-height plane of the sample surface h_1 and that of the polishing plate h_2, both measured from a reference plane. For a given *h*, the truncation of an asperity by a nanoparticle displaced quasi-statically in the horizontal direction yields truncation volume V^*, projected truncation area a^*, and maximum local interference distance *d*, as shown in Fig. 7.3(a). These local parameters are determined numerically for given *h*, sample surface and polishing plate surface height distributions $f_1(z_1)$ and $f_2(z_2)$, respectively, average nanoparticle radius *R*, and nanoparticle density n_p. For simplicity, the truncated asperity is approximated by a sphere of radius R', as shown in Fig. 7.3(b). The projected truncation area a^* and maximum local interference distance *d* in Fig. 7.3(b) are equal to those shown in Fig. 7.3(a). Moreover, the truncation volume V^* (Fig. 7.3(a)) is set equal to the truncation volume of the two spheres V' (Fig. 7.3(b)).

Based on these assumptions, the following relationships can be obtained:

$$a' = \pi (r')^2 = \frac{\pi d^2}{8}\left[1 + \left\{1 + \left(\frac{8a^*}{\pi d^2}\right)^2\right\}^{1/2}\right] \tag{7.6a}$$

$$\delta_1 = R\left[1-\left\{1-\frac{a'}{\pi R^2}\right\}^{1/2}\right] \tag{7.6b}$$

$$V^* \approx V' = \frac{a'}{2}\left[\delta_1\left(1+\frac{\pi\delta_1^2}{3a'}\right)+\delta_2\left(1+\frac{\pi\delta_2^2}{3a'}\right)\right] \tag{7.6c}$$

$$\delta = \delta_1 + \delta_2 \tag{7.6d}$$

where $a' = a^*/\cos\theta$. Equations 7.6(a) and 7.6(b) are used, respectively, to calculate a' and δ_1 in terms of R and the numerically calculated a^* and d. Equation 7.6(c) is then used to calculate δ_2 in terms of δ_1, V^*, and a'. Finally, the local interference δ is obtained from the calculated values of δ_1 and δ_2 using Eq. 7.6(d). Equations (7.6) indicate that the dimensionless local interference δ/r' is a function of h, $f_1(z_1)$, $f_2(z_2)$, R, and n_p.

Considering that contact between two spherical bodies is equivalent to a half-space with effective elastic properties in contact with a rigid sphere of equivalent radius of curvature, Eqs. (7.3)–(7.5) can be used to express the mean contact pressure p_m and real contact area a_r of two spherical bodies in normal contact in terms of δ/r'. The normal load transmitted through a single contact ΔP_i and total normal load P applied to the polished sample are given by

$$\begin{aligned}\Delta P_i &= p_m a_r \cos\theta = p_m a_r \cos\left[\sin^{-1}\left(\frac{d}{2r'}\right)\right] \\ P &= \sum_{i=1}^{N_c}\Delta P_i\end{aligned} \tag{7.7}$$

where N_c is the total number of contacts.

Using Eqs. (7.3)–(7.5) and (7.7), the apparent contact pressure p_a, defined as the ratio of the external normal load P and the apparent sample area A_a, can be expressed as

$$p_a = P/A_a = F(h, f_1(z_1), f_2(z_2), R, n_p, E, Y, H) \tag{7.8}$$

Hence, the global surface distance can be obtained in terms of the apparent contact pressure, surface height distributions of the sample surface and polishing plate, nanoparticle average radius (size) and density, and elastic-plastic material properties of the sample surface by inverting Eq. (7.8).

The load transmitted through each contact is limited by the penetration resistance (hardness) of the soft surface layer of the rigid polishing plate. Therefore, the upper limit of the load at a single contact is defined as

$$\Delta P_{\max} = \pi R^2 H_l \tag{7.9}$$

where H_l is the layer hardness. When $\Delta P_i > \Delta P_{\max}$, it is assumed that the nanoparticle sinks into the soft layer to a depth that satisfies equilibrium condition $\Delta P_i = \Delta P_{\max}$. Because of the effect of nanoparticle sinking (Eq. (7.9)), the modified general formula of the global surface distance is given by

$$h = F^{-1}(p_a, f_1(z_1), f_2(z_2), R, n_p, E, Y, H, H_l) \tag{7.10}$$

To obtain the global surface distance, Eq. (7.10) is solved numerically by an iteration procedure until force equilibrium is satisfied. Then, the removal of material at the asperity level is determined based on the criterion described in the following section.

7.2.5 Criterion of material removal

The calculation process of the material removed by the hard nanoparticles is based on steps (b)–(d) described in the previous section. Since asperity-nanoparticle interactions occur randomly, the local interference and the deformation of each interacting asperity are determined incrementally at tangential displacement increments of 10 nm. Because elastic deformation is fully recovered upon unloading, elastic contacts do not participate in the removal of material and the modification of the surface topography but only support a fraction of the total load. Plastic flow due to plowing at elastic-plastic contacts results in localized surface modification. Thus, elastic-plastic contacts are responsible for changes in the surface topography due to plowing by nanoparticles and do not participate in the removal of material. Figure 7.4 shows surface modification due to plowing at elastic-plastic contacts. The moving direction of the nanoparticle is perpendicular to the plane of the figure. For a given global surface distance, the truncation area A and angle α at each elastic-plastic contact are obtained numerically. It is assumed that the plowed material is evenly displaced at each side, forming ridges whose cross-section areas are approximated by a circular arc of radius R_p and center angle α. Volume conservation yields $A = 2A_p$; thus,

$$A = 2A_p = R_p^2(\alpha - \sin\alpha) \tag{7.11}$$

Only fully-plastic contacts contribute to the removal of material. The volume removed from a fully-plastic contact is equal to the truncation volume V^* (Fig. 7.3(a)). Thus, changes in the topography modification occur at fully-plastic contacts due to the removal of material. Therefore, elastic contacts share a fraction of the total load, elastic-plastic contacts contribute only to topography changes (roughening effect), while fully-plastic contacts are responsible for both the removal of material and the modification of the surface topography (smoothening effect).

The MRR is defined as the average recession rate of the sample surface $dh_1/dt = \upsilon\, dh_1/ds$, where υ is the relative sliding speed. Because the removal of material is controlled by asperity-nanoparticle interactions, the steady-state sample roughness and MRR depend on process

parameters (p_a, υ, R, and n_p), topographies of the sample surface and polishing plate ($f_1(z_1)$ and $f_2(z_2)$, respectively), elastic-plastic material properties of the polished surface (E, Y, and H), and layer hardness (H_l). Results from quasi-static simulations illustrating the effect of these parameters on nanoscale surface polishing are presented next.

7.3 Results and discussion

Simulations were performed for a polishing plate topography with Gaussian surface height distribution, spherical diamond nanoparticles having their centers at the surface of the polishing plate, sample surface exhibiting fractal behavior and elastic-perfectly plastic deformation, frictionless asperity-nanoparticle contacts, and a 1 × 1 μm^2 analysis area with periodic boundary conditions. Results for the roughness of the polished surface, material removal rate, and wear coefficient are presented for the following parameters: $D = 2.5$, $G = 1\times10^{-3}$ nm, $p_a = 356$ kPa, $\upsilon = 133$ mm/s, $R_q = 1$ nm (polishing plate), $R = 50$ nm (i.e., nanoparticle average size = 100 nm), $n_p = 9$ μm^{-2}, $E = 390$ GPa, $Y = 7.3$ GPa, $H = 20$ GPa, and $H_l = 45$ MPa. This set of parameters is representative of nanoscale surface polishing of Al_2O_3-TiC magnetic recording heads (Tjiptoharsono et al., 2010; Shen and Zhong, 2006).

7.3.1 Evolution of sample surface topography and material removal rate

Figure 7.5 shows the variation of the root-mean-square (rms) roughness R_q of the sample surface and MRR with polishing time t. The original topography of the sample surface is shown in Fig. 7.6(a). The roughness decreases rapidly to a steady-state $R_q^{ss} \approx 0.15$ nm after polishing for ~2 s (Fig. 7.5(a)), while the MRR decreases sharply to a steady-state of ~1.05 nm/s after a very short polishing time of ~0.1–0.2 s (Fig. 7.5(b)). The results shown in Fig. 7.5 suggest that steady-state polishing conditions are established after ~2 s from the onset of polishing. The initial sharp decrease of the MRR is attributed to the formation of more contacts upon the rapid removal of the highest surface peaks, resulting in lower contact pressures and fewer fully-plastic contacts due to the increase of the local asperity radius caused by the removal of smaller (sharper) asperities on top of larger asperities. However, the removal of the taller asperities with the onset of polishing does not have a first-order effect on R_q, which is a measure of the standard deviation of surface peaks and valleys from the mean plane of the polished surface at a given polishing time. This explains the time difference between R_q^{ss} and steady-state MRR. The analytical predictions of R_q^{ss} and MRR (Fig. 7.5) are fairly close to experimental measurements of the final roughness and average removal rate of Al_2O_3-TiC magnetic recording heads polished with diamond nanoparticles (Tjiptoharsono et al., 2010; Shen and Zhong, 2006). Considering the proportional dependence of MRR on the apparent contact pressure, the predicted steady-state MRR of ~1.05 nm/s for p_a = 356 kPa and R = 50 nm (Fig. 7.5(b)) is in good agreement with the experimental value of ~0.3 nm/s obtained for a ~3.2 times lower average contact pressure (112 kPa) and slightly larger diamond nanoparticles (R = 75 nm) (Shen and Zhong, 2006).

Figure 7.6 provides further insight into evolution of the sample surface topography during polishing. Figure 7.6(b) shows the transient topography ($R_q = 0.59$ nm) after polishing for 0.4 s, while Fig. 7.6(c) shows the steady-state topography ($R_q^{ss} \approx 0.15$ nm) of the sample surface. The modification of the surface topography shown in Fig. 7.6 reveals that the rapid removal of the highest surface summits during the transient stage is followed by a fairly uniform recess of the sample surface at steady-state polishing, in agreement with phenomenological observations from lapping of Al_2O_3-TiC with diamond nanoparticles. The rapid topography changes are due to the simultaneous occurrence of surface roughening and surface smoothening processes. As discussed earlier, plowing at elastic-plastic contacts causes surface roughening, while the removal of material at fully-plastic contacts leads to surface smoothening. Both of these competing effects occur at the asperity level. For a given polishing plate, a rougher sample surface yields higher local contact pressures and less asperity-nanoparticle interactions, implying fewer elastic-plastic and fully-plastic contacts. The high MRR observed at the onset of polishing (Fig. 7.5(b)) is attributed to the dominance of fully-plastic contacts (smoothening effect) caused by the high local contact pressures generated at the highest surface summits of the original topography. However, the increase of the asperity radius and number of contacts due to the simultaneous occurrence of surface smoothening (Fig. 7.5(a)) leads to the decrease of the local contact pressure, which increases the number of elastic-plastic contacts (roughening effect). Since solid-solid interaction at newly formed contacts occurs at the peaks of small (sharp) asperities on top of large asperities, surface smoothening may also increase the number of fully-plastic contacts; however, the decrease of the local contact pressure due to the load distribution over more contacts yields a less contributing smoothening effect. The intensifying roughening effect (elastic-plastic contacts) and simultaneous weakening of the smoothening effect (fully-plastic contacts) reach eventually an equilibrium stage characterized by a steady-state roughness $R_q^{ss} \approx 0.15$ nm (Fig. 7.5(a)) and a steady-state MRR $dh_1/dt \approx 1.05$ nm/s (Fig. 7.5(b)).

Further insight into the modification scale of the sample surface topography can be obtained by examining the power spectrum of the polished surface. Figure 7.7 shows a comparison between power spectral density functions $P(\omega)$ of surface topographies with R_q = 0.96, 0.59, 0.27, and 0.15 nm. Each power spectrum is an average of 1000 *x*-scans obtained at 1-nm increments in the *y*-direction. The decrease in the slope of $P(\omega)$ with R_q implies an increase in fractal dimension *D* (Eq. (7.2)), suggesting an increase in the amplitude ratios of high-to-low frequency components. This means that high-frequency components dominate the steady-state surface topography of the polished surface. Steady-state polishing conditions are established upon seizure of surface modification involving wavelength components of amplitudes larger than the average nanoparticle size. Thus, steady-state polishing is controlled by frequency components of the sample topography with amplitudes smaller than the nanoparticle average size.

7.3.2 Effect of initial roughness of sample surface

To examine the effect of the initial roughness of the sample surface on the polishing process, simulations were performed for different initial sample topographies obtained from Eq. (7.1) for $D = 2.5$ and *G* values corresponding to various R_q^i values. All other parameters were identical to those given previously. Despite significant differences in the initial roughness, the three

simulation cases yielded very similar steady-state polishing conditions, i.e., $R_q^{ss} \approx 0.15$ nm and $dh_1/dt \approx 1.05$ nm/s, suggesting a secondary effect of the initial roughness of the sample surface on steady-state polishing. This is demonstrated by the power spectral density function (obtained as the average of 1000 *x*-scans, as explained for Fig. 7.7) of the steady-state sample topography shown in Fig. 7.8 for $R_q^i = 0.96$, 0.50, and 0.10 nm. The overlapping of the data implies a secondary effect of initial sample surface roughness on steady-state polishing. This is because polishing mostly filters out the low-frequency components without affecting the high-frequency components with amplitudes less than the nanoparticle average size. Since the power spectral density functions are similar and not affected by the polishing process in the high-frequency range, it may be inferred that the initial roughness of the polished surface, which is mainly determined by the low-frequency topography components removed during the transient stage of polishing, does not play an important role in steady-state polishing.

7.3.3 Effect of apparent contact pressure

As mentioned previously, steady-state polishing conditions are established when competing roughening and smoothening effects reach equilibrium. Since these competing effects are associated with elastic-plastic and fully-plastic contacts, knowledge of the deformation mode at the asperity level provides insight into steady-state polishing. Figure 7.9 shows the variation of asperity-nanoparticle contact fractions with apparent contact pressure for steady-state polishing conditions. N_c, N_c^{ep}, and N_c^{fp} are the numbers of total, elastic-plastic, and fully-plastic contacts, respectively, and *N* is the number of nanoparticles existing in the area of analysis. Except of the polishing plate roughness ($R_q = 5$ nm), all other parameters are the same as those in previous simulation results (Figs. 7.5–7.8). Although the fraction of total contacts N_c/N increases significantly with the apparent contact pressure, the fraction of elastic-plastic contacts N_c^{ep}/N_c remains almost constant, whereas the fraction of fully-plastic contacts N_c^{fp}/N_c decreases slightly. Because N_c^{ep}/N_c is slightly less than 1, while N_c^{fp}/N_c in on the order of 10^{-2}, the number of elastic-plastic contacts is much larger than the number of fully-plastic contacts at steady-state polishing.

The marginal dependence of N_c^{fp}/N_c and N_c^{ep}/N_c on p_a (Fig. 7.9) suggests that the relative contributions of smoothening and roughening on steady-state polishing do not vary with the apparent contact pressure, implying a secondary pressure effect on the steady-state roughness of the sample surface. Indeed, Fig. 7.10(a) shows that R_q^{ss} is virtually independent of p_a, in agreement with experimental results showing an insignificant load (pressure) effect on the steady-state surface roughness of Al_2O_3-TiC ceramic heads polished by diamond nanoparticles (Tjiptoharsono et al., 2010). However, the mere invariance of N_c^{fp}/N_c and the significant increase of N_c/N with the increase of p_a (Fig. 7.9) indicate a marked increase of N_c^{fp} with p_a. Since fully-plastic contacts are responsible for the removal of material, the former trend suggests an increase of the MRR with the apparent contact pressure, consistent with the linear dependence of MRR on p_a shown in Fig. 7.10(b). Polishing of Al_2O_3-TiC ceramic heads by diamond

nanoparticles embedded in the Sn layer of a polishing plate under $p_a = 356$ kPa yielded $R_q^{ss} = 0.2 - 0.3$ nm and MRR = 1.0 nm/s, in fair agreement with the analytical predictions of this study obtained for the same apparent contact pressure, i.e., $R_q^{ss} \approx 0.18$ nm (Fig. 7.10(a)) and MRR ≈ 0.8 nm/s (Fig. 7.10(b)). Moreover, the MRR of ~0.3 nm/s reported for polishing of Al_2O_3-TiC ceramic heads under an average contact pressure of 112 kPa (Shen and Zhong, 2006) is very close to the analytical MRR prediction of ~0.28 nm/s for p_a = 112 kPa (Fig. 7.10(b)).

The MRR can be converted to a dimensionless parameter, known as the wear coefficient *K*, defined as (Rabinowicz, 1995)

$$K = \left(\frac{dh_1}{dt}\right)\left(\frac{H}{p_a \upsilon}\right) \tag{7.12}$$

Figure 7.10(c) shows that $K \approx 4 \times 10^{-4}$ regardless of the apparent contact pressure. The invariance of the wear coefficient with apparent contact pressure is due to the linear variation of dh_1/dt with p_a (Fig. 7.10(b)). The predicted wear coefficient is about two orders of magnitude less than that of macroscale two-body abrasive wear (Rabinowicz, 1995) but typical of polishing. Although the apparent contact pressure does not affect the final roughness of the polished surface (Fig. 7.10(a)) and the dominant wear mechanism, as indicated by the marginal variation of the wear coefficient (Fig. 7.10(c)), it affects significantly the MRR (Fig. 7.10(b)) and, hence, the efficiency of the polishing process.

7.3.4 Effect of surface roughness of polishing plate

The effect of the surface roughness of the polishing plate (i.e., topography of surface layer) on steady-state polishing can be interpreted in light of the results shown in Fig. 7.11. Although N_c / N and N_c^{ep} / N_c do not exhibit a discernible roughness dependence, the roughness effect on N_c^{fp} / N_c is significant. This can be explained by considering the plate roughness effect on the local contact pressure, which controls asperity deformation (Eqs. (7.3)–(7.5)) and nanoparticle sinking (Eq. (7.9)). Because the roughness of the polishing plate ($R_q = 0.5 - 10$ nm) is about an order of magnitude higher than the steady-state roughness of the polished surface ($R_q^{ss} \approx 0.18$ nm), asperity-nanoparticle interactions are mainly controlled by the surface topography of the soft layer of the polishing plate where the abrasive nanoparticles are embedded. The increase of the local contact pressure with the roughness of the polishing plate promotes nanoparticle sinking because of the limited penetration resistance of the soft layer (Eq. (7.9)). Since nanoparticle sinking increases disproportionably the number of asperity-nanoparticle contacts N_c, the local contact pressure decreases and the deformation mode at most newly formed contacts is either elastic or elastic-plastic. This implies a decrease of N_c^{fp} with the increase of the plate roughness, which, considered together with the constancy of N_c because of the compensation of nanoparticle sinking by the formation of new contacts, yields a decrease of N_c^{fp} / N_c with the increase of the polishing plate roughness.

7.3.5 Effects of nanoparticle average size and density

Figure 7.12 shows the dependence of R_q^{ss}, dh_1/dt, and K on nanoparticle radius R (or average size) and rms roughness of polishing plate R_q. Comparisons can be made for fixed values of p_a/R^2 ($R = 25$ and 50 nm) and p_a ($R = 50$ and 75 nm). The decrease of the local surface interference and local contact pressure with the increase of the nanoparticle size promotes elastic and elastic-plastic deformation as opposed to fully-plastic deformation (Eqs. (7.3)–(7.5)), resulting in a more dominant effect of surface roughening compared to surface smoothening. This explains the higher steady-state roughness of the polished surface and the lower MRR and wear coefficient obtained with larger nanoparticles. The results shown in Fig. 7.12 indicate that a decrease in nanoparticle average size by a factor of 3 yields a decrease in final roughness by a factor of ~2 and an increase in MRR by a factor of ~3. The trend of R_q^{ss} to increase with the nanoparticle average size is consistent with experimental observations (Tjiptoharsono et al., 2010).

The variations of R_q^{ss}, dh_1/dt, and K with R_q, shown in Fig. 7.12, can be explained by considering the dependence of N_c^{ep}/N_c (surface roughening effect) and N_c^{fp}/N_c (surface smoothening and material removal effects) on the surface roughness of the polishing plate. For a fixed nanoparticle average size, N_c^{ep}/N_c remains nearly constant while N_c^{fp}/N_c decreases significantly with the increase of the plate roughness (Fig. 7.11). Thus, the trends of R_q^{ss}, dh_1/dt, and K shown in Fig. 7.12 can be attributed to the detrimental effect of plate roughness on surface smoothening and the removal of material, both associated with fully-plastic contacts. This effect is more significant in the low-roughness range ($R_q < 4$ nm) where N_c^{fp}/N_c decreases at a faster rate with the increase of the plate roughness (Fig. 7.11) and the volume of material removed at the asperity level is small due to the low local contact pressures and small surface interferences produced with a low-roughness polishing plate. In the high-roughness range ($R_q > 4$ nm), the marginal decrease of N_c^{fp}/N_c is balanced by the increase of the volume of material removed at the asperity level caused by the higher local contact pressures and larger local surface interferences produced with a high-roughness polishing plate, leading to the establishment of steady-state polishing conditions, as seen by the stabilization of R_q^{ss}, MRR, and K in the roughness range of $R_q > 4$ nm (Fig. 7.12).

To examine the nanoparticle density effect on steady-state polishing, results of R_q^{ss}, dh_1/dt, and K for $n_p = 5$, 9, and 15 μm^{-2} are contrasted in Fig. 7.13. It can be seen that, for a given plate roughness, higher nanoparticle density yields smoother polished surface, faster material removal, and higher wear coefficient. For fixed p_a, higher n_p yields more uniform load distribution, implying lower local contact pressures and smaller local surface interferences, i.e., less surface roughening at elastic-plastic contacts due to the plowing process. Although smaller local surface interference also implies less volume of material removed at fully-plastic contacts, this effect is

offset by the increase of N_c^{fp} with N_c (or n_p). Indeed, N_c^{fp}/N_c remains merely constant as opposed to N_c/N that increases significantly with p_a (Fig. 7.9), suggesting a marked increase of N_c^{fp} with N_c (or n_p). Since surface polishing is a dynamic process, the roughness of the polished surface and the MRR at steady-state polishing depend on the number of asperity-nanoparticle interactions (i.e., nanoparticle density) encountered over a certain time period. The previous interpretations provide an explanation for the trends shown in Fig. 7.13. Therefore, the lower R_q^{ss} and higher dh_1/dt and K predicted for higher n_p are attributed to the increase of fully-plastic contacts with the nanoparticle density.

7.3.6 Effect of material properties of polished surface

Figure 7.14 shows the effect of the material properties of the sample surface on steady-state polishing. These simulation results were obtained by varying either the elastic modulus or the yield strength of the polished surface while fixing all other parameters. Because the hardness of elastic-perfectly plastic materials depends on both the elastic modulus and the yield strength, in the simulations that the elastic modulus or the yield strength of the polished surface was varied, the hardness was modified according to the following relationship (Kogut and Komvopoulos, 2004):

$$\frac{H}{Y} = 0.201 \ln\left(\frac{E}{Y}\right) + 1.685 \tag{7.13}$$

Figures 7.14(a)–7.14(c) show that R_q^{ss} decreases while dh_1/dt and K increase with the elastic modulus of the sample surface. The higher MRR obtained with stiffer sample surfaces is attributed to the higher local contact pressures arising at fully-plastic contacts. Hence, stiffer surfaces acquire smoother topographies and are polished faster because of the dominance of surface smoothening. Figures 7.14(d)–7.14(f) show that R_q^{ss} does not correlate with the yield strength as opposed to the MRR and the wear coefficient that show a strong dependence on the yield strength of the sample surface. The sharp decrease of dh_1/dt and K with increasing yield strength is attributed to the marked decrease of fully-plastic contacts with the increase of the plastic flow resistance of the polished surface.

7.4 Conclusions

In this chapter, a quasi-static mechanics analysis of nanoscale polishing was presented for elastic-plastic surfaces exhibiting multi-scale (fractal) roughness behavior. Numerical results of the steady-state roughness of the polished surface, material removal rate, and wear coefficient were obtained in terms of process parameters, such as apparent contact pressure and polishing time, topographies (roughness) of the interacting surfaces, average size and density of the hard abrasive nanoparticles, and elastic-plastic material properties of the polished surface. Based on the presented results and discussion, the following main conclusions can be drawn from this chapter.

1. The roughness of the polished surface and the material removal rate decrease rapidly in the early stage of polishing, reaching a steady state when smoothening and roughening effects attain equilibrium.

2. The length scales of surface features affected by nanoscale polishing are indicated by the intensity decrease of low-frequency components in the power spectral density function of the evolving surface topography.

3. The effect of the initial roughness of the polished surface on the steady-state roughness and material removal rate is secondary, as shown by the overlap of the power spectral density functions of polished surfaces of different initial roughness.

4. The material removal rate increases with the apparent contact pressure. However, the pressure effect on the steady-state roughness of the polished surface and the wear coefficient is secondary because the fractions of fully-plastic and elastic-plastic contacts are not influenced by the variation of the apparent contact pressure.

5. A rougher polishing plate yields lower material removal rate (wear coefficient) and higher final roughness of polished surface.

6. Smaller size and/or higher density of nanoparticles produce smoother polished surfaces, faster material removal, and higher wear coefficient.

7. Stiff surfaces obtain smoother final topographies and are polished at higher material removal rates than compliant surfaces. While the material removal rate (wear coefficient) decreases sharply with the increase of the yield strength of the polished surface, the effect on the steady-state roughness of the polished surface is secondary.

8. Simulation trends and analytical predictions of the steady-state roughness and material removal rate were shown to be in good agreement with experimental results of Al_2O_3-TiC surfaces polished with diamond nanoparticles under similar conditions.

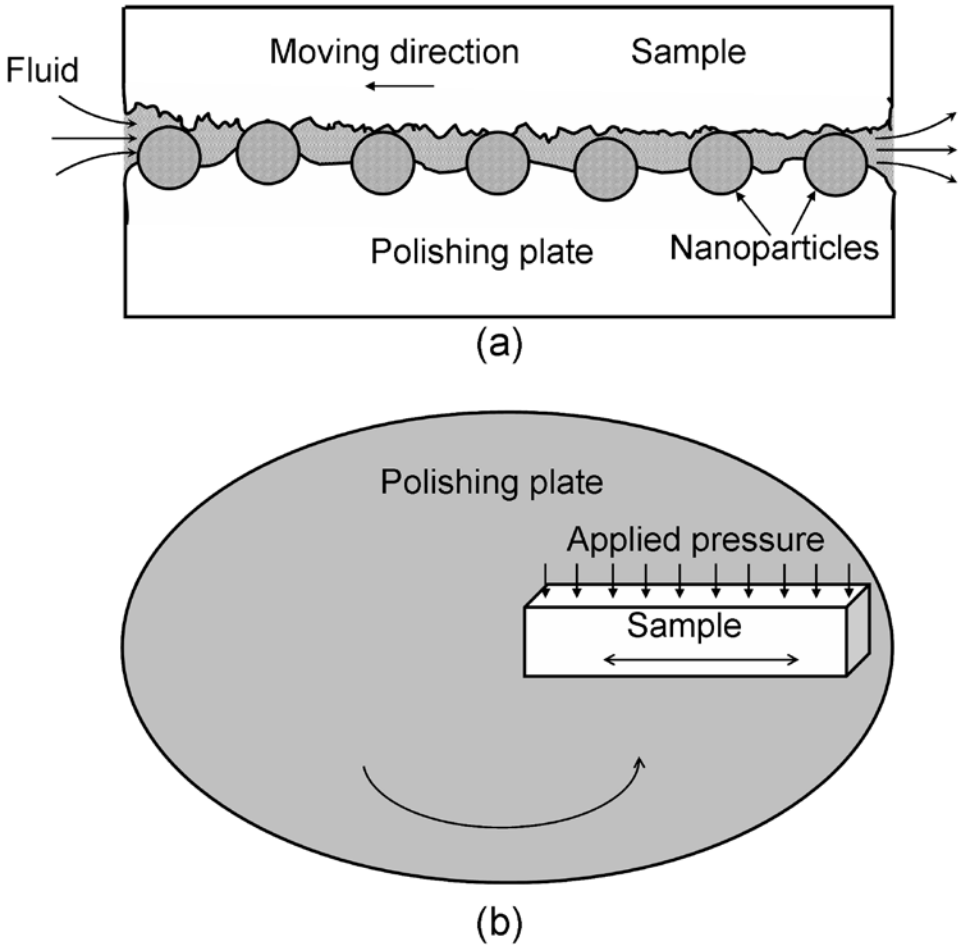

Figure 7.1 (a) Cross-section schematic and (b) kinematics of the polishing process.

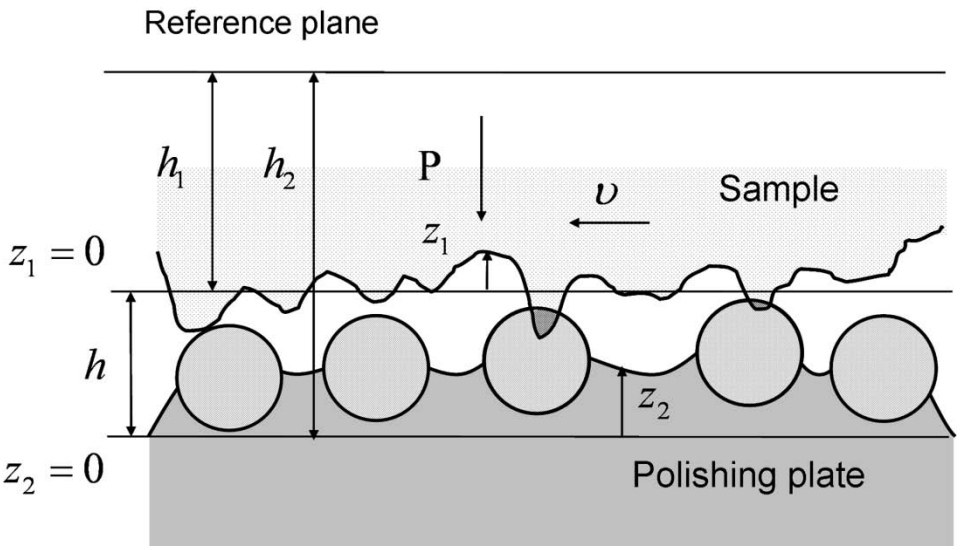

Figure 7.2 Schematic illustration of the polishing process with pertinent nomenclature.

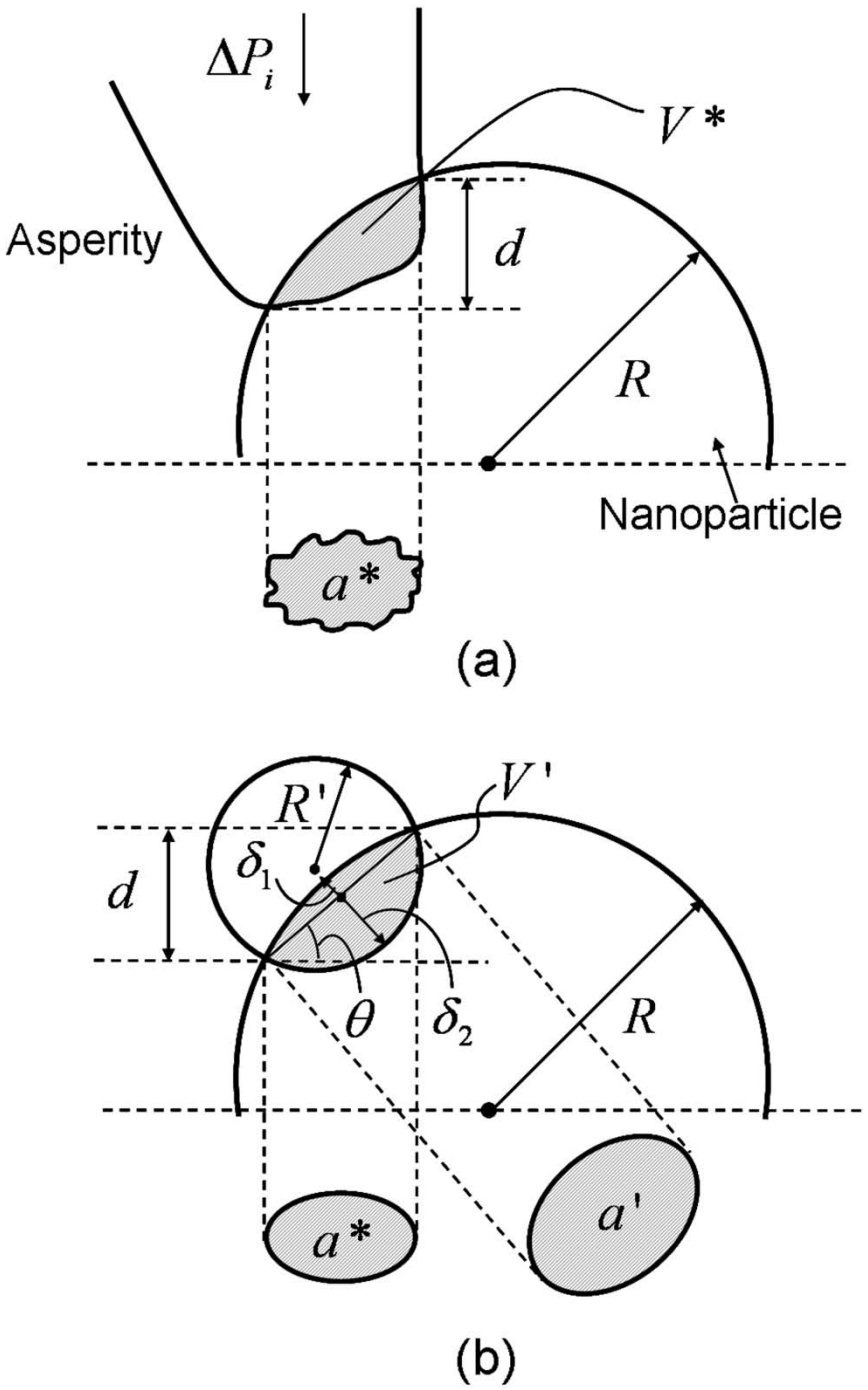

Figure 7.3 (a) Schematic representation of asperity-nanoparticle interaction and (b) equivalent model of an asperity truncated by a nanoparticle.

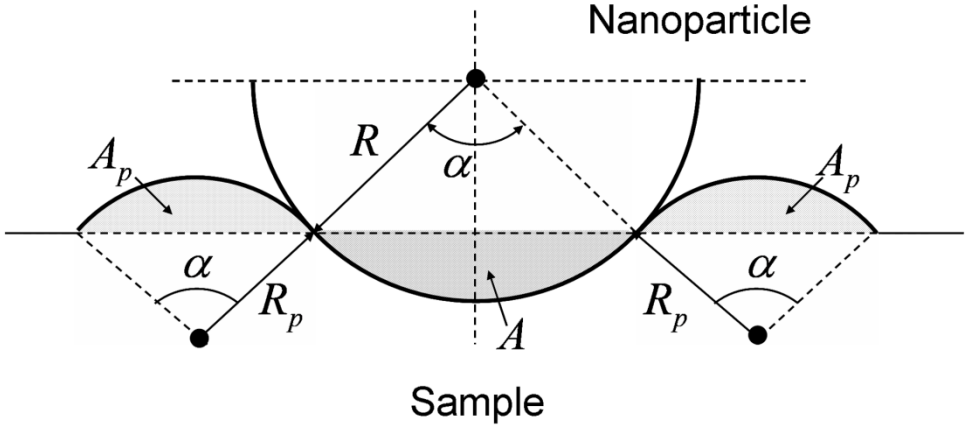

Figure 7.4 Schematic of surface modification at an elastic-plastic contact due to plowing caused by a hard nanoparticle.

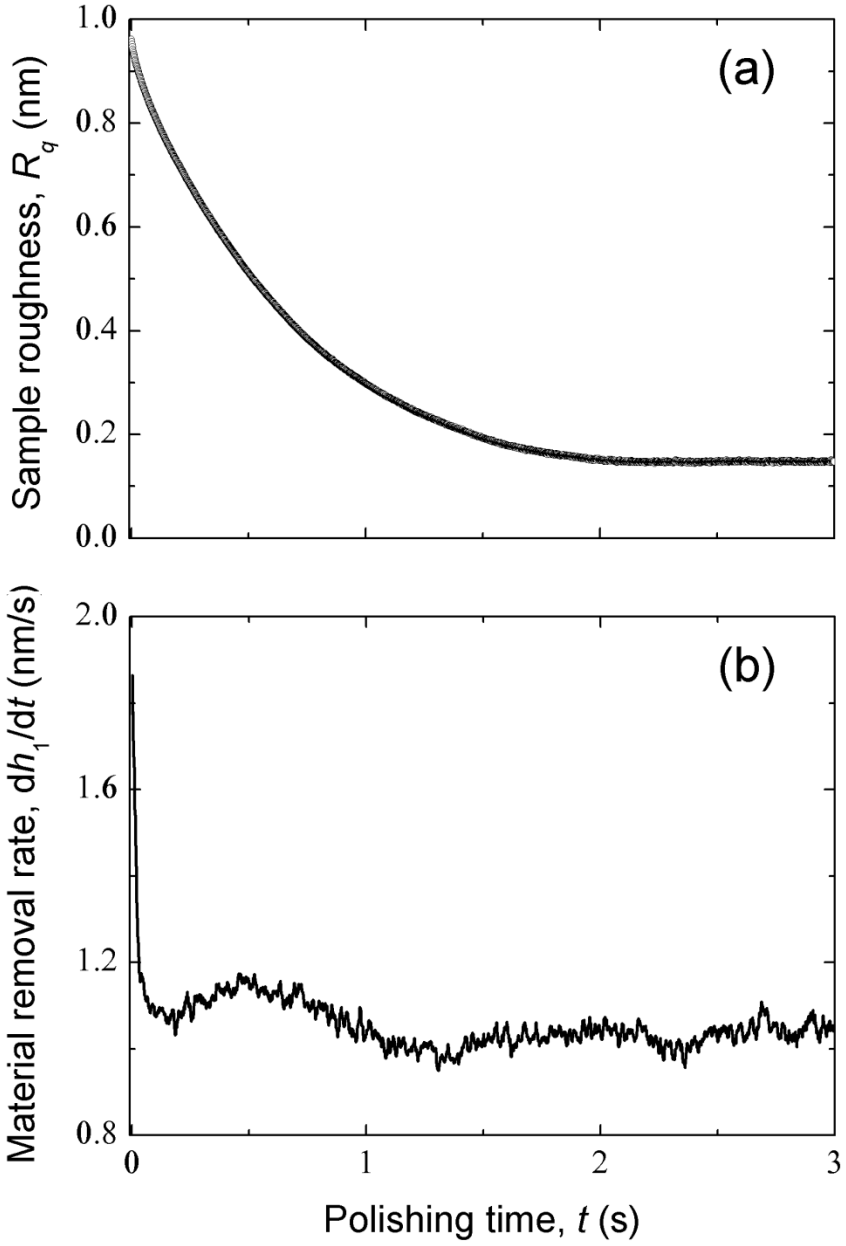

Figure 7.5 (a) Roughness of sample surface R_q and (b) material removal rate dh_1/dt versus polishing time t ($p_a = 356$ kPa, $\upsilon = 133$ mm/s, $R_q = 1$ nm (polishing plate), $R = 50$ nm, $n_p = 9$ μm^{-2}, $E = 390$ GPa, $Y = 7.3$ GPa, $H = 20$ GPa, and $H_l = 45$ MPa).

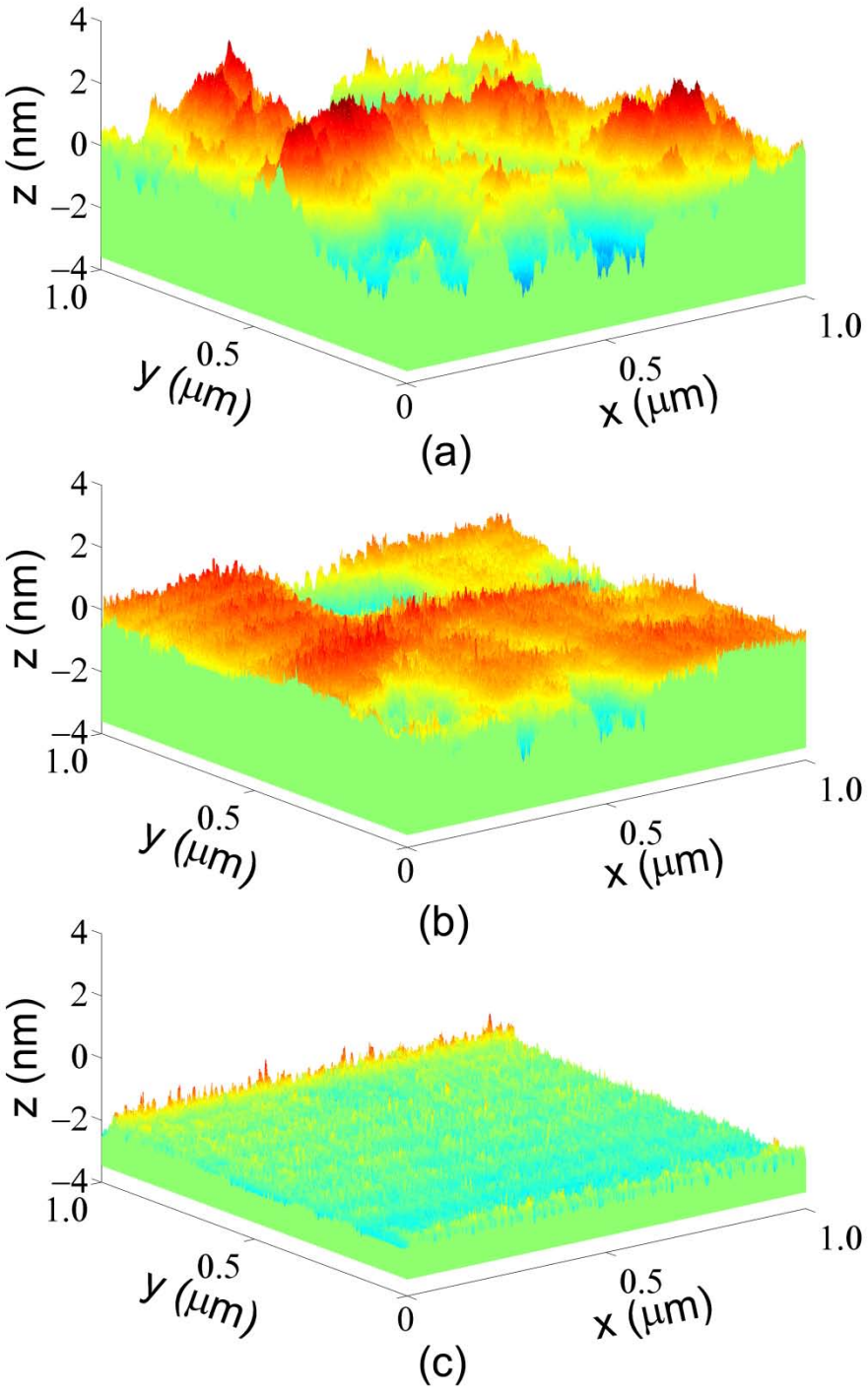

Figure 7.6 (a) Initial ($R_q^i = 0.96$ nm), (b) transient ($R_q^t = 0.59$ nm), and (c) steady-state ($R_q^{ss} = 0.15$ nm) sample surface topographies ($p_a = 356$ kPa, $\upsilon = 133$ mm/s, $R_q = 1$ nm (polishing plate), $R = 50$ nm, $n_p = 9\ \mu m^{-2}$, $E = 390$ GPa, $Y = 7.3$ GPa, $H = 20$ GPa, and $H_l = 45$ MPa).

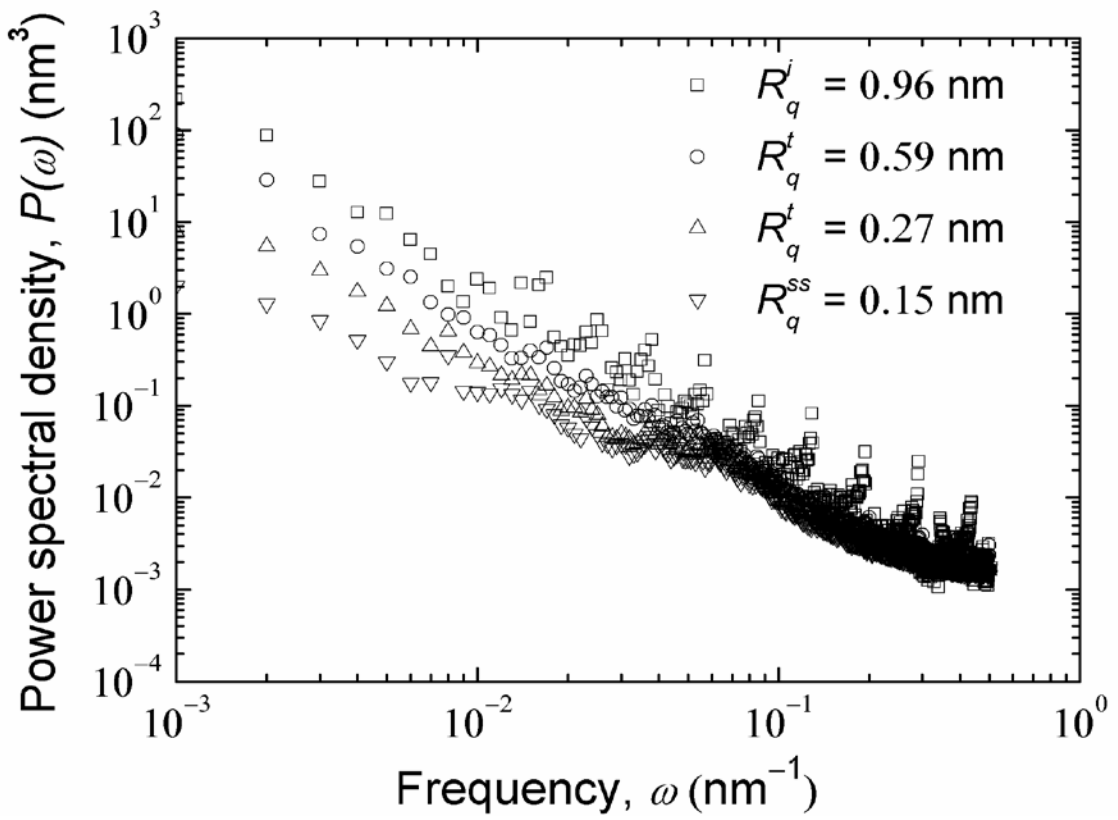

Figure 7.7 Power spectral density $P(\omega)$ of initial ($R_q^i = 0.96$ nm), transient ($R_q^t = 0.59$ and 0.27 nm), and steady-state ($R_q^{ss} = 0.15$ nm) sample surface topographies ($p_a = 356$ kPa, $\upsilon = 133$ mm/s, $R_q = 1$ nm (polishing plate), $R = 50$ nm, $n_p = 9$ μm^{-2}, $E = 390$ GPa, $Y = 7.3$ GPa, $H = 20$ GPa, and $H_l = 45$ MPa).

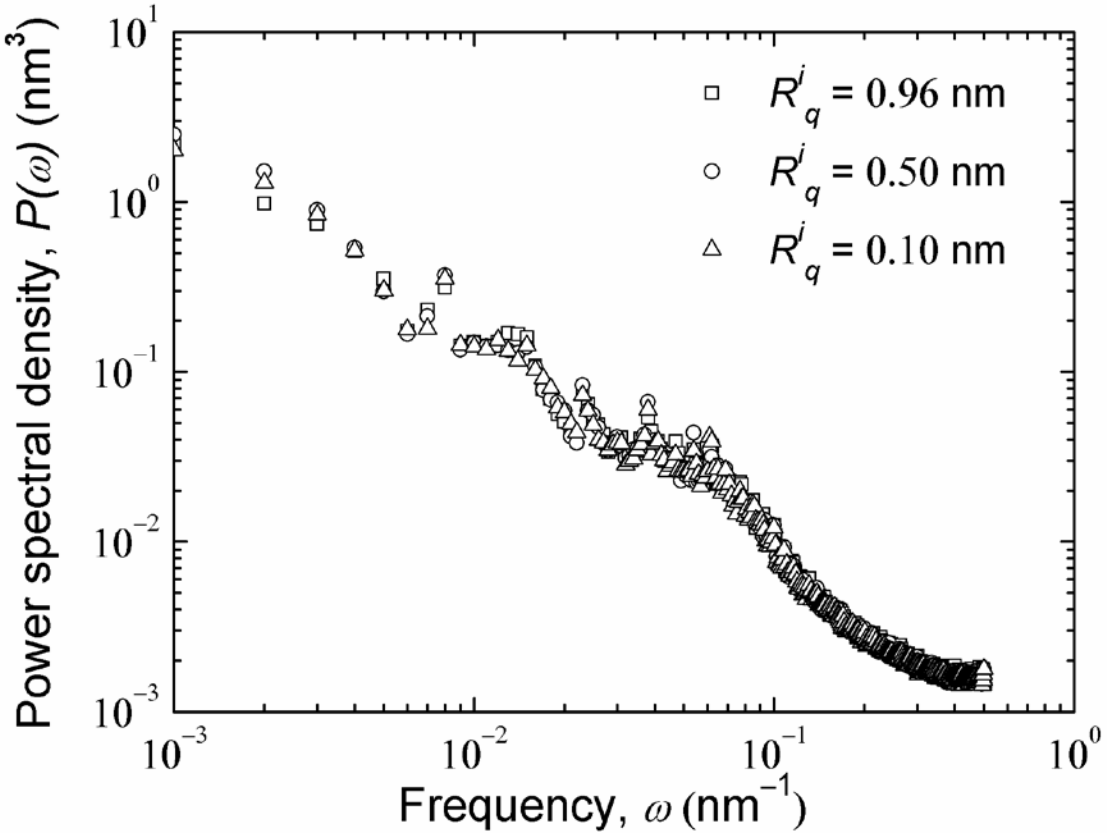

Figure 7.8 Power spectral density $P(\omega)$ of sample surface topography obtained at steady-state polishing for initial roughness of sample surface $R_q^i = 0.96,\ 0.50$, and 0.10 nm ($p_a = 356$ kPa, $\upsilon = 133$ mm/s, $R_q = 1$ nm (polishing plate), $R = 50$ nm, $n_p = 9\ \mu\text{m}^{-2}$, $E = 390$ GPa, $Y = 7.3$ GPa, $H = 20$ GPa, and $H_l = 45$ MPa).

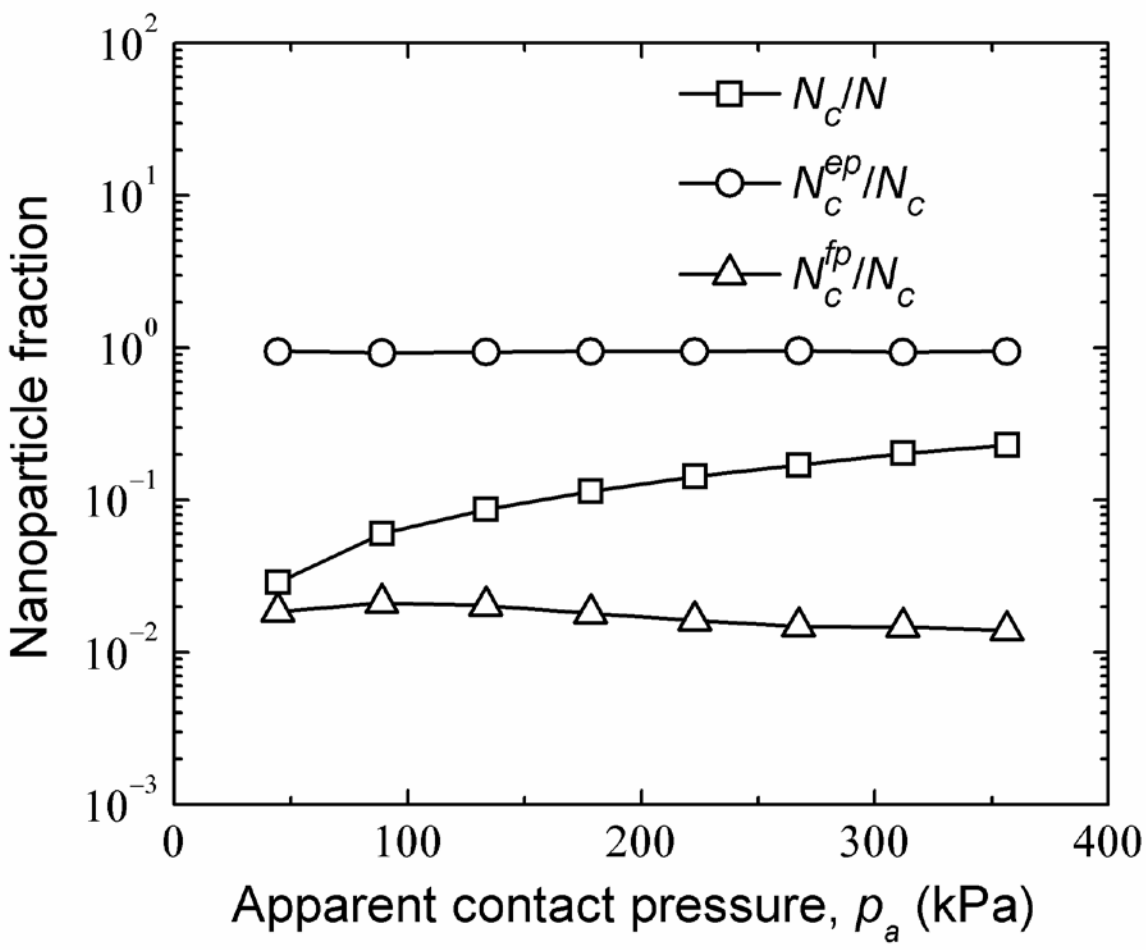

Figure 7.9 Asperity-nanoparticle contact fractions at steady-state polishing versus apparent contact pressure p_a, where N_c = number of total contacts, N_c^{ep} = elastic-plastic contacts, N_c^{fp} = fully-plastic contacts, and N = number of nanoparticles existing in the analysis area ($\upsilon = 133$ mm/s, $R_q = 5$ nm (polishing plate), $R = 50$ nm, $n_p = 9\ \mu\text{m}^{-2}$, $E = 390$ GPa, $Y = 7.3$ GPa, $H = 20$ GPa, and $H_l = 45$ MPa).

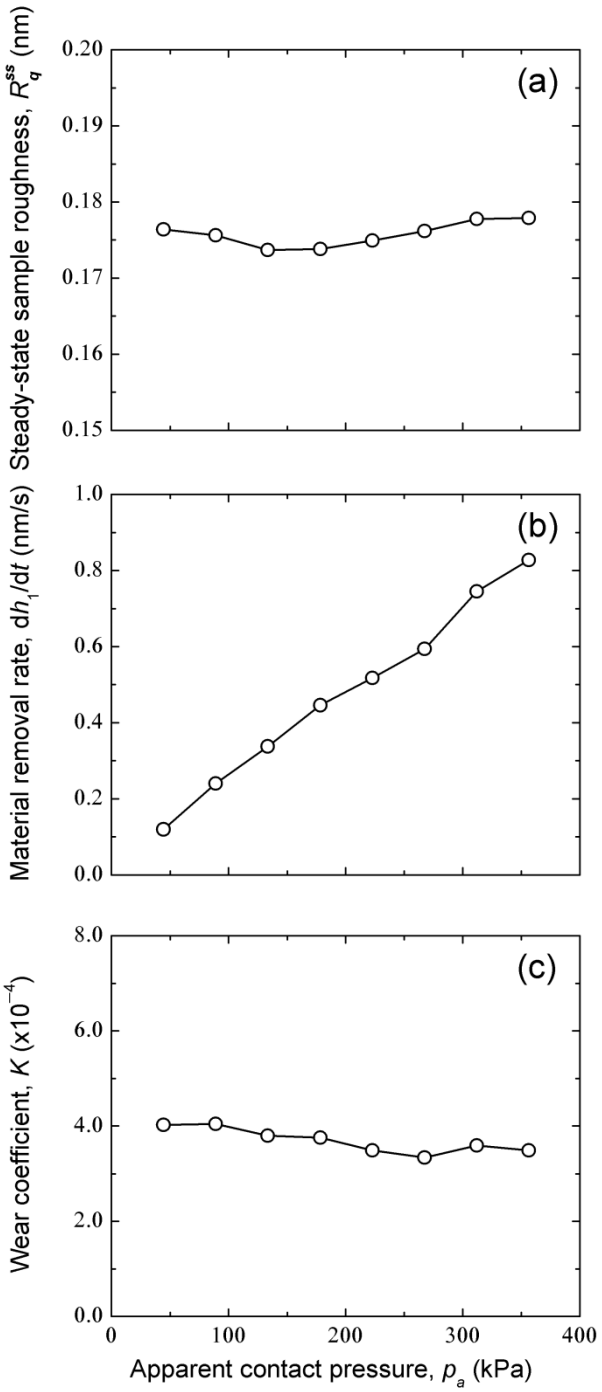

Figure 7.10 (a) Roughness of sample surface R_q^{ss}, (b) material removal rate dh_1/dt, and (c) wear coefficient K versus apparent contact pressure p_a at steady-state polishing ($\upsilon = 133$ mm/s, $R_q = 5$ nm (polishing plate), $R = 50$ nm, $n_p = 9$ μm^{-2}, $E = 390$ GPa, $Y = 7.3$ GPa, $H = 20$ GPa, and $H_l = 45$ MPa).

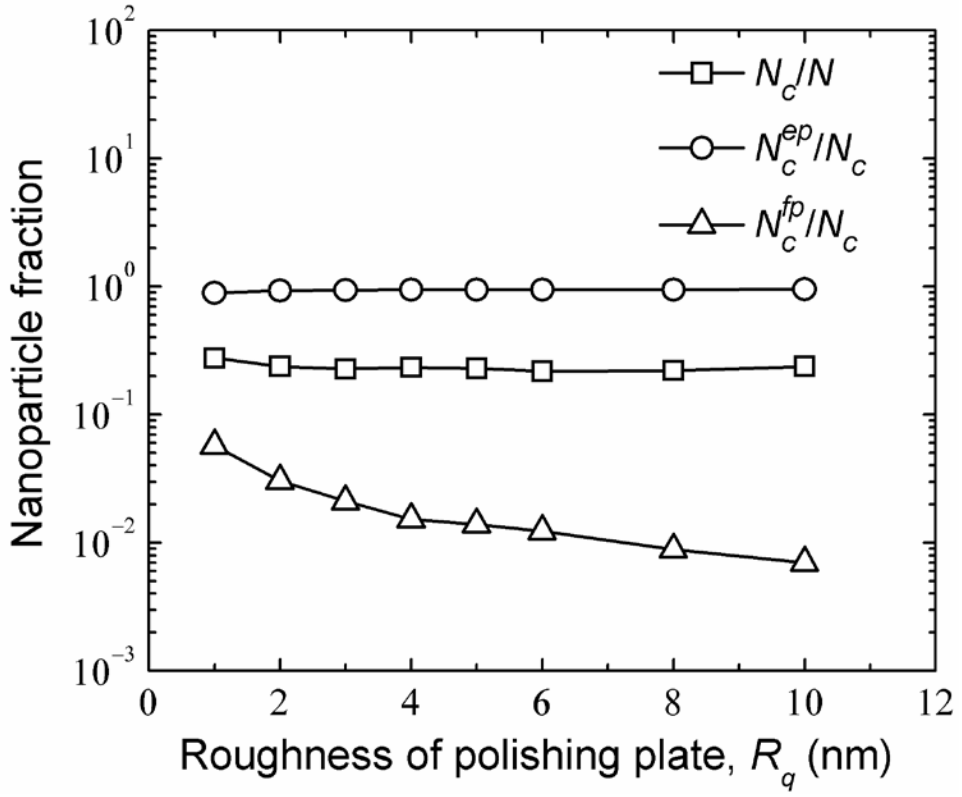

Figure 7.11 Asperity-nanoparticle contact fractions versus surface roughness R_q of polishing plate at steady-state polishing, where N_c = number of total contacts, N_c^{ep} = elastic-plastic contacts, N_c^{fp} = fully-plastic contacts, and N = number of nanoparticles existing in the analysis area ($p_a = 356$ kPa, $\upsilon = 133$ mm/s, $R = 50$ nm, $n_p = 9$ μm^{-2}, $E = 390$ GPa, $Y = 7.3$ GPa, $H = 20$ GPa, and $H_l = 45$ MPa).

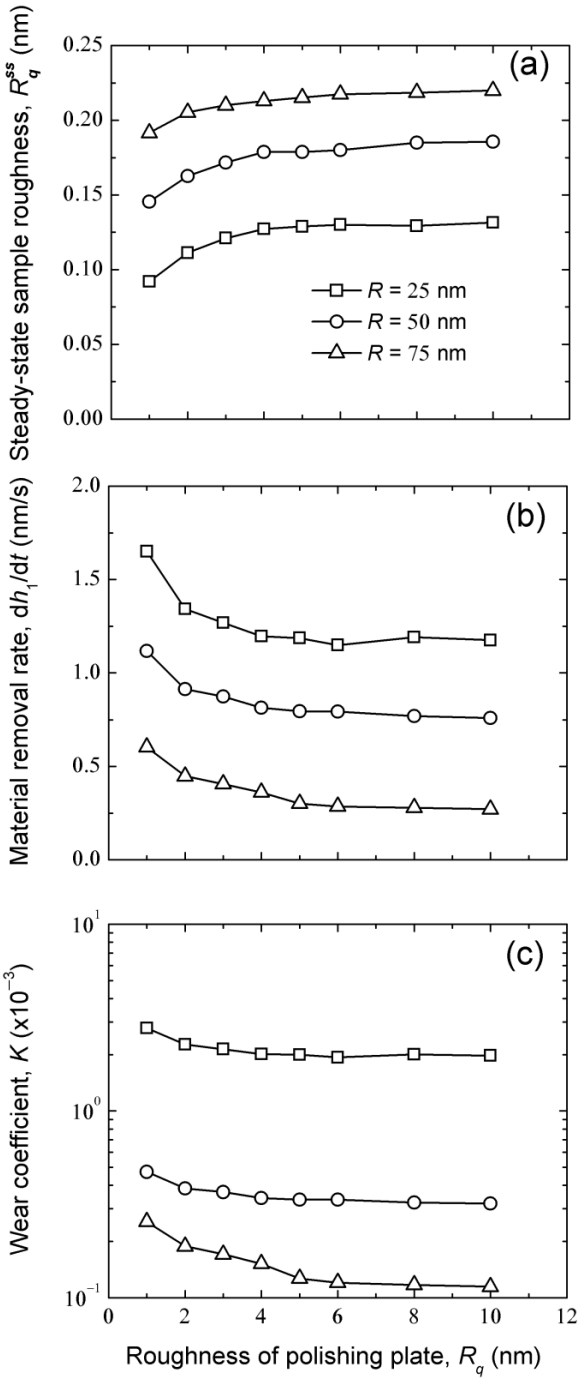

Figure 7.12 (a) Roughness of sample surface R_q^{ss}, (b) material removal rate dh_1/dt, and (c) wear coefficient K versus surface roughness R_q of polishing plate at steady-state polishing (R = 25 nm (p_a = 89 kPa), 50 nm (p_a = 356 kPa), and 75 nm (p_a = 356 kPa), $\upsilon = 133$ mm/s, $n_p = 9\ \mu\text{m}^{-2}$, $E = 390$ GPa, $Y = 7.3$ GPa, $H = 20$ GPa, and $H_l = 45$ MPa).

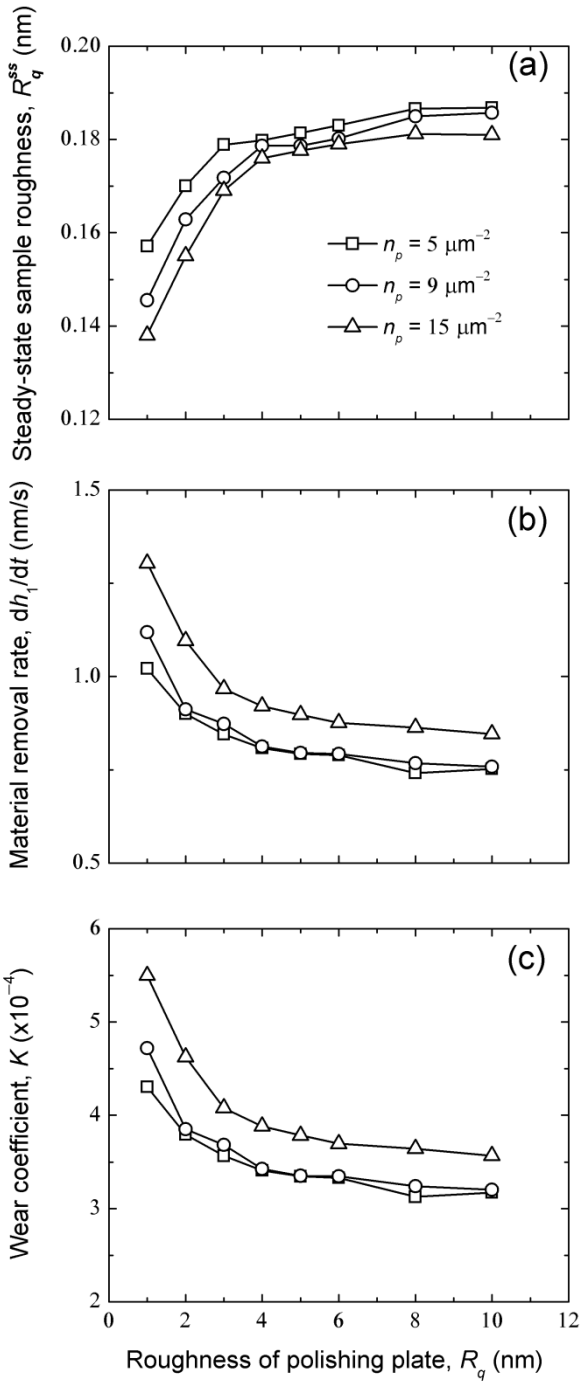

Figure 7.13 (a) Roughness of sample surface R_q^{ss}, (b) material removal rate dh_1 / dt, and (c) wear coefficient K versus surface roughness R_q of polishing plate at steady-state polishing ($n_p = 5$, 9, and 15 μm^{-2}, $p_a = 356$ kPa, $\upsilon = 133$ mm/s, $R = 50$ nm, $E = 390$ GPa, $Y = 7.3$ GPa, $H = 20$ GPa, and $H_l = 45$ MPa).

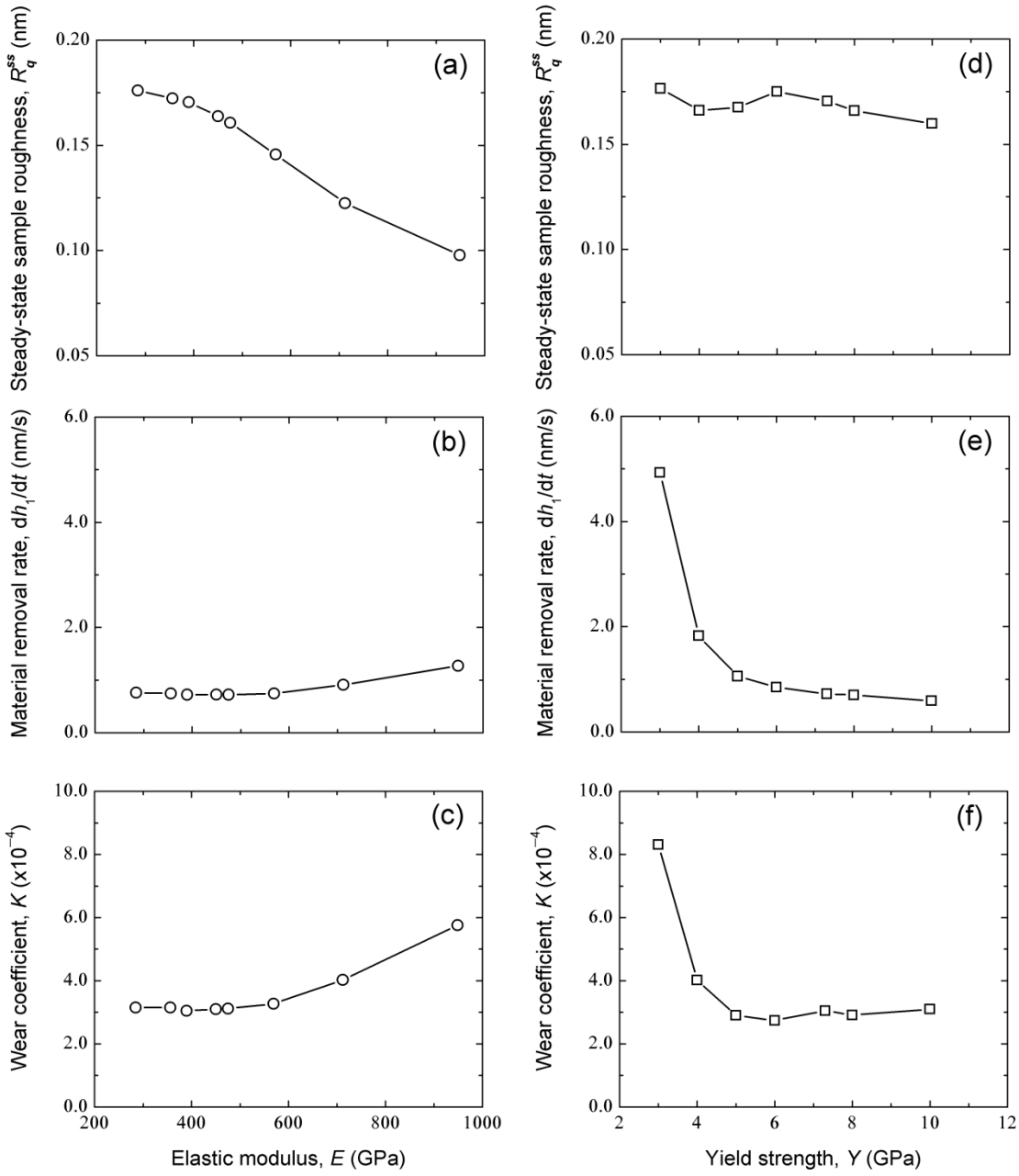

Figure 7.14 (a) Roughness of sample surface R_q^{ss}, (b) material removal rate dh_1/dt, and (c) wear coefficient K versus elastic modulus E of sample surface with $Y = 7.3\,\text{GPa}$; (d) roughness of sample surface R_q^{ss}, (e) material removal rate dh_1/dt, and (f) wear coefficient K versus yield strength of sample surface with $E = 390\,\text{GPa}$ ($p_a = 356\,\text{kPa}$, $\upsilon = 133\,\text{mm/s}$, $R_q = 5\,\text{nm}$ (polishing plate), $R = 50$ nm, $n_p = 9\,\mu\text{m}^{-2}$, and $H_l = 45\,\text{MPa}$).

Chapter 8
A probabilistic analysis of third-body particle embedment

8.1 Introduction

The third-body process under consideration involves two proximity surfaces in relative motion separated by a fluid film containing small particles. The particles may be purposely introduced into the fluid medium, such as in chemical-mechanical polishing and lapping (Evans and Dornfeld, 2003), or accidentally as in the cases of airborne particulate contaminants introduced into the system or wear particles generated during sliding of the bearing surfaces in the boundary lubrication regime (Nilsson et al., 2006). A common cause of failure for contact components or bearing surfaces was through the abrasion caused by solid contaminates in the lubricant (Dwyer-Joyce et al., 1994). The debris in the lubricant caused a significant increase of pressure on the location of debris leading to the debris dents on the bearing surfaces (Kang et al., 2000). Besides, debris dents on bearing surfaces were the sources of crack initiation leading to final fatigue failure, as they were large enough (Nelias and Ville, 2000). Acoustic emission examination showed that a low concentration of contaminates in the lubricant generated very strong AE feedback in the bearings (Miettinen and Andersson, 2000).

Although abrasive wear by particles trapped between proximity surfaces or bearing surfaces was generally detrimental to component longevity, abrasion caused by particles was critical to surface planarization and polishing, such as chemical-mechanical polishing. The material removal rate and surface finishing were affected by plenty of parameters, such as abrasive particle size and concentration (Basim et al., 2000; Zhou et al., 2002; Fu et al., 2001; Zhao and Chang, 2002; Lei and Luo, 2004), abrasive particle shape (Fu et al., 2001), material properties of work-piece (Zhao and Chang, 2002), pad stiffness (Fu et al., 2001; Lei and Luo, 2004), slurry chemistry (Zhao and Chang, 2002; Lei and Luo, 2004) and abrasive particle hardness or density (Ramarajan et al., 1999), etc. However, since the movement, embedment, and plowing of third-body particles at submicron scales are stochastic processes, controlling the material removal to produce ultra-smooth surfaces is still challenging especially for accurate prediction of the number of abrasive particles involved in abrasion, which is of great importance to investigate the material removal process (Luo and Dornfeld, 2003b).

When the size of hard particle exceeded the local surface interference, the hard particle was embedded into the softer surface under relative surface movement and acted as a two-body abrasive particle to the opposed harder surface (Dwyer-Joyce, 1999). The two-body abrasion process was typically used for achieving ultra-smooth surface due to its better surface finish compared with the three-body abrasion process, which had higher material removal rate (Jiang et al., 2003). For example, the lapping process was using the lapping plate, made of a soft lapping plate embedded with hard abrasives, to polish magnetic recording head (Jiang et al., 2003; Tjiptoharsono et al., 2010). To optimize the lapping process of ceramic heads to achieve a root-mean-square (rms) roughness of less than 0.2 nm required for extremely-high-density recording, understanding of the fabrication process of the lapping plate, especially to control the density of embedded diamond nanoparticles of the lapping plate, was important and critical. The objective

of this chapter was to develop a probabilistic model of third-body particle embedment to estimate the particle embedment density in terms of the geometries and topographies of proximity surfaces, particle size distribution, normal applied load, kinematics, surfaces properties and fluid properties of the hydrodynamic film between the moving surfaces.

8.2 Analysis

Figure 8.1 shows a schematic diagram of the problem under consideration. A fluid with suspended hard particles (slurry) forms a hydrodynamic film between a hard surface and a soft surface, corresponding to the top and bottom plates, respectively. Under the compression between the hard plate and the soft plate, the hard particles are embedded into the soft plate finally. To achieve the objective for estimating the particle embedment density, the analysis of the problem is divided into two steps or two models, hydrodynamic model and probabilistic model for particle embedment. The hydrodynamic model analyzes the hydrodynamic film as functions of kinematics, slurry properties, geometries, applied load and surface properties such as friction coefficients, and estimates the mean surface separation distance (hydrodynamic film thickness), which is introduced as a parameter into the probabilistic model for particle embedment. The particle embedment density is estimated by the probabilistic model in terms of the mean surface separation distance, particle size distribution, and plates surface topographies.

Figure 8.2 shows the kinematic model of the top and bottom plates. The top plate is loaded by a known normal force L, whereas the bottom plate is spinning at a given angular speed ω_1. Two rollers constrain the top plate to rotate at a speed of ω_2. The bottom and top plate velocities, U_1 and U_2, respectively, are expressed in circumferential and radial directions of polar coordinates (r, θ) as

$$U_1^r = \omega_1 d \sin\theta, \tag{8.1a}$$

$$U_1^\theta = \omega_1 (d \cos\theta + r), \tag{8.1b}$$

$$U_2^r = 0, \tag{8.1c}$$

$$U_1^\theta = \omega_2 r, \tag{8.1d}$$

where $r_{min} \le r \le r_{max}$. d is the distance between the two plate centers, r is the radius of the top plate for given position, and r_{min} and r_{max} are the inner radius and outer radius of the top plate, respectively.

8.2.1 Hydrodynamic model

The normal load applied on the top (hard) plate is balanced by two aspects, fluid pressure due to hydrodynamic effect and the contact force with nano-particles in the interface, which is equal to the contact force between nano-particles and bottom (soft) plate. Due to the low hardness of soft plate, the contact force is negligible compared with the normal force due to hydrodynamic effect, especially for thinner slurry film thickness, which produces significantly high pressure. In current analysis, only hydrodynamic effect is taken into consideration to calculate the thickness of slurry film between two plates.

The slurry film thickness is obtained from a hydrodynamic model on the basis of the following assumptions: (a) two plates had flat plate surfaces, (b) the bottom plate is level positioned and the top plate is tilting, (c) the center of top plate is blank, (d) the top plate is constrained by two rollers, and (e) the particle effect on hydrodynamic film formation is negligible due to small concentration of particles. Substituting Eqs. (8.1) into the two-dimensional Reynolds' equation and assuming incompressible flow with constant density gives

$$\frac{\partial}{\partial r}\left(rh^3\frac{\partial p}{\partial r}\right)+\frac{1}{r}\frac{\partial}{\partial \theta}\left(h^3\frac{\partial p}{\partial \theta}\right)=6\mu\left\{r\omega_1 d\,sin\,\theta\frac{\partial h}{\partial r}+[\omega_1(d\,cos\,\theta+r)-\omega_2 r]\frac{\partial h}{\partial \theta}\right\}, \qquad (8.2)$$

where h is the local slurry film thickness (local gap), p is the pressure, and μ is the absolute viscosity of the fluid.

For the general case of top plate tilting (Fig. 8.3) by angles α and β with respect to the x and y coordinates, respectively, the local gap h is expressed as

$$h=h\left(\bar{h},\alpha,\beta\right)=\bar{h}-r\cos\theta\sin\alpha-r\sin\theta\sin\beta\ , \qquad (8.3)$$

where $\bar{h}$ is the film thickness at the center of the top plate and also is defined as the mean surface separation distance between top plate and bottom plate.

The pressures of inside edge and outside edge are both equal to ambient pressure p_0. Therefore, the boundary conditions are defined as

$$p(r=r_{min})=p_0, \qquad (8.4a)$$

and

$$p(r=r_{max})=p_0. \qquad (8.4b)$$

By given $\bar{h}$, α, β and ω_2, pressure distributions are numerically obtained by solving Eq. (8.2) combined with Eq. (8.3) and Eqs. (8.4) based on finite difference method (Park et al., 2000). The mesh used for the finite difference method is generated by dividing the circumferential and radial length by 80 and 30, respectively. The shear stresses at the bottom surface of the top plate in x and y directions, τ_x and τ_y, are obtained from the following relationships (Sun, 1997):

$$\tau_x=\frac{1}{2}\frac{\partial p}{\partial x}h-\mu\frac{U_2^x-U_1^x}{h}, \qquad (8.5a)$$

and

$$\tau_y=\frac{1}{2}\frac{\partial p}{\partial y}h-\mu\frac{U_2^y-U_1^y}{h}. \qquad (8.5b)$$

The resultant forces and moments at point O (the central point of bottom surface of top plate, shown by Fig. 8.4) are given by

$$F=\iint_\Omega\ p\,dx\,dy, \qquad (8.6a)$$

$$F_{\tau x} = \iint_{\Omega} \tau_x dxdy, \tag{8.6b}$$

$$F_{\tau y} = \iint_{\Omega} \tau_y dxdy, \tag{8.6c}$$

$$M_x = \iint_{\Omega} pydxdy, \tag{8.6d}$$

$$M_y = \iint_{\Omega} -pxdxdy, \tag{8.6e}$$

$$M_z = \iint_{\Omega} \left(\tau_y x - \tau_x y\right)dxdy, \tag{8.6f}$$

where Ω is the circular area within $r_{min} \le r \le r_{max}$. F, $F_{\tau x}$ and $F_{\tau y}$ are resultant forces applied on bottom surface of top plate in *x*, *y* and *z* directions, respectively. M_x, M_y and M_z are resultant moments applied on bottom surface of top plate in *x*, *y* and *z* directions, respectively. Based on Eqs. (8.6), the resultant forces and moments are functions of pressure *p* and shear stresses τ_x and τ_y, which are functions of $\bar{h}$, α, β and ω_2 according to Eqs. (8.5).

As shown by Fig. 8.4, F_{x1}, F_{y1} and F_{z1} are forces applied on top plate through roller *R*1 in *x*, *y* and *z* directions, respectively; whereas F_{x2}, F_{y2} and F_{z2} are forces applied on top plate through roller *R*2 in *x*, *y* and *z* directions, respectively. F_{y1} and F_{y2} are normal contact forces, whereas F_{x1}, F_{z1}, F_{x2}, and F_{z2} are friction forces given by

$$F_{x1} = f_1 F_{y1}, F_{z1} = f_2 F_{y1}, F_{y2} = f_1 F_{x2}, F_{z2} = f_2 F_{x2}, \tag{8.7}$$

where f_1 and f_2 are the coefficient of friction in the circumferential and vertical directions, respectively. Since the rollers are rotating, the friction in circumferential direction is rotational friction, whereas the friction in vertical direction is sliding friction.

From equilibrium considerations, the following force and moment balance equations are achieved:

$$F - F_{z1} - F_{z2} - L = 0, \tag{8.8a}$$

$$M_z - \left(F_{x1} + F_{y2}\right)r_{max} = 0, \tag{8.8b}$$

$$F_{x1} + F_{\tau x} - F_{x2} = 0, \tag{8.8c}$$

$$M_x + \left(F_{y1} + F_{y2}\right)h_{top} - F_{z1} r_{max} = 0, \tag{8.8d}$$

$$F_{\tau y} - F_{y1} - F_{y2} = 0, \tag{8.8e}$$

$$M_y + (F_{x1} - F_{x2})h_{top} + F_{z2} r_{max} = 0, \tag{8.8f}$$

where h_{top} is the vertical distance between rollers and the bottom surface of the top plate.

Combining Eqs. (8.7) and Eqs. (8.8), the force and moment balance equations are reduced to four equations (Eqs. (8.9)) expressed by the resultant forces and the resultant moments in terms of pressure p and shear stresses τ (τ_x and τ_y), which are functions of $\bar{h}$, α, β and ω_2.

$$g_1(\bar{h},\alpha,\beta,\omega_2) = g_1(p,\tau_x,\tau_y) = F - \frac{f_2(F_{\tau y}-f_1F_{\tau x})}{1+f_1^2} - \frac{f_2(f_1F_{\tau y}+F_{\tau x})}{1+f_1^2} - L = 0, \tag{8.9a}$$

$$g_2(\bar{h},\alpha,\beta,\omega_2) = g_2(p,\tau_x,\tau_y) = M_z - \frac{f_1(F_{\tau y}-f_1F_{\tau x})+f_1(f_1F_{\tau y}+F_{\tau x})}{1+f_1^2} r_{max} = 0, \tag{8.9b}$$

$$g_3(\bar{h},\alpha,\beta,\omega_2) = g_4(p,\tau_x,\tau_y) = M_x + F_{\tau y}h_{top} - \frac{f_2(F_{\tau y}-f_1F_{\tau x})}{1+f_1^2} r_{max} = 0, \tag{8.9c}$$

$$g_4(\bar{h},\alpha,\beta,\omega_2) = g_4(p,\tau_x,\tau_y) = M_y + F_{\tau x}h_{top} + \frac{f_2(f_1F_{\tau y}+F_{\tau x})}{1+f_1^2} r_{max} = 0. \tag{8.9d}$$

Using the Newton-Raphson method (Park et al., 2000; Chen and Chen, 2005) to solve Eqs. (8.9), the values of the mean surface separation distance, top plate rotational speed and tilting angles are calculated in terms of the input parameters, such as the applied load, slurry viscosity, rotational speed of the bottom plate, friction coefficients and geometrical parameters, etc.

8.2.2 Probabilistic model of particle embedment

Since the soft bottom plate has weak deformation resistance due to its small hardness, the contact between nano-particle and soft bottom plate causes unrecoverable plastic deformation easily even under very small contact force. Besides, due to the nano-scale size, the interfacial adhesion between nano-particle and soft bottom plate is significant once they are in contact with each other. Therefore, the nano-particle is assumed to be embedded into the soft bottom plate once the particle size was greater than the local gap. The nano-particle is hard to be removed from soft bottom plate due to high interfacial adhesion and significant plastic deformation of bottom plate. Based on previous assumption, the number of particles N_A embedded into a given area A of the bottom plate can be expressed as

$$N_A = \int_{-\infty}^{+\infty} Nf(D)\,P(z<D)dD, \tag{8.10}$$

where $P(z<D)$ is the probability that the local gap distance z is smaller than the particle size D, $f(D)$ is the probability density function of the particle size distribution and N is the particle number in the slurry on a given area A.

According to Fig. 8.5, the local gap distance between the two plate surfaces is written as

$$z = z_1 + z_2 + \bar{h}, \tag{8.11}$$

where z_1 and z_2 are local surface heights of top and bottom plates referring to their mean planes (as shown by Fig. 8.5), respectively.

The probability for local gap distance less than a given particle size D is expressed as

$$P(z < D) = P\left(z_1 + z_2 + \bar{h} < D\right) = \int_{-\infty}^{+\infty} f'(z_1) \int_{-\infty}^{D-\bar{h}-z_1} f"(z_2)\, dz_2 dz_1, \quad (8.12)$$

where $f'(z_1)$ and $f"(z_2)$ are probability density functions of surface height distributions for the top and bottom plates, respectively. By substituting Eq. (8.12) into Eq. (8.10), the number of embedded particles N_A on a given area A is expressed as

$$N_A = \int_{-\infty}^{+\infty} N\, f(D) \int_{-\infty}^{+\infty} f'(z_1) \int_{-\infty}^{D-\bar{h}-z_1} f"(z_2)\, dz_2 dz_1 dD. \quad (8.13)$$

The particle number N in the slurry of a given area A is dependent on the particle concentration in the slurry. If the entire area A was occupied by the particles and one particle with diameter of D occupied an area of D^2, the relationship between area A and particle number N is expressed by

$$A = \int_{-\infty}^{+\infty} N\, D^2 f(D) dD. \quad (8.14)$$

Eq. (8.14) almost estimates the maximum number of particles staying on the area A. Therefore, the maximum embedded particle density $n = N_A / A$ is obtained by combining Eq. (8.13) and Eq. (8.14) in terms of the particle size distribution, the plates surface topographies and the mean surface separation distance. The value of n is expressed as

$$n = \int_{-\infty}^{+\infty} f(D) \int_{-\infty}^{+\infty} f'^{(z_1)} \int_{-\infty}^{D-\bar{h}-z_1} f"(z_2)\, dz_2 dz_1 dD \,/\, \int_{-\infty}^{+\infty} D^2 f(D) dD. \quad (8.15)$$

8.3 Results and discussion

8.3.1 Hydrodynamic model

Since the mean surface separation distance is of great importance for estimating particle embedment density and the measurement of top plate rotational speed is a suitable *in-situ* method in experiments, the present hydrodynamic model mainly illustrates the variations of the top plate rotational speed and the mean surface separation in terms of the adjustable parameters in experiments, such as slurry properties, applied load, bottom plate rotational speed, height of rollers and friction coefficients between rollers and top plate. In current study, d is set to be 130 mm, f_1 is assumed to be 0.095, and r_{max} and r_{min} are set to be 67.5 mm and 30 mm, respectively.

Figures 8.6 illustrate the effects of normal applied load L and slurry viscosity μ on the mean surface separation distance $\bar{h}$ and the top plate rotational speed ω_2. The value of $\bar{h}$ increases with the reduction of L. At the range of large L, the log-log curve of $\bar{h}$ versus L is linear and $\bar{h}$ is inversely proportional to L. For example, at μ = 3.2 cp, when the values of L are 10 N and 100 N, the values of $\bar{h}$ are equal to 446 nm and 45 nm, respectively. The value of $\bar{h}$ increases with the slurry viscosity μ and the increment of $\bar{h}$ under the effect of μ is weakened by decreasing L. At the range of small $\bar{h}$ or large L, $\bar{h}$ is proportional to μ. For example, at L = 100 N, the values of $\bar{h}$ are equal to 14 nm, 45 nm and 70 nm, with μ equal to 1 cp, 3.2 cp and 5 cp, respectively. The top-plate rotational speed ω_2 is reduced by increasing the normal load L and achieves a low limit value as L is large enough. The value of ω_2 increases with slurry viscosity μ and the increment of ω_2 is also weakened by increasing L until ω_2 is independent on μ at the range of large L.

Figures 8.7 show the effect of the bottom plate rotational speed ω_1 on the mean surface separation distance $\bar{h}$ and the top plate rotational speed ω_2. The value of $\bar{h}$ increases with ω_1 and the increment of $\bar{h}$ is weakened by decreasing L. At the range of small $\bar{h}$ or large L, $\bar{h}$ is proportional to ω_1. For example, at L = 100 N, the values of $\bar{h}$ are equal to 22.5 nm, 45 nm and 90 nm, with ω_1 equal to 15 rpm, 30 rpm and 60 rpm, respectively. The top-plate rotational speed ω_2 increases with the value of ω_1 and the ratio of ω_1/ω_2 is about 1.5 at the large values of L. The effect of ω_1 on ω_2 is much stronger than the effects of L and μ, which just cause <5% variation of ω_2.

Figures 8.8 show the effect of the roller position h_{top} on the mean surface separation distance $\bar{h}$ and the top plate rotational speed ω_2. The value of $\bar{h}$ decreases but the value of ω_2 increases with the increase of h_{top}. At the range of small $\bar{h}$ or large L, the values of both $\bar{h}$ and ω_2 keep constant and are independent on the roller position h_{top}.

Figures 8.9 illustrate the effect of the ratio of the vertical friction coefficient f_2 over the circumferential friction coefficient f_1 on the mean surface separation distance $\bar{h}$ and the top plate rotational speed ω_2. The value of $\bar{h}$ increases with f_2/f_1 and the increment of $\bar{h}$ under effect of f_2/f_1 is weakened by decreasing L. At the range of small $\bar{h}$ or large L, $\bar{h}$ is linear proportional to f_2/f_1. For instance, at L = 100 N, as f_2/f_1 are equal to 1, 2 and 3, the values of $\bar{h}$ are equal to 15 nm, 30 nm and 45 nm, respectively. The value of ω_2 increases with f_2/f_1 and the increment of ω_2 is weakened by increasing L until the effect of ω_2 on f_2/f_1 is negligible at large value of L.

8.3.2 Analysis of mean surface separation distance in nano-scale

When the mean surface separation distance $\bar{h}$ is in nano-scale, $\bar{h}$ is independent on height of roller position h_{top} and is inversely proportional to applied load L and proportional to slurry viscosity μ, bottom-plate rotational speed ω_1 and ratio of friction coefficients f_2/f_1. The value of $\bar{h}$ in nano-scale is expressed as

$$\bar{h} = \frac{15.747\mu\omega_1}{L}\left(\frac{f_2}{f_1}\right). \tag{8.16}$$

Figures 8.10 illustrate the comparison of the values of $\bar{h}$ in nano-scale obtained from simulation of hydrodynamic model and calculated from Eq. (8.16) in terms of applied load L, slurry viscosity μ, bottom-plate rotational speed ω_1 and ratio of friction coefficients f_2/f_1. The difference of the results from simulation and calculation is negligible.

Since the tilting angles of top plate are very small and close to zero based on simulation results, the values of $\bar{h}$ are the same everywhere and the two plates are treated to be parallel to each other. Since the particles have the chances to be embedded into the soft bottom plate just when the gap between two plates is comparable to the particle size, Eq. (8.16) is of great accuracy to estimate the value of $\bar{h}$ in probabilistic model if the size of hard particle was in nano-scale.

8.3.3 Probabilistic model of particle embedment

As the particle size and surface topographies of two surfaces are assumed to be normal distributed, the numerical results for the embedded particle density are obtained for different values of surface roughness and different particle size distributions. The probability density functions of surface height distributions ($f'(z_1)$ and $f'(z_1)$) and particle size distributions ($f(D)$) are expressed by

$$f'(z_1) = \frac{1}{\sigma_1\sqrt{2\pi}} exp\left(-\frac{z_1-\mu_1}{2\sigma_1^2}\right), \tag{8.17a}$$

$$f"(z_2) = \frac{1}{\sigma_2\sqrt{2\pi}} exp\left(-\frac{z_2-\mu_2}{2\sigma_2^2}\right), \tag{8.17b}$$

$$f(D) = \frac{1}{\sigma_d\sqrt{2\pi}} exp\left(-\frac{D-\mu_d}{2\sigma_d^2}\right), \tag{8.17c}$$

where μ_1 and μ_2 are the mean height of the top-plate and bottom-plate respectively; σ_1 and σ_2 are the root-mean-square (rms) roughness of the surfaces of top-plate and bottom-plate respectively; μ_d and σ_d are the mean and standard deviation of the particle size respectively.

By substituting the three probability density functions (Eqs. (8.17)) into the function of the embedded particle density (Eq. (8.15)), the embedded particle density n is obtained through numerical calculation. According to the definition of z_1 and z_2, μ_1 and μ_2 are set to zero, and the density of embedded particles is estimated in current study in terms of the mean surface separation distance $\bar{h}$, the surface roughness of plates σ_1 and σ_2, the mean and standard deviation of particle size μ_d and σ_d.

Figures 8.11 illustrate the variations of embedded particle density n as functions of the mean surface separation distance $\bar{h}$, and the mean and standard deviation of the particle size, μ_d and σ_d. The embedded particle density n decreases with the increase of $\bar{h}$. The embedded particle density n reaches an upper limit as the value of $\bar{h}$ is small enough, whereas at large value of $\bar{h}$, n achieves a lower limit, which is equal to zero. The value of n transits from the upper limit to the lower limit with increasing of $\bar{h}$ as the value of $\bar{h}$ around the mean particle size μ_d, since all particles are embedded into soft plate with $\bar{h}$ much smaller than μ_d and no particle is embedded into soft plate with $\bar{h}$ much larger than μ_d. Besides, the upper limit of n increases by decreasing the mean particle size μ_d, since more particles are distributed on the same area of the soft substrate before embedment. The increase of standard deviation of the particle size σ_d reduces the upper limit of n but enlarges the transition range of $\bar{h}$ making n from the upper limit to the lower limit. The embedded particle density n increases with σ_d as $\bar{h} > \mu_d$, and vice vesa.

Figures 8.12 show the effects of roughness of the top-plate and the bottom-plate σ_1 and σ_2 on the density of embedded particles n. The effects of σ_1 and σ_2 on embedded particle density n are quite similar. The upper limit of n is independent on σ_1 and σ_2. The increase of σ_1 or σ_2 enlarges the transition range of $\bar{h}$ making n from upper limit to lower limit. The embedded particle density n increases with σ_1 or σ_2 as $\bar{h} > \mu_d$, and vice vesa.

Above all, the embedded particle density n is dependent on the correlation between the particle sizes, the interface gap and the surface topographies of two plates. The increase of μ_d induces the variation of n and a higher particle embedment density is achieved by reducing the value of the reduction of $\bar{h}$, which depends on applied load L, slurry viscosity μ, bottom-plate rotational speed ω_1 and ratio of friction coefficients f_2/f_1 according to the hydrodynamic analysis. For the embedment of nano-scale particles, the effective value of $\bar{h}$ to make nano-particle embed into soft substrate is also in nano-scale, therefore, the value of $\bar{h}$ can be estimated by using Eq. (8.16). By substituting Eq. (8.16) into Eq. (8.15), the variation of n is analyzed in terms of L, μ, ω_1 and f_2/f_1, as shown by Figs. 8.13. The embedded particle density n increases with the increase of L or the reductions of μ, ω_1 and f_2/f_1, which reduces the value of $\bar{h}$.

The density of embedded diamond nanoparticles in lapping plates for magnetic recording heads estimated by the present analysis was found to be in good agreement with measurements obtained from microscopy observations of such lapping plates. The good agreement between analytical and experimental results indicates that the present model provides insight into the effects of key process parameters and guidance for optimizing the embedded particle density in lapping plates.

8.4 Conclusions

A probabilistic analysis of third-body particle embedment was presented in this chapter for proximity surfaces separated by a hydrodynamic film. The analysis yields accurate estimates of the density of embedded particles in terms of the geometries and topographies of proximity surfaces, particle size distribution, normal load, kinematics, friction coefficients between rollers and top plate, and fluid properties of the hydrodynamic film forming between the moving surfaces. Based on the presented results and discussion, the following main conclusions can be drawn from this chapter.

1. The dependences of the mean surface separation distance on the applied normal load, the slurry viscosity, the bottom-plate rotational speed, the roller position and the ratio of friction coefficients were obtained from a hydrodynamic analysis. Increase of the applied normal load, or decreases of the slurry viscosity, the bottom-plate rotational speed and the ratio of friction coefficients on rollers achieve a smaller mean surface separation distance. The effect of the roller position on the mean surface separation distance is secondary.

2. At nano-scale mean surface separation distances, the mean surface separation distance varies inversely with the applied normal load, and is proportional to the slurry viscosity, the top-plate rotational speed and the ratio of friction coefficients on rollers.

3. The density of embedded particles is mainly correlated to the mean surface separation distance and the mean particle size according to probabilistic model. The effects of standard deviation of the particle size and the surface topographies on the embedded particle density are secondary. The embedded particle density increases by increasing the applied normal load, or decreasing the slurry viscosity, the bottom-plate rotational speed and the ratio of friction coefficients on rollers.

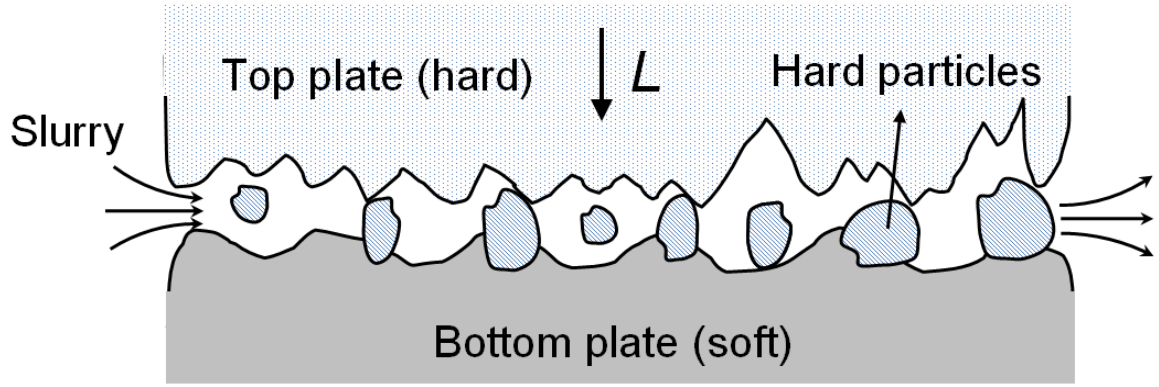

Figure 8.1 Schematic of third-body particle embedment process.

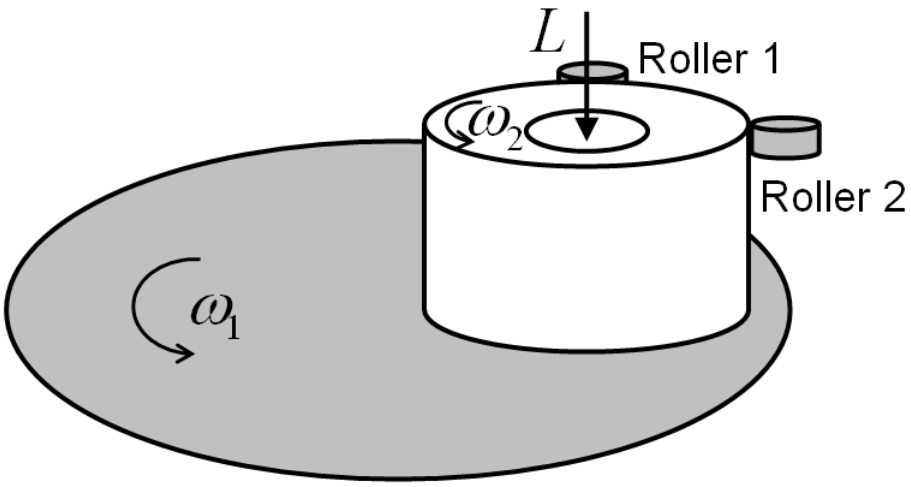

(a)

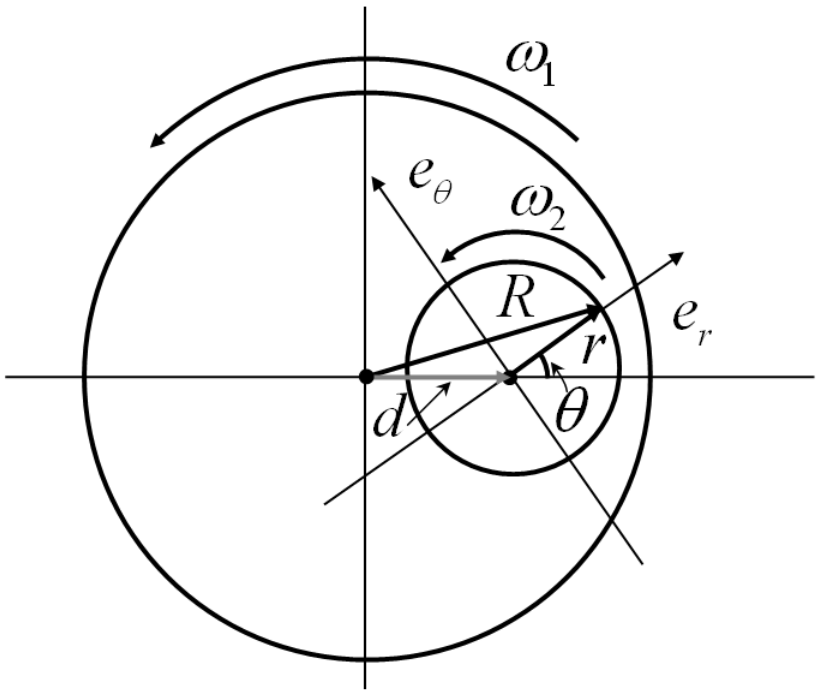

(b)

Figure 8.2 (a) Schematic and (b) kinematic model of the rotating top and bottom plates.

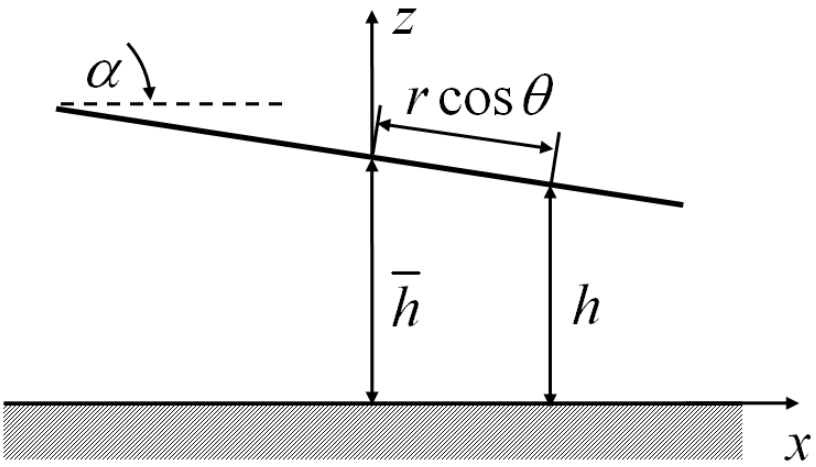

(a)

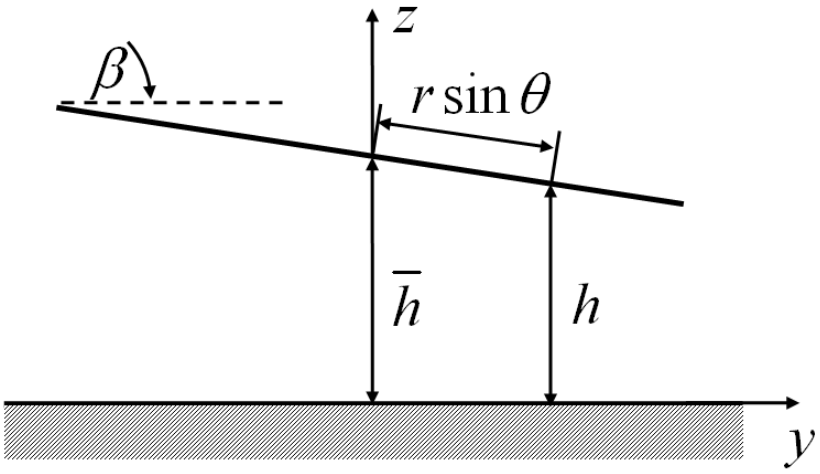

(b)

Figure 8.3 Schematics of the top plate tilting: (a) x-z coordinate, (b) y-z coordinate.

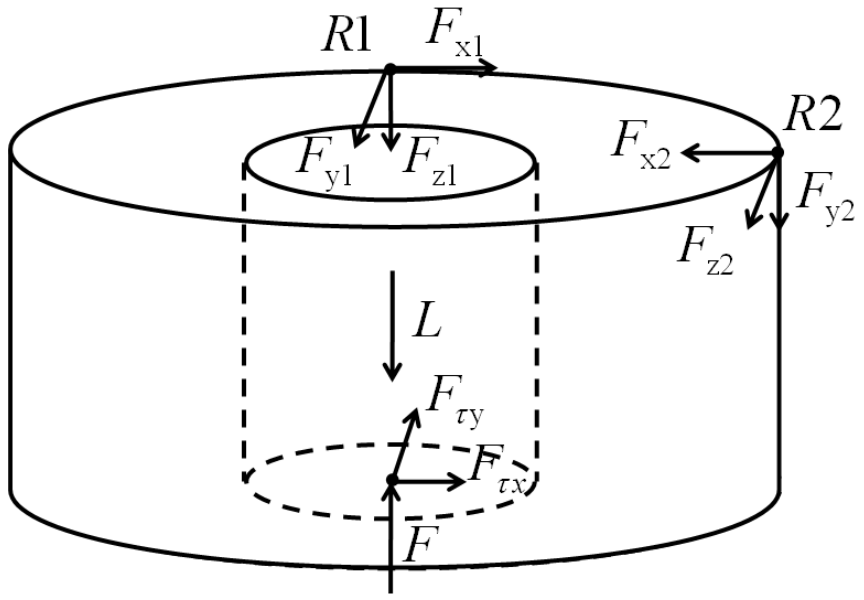

Figure 8.4 Forces applied by the two rollers to the top plate. (The reaction forces of rollers 1 and 2 are applied to points R1 and R2, respectively).

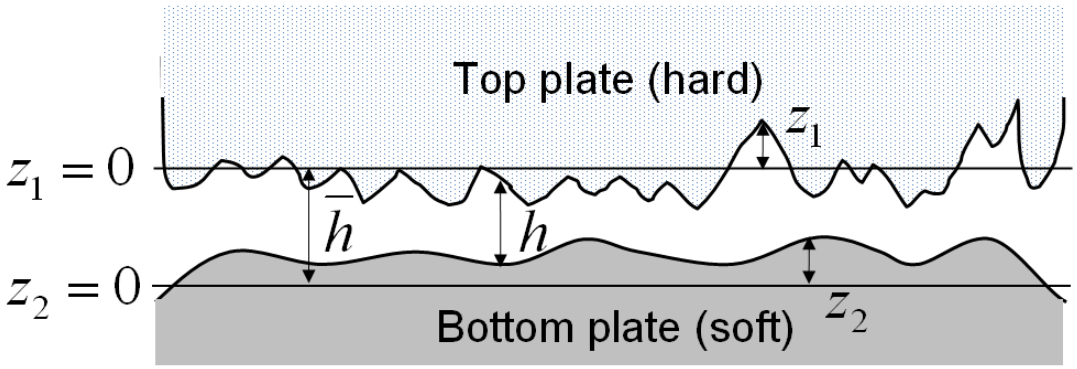

Figure 8.5 Schematic of probabilistic model of the particle embedment.

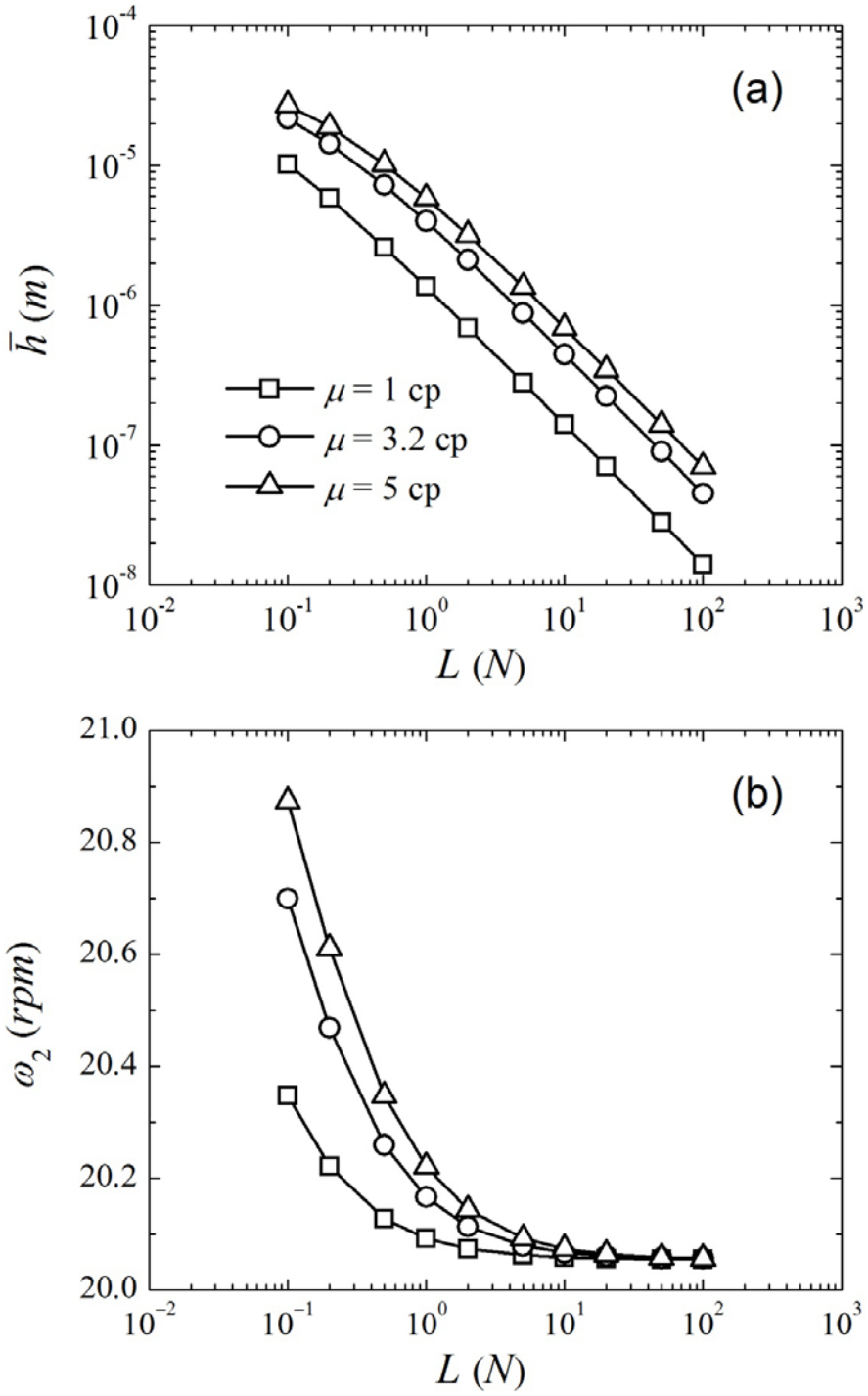

Figure 8.6 (a) Mean surface separation distance $\bar{h}$ and (b) top-plate rotational speed ω_2 versus applied normal load L for slurry viscosity μ = 1 cp, 3.2 cp and 5 cp for ω_1= 30 rpm, h_{top} = 50 mm, and $f_2/ f_1 = 3$.

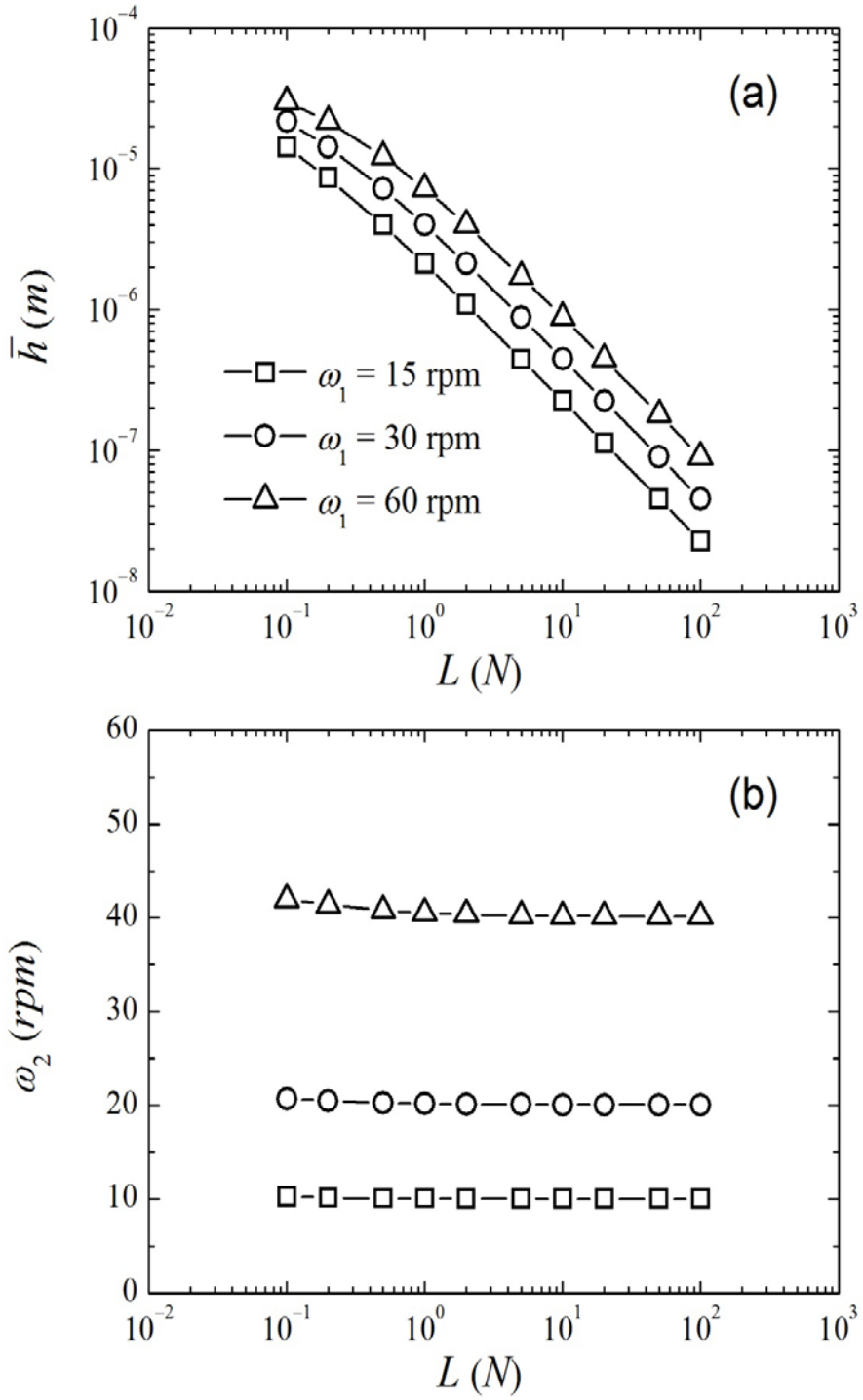

Figure 8.7 (a) Mean surface separation distance $\bar{h}$ and (b) top-plate rotational speed ω_2 versus applied normal load L for bottom-plate rotational speed ω_1 = 15 rpm, 30 rpm and 60 rpm for μ = 3.2 cp, h_{top} = 50 mm, and f_2/f_1 = 3.

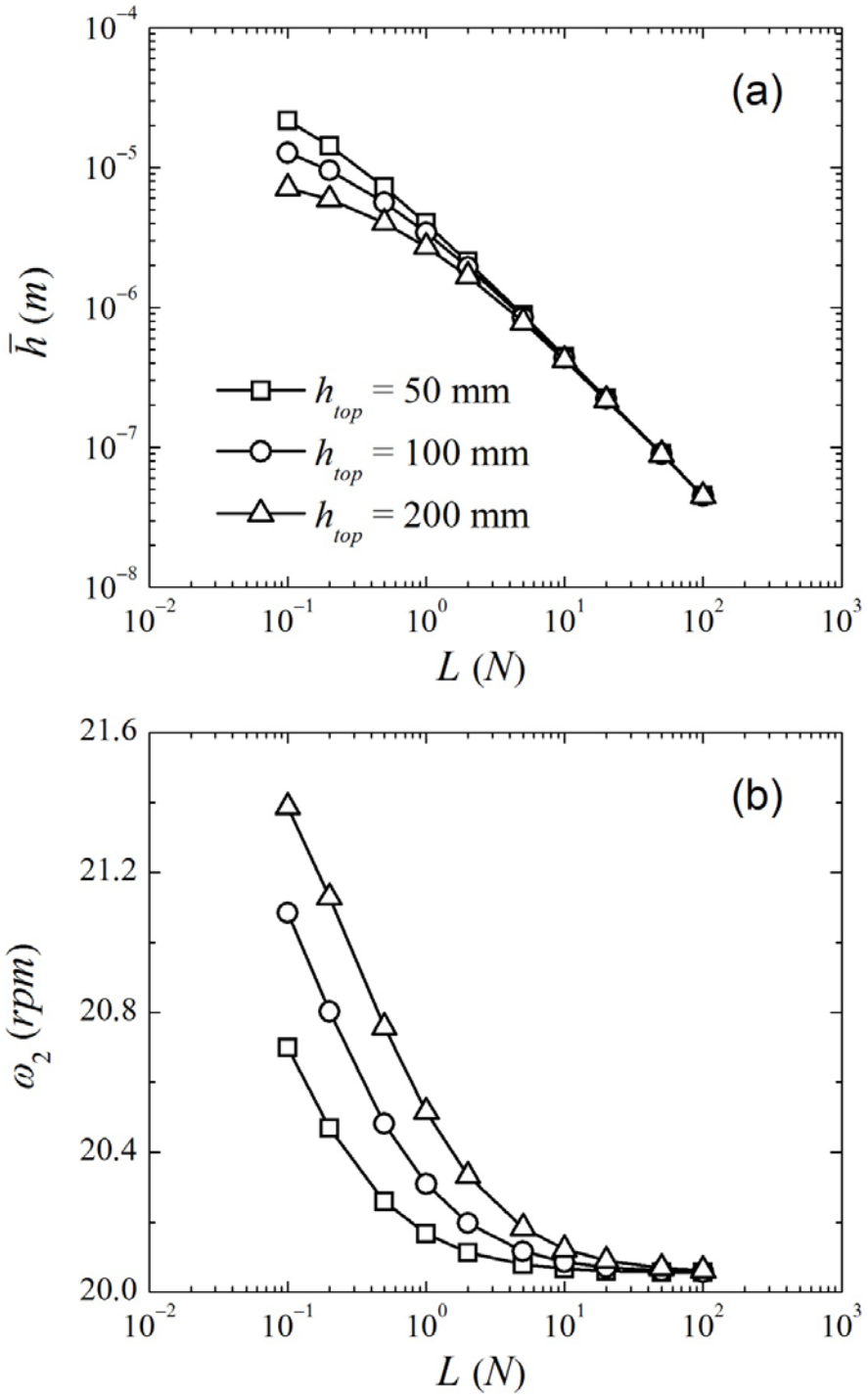

Figure 8.8 (a) Mean surface separation distance $\bar{h}$ and (b) top-plate rotational speed ω_2 versus applied normal load L for the height of the top plate h_{top} = 50 mm, 100 mm and 200 mm for μ = 3.2 cp, ω_1= 30 rpm, and f_2/f_1 = 3.

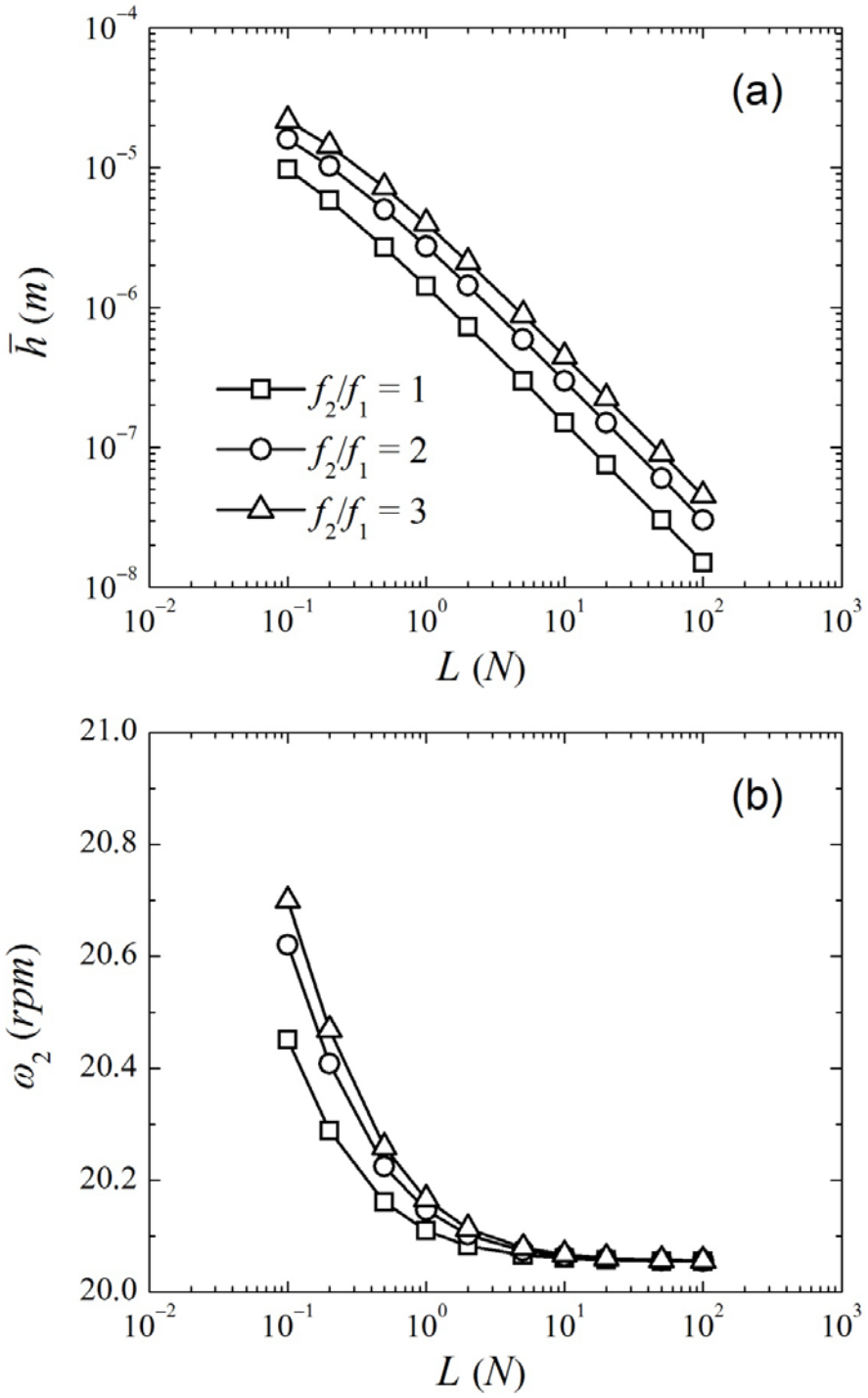

Figure 8.9 (a) Mean surface separation distance $\bar{h}$ and (b) top-plate rotational speed ω_2 versus applied normal load L for the ratio of friction coefficients f_2/f_1 = 1, 2 and 3 for μ = 3.2 cp, ω_1= 30 rpm, and h_{top} = 50 mm.

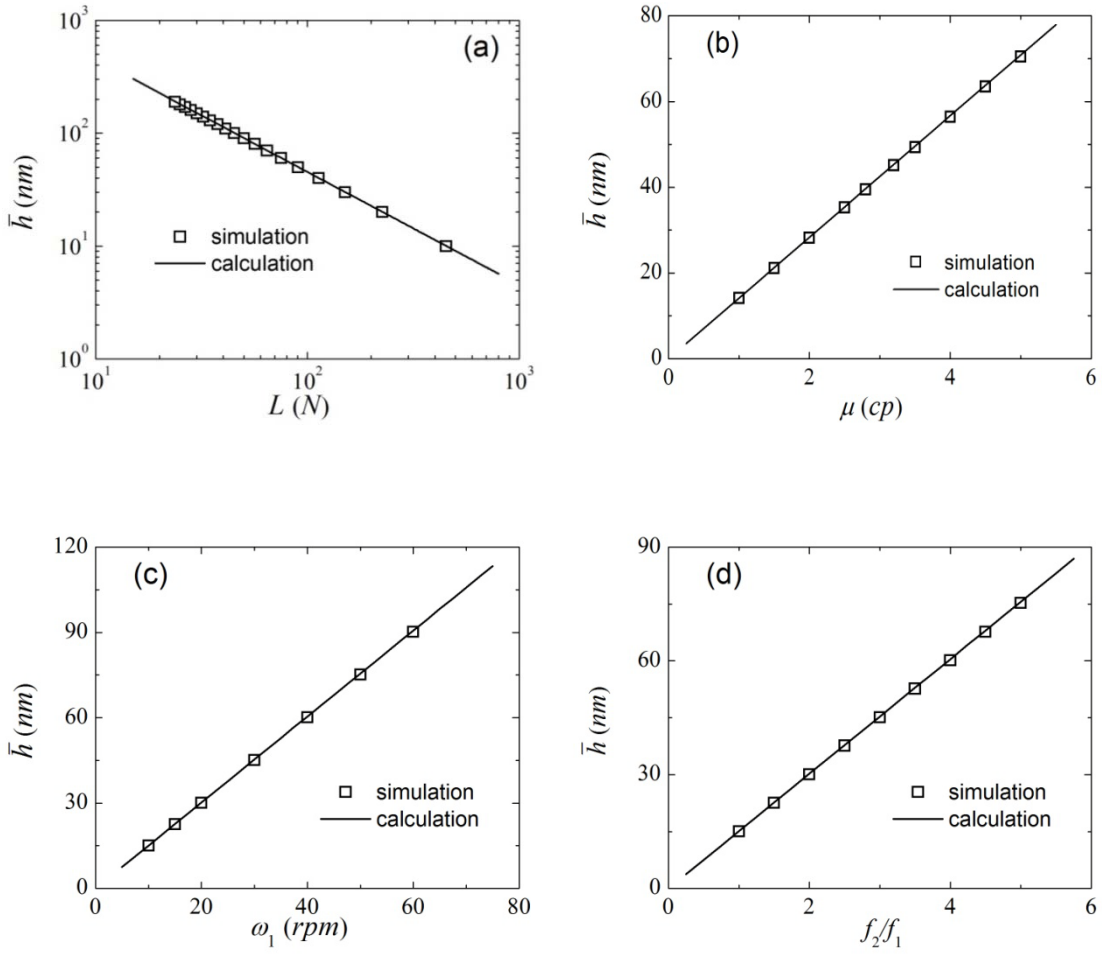

Figure 8.10 Comparisons between simulation results of hydrodynamic model and calculation values from Eq. (16) for nano-scale mean surface separation distance $\bar{h}$ based on the effects of (a) applied normal load L (μ = 3.2 cp, ω_1= 30 rpm, h_{top} = 50 mm, and f_2/f_1 = 3), (b) slurry viscosity μ (L = 100N, μ = 3.2 cp, ω_1= 30 rpm, h_{top} = 50 mm, and f_2/f_1 = 3), (c) bottom-plate rotational speed ω_1 (L = 100N, μ = 3.2 cp, h_{top} = 50 mm, and f_2/f_1 = 3), and (d) ratio of friction coefficients between rollers and top plate f_2/f_1 (L = 100N, μ = 3.2 cp, ω_1= 30 rpm, and h_{top} = 50 mm).

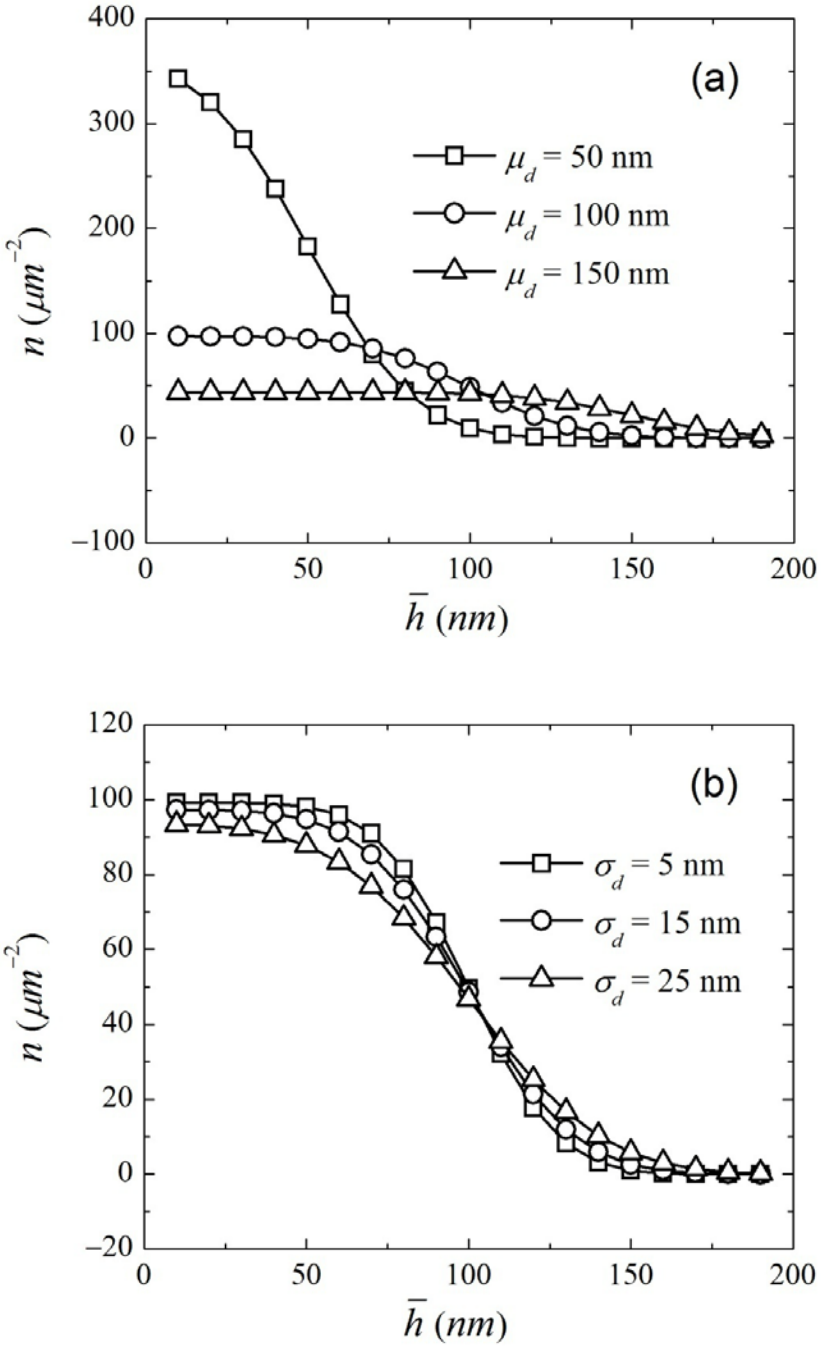

Figure 8.11 Embedded particle density n versus the mean surface separation distance $\bar{h}$ for (a) mean particle size μ_d = 50 nm, 100 nm and 150 nm (σ_d = 15 nm, σ_1 = 15 nm and σ_2 = 15 nm), and (b) standard deviation of the particle size σ_d = 5 nm, 15 nm and 25 nm (μ_d = 100 nm, σ_1 = 15 nm and σ_2 = 15 nm).

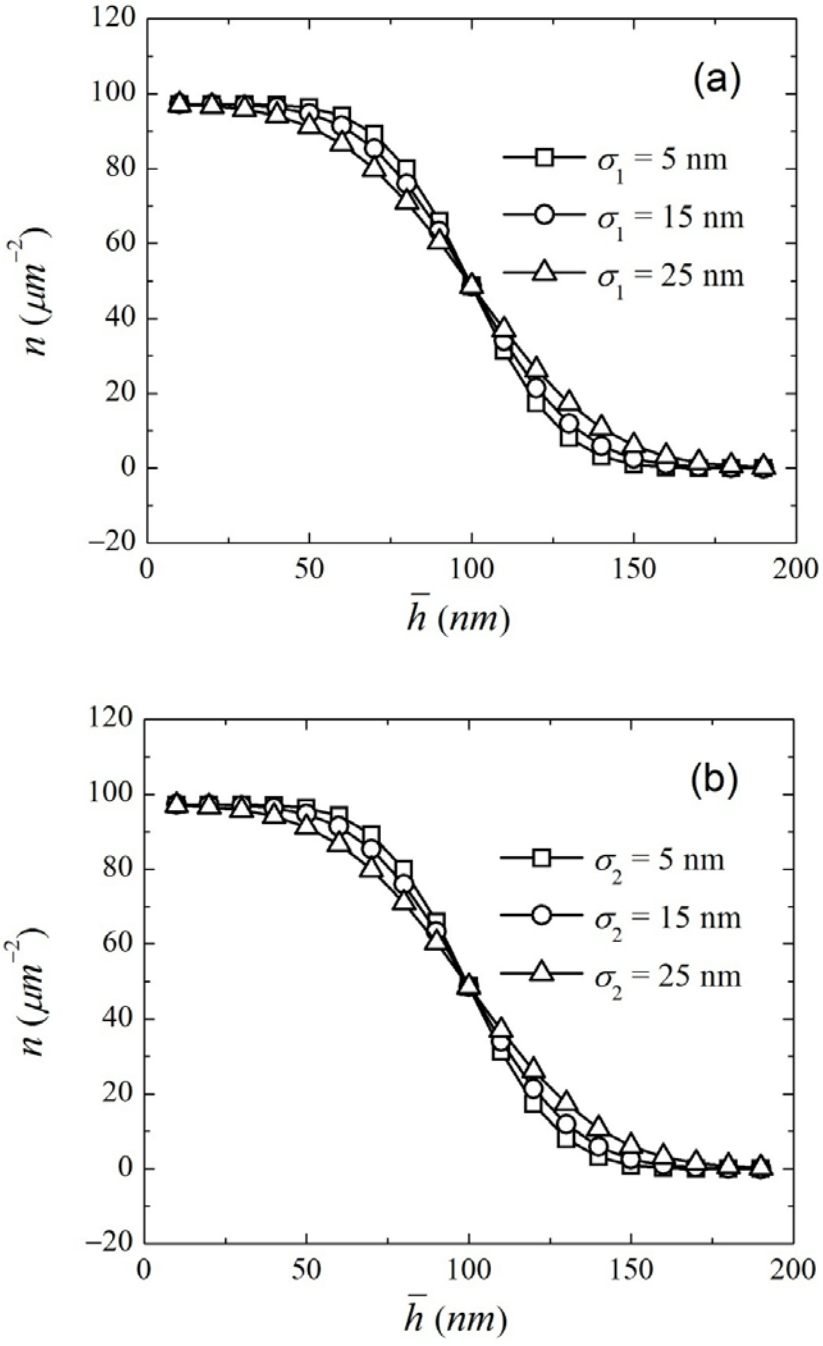

Figure 8.12 Embedded particle density n versus the mean surface separation distance $\bar{h}$ for (a) rms roughness of top plate σ_1 = 5 nm, 15 nm and 25 nm (μ_d = 100 nm, σ_d = 15 nm and σ_2 = 15 nm), and (b) rms roughness of bottom plate σ_2 = 5 nm, 15 nm and 25 nm (μ_d = 100 nm, σ_d = 15 nm and σ_1 = 15 nm).

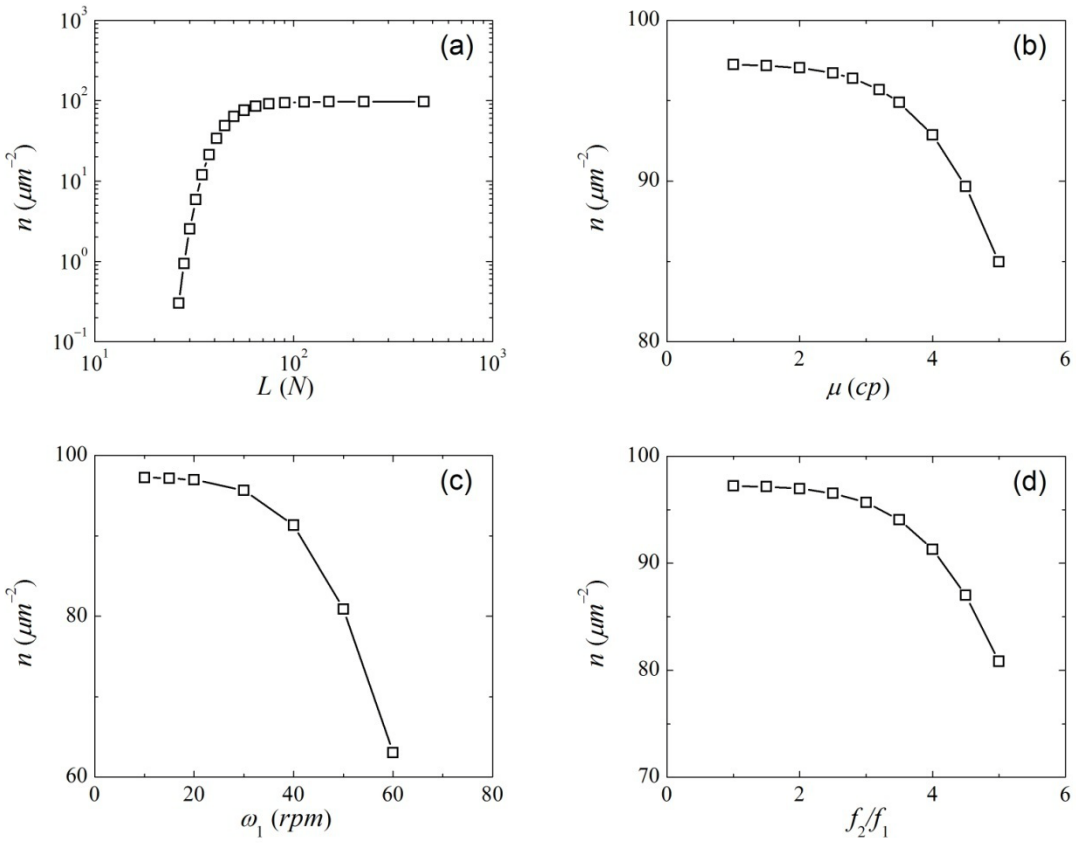

Figure 8.13 Effects of (a) applied normal load L (μ = 3.2 cp, ω_1= 30 rpm, h_{top} = 50 mm, and f_2/ f_1 = 3), (b) slurry viscosity μ (L = 100N, μ = 3.2 cp, ω_1= 30 rpm, h_{top} = 50 mm, and f_2/ f_1 = 3), (c) bottom-plate rotational speed ω_1 (L = 100N, μ = 3.2 cp, h_{top} = 50 mm, and f_2/ f_1 = 3), and (d) ratio of friction coefficients between rollers and top plate f_2/ f_1 (L = 100N, μ = 3.2 cp, ω_1= 30 rpm, and h_{top} = 50 mm) on the embedded particle density. (μ_d = 100 nm, σ_d = 15 nm, σ_1 = 15 nm and σ_2 = 15 nm)

Chapter 9
Conclusions

Contact mechanics analyses of nano/micro-scale solid surface interaction were performed for homogenous and layered media with smooth and rough surfaces. Based on the presented analyses, simulation results, and discussions, the following conclusions can be drawn from the work comprising this thesis.

To understand the effect of adhesion on the deformation behavior of sliding contacts, two-dimensional analytical and FEM models of a rigid asperity moving over an elastic-plastic half-space were developed. A constitutive relation derived from the L-J potential was used as the constitutive force-distance law of nonlinear spring elements used to model adhesive surface interaction. The appropriateness of these models was demonstrated by their capability to reproduce a nonzero friction force under a zero normal force and the good agreement between analytical solutions of the pull-off force with numerical results for adhesive line contacts showing a smooth transition from rigid contact behavior (Bradley model) to elastic contact behavior (JKR model) with the increase of the Maugis parameter. A nonlinear interdependence between normal and friction forces was observed at steady-state sliding. The important effect of adhesion was shown by the fact that a higher work of adhesion produced a higher attractive normal force component and more plasticity consequently achieved lower normal force and higher friction force at steady-state sliding. The pile-up of material ahead of the sliding asperity and the asymmetry of the deformed surface profile and the normal stress field increased with the work of adhesion, while the increase of the interaction distance and plasticity parameter and the decrease of the Maugis parameter intensified the friction force which, in turn, increased the plasticity and the asymmetry of the normal stress field.

The elastic analysis of adhesive sliding contact was extended to study adhesive sliding of a rigid asperity over an elastic-plastic half-space exhibiting EPP or ELKP behavior. Steady-state sliding conditions, indicated by the invariance of the friction and normal forces and the subsurface stresses with the increase of the sliding distance, were achieved after the first sliding cycle (EPP) or after the third or fourth sliding cycle (ELKP). Steady-state deformation modes were examined in the light of stress-strain responses and subsurface plastic strain distributions. Contact behavior was characterized by the sequential development of elastic deformation, elastic shakedown, plastic shakedown, and ratcheting. This sequence of deformation modes emerged with the increase of the plasticity parameter and the interaction distance or the decrease of the Maugis parameter. Strain hardening fully suppressed ratcheting, even in the case of very low-strength materials because of the profound decrease of plasticity accumulation at each sliding cycle, in qualitative agreement with results of previous studies. This trend was also reflected by deformation maps showing markedly larger domains of plastic shakedown for ELKP than EPP material behaviors and a decrease in the elastic limit with increasing interaction distance.

LEFM and FEM were used to analyze subsurface cracking in a layered medium due to adhesive sliding contact of a rigid asperity. The repetitive passage of the rigid asperity over the subsurface crack resulted in cyclic variation of the crack-tip stresses and, in turn, the mode I and

mode II SIFs, K_{I} and K_{II}. Adhesion between the sliding asperity and the layered medium intensified the crack-tip stresses, resulting in fluctuations of the normal and friction forces. The fracture direction due to the tensile and shear modes was obtained as the direction of maximum K_{σ}^{max} and K_{τ}^{max}, respectively; while the fatigue crack direction due the tensile and shear modes was obtained as the direction of maximum ΔK_{σ}^{max} and ΔK_{τ}^{max}, respectively. The propensity of fracture or fatigue cracking was enhanced by the increase of the interaction depth and the Maugis parameter and the decrease of the layer thickness and crack depth. It was shown that fracture cracks tend to only grow in out-of-plane tensile mode, while fatigue cracks exhibit a transition in their dominant mode of growth from in-plane shear mode to out-of-plane tensile mode with the increase of the Maugis parameter and the layer thickness and the decrease of the interaction depth and crack depth.

Surface cracking in an elastic asperity rubbing against a rigid plane was studied by LEFM, using a FEM model in which adhesion was modeled by nonlinear spring elements with a constitutive law derived from the L-J potential. Contact instabilities, such as abrupt surface contact (jump-in) and detachment (jump-out) affected the variation of the SIFs with the indentation displacement. This effect was especially pronounced for high values of the Maugis parameter (high adhesion), but rather insignificant for low values of the Maugis parameter (low adhesion). The direction and dominant mode of crack growth were determined by the ranges of maximum SIFs, $\Delta K_{\sigma}^{\max}$ and $\Delta K_{\tau}^{\max}$. Tensile mode crack growth was enhanced with the increase of the Maugis parameter, as shown by the increase of the opening crack mechanism region of the crack mechanism map and the more pronounced increase of $\Delta K_{\sigma}^{\max}$ compared to $\Delta K_{\tau}^{\max}$. The increase of the maximum indentation displacement increased $\Delta K_{\tau}^{\max}$ without changing $\Delta K_{\sigma}^{\max}$, thus increasing the likelihood for shear mode crack growth.

Asperity surface cracking due to repetitive sliding against a rigid asperity was also studied by LEFM and the FEM. Numerical results showed an enhancement of tensile-mode crack growth with increasing sliding friction and interaction depth, as demonstrated by the more pronounced increase of $\Delta K_{\sigma}^{\max}$ than $\Delta K_{\tau}^{\max}$ and the increase of the opening crack mechanism region of the crack mechanism map. For crack growth dominated by the tensile mode, the crack propagation angle (measured from the crack plane) increased with the sliding friction and interaction depth. The effects of the initial crack position and the crack-face friction on the mode and direction of crack propagation were found to be secondary.

A three-dimensional stochastic model of rough (fractal) surfaces that accounts for elastic, elastic-plastic, and fully-plastic deformation at the asperity level was used to analyze nanoscale surface polishing by hard abrasive nanoparticles embedded in the soft surface layer of a rigid plate. After an initial stage characterized by the rapid decrease of the roughness of the polished surface and the rate of the removal of material, steady-state polishing conditions were established as surface smoothening (removal of material) and roughening (surface plowing) reached an equilibrium stage. The decrease of the intensity of low-frequency components in the power spectral density function of the evolving surface topography revealed the length scales of surface features affected by nanoscale polishing. A smoother finished surface and a higher material removal rate were achieved with decreasing the surface roughness of the polishing plate and the size of the abrasive nanoparticles on the polishing plate or with increasing nanoparticle density and stiffness of the polished surface. The increase of the apparent pressure or the decrease of the

yield strength of the polished surface yielded higher material removal rates; however, the effect on the final roughness of the polished surface was negligible. The validity of the stochastic model developed in this thesis was confirmed by favorable comparisons between numerical and experimental results of the steady-state roughness and material removal rate of Al_2O_3-TiC surfaces polished by diamond nanoparticles. Because of the significant effect of the nanoparticle density on surface finish and the removal rate of material, a probabilistic model was incorporated in a hydrodynamic analysis to analyze third-body particle embedment between two plates separated by a thin hydrodynamic fluid film. The nano-scale mean surface separation distance between the two surfaces separated by the hydrodynamic film was found to be inversely proportional to the applied normal load and proportional to the slurry viscosity, the rotational speed of the moving upper surface, and the ratio of the friction coefficients between the top plate and the rollers. The nanoparticle density increased with the applied normal load or the decrease of the slurry viscosity, bottom-plate rotational speed, and ratio of friction coefficients between the top plate and the rollers. Moreover, the density of the embedded nanoparticles was found to strongly correlate with the mean nanoparticle size, while the effects of the standard deviation of the nanoparticle size and the surface topographies were found to be negligibly small.

Summarizing, the significance of interfacial and material properties on adhesive sliding contact and asperity surface/subsurface cracking and the dependence of the surface topography evolution during nanoscale polishing on the surface topographies, material properties, and abrasive nanoparticle size were investigated in the light of analytical and numerical results. The findings of this thesis elucidate the deformation behavior of adhesive contacts, both homogeneous and layered contacts involving real surfaces exhibiting multi-scale roughness. Simulation results provide insight into the underlying reasons for mechanical failure in nano/microscale engineering components and surfacing processes, such as hard-disk drives, micro-electro-mechanical systems, and nanoscale surface polishing. The presented numerical and analytical results for single-asperity contacts can be integrated into probabilistic sliding contact analyses of adhesive rough surfaces.

References

Archard, J.F., 1953, “Contact and rubbing of flat surfaces,” *J. Appl. Phys.*, **24**, pp. 981-988.

Attard, P., and Parker, J. L., 1992, “Deformation and adhesion of elastic bodies in contact,” *Phys. Rev. A*, **46**, pp. 7959-7971.

Ausloos, M., and Berman, D. H., 1985, “A Multivariate Weierstrass–Mandelbrot Function,” *Proc. R. Soc. London, Ser. A.*, **400**, pp. 331–350.

B. Liu, S.H. Soh and A. Chekanov, et al., 1996, “Particle Build-up on Flying Sliders and Mechanism Study of Disk Wear and Head-Disk Interface Failure in Magnetic Disk Drives,” *IEEE T. Magn.*, **32**, pp. 3687-3689.

Basim, G. B., Adler, J. J., Mahajan, U., Singh, R. K., and Moudgilz, B. M., 2000, “Effect of Particle Size of Chemical Mechanical Polishing Slurries forEnhanced Polishing with Minimal Defects,” *J. Electrochem. Soc.*, **147**, pp. 3523-3528.

Bassani, R., and D’Acunto, M., 2000, “Nanotribology: tip-sample wear under adhesive contact,” *Tribol. Int.*, **33**, pp. 443-452.

Berry, M. V., and Lewis, Z. V., 1980, “On the Weierstrass–Mandelbrot Fractal Function,” *Proc. R. Soc. London, Ser. A*, **370**, pp. 459–484.

Bhargava, V., Hahn, G.T., Rubin, C.A., 1985, “An elastic-plastic finite element model of rolling contact – part 2: analysis of repeated contacts,” *ASME J. Appl. Mech.*, **52**, pp. 75–82.

Bogy, D.B., Yun, X., and Knapp, B.J., 1994, “Enhancement of head-disk interface durability by use of diamond-like carbon overcoats on the slider's rails,” *IEEE T. Magn.*, **30**, pp. 369-374.

Bower, A.F., Johnson, K.L., 1989, “The influence of strain hardening on cumulative plastic deformation in rolling and sliding line contact,” *J. Mech. Phys. Solids*, **37**, pp. 471–493.

Bower, A.F., Johnson, K.L., 1991, “Plastic flow and shakedown of the rail surface in repeated wheel-rail contact,” *Wear*, **144**, pp. 1–18.

Bradley, R. S., 1932, “The cohesive force between solid surfaces and surface energy of solids,” *Phil. Mag.*, **13**, pp. 853-862.

Burwell, J. T., and Strang, C. D., 1952, “On the Empirical Law of Adhesive Wear,” *J. Appl. Phys.*, **23**, pp. 18-28.

Carpick, R. W., Agraït, N., Ogletree, D. F., and Salmeron, M., 1996, “Variation of the Interfacial Shear Strength and Adhesion of a Nanometer-Sized Contact,” *Langmuir*, **12**, pp. 3334–3340.

Chan, S.K., Tuba, I.S., and Wilson, W.K., 1970, "On the Finite Element Method in Linear Fracture Mechanics," *Eng. Fract. Mech.*, **2**, pp. 1-17.

Chandross, M., Lorenz, C. D., Stevens, M. J., and Grest, G. S., 2008, "Simulations of Nanotribology with Realistic Probe Tip Models," *Langmuir*, **24**, pp. 1240–1246.

Chaudhury, M. K., Weaver, T., Hui, C. Y., and Kramer, E. J., 1996, "Adhesive contact of cylindrical lens and a flat sheet," *J. Appl. Phys.*, **80**, pp. 30-37.

Chen, H., and Chen, D., 2005 "Modified Reynolds Equation for Non-Newtonian Fluid with Rheological Model in Frequency Domain," *J. Tribol.*, **127**, pp. 893–897.

Cho, S.S., and Komvopoulos, K., 1997a, "Wear Mechanisms of Multi-Layer Coated Cemented Carbide Cutting Tools," *ASME J. Tribol.*, 119, pp. 8-17.

Cho, S.-S., and Komvopoulos, K., 1997b, "Thermo-elastic Finite Element Analysis of Subsurface Cracking due to Sliding Surface Traction," *ASME J. Eng. Mater. Tech.*, **119**, pp. 71-78.

D.M. Tanner, 2000, "Reliability of Surface Micromachined Micro-Electro-Mechanical Actuators," *Proc 22nd International Conference on Microelectronics*, **1**, pp. 97-104.

Deng, Z., Yenilmez, E., and Leu, J., et al., 2004, "Metal-coated carbon nanotube tips for magnetic force microscopy ," *Appl. Phys. Lett.*, **85**(25), pp. 6263-6265.

Derjaguin, B. V., 1934, "Untersuchungen uber die reibung und adhasion: IV. Theorie des anhaftens kleiner teilchen," *Kolloid Z.*, **69**, pp. 155-14.

Derjaguin, B. V., Muller, V. M., and Toporob, Y. P., 1975, "Effect of contact deformations on the adhesion of particles," *J. Colloid Interface Sci.*, **53**, pp. 314-326.

Dwyer-Joyce, R.S., 1999, "Predicting the Abrasive Wear of Ball Bearings by Lubricant Debris," *Wear*, **233–235**, pp. 692–701.

Dwyer-Joyce, R.S., Sayles, R.S., and Ioannides, E., 1994, "An Investigation into the Mechanisms of Closed Three-body Abrasive Wear," *Wear*, **175**, pp. 133-142.

Erdogan, F., and Sih, G.C., 1963, "On the Crack Extension in Plates under Plane Loading and Transverse Shear," *J. Basic Eng.*, **85**, pp. 519-527.

Evans, C.J., Paul, and E., Dornfeld, D., *et al.*, 2003, "Material Removal Mechanisms in Lapping and Polishing," *Ann. CIRP – Manuf. Technol.*, **52**, pp. 611–633.

Fu, G., Chandra, A., Guha, S., and Subhash, G., 2001, "A Plasticity-Based Model of Material Removal in Chemical–Mechanical Polishing (CMP)," *IEEE Trans. Semicond. Manuf.*, **14**, pp. 406-417.

Gao, G., Cannara, R. J., Carpick, R. W., and Harrison, J. A., 2007, "Atomic-Scale Friction on Diamond: A Comparison of Different Sliding Directions on (001) and (111) Surfaces Using MD and AFM," *Langmuir*, **23**, pp. 5394–5405.

Georges, J.M., and Rabinowicz, E., 1969, "The effect of film thickness on the wear of hard electro-deposits," *Wear*, **14**, pp. 171-180.

Gong, Z.-Q., and Komvopoulos, K., 2005, "Contact Fatigue Analysis of an Elastic-Plastic Layered Medium with a Surface Crack in Sliding Contact with a Fractal Surface," *ASME J. Tribol.*, **127**, pp. 503-512.

Greenwood, J. A., 1997, "Adhesion of elastic spheres," *Proc. R. Soc. Lond. A*, **453**, pp. 1277-1297.

Hintermann, H.E, 1984, "Adhesion, friction and wear of thin hard coatings," *Wear*, **100**, pp. 381-397.

Hoivik, N.D., Elam, J.W., and Linderman, R. J., et al., 2003, "Atomic layer deposited protective coatings for micro-electromechanical systems," *Sensor actuator*, **A103**, pp. 100-108.

Hu, J., Xiao, X.-D., Ogletree, D. F., and Salmeron, M., 1995, "Atomic Scale Friction and Wear of Mica," *Surf. Sci.*, **327**, pp. 358–370.

Israelachvili, J. N., 1992, "Intermolecular and surface forces," Academic Press, San Diego, CA.

Jahanmir and N. P. Suh, 1977, "Mechanics of Subsurface Void Nucleation in Delamination Wear," *Wear*, **25**, pp. 17-38.

Jiang, M., Hao, S., and Komanduri, R., 2003, "On the advance lapping process in precision finishing of thin-film magnetic recording heads for rigid disc drives," *Appl. Phys. A*, **77**, pp. 923-932.

Johnson, K.L., 1962, "A shakedown limit in rolling contact," Proceedings of the Fourth National Conference on Applied Mechanics, Berkeley, CA, pp. 971–975.

Johnson, K.L., 1985, "Contact Mechanics," Cambridge University Press, Cambridge, UK.

Johnson, K. L., and Greenwood, J. A., 1997, "An Adhesion Map for the Contact of Elastic Spheres," *J. Colloid Interface Sci.*, **192**, pp. 326-333.

Johnson, K.L., Greenwood, J.A., 2008, "Maugis analysis of adhesive line contact," *J. Phys. D: Appl. Phys.*, **41**, pp. 155315(1)–155315(6).

Johnson, K.L., Jefferis, J.A., 1963, "Plastic flow and residual stresses in rolling and sliding contact," Proceedings of the Institution of Mechanical Engineers of London, Symposium on Rolling Contact Fatigue, London, UK, pp. 50–61.

Johnson, K. L., Kendall, K., and Robert, A. D., 1971 “Surface energy and the contact of elastic solids,” *Proc. R. Soc. Lond. A*, **324**, pp. 301-313.

Kadin, Y., Kligerman, Y., and Etsion, I., 2008a, “Loading–Unloading of an Elastic–Plastic Adhesive Spherical Microcontact,” *J. Colloid Interface Sci.*, **321**, pp. 242–250.

Kadin, Y., Kligerman, Y., and Etsion, I., 2008b, “Cyclic Loading of an Elastic-Plastic Adhesive Spherical Microcontact,” *J. Appl. Phys.*, **104**, pp. 073522(1) –073522(8).

Kang, Y.S., Sadeghi, F., and Ai, X., 2000, “Debris Effects on EHL Contact,”*J. Eng. Tribol*., **122**, pp. 711–720.

Kapoor, A., Williams, J.A., 1994, “Shakedown limits in sliding contacts on a surface-hardened half-space,” *Wear*, **172**, pp. 197–206.

Kim, S. H., Asay, D. B., and Dugger, M. T., 2007, “Nanotribology and MEMS,” *Nano Today*, **2**, pp. 22–29.

Ko, P. L., Iyer, S.S., and Vaughan, H., et al., 2001, “Finite Element Modeling of Crack Growth and Wear Particle Formation in Sliding Contact,” *Wear*, **251**, pp. 1265-1278.

Kogut, L., and Komvopoulos, K., 2004, “Analysis of the Spherical Indentation Cycle for Elastic–Perfectly Plastic Solids,” *J. Mater. Res.*, **19**, pp. 3641–3653.

Koiter, W.T., 1956, “A new general theorem on shakedown of elastic-plastic structures,” *Koninkl. Ned. Ak. Wetenschap*, **B59**, pp. 24–50.

Komvopoulos, K., 1996, “Surface Engineering and Microtribology for Microelectromechanical Systems,” *Wear*, **200**, pp. 305–327.

Komvopoulos, K., 2000, “Head-Disk Interface Contact Mechanics for Ultrahigh Density Magnetic Recording,” *Wear*, **238**, pp. 1–11.

Komvopoulos, K., 2003, “Adhesion and friction forces in microelectromechanical systems: mechanisms, measurement, surface modification techniques, and adhesion theory,” *J. Adhes. Sci. Technol.*, **17**, pp. 477–517.

Komvopoulos, K., 2012, “Adhesive Wear,” In Handbook of Lubrication and Tribology, Volume II: Theory and Design, second ed. (ed. R.W. Bruce), CRC Press, Boca Raton, FL.

Komvopoulos, K., and Cho, S.-S., 1997, “Finite Element Analysis of Subsurface Crack Propagation in a Half-space due to a Moving Asperity Contact,” *Wear*, **209**, pp. 57-68.

Komvopoulos, K., and Yan, W., 1997a, “A Fractal Analysis of Stiction in Microelectromechanical Systems,” *ASME J. Tribol.*, **119**, pp. 391–400.

Komvopoulos, K., and Yan, W., 1997b, “Molecular Dynamics Simulation of Single and Repeated Indentation,” *J. Appl. Phys.*, **82**, pp. 4823–4830.

Komvopoulos, K., and Ye, N., 2001, “Three-Dimensional Contact Analysis of Elastic–Plastic Layered Media With Fractal Surface Topographies,” *ASME J. Tribol.*, **123**, pp. 632–640.

Komvopoulos, K., Saka, N., and Suh, N.P., 1987, “The Role of Hard Layers in Lubricated and Dry Sliding,” *ASME J. Tribol.*, **109**, pp. 223-231.

Kral, E. R., and Komvopoulos, K., 1996a, “Three-Dimensional Finite Element Analysis of Surface Deformation and Stresses in an Elastic-Plastic Layered Medium Subjected to Indentation and Sliding Contact Loading,” *ASME J. Appl. Mech.*, **63**, pp. 365–375.

Kral, E.R., Komvopoulos, K., 1996b, “Three-dimensional finite element analysis of subsurface stress and shakedown due to repeated sliding on a layered medium,” *ASME J. Tribol.*, **63**, pp. 967–973.

Kral, E. R., and Komvopoulos, K., 1997, “Three-Dimensional Finite Element Analysis of Subsurface Stress and Strain Fields Due to Sliding Contact on an Elastic-Plastic Layered Medium,” *ASME J. Tribol.*, **119**, pp. 332–341.

Kulkarni, S.M., Hahn, G.T., Rubin, C.A., Bhargava, V., 1990, “Elastoplastic finite element analysis of three-dimensional, pure rolling contact at the shakedown limit,” *ASME J. Appl. Mech.*, **57**, pp. 57–65.

Kulkarni, S.M., Hahn, G.T., Rubin, C.A., Bhargava, V., 1991, “Elasto-plastic finite element analysis of three-dimensional pure rolling contact above the shakedown limit,” *ASME J. Appl. Mech.*, **58**, pp. 347–353.

Larsen-Basse, J., and Liang, H., 1999, “Probable Role of Abrasion in Chemo–Mechanical Polishing of Tungsten,” *Wear*, **233**–**235**, pp. 647-654.

Lei, H., and Luo, J., 2004, “CMP of hard disk substrate using a colloidal SiO2 slurry: preliminary experimental investigation,” *Wear*, **257**, pp. 461-470.

Leng, Y. S., Hu, Y. Z., and Zheng, L. Q., 2000, “Adhesion of smoothly flat-ended wedges,” *Proc. R. Soc. Lond. A*, **456**, pp. 185-204.

Lisowski, Z., and Stolarski, T.A., 1981, “A modified theory of adhesive wear in lubricated contacts,” *Wear*, **68**, pp. 333 ‑ 345.

Lu, W., and Komvopoulos, K., 2001, “Nanomechanical and Nanotribological Properties of Carbon, Chromium, and Titanium Carbide Ultrathin Films,” *ASME J. Tribol.*, **123**, pp. 717–724.

Luan, B., Robbins, M.O., 2005, “The breakdown of continuum models for mechanical contacts,” *Nature*, **435**, 929–932.

Luo, J. F., and Dornfeld, D. A., 2003a, “Material Removal Regions in Chemical Mechanical Planarization for Submicron Integrated Circuit Fabrication: Coupling Effects of Slurry

Chemicals, Abrasive Size Distribution and Wafer-pad Contact Area," *IEEE Trans. Semicond. Manuf.*, **16**, pp. 45–56.

Luo, J. F., and Dornfeld, D. A., 2003b, "Material removal mechanism in chemical mechanical polishing: Theory and modeling," *IEEE Trans. Semicond. Manuf.*, **14**, pp. 112–133.

Maboudian, R., Ashurst, W.R., Carraro, C., 2002, "Tribological challenges in micromechanical systems," *Tribol. Lett.*, **12**, pp. 95–100.

Mageed, A.M.A., and Pandey, R. K., 1992, "Studies on Cyclic Crack Path and the Mixed-Mode Crack Closure Behaviour in Al Alloy," *Int. J. Fatigue*, **14**, pp. 21-29.

Mailhot, B., Komvopoulos, K., Ward, B., Tian, Y., and Somorjai, G. A., 2001, "Mechanical and Friction Properties of Thermoplastic Polyurethanes Determined by Scanning Force Microscopy," *J. Appl. Phys.*, **89**, pp. 5712–5719.

Majumdar, A., and Bhushan, B., 1990, "Role of Fractal Geometry in Roughness Characterization and Contact Mechanics of Surfaces," *ASME J. Tribol.*, **112**, pp. 205–216.

Majumdar, A., and Bhushan, B., 1991, "Fractal Model of Elastic–Plastic Contact Between Rough Surfaces," *ASME J. Tribol.*, **113**, pp. 1–11.

Majumdar, A., and Tien, C. L., 1990, "Fractal Characterization and Simulation of Rough Surfaces," *Wear*, **136**, pp. 313-327.

Mandelbrot, B. B., 1967, "How Long is the Coast of Britain? Statistical Self-Similarity and Fractional Dimension," *Science*, **156**, pp. 636–638.

Maugis, D., 1992, "Adhesion of spheres: the JKR-DMT transition using a Dugdale model," *J. Colloid Interface Sci.*, **150**, pp. 243-269.

Mayer, T.M., Elam, J.W., and George, S.M., et al., 2003, "Atomic-layer deposition of wear-resistant coatings for microelectromechanical devices," *Appl. Phys. Lett.*, **82**(17), pp. 2883-2885.

Melan, E., 1938, "Der Spannungszustand eines "Hencky-Mises'schen" Kontinuums bei veraenderlicher Belastung," *Sitzungsberichte der Akademie der Wissenschaften in Wien*, **147**, pp. 73–87.

Merwin, J.E., Johnson, K.L., 1963, "An analysis of plastic deformation in rolling contact," *Proceedings of the Institution of Mechanical Engineers of London*, **177**, pp. 676–690.

Miettinen, J., and Andersson, P., 2000, "Acoustic emission of rolling bearings lubricated with contaminated grease," *Tribol. Inter.*, **33**, pp. 777-787.

Mishra, M., and Szlufarska, I., 2012, Analytical Model for Plowing Friction at Nanoscale," *Tribol. Lett.*, **45**, pp. 417–426.

Mo, Y., Turner, K. T., and Szlufarska, I., 2009, "Friction Laws at the Nanoscale," *Nature*, **457**, pp. 1116–1119.

Muller, V. M., Yushchenko, V. S., and Derjaguin, B. V., 1980, "On the influence of molecular forces on the deformation of an elastic sphere and its sticking to a rigid plane," *J. Colloid Interface Sci.*, **77**, pp. 91-101.

Nelias, D., and Ville, F., 2000, "Detrimental Effects of Debris Dents on Rolling Contact Fatigue," *J. Eng. Tribol*., **122**, pp. 55–64.

Nilsson, R., Dwyer-Joyce, R.S., and Olofsson, U., 2006, "Abrasive Wear of Rolling Bearings by Lubricant Borne Particles," *J. Eng. Tribol*., **220**, pp. 429–439.

Otsuka, A., Mori, K., and Miyata, T., 1975, "The condition of fatigue crack growth in mixed mode condition," *Eng. Fract. Mech.*, **7**, pp. 429-439.

Paldey, S. and Deevi, S.C., 2003, "Single layer and multilayer wear resistant coatings of (Ti,Al)N: a review," *Mater. Sci. Eng.*, **A342**, pp. 58-79.

Paris and F. Erdogan, 1963, "A Critical Analysis of Crack Propagation Laws," *J. Basic Eng.*, **85**, pp. 528-534.

Park, S.S., Cho, C-H., and Ahn, Y., 2000, "Hydrodynamic Analysis of Chemical Mechanical Polishing Process", *Tribol. Int.*, **33**, pp. 723–730.

Ponter, A.R.S., Hearle, A.D., Johnson, K.L., 1985, "Application of the kinematical shakedown theorem to rolling and sliding point contacts," *J. Mech. Phys. Solids*, **33**, pp. 339–362.

Prabhakaran, V. and Talke, F.E., 2000, "Wear and hardness of carbon overcoats on magnetic recording sliders," *Wear*, **243**, pp. 18–24.

Preston, F. W., 1927, "The Theory and Design of Plate Glass Polishing Machines," *J. Soc. Glass Technol.*, **11**, pp. 214–256.

Rabinowicz, E., 1995, *Friction and Wear of Materials*, 2nd edition, Wiley, New York.

Ramarajan, S., and Hariharaputhiran, M., Her, Y.S., and Babu, S.V., 1999, "Hardness of Submicrometre Abrasive Particles and Polish Rate Measurements," *Surf. Eng.*, **15**, pp. 324-328.

Riedo, E., Chevrier, J., Comin, F., and Brune, H., 2001, "Nanotribology of Carbon Based Thin Films: The Influence of Film Structure and Surface Morphology," *Surf. Sci.*, **477**, pp. 25–34.

Ringlein, J., and Robbins, M. O., 2004, "Understanding and Illustrating the Atomic Origins of Friction," *Am. J. Phys.*, **72**, pp. 884–891.

Shen, R., and Zhong, J., 2006, "Ultra Precision Polishing of GMR Hard-Disk Magnetic Head," 7th Int. Conf. Elect. Packaging Technol., 26-29 August 2006.

Sih, G.C., 1974, “Strain-Energy-Density Factor Applied to Mixed Mode Crack Problems,” *Inter. J. Fracture*, **10**, pp. 305-321.

Sih, G.C., and Barthelemy, B.M., 1980, “Mixed mode fatigue crack growth predictions,” *Eng. Fract. Mech.*, **13**, pp. 439-451.

Song, Z., Komvopoulos, K., 2011, “Adhesion-induced instabilities in elastic and elastic–plastic contacts during single and repetitive normal loading,” *J. Mech. Phys. Solids*, **59**, 884–897.

Suh, N. P., 1973, “The Delamination Theory of Wear,” *Wear*, **25**, pp. 111-124.

Suh, N. P., 1977, “An Overview of the Delamination Theory of Wear,” *Wear*, **25**, pp. 1-16.

Sun, D.C., 1997, “Equations Used in Hydrodynamic Lubrication,” *Lubr. Eng.*, **53**, pp. 18–25.

Tabor, D., 1977, “Surface forces and surface interactions,” *J. Colloid Interface Sci.*, **58**, pp. 2-13.

Tian, H., and Saka, N., 1991, “Finite Element Analysis of an Elastic-Plastic Two-Layer Half-Space: Sliding Contact,” *Wear*, **148**, pp. 261–285.

Tichy, J., Levert, J. A., Shan, L., and Danyluk, S., 1999, “Contact Mechanics and Lubrication Hydrodynamics of Chemical Mechanical Polishing,” *J. Electrochem. Soc.*, **146**, pp. 1523–1528.

Tjiptoharsono, F., Gonzaga, L. V., Zhang, M., Hua, W., and Liu, B., 2010, “Slider Surface Control for Ultra-High Density Recording,” *Microsyst. Technol.*, **16**, pp. 301–307.

Touge, M., and Matsuo, T., 1996, “Removal Rate and Surface Roughness in High-Precision Lapping of Mn-Zn Ferrite,” *Annals of the CIRP*, **45**, pp. 307–310.

Wei, B., and Komvopoulos, K., 1996, “Nanoscale Indentation Hardness and Wear Characterization of Hydrogenated Carbon Thin Films,” *ASME J. Tribol.*, **118**, pp. 431–438.

Wu, J.-J., 2009, “Adhesive contact between a cylinder and a half-space,” *J. Phys. D: Appl. Phys.*, **42**, pp. 155302.

Yan, W., and Komvopoulos, K., 1998a, “Contact Analysis of Elastic–Plastic Fractal Surfaces,” *J. Appl. Phys.*, **84**, pp. 3617–3624.

Yan, W., and Komvopoulos, K., 1998b, “Three-Dimensional Molecular Dynamics Analysis of Atomic-Scale Indentation,” *ASME J. Tribol.*, **120**, pp. 385–392.

Yang, J., and Komvopoulos, K., 2005a, “A Mechanics Approach to Static Friction of Elastic–Plastic Fractal Surfaces,” *ASME J. Tribol.*, **127**, pp. 315–324.

Yang, J., and Komvopoulos, K., 2005b, “A Molecular Dynamics Analysis of Surface Interference and Tip Shape and Size Effects on Atomic-Scale Friction,” *ASME J. Tribol.*, **127**, pp. 513–521.

Yu, M., Moran, B., Keer, L.M., 1993, “A direct analysis of two-dimensional elastic-plastic rolling contact,” *ASME J. Tribol.*, **115**, 227–236.

Zhao, Y., and Chang, L., 2002, “A Micro-Contact and Wear Model for Chemical–Mechanical Polishing of Silicon Wafers,” *Wear*, **252**, pp. 220-226.

Zhou, C., Shan, L., Hight, J. R., Danyluk, S., Ng, S. H. and Paszkowski, A. J., 2002, “Influence of Colloidal Abrasive Size on Material Removal Rate and Surface Finish in SiO2 Chemical Mechanical Polishing,” *Tribol. T.*, **45**, pp. 232-238.